The Pennsylvania State University

The Graduate School

College of Engineering

MULTIPLE SCATTERING MEASUREMENTS USING MULTISTATIC LIDAR

A Dissertation in

Electrical Engineering

by

Jin Hyen Park

Submitted in Partial Fulfillment
of the Requirements
for the Degree of

Doctor of Philosophy

May 2008

The dissertation of Jin Hyen Park was reviewed and approved* by the following:

C. Russell Philbrick
Professor of Electrical Engineering
Thesis Advisor
Chair of Committee

Victor Pasko
Associate Professor of Electrical Engineering

Zhiwen Liu
Assistant Professor of Electrical Engineering

Anne M. Thompson
Professor of Meteorology

W. Kenneth Jenkins
Professor of Electrical Engineering
Head of the Department of Electrical Engineering

* Signatures are on file in the Graduate School.

ABSTRACT

This thesis addresses the problem of multiple scattering in atmosphere. Multiple scattering is an important factor in treating the penetration of radiation through an optically thick medium, such as clouds and fog. A multistatic lidar system, which was developed at Pennsylvania State University, has the ability to evaluate multiple scattering effects in a dense medium by measuring polarization ratio of the scattering phase function at different scattering angles and radial distributions of a transmitted laser beam. Measurements of aerosol properties as a function of scattering angle are particularly important for extracting information on the characteristics of the optical scatterers, such as particles sizes and number density. It was known that the width of the intensity peak is inversely proportional to the particle size and also explains multiple scattering effects along the beam path. Therefore, the effects of a multiple scattering during propagation of narrow light beams in aerosols have been investigated using two features; the radial distribution of scattered light and the changes of polarization ratio compared to single particle scattering.

Laboratory experiments were conducted in the Aerosol Research Chamber of the Defense Research and Development Canada (DRDC) in Quebec and in a small chamber that we constructed at PSU. These chamber environments have been used to conduct scattering experiments under a better controlled laboratory environment. An outdoor field study was performed in State College in the summer of 2007. The field experiments were made under sufficiently high relative humidity conditions that during light and heavy foggy nights that it is reasonable to use a spherical model to describe scattering particles. These conditions provide excellent situations to investigate multiple scattering effects.

A theoretical investigation of multiple scattering using a Bistatic Monte Carlo (BMC) method showed that multiple scattering effects increase as particle sizes of a scattering medium increase. Multiple scattering contributions in atmospheric models having large particles is comparable to or larger than those of single scattering. However, in case of models having small particles, single scattering is dominant at both forward

and backward directions. Experimental results obtained from chamber tests revealed that even in the same particle distribution, multiple scattering effects in terms of optical depth increase with number density within the scattering volume. Specifically, multiple scattering increases depolarization of the scattered intensity as the scattering angle increases from 0° and 180°. Results of measurements of the radial distribution of a laser beam into optically dense media showed that multiple scattering effects increase with optical depth, lead to beam broadening along the beam path, and exhibit a slope in the gradient of the radial distribution of intensity that is much less than for the clear atmospheric condition. The results show good agreement with the previous calculations and measurements conducted by Bissonnette.

TABLE OF CONTENTS

LIST OF TABLES

LIST OF FIGURES

ACKNOWLEDGEMENTS

Almost five years ago, when I was chosen by the Korea Army to leave my country and study "something" in the United States, I didn't know exactly what I was going to do, whom I was going to work with. Now, I realize that I was very lucky to have C. Russell Philbrick as my advisor and mentor for my time at the Pennsylvania State University. There is an old saying in my country that says benefits from parents and a teacher are the same, which means that a teacher is an important aspect of one's mental life. I have never worked with someone like C. Russell Philbrick who made me so comfortable and happy. He made me change; looking at the bright side of the world. With his enthusiasm, his inspiration, and his great efforts to explain things clearly and simply, he helped make everything fun for me. Throughout my thesis-writing period, he provided encouragement, sound advice, good teaching, friendly company, and lots of sparkling ideas. I would have been lost without him. I am forever thankful to him.

My committee members, Zhiwen Liu, Victor Pasko, and Anne M. Thompson provided the ongoing consultation essential for keeping me focused. Without their continued support, patience, and advice, I could never have focused and completed my dissertation when I did.

I would like to thank the researchers Gilles Roy, Sylvain Cantin, and Marc Grenier at Defence Research and Development Canada (DRDC) in Quebec for the opportunity to use the DRDC facilities. I would also like to thank Sergei M. Prigarin for allowing me to use the Bistatic Monte Carlo program.

I have had the privilege of developing friendships with my colleagues. Adam Willitsford, Dave Brown, and Sachin Verghese all deserve thanks. Especially Dave Brown, who contributed and stimulated many ideas to this work from casual conversation and helped in the creation and production of experimental devices.

To my family, Soonyeop Seo, Gayoung Park, Daniel Park, and my parents, my life's journeys would have lost a great deal of meaning without all of you. Your support

during the tough and hard times and your sharing and giving during my many joys will never be forgotten. I will be eternally grateful.

And finally, I would like to thank all personnel in the Korea Army who gave me the opportunity and support to study.

Chapter 1

INTRODUCTION

1.1 Introduction

The goal of this research is to develop a multistatic imaging lidar system and extend the interpretation to measurements under conditions of multiple-scattering. Multiple scattering is a well-known phenomenon that frequently affects various systems, and is important in treatments of the penetration of radiation through optically dense media, such as clouds and fog. The early tasks in this field were just focused on correcting the multiple scattering effects, but it was soon discovered that retrievable information on the microphysical properties of a scattering medium was contained in the multiple scattering contributions.

In order to visualize the multiple scattering effects, three different methods were used previously: (1) changing the field of view (FOV) of the receiver to detect the multiple scattering associated with beam spread, (2) measuring polarization ratio to detect depolarization deviations caused by multiple scattering, and (3) measuring the temporal pulse stretching caused by multiple scattering. In this work, the polarization ratio and spatial beam spreading are investigated by using a multistatic lidar. Measurement of polarization ratio of the scattering phase function provides a good experimental approach to investigate atmospheric aerosol properties not only in single-scattering dominant atmospheric conditions but also in optically dense media, since the ratio reduces nonlinearities across the face of the imaging device and removes differences due to extinction of signals from different locations along the path between the measuring volume and the detector (Novitsky, 2002; Stevens, 1996). These measurements provide us a quantitative explanation regarding angular-dependent multiple scattering. In addition, measurements of radial distribution of a scattered intensity provide further qualitative information. These approaches are hypothesized to provide complementary

information of improved interpretation of the scattering under multiple scattering conditions.

Traditional lidar studies of atmospheric multiple scattering, which use backscatter lidar measurements, have been based on a technique that uses a linearly polarized laser beam, which is depolarized and spatially broadened while transmitting through a multiple scattering region of the atmosphere. Previous attempts suffered from difficulty about the manipulation of lidar systems, weak signal intensity, and sophisticated detection system. They could not investigate angular dependent information to study multiple scattering. Earlier methods to describe particle properties from the scattering phase function were also limited due to the differences in path integrated extinction as a function of angle, and the ineffectiveness of monostatic lidar systems for measuring the lower atmosphere. Formerly in PSU Lidar Laboratory, bistatic lidar (Stevens, 1996) and multistaic lidar (Novitsky, 2002) arrangements were used to extract the optical properties of particles along the horizontal and vertical paths which focused on single scattering analysis. In this work, we apply their measurement technique and data analysis procedure, and investigate multiple scattering effects using a multistatic lidar arrangement in the horizontal configuration. Measurements in the forward direction are also used to visualize radial distribution simply due to absence of the complicated angular distribution of phase function structure in the backscatter direction, and are used to calculate polarization ratio in multiple scatter signals because the scattered intensity is very sensitive to polarization state. The Bistatic Monte Carlo (BMC) method, which was developed by Sergei M. Prigarin, is used to investigate the relationship between multiple scattering and lidar geometry, such as laser beam divergence and detector's field of view, and simulate angular-dependent multiple scattering effects under similar atmospheric conditions to those encountered in field experiments.

Three different experiments were performed in the laboratory aerosol chambers, and in open atmosphere. In laboratory experiments, various kinds of aerosol properties were studied using an aerosol generator to control the measurement conditions. Multiple scattering effects were also investigated during experiments performed in heavily foggy nights. The details of the measurement technique and data analysis approaches are shown

through this thesis. The following sections describe the aerosol conditions investigated in atmosphere, and summarize some of the past bistatic and multistaic lidar techniques used in PSU Lidar Laboratory.

1.2 Aerosol Effects

As one reads articles or books in atmospheric science world, one will confront frequently a term "Aerosol". However, it is really hard to define or describe the aerosols because there is no universally accepted definition of aerosols. The atmosphere actually contains very different kinds of particulate matter such as chemical type, size, and concentration. The size of those particles spans more than four orders of magnitude, from a few nanometers to around 100 μm (Seinfeld and Pandis, 1998). Depending on their microphysical properties, the optical properties of aerosols can be significantly different. The primary concern of this thesis is the multiple scattering produced by atmospheric aerosols. In order to extend our understanding of the multiple scattering, first of all, we should know about aerosol properties. The following questions should be answered: what materials compose aerosols, what processes govern aerosol formation, and why are aerosols important to us. In this chapter, these three questions about the aerosol focused on the interaction with light will be answered.

1.2.1 What are aerosols?

A widely used definition has been given by Seinfeld and Pandis. Aerosols are particulates both solid and liquid phase, suspended in air (Seinfeld and Pandis, 1998). Due to the large spatial and temporal variability of aerosols in both their composition and distribution, one of the conventional ways of classifying atmospheric aerosols is by its size range. The typical ranges of particle size commonly observed in atmosphere are shown in Figure 1.1. This figure indicates why it is hard to categorize atmospheric aerosols by particle size. Instead, it can be represented by a combination of the different

particle size, or particle size distribution (PSD). Different PSDs have been described using the following mathematical functions (Deepak and Box, 1982):

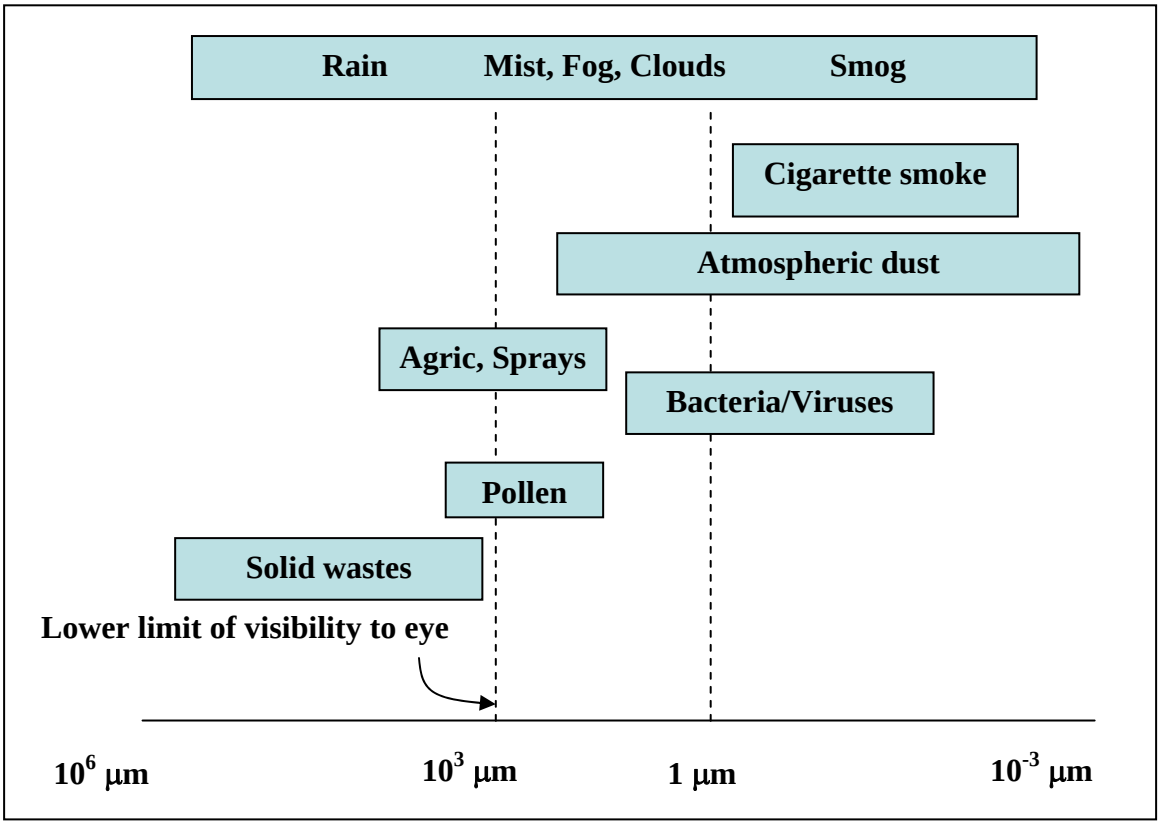

Figure 1.1 Typical ranges of particle size in atmosphere (after from Measures, 1984).

1. Power Law Distribution
2. Regularized Power Law Distribution
3. Modified Gamma Distribution
4. Inverse Modified Gamma Distribution
5. Log-normal Distribution
6. Normal Distribution
7. Generalized Distribution
8. Power Law Generalized Distribution.

Descriptions of the expressions and the mathematical properties of each function are too extensive for this thesis. An interested reader who wants the detailed explanations on these distribution functions should see the paper of Deepak and Box (1982). In this thesis, log-normal distribution and modified gamma distribution are primarily used. Log-normal size distribution has been used successfully to represent continental and maritime aerosols as sum of three log-normal distributions, which is called "trimodal log-normal size distribution". A size spectrometer, TSI 3934 Scanning Mobility Particle Sizer (SMPS) used in our experiments to determine size properties described using the log-normal function. This function is used to analyze fog particles generated from two different fog machines. The log-normal size distribution is formally expressed as (Seinfeld and Pandis, 1998),

$$\frac{dN}{d\ln D_p} = \frac{N}{\sqrt{2\pi}\ln\sigma_g}\exp\left(-\frac{(\ln D_p - \ln \bar{D}_{pg})^2}{2\ln^2\sigma_g}\right), \tag{1.1}$$

where N is the total aerosol number concentration, $\bar{D}_{pg}$ is the median diameter, that is, the diameter for which exactly one-half of the particles are smaller and one-half are larger, and σ_g is the geometric standard deviation. A noted discussion of this distribution was given by Kerker (1969), Deepak and Box (1982), and Novitsky (2002). Our results show artificial fog particles are well represented by log-normal size distribution. There have been extensive measurements of the size of fog and cloud particles in the atmosphere, which are the main focus in this thesis. Scientific data showed these particles are well represented by modified gamma size distribution. This size distribution is also an input parameter for a Bistatic Monte Carlo method, which is discussed in detail in Chapter 3.

Aerosols can strongly interfere with light in atmosphere. The two main interaction mechanisms between aerosols and light are scattering and absorption. Absorption effects are related mainly to the imaginary part of refractive index of aerosols, and do not depend much to aerosol shape and size. Light scattering strongly depends on the particle size

distribution. Aerosols with small size compared to the light wavelength are described by Rayleigh scattering, whereas those with larger than or comparable to that of incident radiation are described by Mie scattering. It is known that the intensity of Rayleigh scattering is proportional to the sixth power of the size of an aerosol (van de Hulst, 1957). Figure 1.2 shows the extinction cross section for different particle sizes. This calculation is done at the 532 nm wavelength for particles with refractive index of 1.33 by using an electromagnetic scattering theory for dielectric spheres. The Rayleigh scattering region is considered to apply to particle radius smaller than around 0.05 μm. Mie scattering theory applies to large particles, and the particle size radius between ~ 0.05 μm and ~ 5 μm is referred to as the resonance region because of the large variations in the scattering parameters found with changing particle size (Thomas, 1987).

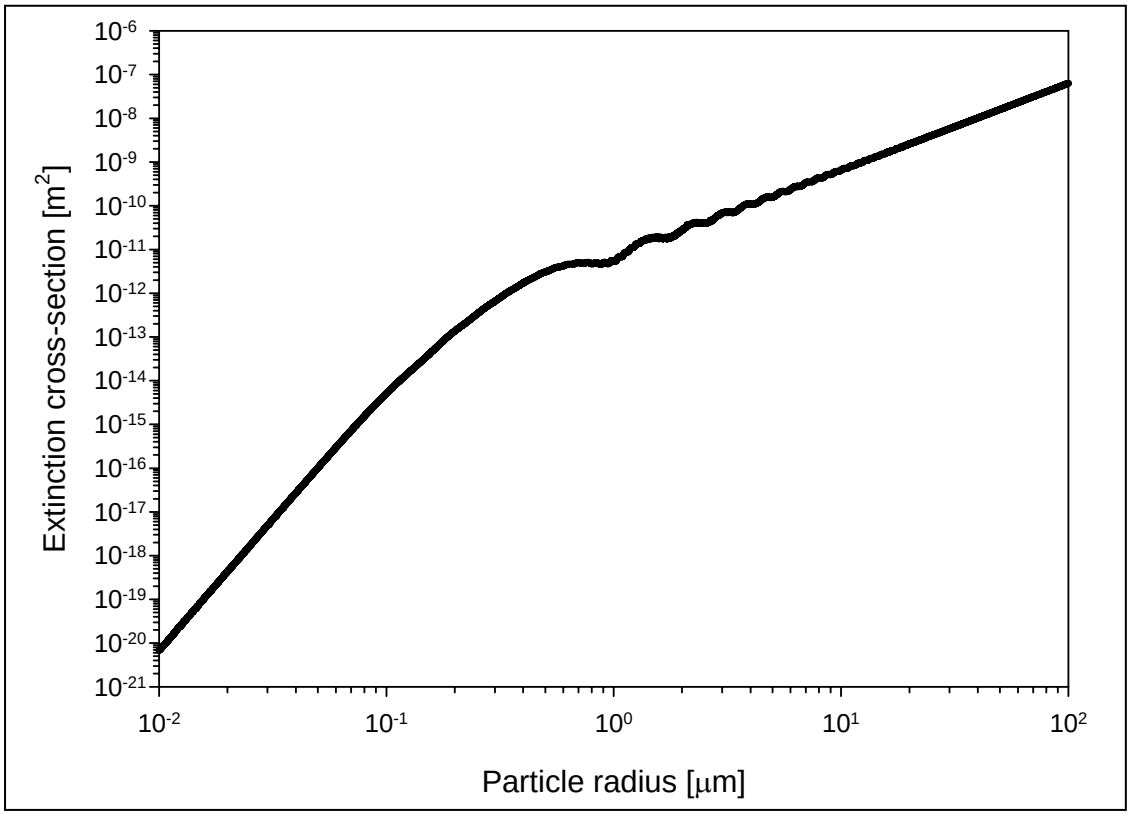

Figure 1.2 Extinction cross section at the 532nm wavelength for particles with refractive index of 1.33 using an electromagnetic scattering theory for dielectric spheres.

The current classification of an aerosol is principally identified by its solid component, and thus an aerosol is often referred to as particulate matter. Atmospheric aerosols come from a wide variety of natural and anthropogenic sources and have typical radii ranging from 0.001 to 10 μm (Haywood and Boucher, 2000). Figure 1.3 shows typical aerosol mass distribution found in the lower troposphere (Watson and Chow, 1999). There are three major modes (Ultrafine, Accumulation, and Coarse) each covering roughly 1 ~ 2 decades. A normalized plot of the number, size, and volume distribution of atmospheric aerosols is also shown in Figure 1.4. It was known that the accumulation mode is most efficient in terms of optical scattering because light scattering is most strongly dependent on cross-section of surface area.

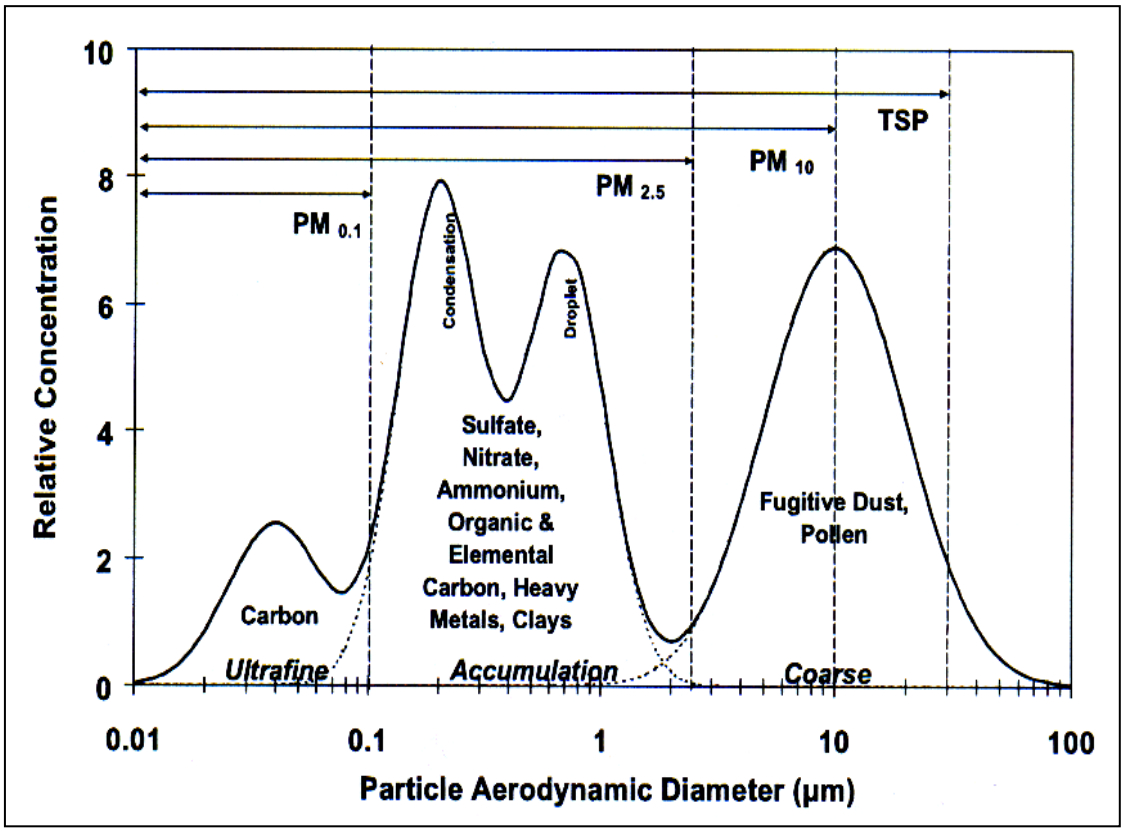

Figure 1.3 Aerosol modes in the lower troposphere (adapted from Watson and Chow, 1999).

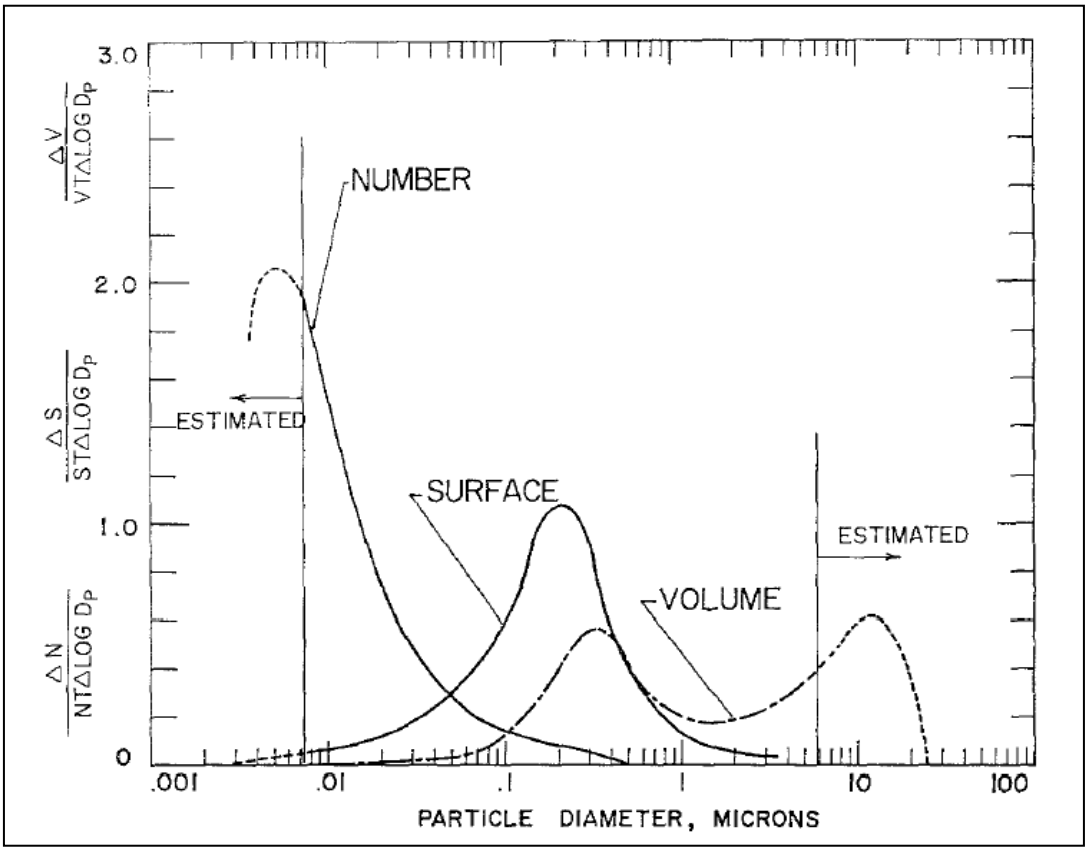

Figure 1.4 Total probability density functions of particle number, surface area, and volume (Whitby *et al*., 1972).

Aerosols are also distinguished between being primary and secondary. Primary aerosols are emitted directly at the source, whereas secondary aerosols are generally formed from gaseous precursors by various oxidation pathways (Haywood and Boucher, 2000). Primary aerosols include, for instance, fly ash from industrial activities, sea-salt particles emitted at the ocean surface, or mineral dust aerosols that are injected by the effects of wind erosion on arid land. An example of a secondary aerosol is sulfate aerosols that are formed from di-methyl sulfide (DMS) emission by marine phytoplankton and from the sulfur emissions of fossil fuel burning. Aerosols can also be classified as natural or anthropogenic aerosols. Natural aerosols include sea salt, dust, forest fires, volcanoes, and organics as the primary sources, and include di-methyl

sulfide, H_2S, volcanic SO_2, biogenic NO_x, and volatile organic compounds (VOCs) as the secondary sources. Anthropogenic aerosols include industrial dust and combustion products (soot, biomass burning) as the primary sources, and SO_2 from smelters and power plants, NO_x from vehicles and power plants as the secondary sources. Table 1.1 summarizes this classification.

Table 1.1 Classification of atmospheric aerosols.

Aerosol	Primary	Secondary
Natural	Sea salt, Dust, Forest fires, Volcanoes, Organics	DMS, H_2S, Vocanic SO_2, Biogenic NO_x, VOC
Anthropogenic	Industrial dust and combustion(soot, biomass burning)	SO_2, NO_x(Smelters, vehicles and power plant)

1.2.2 What are the effects of aerosols?

There are two primary mechanisms of atmospheric aerosols affecting climate change. The first one is direct radiative forcing and the second is indirect radiative forcing. Atmospheric aerosols reduce the solar radiation absorbed by the Earth through direct and indirect mechanisms. Direct radiative forcing results when radiation is scattered or absorbed by the aerosol itself. Scattering of shortwave radiation enhances the radiation reflected back to space, therefore increasing the reflectance of the Earth and cooling the climate system. Absorption of solar and longwave radiation changes the atmospheric heating rate, which in turn may result in changes to the atmospheric circulation. It is important to know what optical parameters determine the direct radiative forcing. The optical properties of atmospheric aerosols are described by three parameters: extinction coefficient σ_{ext}, which determines the degree of interaction, both scattering and absorption of radiation and the aerosol particles, single scattering albedo ω_0, which

determines the degree of absorption, and scattering phase function $p(\theta)$, which determines the angular distribution of scattered radiation.

Indirect radiative forcing results when enhanced concentration of aerosol particles modify cloud properties, resulting in increasing and decreasing the size of particles, which generally increase the albedo of clouds in the Earth's atmosphere. Aerosols can play a role in indirect aerosol radiative forcing in two ways. First, aerosols absorb solar radiation changing the vertical and horizontal thermal structure of the atmosphere and the surface. Second, aerosols acting as cloud condensation nuclei (CCN) are incorporated in cloud droplets and absorb solar radiation, thereby heating the droplets and the air around them. Figure 1.5 shows direct and indirect radiative effects of aerosols. The upper part of Figure 1.5 (a ~ d) is related mostly to aerosol effects that reduce the solar radiation absorbed by the Earth through direct (scattering of short incoming solar radiation) and indirect (increased concentrations of cloud CCN, as well as changes in cloud characteristics) processes. In contrast, the lower part of Figure 1.5 (e ~ g) shows the absorption effects of aerosols that exert a positive (warming) climate forcing.

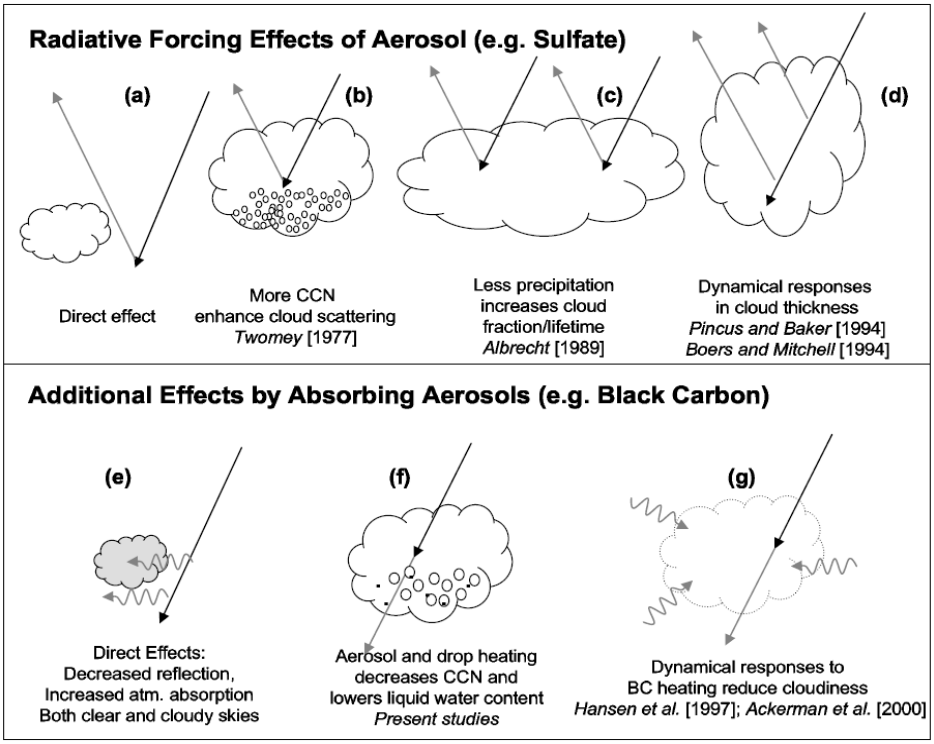

Figure 1.5 Direct and indirect radiative effects of aerosols (adapted from Conant *et al*., 2002).

1.2.3 Why are aerosols important?

It is time to answer our last question, "Why are aerosols important to us?" Since the spatial and temporal distribution of aerosols is known in global scale, or even on a local scale, it is difficult to predict what is really going on in atmosphere. However, atmospheric aerosols surely affect our environment on the local, regional, and global levels. At the local level, aerosols are now becoming recognized as a significant health problem, especially in regard to respiratory illness, including asthma (Kunzli *et al*., 2000). The atmosphere has also shown changes that have been demonstrated to influence our activities due to optical visibility changes that affect air traffic control. At the global level, aerosols cause concern for stability of our global environment by causing increases and decreases of the temperature of the Earth environment. Increasing anthropogenic aerosols reduces the direct and indirect flux of solar radiation at the surface due to changes in the planetary albedo. Increases in optical scattering by atmospheric aerosols result in reduction of global temperature by increasing the planetary albedo, thus counteracting the increases expected from the greenhouse effect, and leading to a complicated non-linear response (Philbrick, 2002). It also has been estimated that the unstable conditions of the local atmosphere and changes in convective patterns over the eastern section of the United States has effectively reduced the annual crop growing season by one week. (http://www.phys.unsw.edu.au/RESEARCH/ATMOSPHERIC/atmospheric_research.htm)

It is very important that we are able to build up a complete picture of aerosols across the globe, so that we can understand how they vary in both time and space and how they affect our climate system. In order to do that, it is even more important to understand optical properties of aerosols with radiation because a significant impact on the global climate change comes from the interaction with aerosols and light.

1.3 Bistatic and Multistatic Methodology

Measurement of the angular scattering pattern of electromagnetic waves scattered by single and multiple targets provides a powerful tool for characterizing the properties of the targets (Reagan, 1982). Simple backscatter or monostatic lidar was first implemented in early 1960. However, the disadvantages of monostatic lidar system in which transmitter and receiver are collocated, are such that they can measure only backscattered intensities at limited angular region and they can not measure the scattered intensities at near range because the transmitted laser beam does not overlap the detector's field of view (FOV). The first attempt of the bistatic lidar configuration was developed using a conventional search light in early 1930s and 1950s before laser was invented. Hulburt (1937) and Elterman (1953) used bistatic technique with high intensity searchlights to measure the scattered intensity from atmospheric molecules up to the range 20 km and 70 km. However, the difficulty of adjusting the elevation angle of the transmitter and the receiver for the range resolution has prevented widespread use of such a bistatic system (Meki *et al*., 1996). After the invention of the laser in 1960, modern lidar technology was developed rapidly.

Reagan (1982) developed bistatic lidar technique and prepared a theoretical analysis for the bistatic lidar system to study angular scattering properties and aerosol size distribution. Figure 1.6 shows typical bistatic lidar geometry. The bistatic lidar equation is represented by the following equation (Meki, 1996).

$$P_r = \frac{C}{D}\beta T_t T_r d\alpha \tag{1.2}$$

where C is lidar parameters, D is distance between a transmitter and a detector, β is scattering coefficient, T is transmittance, the subscript t and r mean transmitted and received signal, and $d\alpha$ is FOV of one pixel.

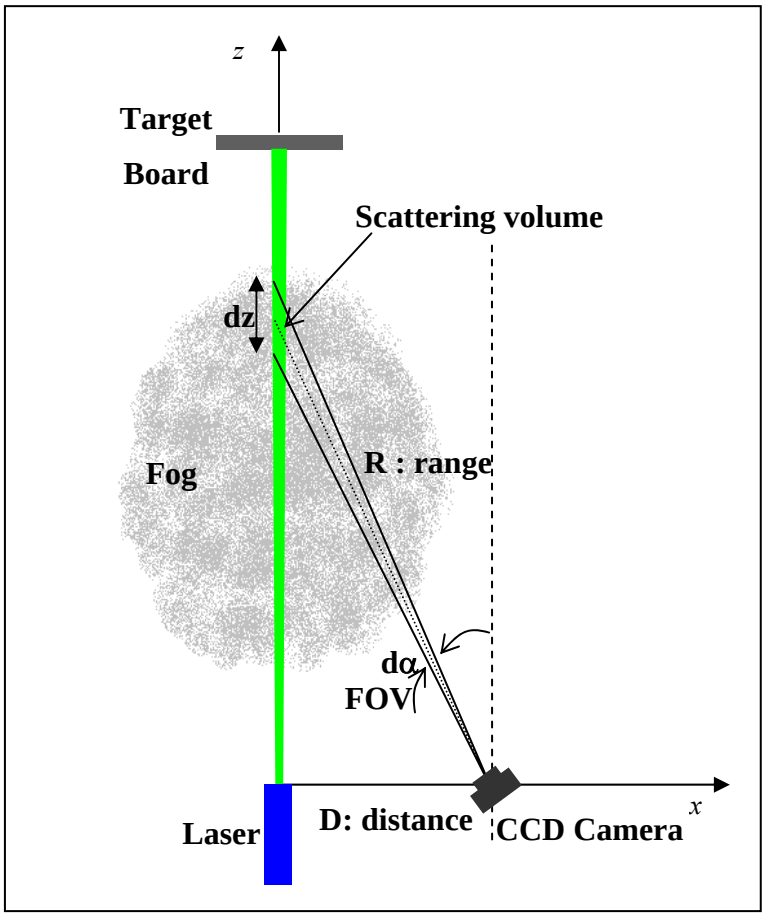

Figure 1.6 Bistatic lidar geometry.

The benefit of bistatic arrangement is that the received signal intensity does not depend on the square of the range, $\frac{1}{R^2}$ as shown in a typical monostatic lidar equation due to the relationship, $dz = \frac{R^2}{D} d\alpha$. A detail derivation for this relationship will be discussed in

Section 4.1. The reduced dependence on $1/R^2$ means that the detector is not required to have a large dynamic range for signal detection, and the scattered intensity is measured over a wide angular region by varying the transmitter and receiver pointing angles and/or changing the detector's FOV. The dynamic ranges of the bistatic lidar signal with altitude for the case of polarization angle, $\phi = 90°$ and $\phi = 0°$ are plotted in Figure. 1.7. For the purpose of comparison, a typical monostatic lidar signal from atmospheric molecules is also plotted in the same figure. The signal of the typical monostatic lidar covers 5 orders of magnitude. However, in case of the bistatic lidar, the molecular signal changes less than 1 order of magnitude (Barnes *et al*., 2003).

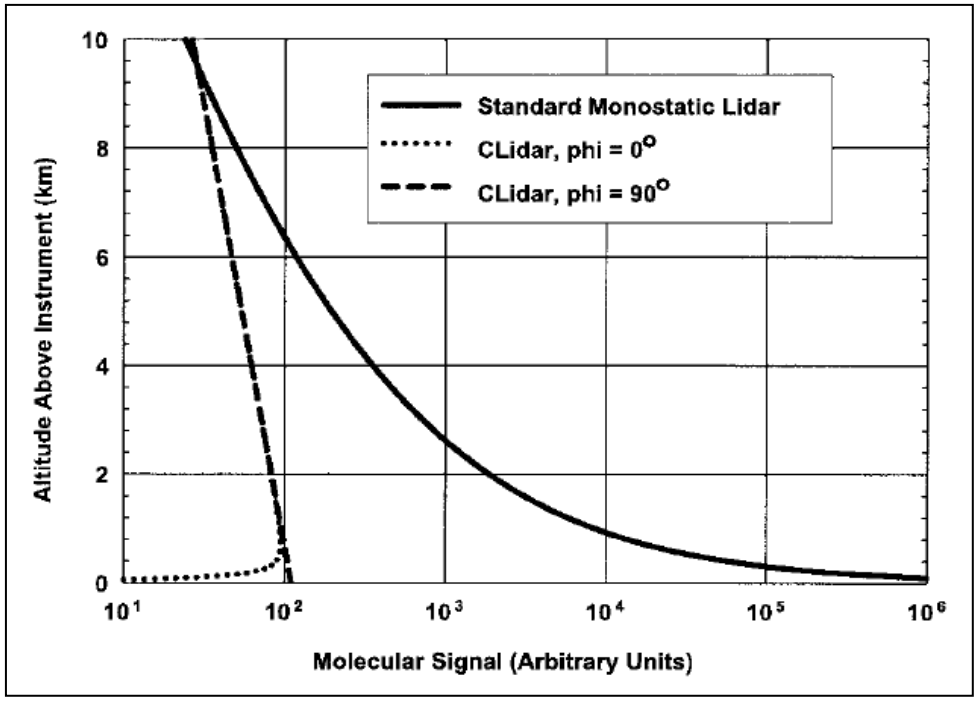

Figure 1.7 Comparison of bistatic lidar and standard monostatic lidar signal ranges (Barnes *et al*., 2003).

Measurements of scattered intensity itself give us the device non-linearities as well as setup uncertainties due to the bistatic lidar geometry. The polarization ratio is a

useful parameter because spatial and temporal aerosol number density variations in measurements made at different scattering angles are canceled out (Reagan *et al*., 1982). In PSU Lidar laboratory, Stevens (1996) and Novitsky (2002) used bistatic and multistatic lidar arrangement to measure polarization properties of atmospheric aerosols using imaging detectors.

Figure 1.8 shows Stevens' bistatic lidar arrangement that he used to measure the light scattered from a 140-meter horizontal path. He used one diode array camera (35 SLR Camera) to collect the parallel and perpendicular polarization image by rotating the laser polarization plane. By extracting the polarization ratio from two polarization images, Stevens was able to avoid many instrument-related errors and range and volume corrections to each pixel in CCD pictures (Stevens, 1996 and Novitsky, 2002).

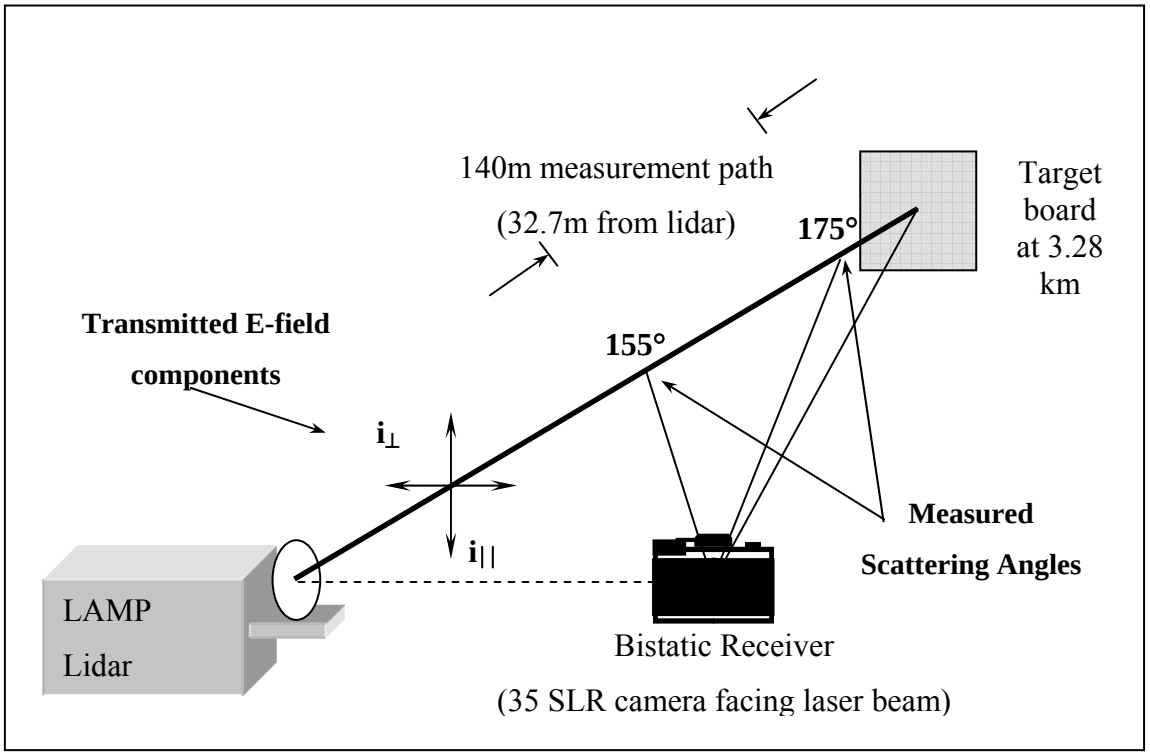

Figure 1.8 Bistatic lidar arrangement used by Stevens (Novitsky, 2002).

Figure 1.9 shows Novitsky's multistatic lidar arrangement, which shows three detectors in-line, and thus forms a scattering plane with the laser. Instead of using one receiver, he used three cameras to measure the light scattered from a vertical path. He found that one scattering angle is not enough to determine aerosol particle size. Therefore, he measured the scattered intensity at off-axis angle, particularly making use of the angular sensitivity of the polarization ratio of the scattering phase function in the range of 145 to 175° by changing the distance between a transmitter and three CCD cameras. The benefit of using multistatic receivers is that one can collect scattered intensities from the same scattering volume at three different angles, which give independent information for use in determining aerosol particle number and size. When the particle size distribution is changing rapidly with angle, such as in the vertical distribution of atmospheric layers of haze or clouds, it was found to be very difficult to extract the information on number density and particle size using a single camera.

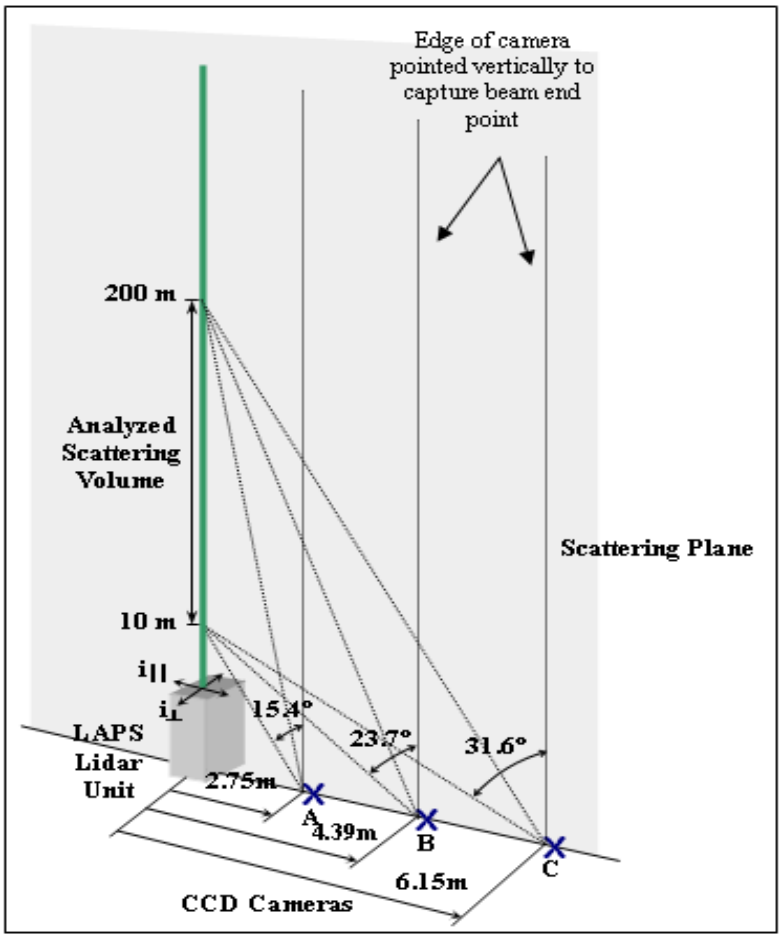

Figure 1.9 Multistatic receiver equipment and configuration (Novitsky, 2002).

A polarization rotator, remotely-controlled, was inserted to change the orientation for measuring the components of parallel and perpendicular polarization. Novitsky used same polarization ratio approach as Stevens did. Novitsky has shown the presence of strong altitude dependence in the vertical profiles of the aerosols, which were found to vary in size and composition, based on measuring polarization ratio in scattered direction over the range of scattering angles from about 145 to 175°.

The pictures of on-site operation of bistatic lidar at Wallop Island Virginia in 1995, and multistatic lidar at Philadelphia in the NARSTO-NEOPS campaign are shown in Figure 1.10.

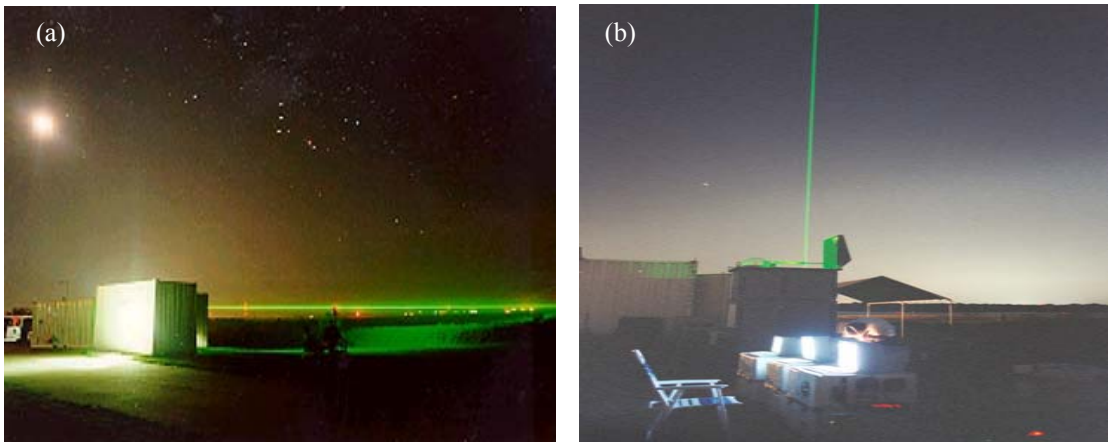

Figure 1.10 On-site operation of (a) bistatic and (b) multistatic lidar receivers.

1.4 Objectives of Thesis and Organization

The primary goal of this thesis is to extend our understanding of optical scattering using a multistatic lidar system with particular emphasis on multiple scattering. Based on the previous work and this research, three questions are answered through this thesis.

The first objective of this work is to check out the possibility of multistaic lidar technique for measuring multiple scattering and find out the meaning of multiple scattering in our experiments.

The second objective is how multiple scattering can be visualized from our measurements. In this work, two methods are applied to do that. The best ways are to visualize polarization ratio as a function of scattering angle and cross-sectional

distribution along the beam propagation path as a function of beam radius. The particle size information in the chamber is measured with two different devices, a size spectrometer and a particle counter, and the number density is converted to optical depth or extinction by measuring transmittance with a power-meter at the same time. Multiple scattering can actually increase transmission through a scattering volume because normal extinction calculation assumes that all the energy scattered out of the optical beam is lost forever. However, multiple scattering allows some of this lost light back into the field of view of a receiver.

Finally, we want to determine the limits for using the single scattering assumption in lidar application. The important parameter separating single from multiple scattering is optical depth. In this work, optical depth strongly depends on number concentration in a scattering medium.

This thesis is organized as follow. Chapter 1 introduces aerosol effects and bistatic and multistatic lidar techniques. First, aerosols are defined. Information such as aerosol effects (direct and indirect radiative forcing) and importance of aerosols in our climate change are discussed. Second, the benefits of bistatic and multistatic lidar techniques are given by explaining the lidar equation compared to a standard monostatic lidar approach. Past measurement techniques for measuring polarization properties of atmospheric aerosols are also introduced.

Chapter 2 explains multiple scattering theory along with comparison with single Mie scattering. This chapter describes importance of multiple scattering in analyzing lidar data and three important factors related to the measurements of multiple scattering effects, such as depolarization, detector's field of view, and pulse stretching. Finally, remote measurement techniques and their experimental results from four different groups are explained briefly.

Chapter 3 describes a unique Bistatic Monte Carlo (BMC) simulation with the permission of Sergei M. Prigarin at Novosibirsk State University, Russia. Geometry and input parameters for the simulation are explained. Finally, this chapter presents the simulation results of four different fog models, which may be encountered in our field experiments, and a Haze Model for the comparison with multiple scattering results.

Chapter 4 describes a mutistatic lidar configuration used in the chamber and field experiments for the measurement of scattered light along the horizontal path. Lidar equation is explained in more detail. Lidar hardware (laser and cameras) and two supporting instruments are described along with the dark image analysis of a new camera.

Chapter 5 describes aerosol research chamber experiments at Defense Research and Development Canada (DRDC) in Quebec. Experiment geometry and data collection process are explained.

Chapter 6 presents the data obtained from both chamber experiments (DRDC experiments and PSU small aerosol chamber experiments) and field experiments in State College area. Field experimental data are shown for two different conditions, clear and foggy nights in order to distinguish multiple scattering from single scattering. Polarization ratio and cross-sectional distributions of a transmitted laser beam are used to visualize the multiple scattering effects by analyzing the measured data.

Finally, the last chapter, Chapter 7, draws some conclusions and gives suggestions for the future work.

Chapter 2

MULTIPLE SCATTERING THEORY

When considering the analysis of the conventional backscattering lidar signals, multiple scattering often influences measurements, particularly in dense media such as clouds and fog. This process leads to errors in the quantities derived from the lidar signals (Widada *et al*., 2001). Multiple scattering is essentially a consequence of the finite beamwidths of the lidar system coupled with the strong scattering interaction of laser light by aerosols in the Mie scattering domain. Although it has long been recognized that

the effects of multiple scattering generally need to be considered in the analysis of lidar signal, this is still a difficult problem.

The multiple scattering is controlled by the size of the lidar beamwidth, the distance to the target, and detector's field of view. It was known that the intensity of multiple scattering increases with the increase of these three factors. However on some level, multiple scattering can be significant even for the case of small optical thickness, such as in haze (Kunkl and Weinman, 1976). Typical cloud and fog particles which are the main targets in our work are nonabsorbing, and large relative to visible laser wavelength. They display angular scattering patterns strongly peaked in the forward and backward directions. Aerosol microphysical properties (particle size, concentration, and shape) exert a strong influence on the scattering distribution in the forward direction, and polarization properties of the transmitted laser beam in the backscattering region.

In this chapter, importance of multiple scattering is briefly introduced, and three important physical factors related to multiple scattering are described. Finally, remote measurement techniques are explained, and their effects and experimental results are described.

2.1 Importance of Understanding Multiple Scattering

Multiple scattering is a well-known phenomenon and is important in treatment of the penetration of radiation through optically dense media such as clouds and fog. The early tasks in this field were focused on correcting the multiple scattering effects as error sources, but it was soon discovered that retrievable information on the microphysical properties of an optically thick medium was contained in the multiple scattering contributions. As indicated in Chapter 1.2, there are two interaction mechanisms between aerosols and light, scattering and absorption. The absorption effect is related mainly to the imaginary part of refractive index of aerosols, and not so much related to aerosol size or shape. It also depends upon the incident wavelength. The wavelength of the radiation

source of interest in this work is 532 nm. The imaginary part of refractive index of aerosol water vapor at the middle of the visible spectrum is between 1.7×10^{-9} and 2.5×10^{-9} (Segelstein, 1981). Figure 2.1 shows refractive index as a function of wavelength by a log-log scale plot. In our investigations of multiple scattering experiments in fog, absorption effects can be neglected.

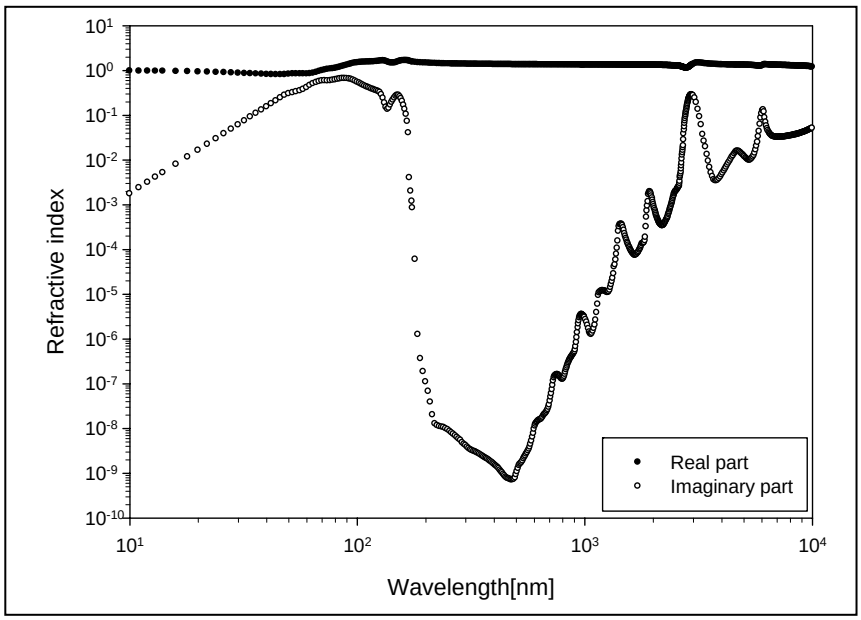

Figure 2.1 Refractive index as a function of wavelength (replotted from Segelstein, 1981).

In order to understand multiple scattering, two important concepts should be mentioned in advance, single scattering and independent scattering. Sometimes, these two concepts are considered as necessary assumptions in lidar remote sensing. However, one has to know what physical theory is behind these two concepts, and consider when one can understand atmospheric scattering process based on these concepts. These two scattering processes are represented in Figure 2.2. If light traverses a perfectly homogeneous medium, it is not scattered. For instance, in a perfect crystal at zero absolute temperature the molecules are arranged in a very uniform way, and the waves scattered by each molecule interfere in such a way as to cause no scattering at all but just a change in overall velocity of propagation (van de Hulst, 1957). In the case of atmospheric scattering, where most particles are in state of gas or aerosols, statistical

fluctuations in the arrangement of the atmospheric molecules cause scattering with incident radiation. However, it is difficult to describe the interaction between particles themselves, which is called dependent scattering. If atmospheric particles or aerosols are sufficiently far from each other, it is possible to study the scattering by one particle or aerosol without considering interaction with other particles. This process is referred to as independent scattering, and is shown in the upper part of Figure 2.2. In the case of heavy advective fog having an effective radius of 10 μm, there are 20 droplets in 1 cm^3, which means the mutual distances are typically 300 times the radii of the droplets. Therefore, it is reasonable to assume that there will be independent scattering in the scattering medium.

Single scattering concept must be explained with multiple scattering. When radiation is only scattered by one localized scattering particle, this is called "single scattering". Light scattered by a particle of comparable dimension, or larger, than the wavelength of the incident light results in increasing the intensity of forward-scattered light confined in a very narrow angular region as the particle size increases (see Figure 2.2 and 2.3). However, it is very common that scattering particles are grouped together, and in those cases the radiation may scatter many times, which is known as "multiple scattering". In case of single and independent scattering, the intensity scattered by n particles is just n times the intensity scattered by only one particle. Figure 2.3 shows scattering phase function of single spherical particle. Simply, it is the scattered intensity at a particular scattering angle relative to the incident beam. In other words, it is probability that a photon is scattered at specific angle. Therefore, this can be compared with our multiple scattering results. In this plot, particle size information is contained in the parameter, ka, where k is wave number and a is a particle radius. The i_1 is a perpendicular component and i_2 is a parallel component of scattered intensity. As one can see, the scattering phase function becomes peaked in the forward direction and the intensity increase rapidly as the particle size increases. The structure becomes more complicated.

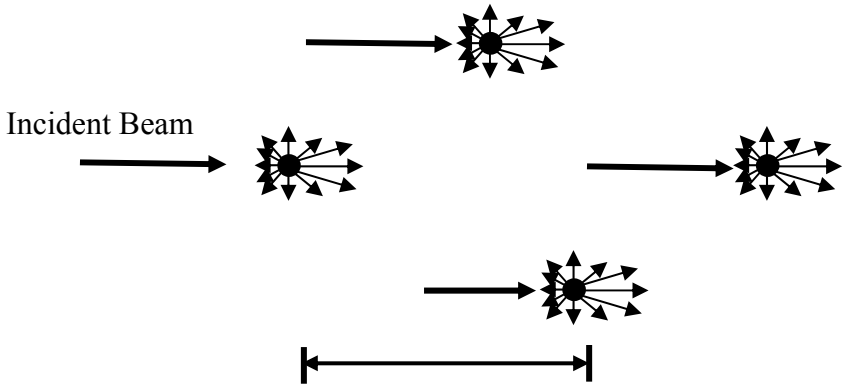

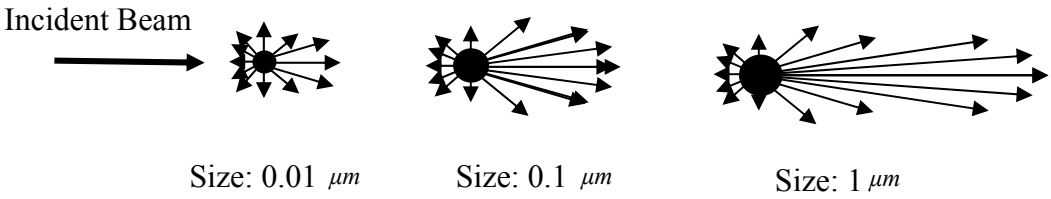

Figure 2.2 Single and independent scattering (Mie, 1908).

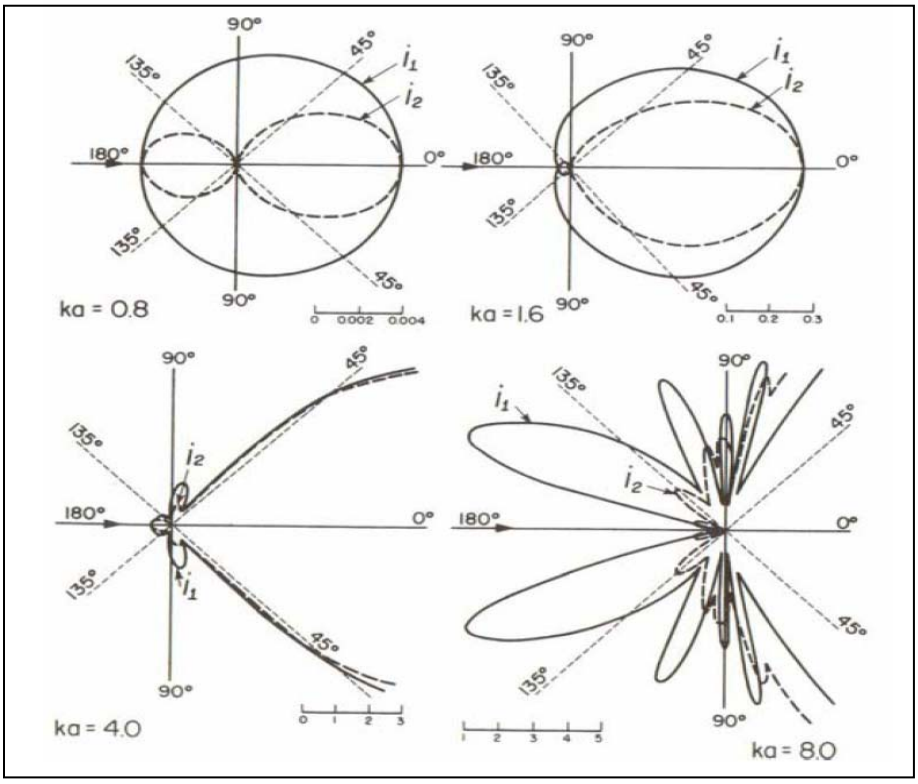

Figure 2.3 Scattering phase function of spherical particle of refractive index n = 1.5 (Born and Wolf, 1980).

However, in the situation of multiple scattering, this simple relationship does not hold. The graphical concept of multiple scattering is represented in Figure 2.4. The first particle removes the incident light by scattering just once, i.e., single scattering, in all directions. Meanwhile, a portion of this scattered light reaches the 2nd particle which scatters isotropically again, referred to as 2nd order scattering. Likewise, these phenomena will take place repeatedly resulting in scattering more than once, which is called multiple scattering. When the particles are comparable to or larger than the wavelength of the scattering light, the distribution is modified with each scattering event.

Multiple scattering effects should be considered when the optical depth of the atmospheric path is not negligible or the phase function of the scattering particles is strongly peaked in the forward direction, as in cirrus cloud and fog, or the observation is far from the atmospheric target as in the case of a space-based lidar (Wang *et al*., 2005).

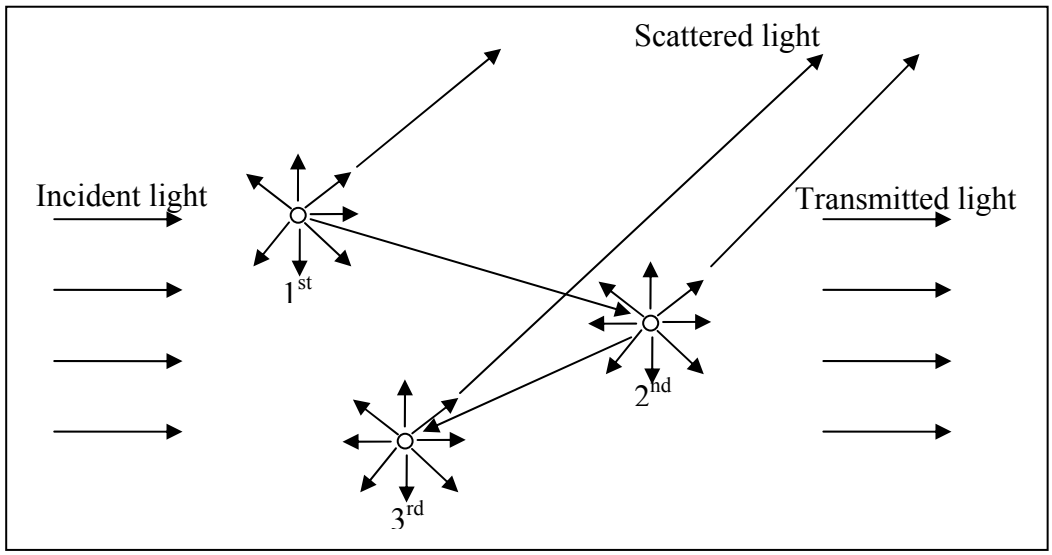

Figure 2.4 Multiple scattering process involving first, second, and third order scattering (after Liou, 2002).

There are many situations where multiple scattering should be considered. Its importance essentially arises when the lidar technique is applied to optically dense media such as clouds and fogs. However, it has been assumed that atmospheric molecules and aerosols are separated widely enough so that each particle scatters light in exactly the same way as if all other particles do not exist, which was mentioned early in this chapter in case of independent scattering, or single scattering. This assumption simplifies the problem of light scattering by a collection of particles, because it allows the use of energy quantity instead of electric field intensity in the analysis of the propagation of electromagnetic waves in planetary atmospheres. In the case of single scattering, the received signals due to multiply scattered events are typically assumed negligible. However, in reality, there are many particles exposed to radiation that has already been scattered by other particles. Van de Hulst (1957) suggested that multiple scattering cannot be ignored unless the optical depth (τ) of the scattering medium is less than 0.1. Recently, Roy *et al*. (1997) calculated the scattered intensity differences between two consecutive scattering orders in the backscattered lidar signal as function of the optical depth and their result is shown in Figure 2.5.

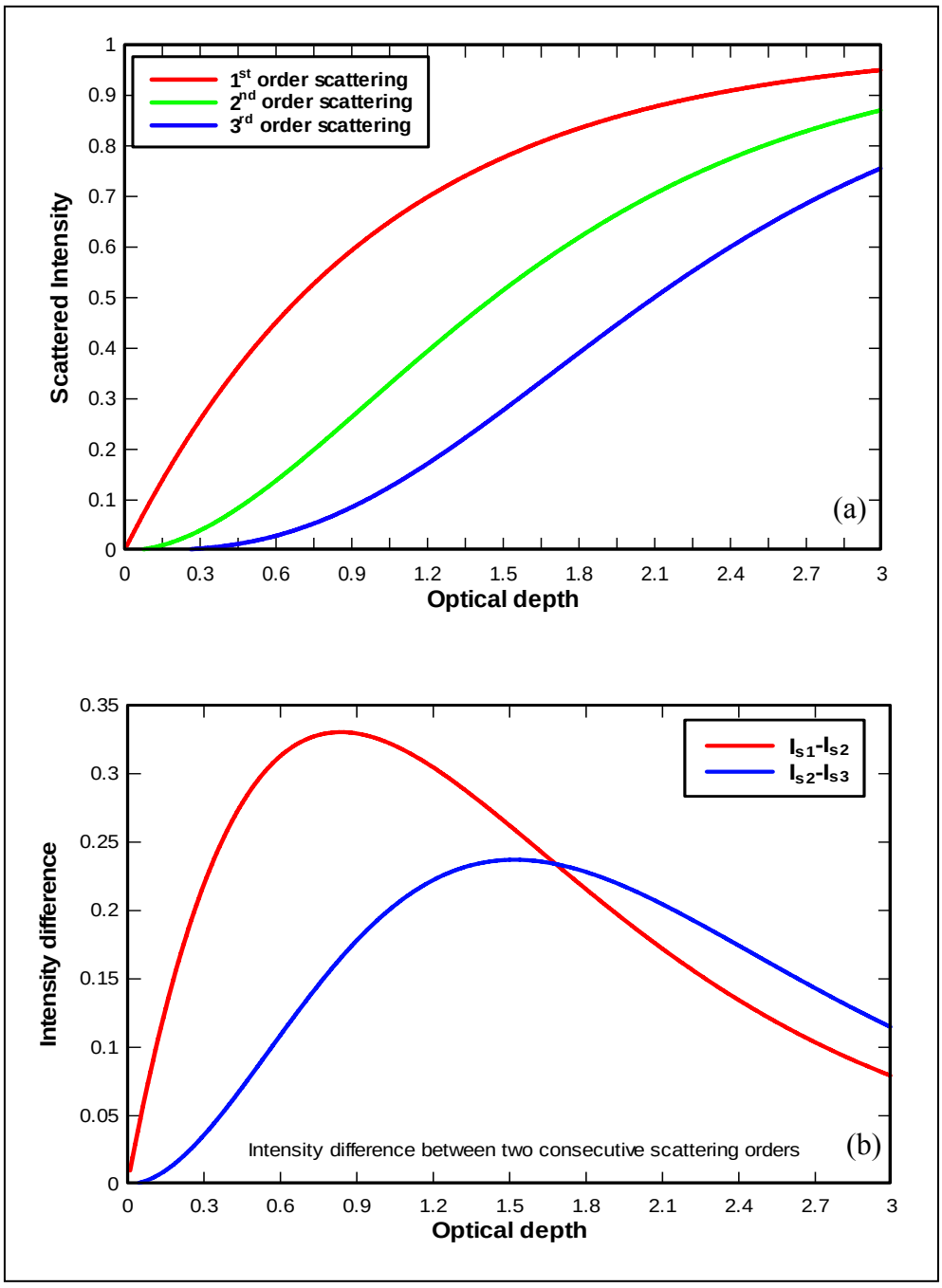

Figure 2.5 (a) The scattered intensities from the different orders of scattering (b) The intensity difference between two consecutive scattering orders (after Roy *et al*., 1997).

In this plot, the higher scattering orders sequentially become dominant as the optical depth increases. Clearly, the contributions of second order scattering cannot be neglected for optical depths greater than 0.3. In general, optical depths encountered in atmospheric lidar measurements frequently exceed this limit. For example, in typical cirrus clouds, the presence of multiple scattering can lead to an underestimation of the extinction coefficient by as large as 200%, whereas the backscattering coefficient is almost unaffected for the Rayleigh lidar technique (Wang *et al*., 2005). This phenomenon is also shown in our experimental results described in Chapter 6.

Several scientists have recognized the importance of multiple scattering, calculated multiply scattered lidar returns theoretically, and conducted field experiments. Liou and Schotland (1971) developed a computational approach for the multiple backscatter from spherical cloud droplets for a collimated pulsed radar system. Eloranta (1972) found a lidar transfer equation describing the magnitude and polarization of the doubly scattered return signal from the illumination of a homogeneous cloud of spherical particles. Pal and Carswell (1973) measured the polarization properties of the backscatter of a lidar pulse from atmospheric clouds. They found that the contribution of multiple scattering can be deduced from the spatial variation of the depolarization. Sassen and Petrilla (1986) found that multiple scattering effects in marine stratus clouds could be deduced from the measurement of the lidar returns using different fields of view. Hutt *et al*. (1994) designed a multiple field-of-view (MFOV) lidar system for investigation of the multiple scattering effects. Miller and Stephens (1999) explained the relationship between multiple scattering and pulse stretching, where temporal pulse stretching of the returned signals increases with the residence time in the target media. The maximum pulse stretching observed for nanosecond (15 ns) laser pulses was 20 μs for clouds of 1.5 km thickness (Mooradian and Geller, 1982). More recently, an imaging device was used to multiple scattering measurements (Roy *et al*., 2005).

In summary, multiple scattering in optically dense objects should be considered to extract useful information about atmospheric particles.

2.2 Multiple Scattering Theory

Multiple scattering effects in optically dense media can be revealed measuring the polarization ratio of the received lidar signals, the received signal difference of lidar returns at different fields of view of detector, or the temporal or spatial pulse stretching of the lidar signals. Multiple scattering in lidar manifests itself as greater signal strength and alteration of polarization state. Depolarization values in excess of about 0.02 can arise from spherical particles (such as water vapor) in the event of multiple scattering (Measures, 1984). Among the lidar system parameters, the receiver's field of view is the most important factor determining the magnitude of multiple scattering effects. Finally, the pulse stretching phenomena can only be seen in case of space-based lidar systems because conventional pulse lidar systems use short temporal and narrow spatial pulses. In order to recognize the difference between an incident and returned pulse, the distance to scattering medium should be long enough. In next section, the above three factors are discussed in more detail.

2.2.1 Depolarization

In electromagnetic scattering theory, the orientation of the electric field of the scattered radiation follows the dipole pattern such that the vibration induced in the atom is parallel to the E-field of the incident light wave and so is perpendicular to the propagation direction (Hecht, 1987). The classical lidar equation determines the power of the received radiation in terms of two unknown quantities: the backscatter and extinction coefficients as functions of the range. Hence additional measurements or theoretical assumptions are needed to solve the single-scatter nonlinear lidar equation, and its solutions are subject to instabilities. For example, most of the quantities derived from Raman lidar data are based on ratio of lidar signals, so the multiple scattering influences tend to cancel in the ratio. Examples of these quantities are the water-vapor mixing ratio, the liquid water mixing ratio, the aerosol scattering ratio, and the aerosol backscatter

coefficient. However, aerosol extinction (σ_{ext}) and optical depth (τ) are calculated from only a single lidar signal (for example, Raman scatter from nitrogen, N_2). In the case of large particles, these parameters can be significantly affected by multiple scattering when the scattering volume is of high optical density (Whiteman, 2003). To properly describe the lidar signal under such conditions, one needs to know the scattering phase function as a function of the range and the scattering angle (Tatarov *et al*., 2000; Stevens, 1996).

Scattering processes lead to changes not only in the signal power, but also in its state of polarization. The polarization state of the scattered radiation does not change in cases of nearly forward- and backward scattering from spherical particles (Van de Hulst, 1957). The change of polarization state of the scattered light can be expressed many different terms. Spectroscopists use depolarization ratio, ρ, of a Raman line, which is the ratio of the intensities, I, of the scattered light with polarizations perpendicular and parallel to the plane of polarization of the incident radiation (Atkins and de Paula, 2002)

$$\rho \equiv \frac{I_{\perp}}{I_{//}}. \tag{2.1}$$

Some remote sensing scientists use same definition with different notation as "linear depolarization ratio" (Sassen, 1976; Piironen, 1994; Tatarov, 1998; Sugimoto, 2000). However, in this case, $I_{\perp}$ and $I_{//}$ are the measured perpendicular and parallel backscatter intensities with respect to the transmitter polarization axis. Care should be taken in using this notation. Mannoni *et al*. (1995) used depolarization given by the quantity,

$$\delta \equiv \frac{I_{\perp}}{I_{//} + I_{\perp}}. \tag{2.2}$$

Another useful parameter that is often found in literature is the degree of polarization $\Im$, which is defined by (Measures, 1984)

$$\Im \equiv \frac{I^{//} - I^{\perp}}{I^{//} + I^{\perp}}. \tag{2.3}$$

The degree of polarization is the ratio of the difference intensity in the polarized components of an electromagnetic wave compared to the total intensity. In this thesis, polarization ratio δ_p, which is defined as Eq. (2.4), will be used. The detail explanation of this definition will be shown later. In the case of single scattering, it is known that Rayleigh backscatter from atmospheric molecules, which are much smaller than the wavelength of the incident radiation, and Mie backscatter, which describes scattering from spherically symmetric particles larger than 0.1λ, do not appreciably change the incident polarization. Thus the most probable source of the observed depolarization in lightly scattering atmosphere would be the scattering from the aerosol particles of irregular shape and complex refractive index. However, when one considers multiple scattering, the lidar return is also depolarized, even if scattering from spherical particles take place (Pal and Carswell, 1973). When one shines a laser light into atmosphere, depolarization rises from three different causes. The sources of de-polarization of incident radiation in atmosphere are molecular anisotropies, the presence of non-spherical particles in the air, and the depolarizing effects of multiple scattering. Among the effects listed above, the multiple scattering is the one which gives the strongest contribution to the depolarization (Losacco *et al*., 2004). In the following paragraphs, these topics are discussed.

First, in the case of single molecular scattering, depolarization is related to the anisotropy in the polarizability of the molecules. An electric field applied to a molecule results in its structural distortion, and the distorted molecule gains a contribution to its dipole moment as shown in Figure 2.6 (Atkins and Paula, 2002). If the polarizability is different when the electric field is applied parallel or perpendicular to the molecular axis, then the molecule has an anisotropic polarizability. This makes scattered radiation depolarized. All linear and diatomic molecules have anisotropic polarizabilites. However, in case of isotropic scatterers such as monoatomic gases, for example, Ar, and He, or

polyatomic gases such as CH_4, which has symmetric structure in all directions, the polarization ratio is almost zero. The polarization ratios of linear-diatomic molecules such as molecular nitrogen (N_2) and oxygen (O_2) are 0.036 and 0.065 respectively (Measures, 1984). Table 2.1 provides the observed values of the depolarization ratio for a number of molecules found in atmosphere.

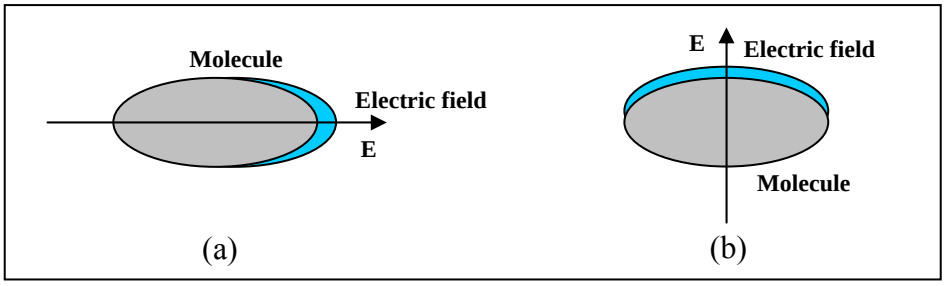

Figure 2.6 Electric field applied to a molecule (after Atkins and de Paula, 2002).

Table 2.1 Depolarization of light scattering by gases (adapted from Measures, 1984).

Gas	Formula	Polarization ratio (δ_p)
Argon	Ar	0
Methane	CH_4	0
Nitrogen	N_2	0.036
Oxygen	O_2	0.065
Chlorine	Cl_2	0.041
Air	.	0.042
Nitric oxide	NO	0.027
Ethane	C_2H_6	0.005
Carbon monoxide	CO	0.013
Hydrogen chloride	HCl	0.007
Hydrogen bromide	HBr	0.008
Carbon dioxide	CO_2	0.097
Carbon disulfide	CS_2	0.115
Water	H_2O	0.02
Hydrogen sulfide	H_2S	0.003
Sulfur dioxide	SO_2	0.031
Ammonia	NH_3	0.01

These values were measured using an unpolarized light source before the advent of laser. Pal and Carswell (1973) were among the first to experimentally study the variation of the polarization ratio, δ_p, associated with scattering from homogeneous spheres (Measures, 1984). In mathematical form, the polarization ratio is given by,

$$\delta_p \equiv \frac{I_{//}(\theta)}{I_{\perp}(\theta)} = \frac{\int \left|S_2(r,\theta)\right|^2 y(r)dr + Molecular_{//}}{\int \left|S_1(r,\theta)\right|^2 y(r)dr + Molecular_{\perp}}, \tag{2.4}$$

where $I_{//}(\theta)$ is scattered intensity from incident parallel polarization, $I_{\perp}(\theta)$ is scattered intensity from incident perpendicular polarization, $\left|S_{1,2}(r,\theta)\right|^2$ are scattering matrices (for a given wavelength and index of refraction), and $y(r)$ is the particle density distribution versus particle size (radius) with units of number per cubic meter (#/m^3). The difference between polarization ratio and linear depolarization ratio is that the intensity signals in polarization ratio are measured with polarization insensitive detectors by sending linearly polarized incident light whereas the intensity signals in linear depolarization ratio are measured with polarization sensitive detector using two polarization channels. One benefit of using a polarization ratio of the scattering phase function is that many of the device non-linearities as well as setup uncertainties are cancelled out in bistatic and multistatic lidar systems (Novitsky, 2002).

Second, depolarization comes from nonsphericity of atmospheric particles. Mishchenko *et al*. (2002) found the relationship between nonsphericity and depolarization by using T-matrix calculations. The T-matrix method was initially introduced by Waterman (1971) as a technique for computing electromagnetic scattering by single, arbitrary shaped particles, and is based upon the Huygens principle. However, the concept of expanding the incident and scattered waves in spherical vector wave functions and relating these expansions by means of a transition (or T) matrix has proved to be powerful tool to understand the multiple scattering in discrete random media (Mishchenko *et al*., 2002). Mishchenko *et al*. (2002) compared the polydisperse

polarization for randomly oriented spheroids with that for spheres. At scattering angles larger than 60°, it was found that the depolarization was strongly dependent upon the aspect ratio, ε, which is defined as the ratio of the longer to the shorter spheroid axes. The spherical-nonspherical difference became more pronounced with increases of ε. This indicates that Mie scattering theory is not an appropriate approximation for nonspherical particles in that region. However, at scattering angles less than 60°, the linear polarization is weekly dependent on particle shape, thereby suggesting that polarization measurements at near-forward-scattering angles coupled with Mie theory are potentially useful for sizing nonspherical particles. It is a good approximation that the polarization ratio from nonsphericity of particles can be ignored near the forward direction. This is easily shown in Figure 2.7.

Finally, as mentioned above, depolarization comes from multiple scattering. Depolarization generated from multiple scattering depends on factors such as the particle number concentration and size distribution of the scattering medium, the lidar transmitter/receiver beamwidth characteristics, and the distance to the target (Eloranta, 1972). When only single scattering occurs the lidar equation for a linearly polarized transmitted pulse can be written as (Pal and Carswell, 1976),

$$P_{//}^{S} = \frac{C}{R^2}\beta \exp(-2\kappa), \tag{2.5}$$

where C includes the usual lidar parameters such as pulse length, transmitted power, and area of the receiver, R is the distance to the scattering volume, $\kappa = \int_0^R \sigma dR$ is the attenuation coefficient, β and σ are the volume scattering coefficient and extinction coefficient, respectively. In an optically thick medium, the multiple scattered component of small-angle forward scattering effectively reduces the extinction coefficient because it tends to refill the component of scattered radiation that reaches at the detector. Since some single scattering photon loss is compensated by the presence of multiple scattering

within the field-of-view of the receiver, the attenuation in the lidar equation for single scattering is reduced by a coefficient κ_m.

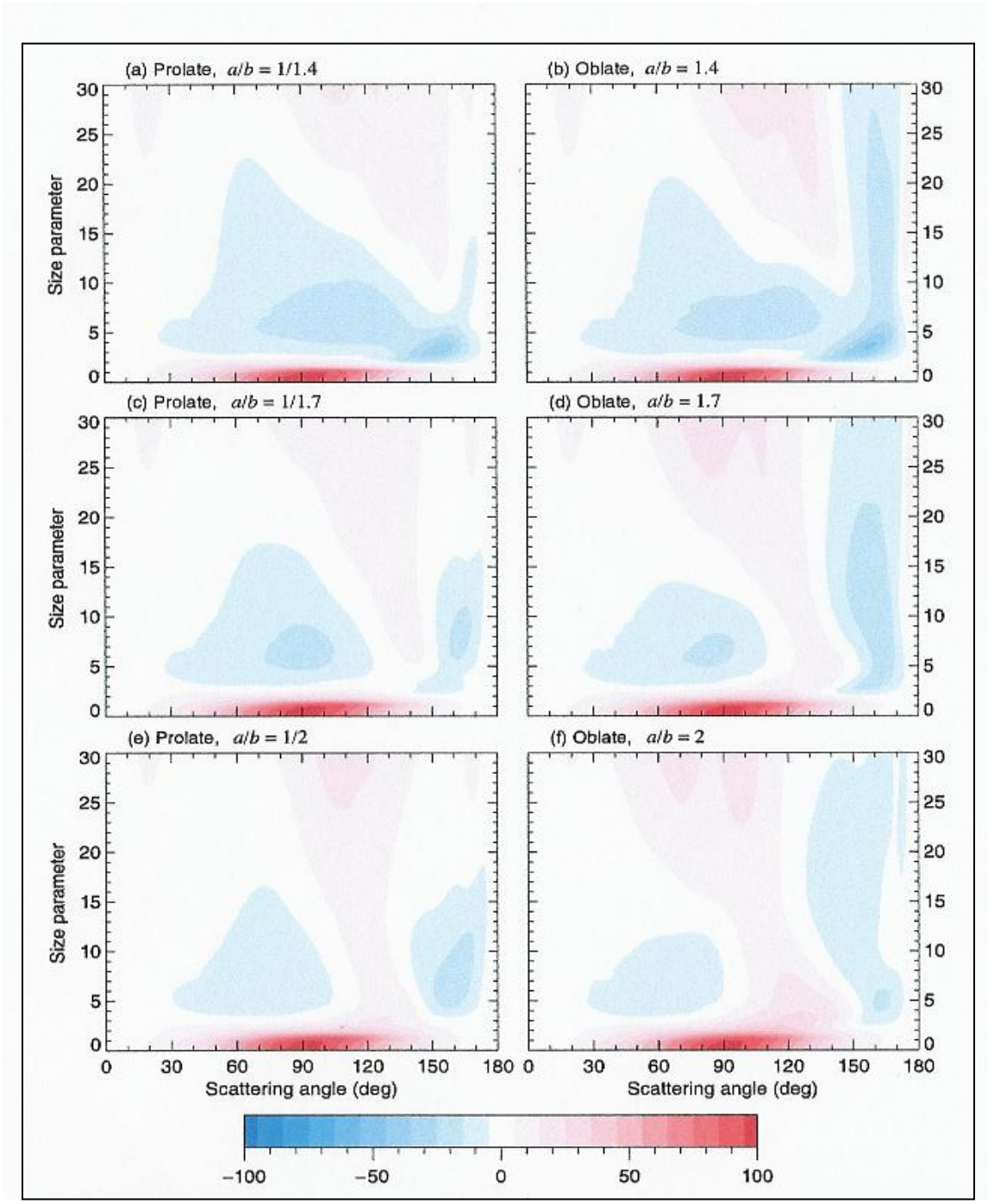

Figure 2.7 Linear polarization (in %) versus scattering angle and size parameter for polydisperse randomly oriented spheroids with various aspect ratio $\varepsilon = a/b$ (Mishchenko *et al*., 2002).

Therefore, the lidar equation in the case of multiple scattering case can be written as,

$$P_{//} = \frac{C}{R^2}\beta \exp[-2(\kappa - \kappa_m)]. \tag{2.6}$$

$P_{//}$ represents the intensity measured in the receiver with a polarizer aligned parallel to the transmitted polarization and includes the multiple scattering contribution in this plane. If it can be assumed that the multiple scattering is the only source of variation of the polarization ratio of the scattered phase function, such as in the case of the target medium being clouds and fog, it is possible to separate the multiple scattering contributions from the intensity measured in the receiver.

In summary, the backscatter signal of a linearly polarized laser beam from spherical particles is totally linearly polarized ($\delta_p = 0$). The particles can be assumed to be spherical in case of wet haze, fog, cloud droplets, and small raindrops. The polarization ratio of the pure molecular atmosphere is nonzero because of the anisotropy of the air, and therefore a 0.0037 ~ 0.004 depolarization for the Cabannes line is expected. The polarization of the air that includes the Cabannes line and the rotational Raman line is about 0.015 (Young, 1982). If particles are nonspherical, as mentioned by Mishchenko *et al*. (2002), for example, ice crystals, snow flakes or dust particles, or if the backscatter signal has a multiple scattering contribution, then the backscattered signal contains a cross-polarized component depending on the characteristics of the medium and the lidar geometry ($0 < \delta_p < 1$). Typically the δ_p values for ice are at least an order of magnitude higher than those generated by multiple scattering in the water cloud (Sassen and Liou, 1979). Figure 2.8 presents the results of early laboratory and field studies showing the wide range of linear polarization ratios encountered from various types of hydrometeors at visible wavelengths (Sassen, 1976).

2.2.2 Detector's Field of View (FOV)

The FOV of the lidar receiver is the most important system parameter influencing the multiply scattered contributions to the signal (Hutt *et al*., 1994). Multiple scattering causes beam spread. Therefore, the multiple scattering can be measured with different fields of view for the receiver optics. Allen and Platt (1977) proposed a lidar system that could measure multiple scattering and depolarization simultaneously in the atmosphere, and Bissonnette *et al*. have used such a system to study multiple scattering.

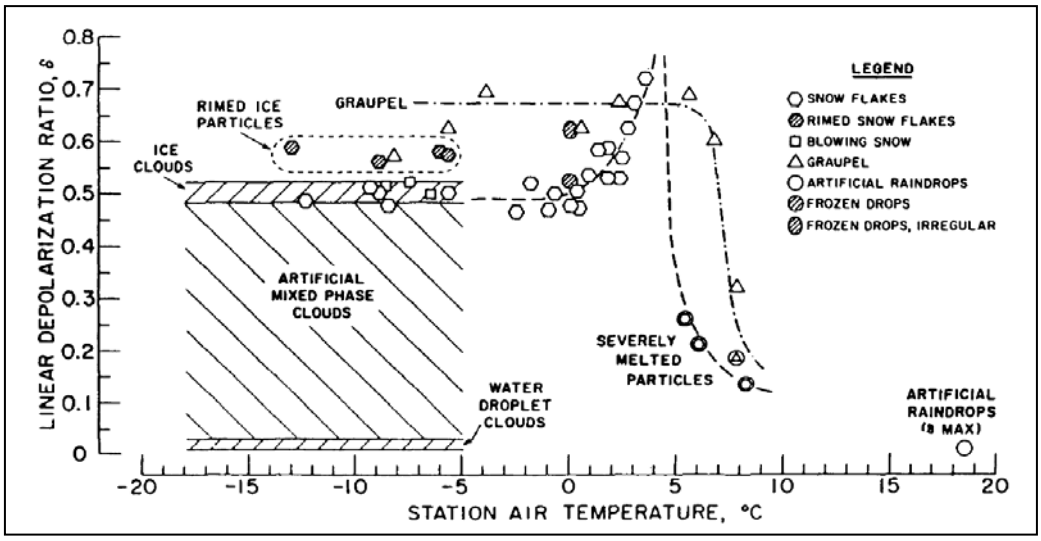

Figure 2.8 Results of early laboratory and field studies showing the wide range of linear polarization ratios using a CW laser/lidar (Sassen, 1976).

The multiple-scattered components of backscattered light were determined by inserting a center-blocked field stop to restrict the receiver field-of-view to the region outside of the diverging transmitted beam. Therefore the measured signal return is backscattered from outside the blocked spatial volume and is indicative of the multiple-scattered components of energy from the scattering volume. It was also known that the multiple scattering contributions detected by the different field-of-view receivers yield enough independent information to make possible the unambiguous determination of the aerosol extinction

coefficient (Bissonnette and Hutt, 1990). Four concentric silicon detectors (PIN photodiodes) with four different FOV lens were used to measure the backscattered lidar returns from a ground fog layer, see Figure 2.9. In the first 400 m, single scattering dominated in all detectors. However, starting at around 400 m, multiple scattering effects could be seen in wide FOV detectors. The oscillations are due to the density fluctuation of fog particles. Hutt *et al*. (1994) designed a multiple field-of-view (MFOV) lidar to measure simultaneously the backscattered power from the central pulse (single scattering) and multiply scattered power arising from the scattered component. Bissonnette and Hutt (1995) reported the optical properties of cloud and fog by using the MFOV lidar. Multiple scattering contributions have also been studied by varying the FOVs of the detector of the lidar in the case of radiation fog and in strata cumulus clouds (Tatarov *et al*., 1998). This study opened the possibility of determining the dimensions of multiple scattering area using the depolarization coefficient values.

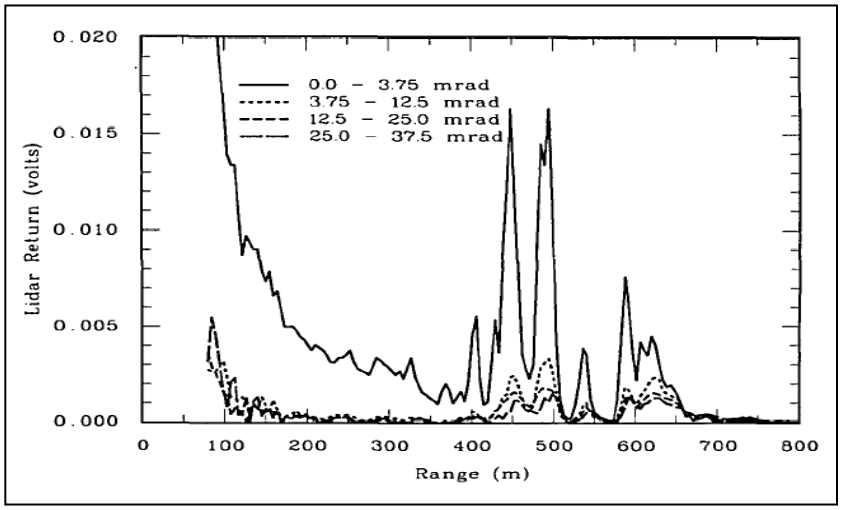

Figure 2.9 Simultaneous lidar returns measured at four fields of view for a laser shot at 11.5° elevation into a ground fog layer. The curve labels are half-angle fields of view (Bissonnette and Hutt, 1990).

Figure 2.10 shows the experimentally determined relation between polarization ratio and the field of view of the lidar receiver at different sounding path lengths 360, 400, and 450 m respectively. The atmospheric conditions during this experiment were described as a visibility of 1 km and air temperature of -3°C. The experiment was conducted along a slanted path elevation of around 21° and the extinction coefficient was determined to be $\sigma = 4\ km^{-1}$. As can be seen in Figure 2.10, polarization ratio increases with the increase of the FOV of the detector. In the case of fog, viewing angles close to the laser beam divergence yield polarization ratios about 1% and remain constant at angles up to ≈ 6 mrad, as expected for scattering by large spherical particles. Multiple scattering effects are detectable within the spatial area determined by FOVs of the detector larger than about 10 mrad.

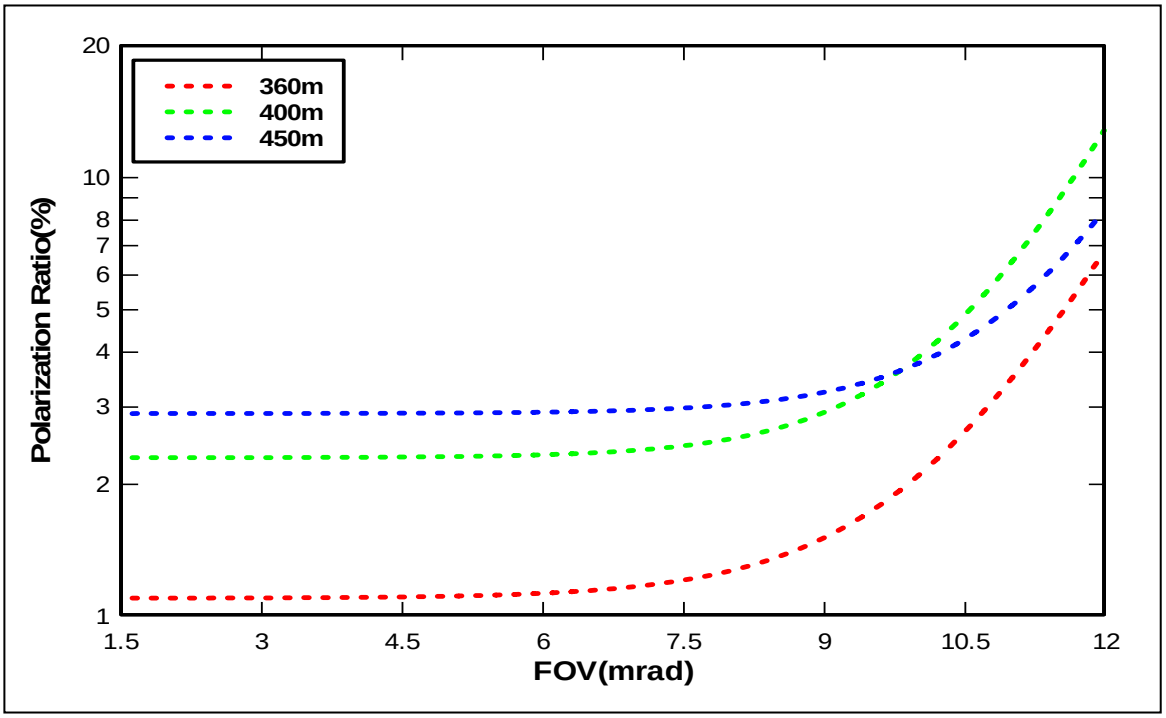

Figure 2.10 Polarization ratio versus FOV of the detector in case of fog (Tatarov *et al.*,1998).

2.2.3 Pulse Stretching

In most lidar applications pulse stretching is disregarded. However, pulse stretching plays an important role in applications demanding high spatial and temporal resolution such as profiling of scattering layers, temperature profiling using inelastic Raman scattering, and detection of submerged targets (Walker and Mclean, 1999). Beam spreading in scattering media is shown in Figure 2.11. Laser beam spreads spatially because photons have various scattering paths due to multiple scattering.

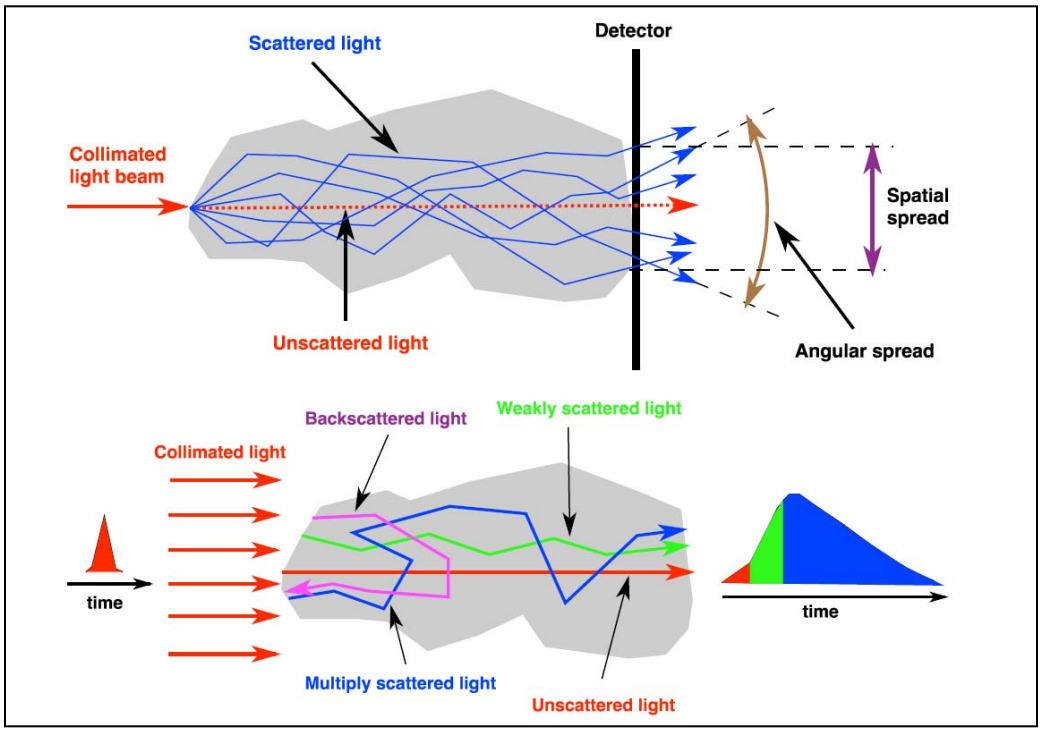

Figure 2.11 Beam spreading due to multiple scattering (Ashikhmin *et al*., 2004).

The multiple scattering observed at a large distance from the optical medium also leads to a measurable lengthening of the time taken for a multi-scattered photon to complete the round trip from a transmitter back to the receiver, compared to a single

scattered photon. This is seen as an effective increase in pulse length and a different pulse shape, with the pulse containing a long tail (Platt and Winker, 1995). It is known that the extent of temporal pulse stretching is dominated by the physical thickness of a scattering medium, while the lateral extent of spatial broadening is influenced strongly by medium optical depth dependent on number concentration (Love *et al*., 2001). The temporal pulse stretching was measured in a well controlled scattering cell by Elliot (1983). Figure 2.12 shows the measured pulse stretching phenomena due to multiple scattering in two optical thickness conditions. The result obtained for an optical thickness $\tau = 9$ (Fig. 2.12 (a)) shows the scattered pulse to be only slightly broader than the reference pulse, while Fig. 2.12 (b), optical thickness $\tau = 63$, shows considerable stretching of the scattered pulse relative to the reference pulse.

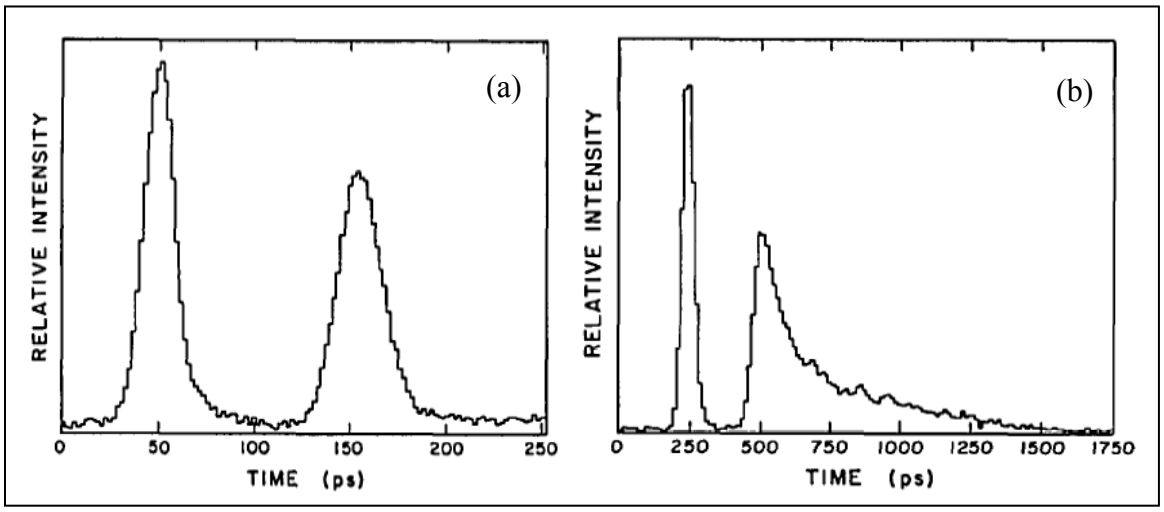

Figure 2.12 Temporal pulse stretching. The left-hand pulse is the reference, and the right-hand is pulse which has passed through the scattering medium (a) $\tau = 9$ (b) $\tau = 63$ (Elliot, 1983).

Typically temporal pulse stretching observed for nano-second pulse is in micro-second range (Elliot, 1983; Zaccanti *et al*., 1990). Because lidar measurements of the pulse stretching by an optically dense medium have proved difficult in practice (Walker

and Mclean, 1999), this effect is typically included in lidar system analyses only in a qualitative way. In some cases, this is acceptable because multiple scattering effects are weakened by the practical reality of the laser transmitter pulse width and the receiver electronic bandwidth. However, in the case of long distance between the lidar and scattering medium, this effect can be significant. Pulse stretching by multiple scattering was measured during the STS-64 mission taken by space shuttle Discovery as a part of LITE (Lidar In-space Technology Experiment) at 1994. It was shown that pulse stretching depended strongly upon the cloud geometry and pulse extensions were maximized in optically thick water clouds, which reside in cloud condensation nuclei-rich environments for homogeneous clouds of fixed geometric thickness (Miller and Stephens, 1999). This phenomenon is really important for space-based lidar systems which have long path length and wide scattering angle, and not so important for ground-based lidar system like a multistatic lidar system.

2.3 Remote Measurement Techniques of Multiple Scattering Effects

Most lidar applications use the same basic physical process: scattering by discrete scatterers (Bissonnette, 2005). The assumption they used is the single scattering approximation. Each scatterer is separated widely enough so that it scatters light in exactly same way as if all other scatters do not exist. However, in many cases, they are affected by multiple scattering. The single scattering approach to some specific lidar measurement techniques is not sufficient for optically dense scattering media. Some of them are using multiple scattering effects to extract physical information of aerosols. Some of them consider multiple scattering as an error source to be corrected. The following sections will describe four lidar techniques that have capability of measuring multiple scattering effects. Multiple-Field-Of-View (MFOV) lidar deals with lidar signals backscattered from atmospheric particles and the other techniques deal with multiple scattering effects on molecular lidar signals. Simple theoretical background, measurement approach and their experimental results of each technique will be described briefly.

2.3.1 Multiple Field of View (MFOV) Lidar

The idea of measuring multiple scattering effects with different receiver FOVs was first proposed by Allen and Platt (1977) and Pal and Carswell (1985). They used this method to discriminate between depolarization caused by multiple scattering and that by single scattering from nonspherical particles. Werner et al. (1992) developed a two-FOV system in which the perpendicular and parallel components of the lidar returns are measured simultaneously at both FOVs. Hutt *et al*. (1994) developed a multiple field of view (MFOV) lidar that measures the lidar return simultaneously with four concentric FOVs. It uses spatial pulse stretching due to multiple scattering when a laser pulse propagates into the atmosphere. The schematic diagram of a modified MFOV lidar design (Roy *et al*., 1999) is shown in Figure 2.13. The MFOV lidar allows measurement of the multiple scattering effects by the different FOVs in a glass disk, shown in the right

side of Figure 2.13. The central FOV detects the single lidar return. At least two scatterings are required for a photon to return into one of the outer FOVs and thus the outer FOVs receive only multiply scattered power. The receiver field of view is changed at the laser repetition frequency by rotating the aluminized glass disk with apertures of different sizes etched at equidistant angular intervals.

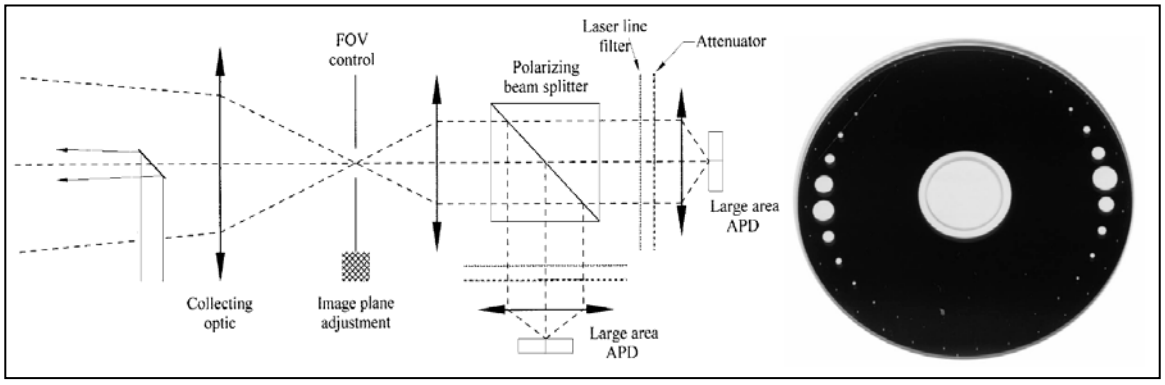

Figure 2.13 Schematic diagram of a multiple-field-of-view lidar (Roy *et al*., 1999).

Hutt *et al*. (1994) used the multiple scattering lidar equation given by,

$$P_t(z) = P_{ss}(z) + P_{ms}(z), \tag{2.7}$$

where $P_t(z)$ is the backscattered power from range z received by a detector, $P_{ss}(z)$ is the single-scattered power, and $P_{ms}(z)$ is the multiply scattered power calculated using the multiple scattering model proposed by Bissonnette (1988). $P_{ss}(z)$ is given by the single scattering lidar equation,

$$P_{ss}(z) = P_0 K \frac{ct}{2}\frac{1}{z^2}\beta(z)\exp(-2\int_0^z \alpha_e(z')dz'), \tag{2.8}$$

where P_0 is the transmitted power, K is the instrument constant, $ct/2$ is the spatial resolution, $\beta(z)$ is the backscatter coefficient, and $\alpha_e(z)$ is the extinction coefficient.

Hutt *et al*. (1994) measured MFOV lidar returns from different atmospheric aerosols which are very similar to the subject of this thesis, advection fog and haze. Their results are shown in Figure 2.14 and Figure 2.15. As the laser light penetrates into the advection fog, there is an increase in strong multiply scattered signals due to the high concentration of aerosols and the bigger particle size. However, this phenomenon can not be seen in case of homogeneous haze because of the much lower extinction coefficient compared with advection fog.

2.3.2 Raman Lidar

The Raman lidar technique makes use of the weak inelastic scattering of light by atmospheric molecules (Cohen *et al*., 1978). Laser light scattered by molecules or aerosols produces an intense return at the laser wavelength, referred to as the elastic Rayleigh scattering process. In addition, molecules such as nitrogen (N_2), and oxygen (O_2) and trace gases like H_2O produce much weaker return signals due to Raman scattering which are at wavelengths shifted from the laser wavelength. About 1 in 10^4 of the incident photons that collide with the molecules gives up some of their energy, and emerges with a lower energy. These scattered photons constitute the longer-wavelength Stokes radiation from the scattering medium. Other incident photons may pick up the additional energy from molecules that are existing in an energy state above ground level, and emerge as short-wavelength anti-Stokes radiation (Atkins and de Paula, 2002). These techniques have been used for atmospheric measurements such as temperature, water vapor, pollution, visibility, and particle size (Cohen *et al*., 1978). There are two ways to extract multiple scattering effects from Raman lidar. The first one is to use backscattered Raman intensity and the other one is to use polarization.

The Raman lidar equation which includes the multiple scattering effect can be written as (Wandinger, 1998),

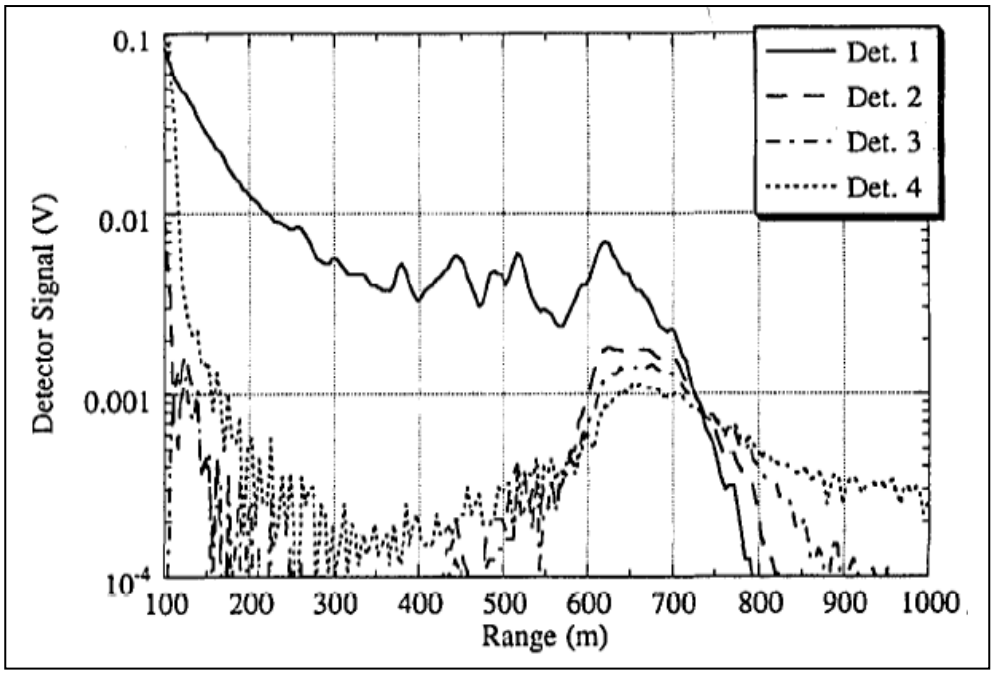

Figure 2.14 MFOV lidar return from advection fog. The solid curve is the central FOV signal. The other curves are returns in the outer FOVs (Hutt *et al*., 1994).

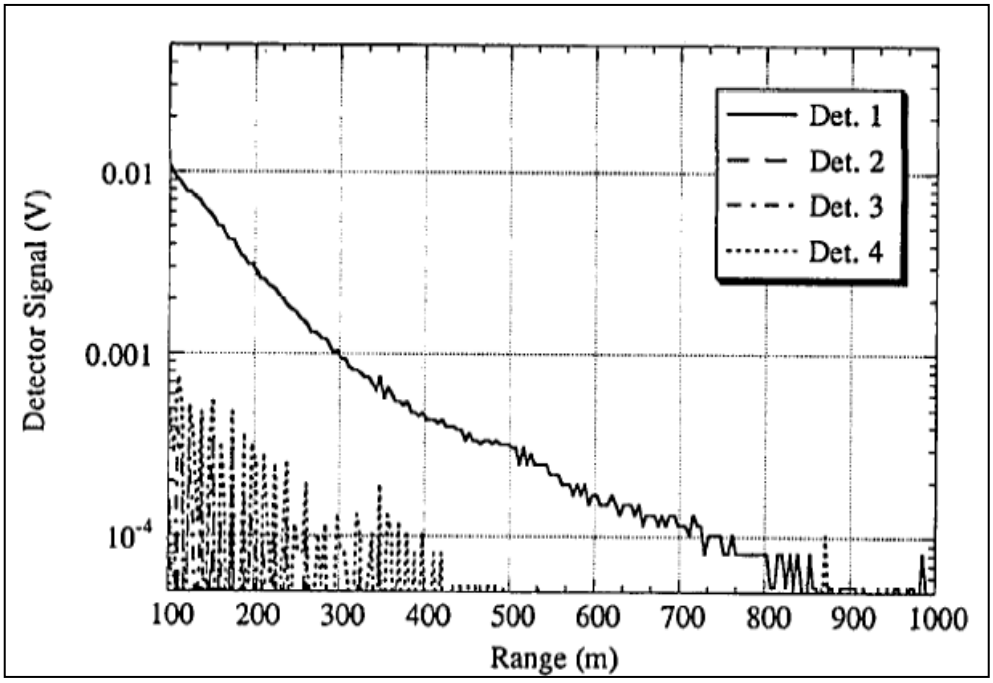

Figure 2.15 MFOV lidar return from homogeneous haze with an extinction coefficient of approximately 0.5 km^{-1}. (Hutt *et al*., 1994).

$$P_R^{(tot)}(z) = \frac{1}{z^2}\beta_R(\lambda_0, z)\exp[-(\int_0^z \{[1 - F_R(\lambda_0, \zeta)][\alpha_{par}(\lambda_0, \zeta) + \alpha_{par}(\lambda_R, \zeta)] + \alpha_{mol}(\lambda_0, \zeta) + \alpha_{mol}(\lambda_R, \zeta)\} d\zeta)]$$

,

(2.9)

where $P_R^{(tot)}(z)$ is the total received power in a Raman channel, $\beta_R(\lambda_0, z)$ is the backscatter coefficient for Raman scattering, $F_R(\lambda_0, \zeta)$ is the multiple scattering function at the laser wavelength λ_0 at the range ζ, α_{par} indicates the extinction coefficient due to particles, α_{mol} indicates the extinction due to molecules. Given the relationship between particle extinction at different wavelengths of $\frac{\alpha_{par}(\lambda_0, \zeta)}{\alpha_{par}(\lambda_R, \zeta)} = (\frac{\lambda_R}{\lambda_0})^k$ where k is the coefficient describing the wavelength dependence of aerosol scattering and the anticipated extinction from Mie scattering, $\alpha_{par}(\lambda_0, z) = \int_0^\infty n(a, z)\sigma_{ext}(a)da$ where $\sigma_{ext}(a)$ is the extinction calculated from Mie theory, the multiple scattering was quantified as follows (Whiteman and Melfi, 1999)

$$F_R(\lambda_0, z) = \frac{(d/dz)\ln[P_R^{(tot)}(z)z^2 / N_R(z)] + \alpha_{mol}(\lambda_0, z) + \alpha_{mol}(\lambda_R, z)}{2\int_0^\infty n(a, z)\frac{d\sigma_{ext}}{d\Omega}(\pi, a)da} + 1. \quad (2.10)$$

This equation represents the multiple scattering parameter as a function of range into the scattering medium. The difference between MFOV lidar technique and Raman lidar technique for quantifying multiple scattering is that the Raman technique starts with measurements of droplet size and then derives multiple scattering whereas the MFOV technique starts by quantifying multiple scattering and then obtains droplet size through a matrix inversion method.

As mentioned in Chapter 2, air molecules do not behave as perfect dielectric spherical particles, but show an anisotropic polarizability. This anisotropy is the reason of inelastic Raman scattering. Rayleigh scattering is the dominant scattering mechanism in

molecular atmosphere, which consists of two components: the elastic Cabannes line and the inelastic rotational-vibrational Raman lines (Young, 1982). In each scattering event in atmosphere, about 4 % of the light is scattered inelastically, whereas the remaining 96 % is scattered elastically as Cabannes scattering (Deelen *et al*., 2005).

Both the elastic and the Raman depolarization ratios of N_2, which is most abundant in atmosphere, were measured using a polarization Raman lidar which was developed by Wandinger *et al*. (1994). By using this lidar, they could separate the depolarization ratio of multiple scattering from that of single scattering from non-spherical particles. While the elastic depolarization ratio in clouds is influenced by single and multiple particle scattering, the Raman depolarization ratio is determined by one Raman scattering process. The measured parallel and perpendicular Raman signal components can be written as (Wandinger *et al*., 1994),

$$\begin{aligned} {}^{//}P_{\lambda_R} &= {}^{//}P^{s}_{\lambda_R} + {}^{//}P^{ms}_{\lambda_R} \\ {}^{\perp}P_{\lambda_R} &= {}^{\perp}P^{s}_{\lambda_R} + {}^{\perp}P^{ms}_{\lambda_R} . \end{aligned} \tag{2.11}$$

Signals were detected at the Raman wavelength, λ_R and each signal contains singly and multiply scattered Raman light of each polarization state respectively. Similar to the common definition of depolarization ratio, the linear Raman depolarization ratio was defined as,

$$\delta_{\lambda_R} = \frac{{}^{\perp}P_{\lambda_R}}{{}^{//}P_{\lambda_R}} = \frac{{}^{\perp}P^{s}_{\lambda_R} + {}^{\perp}P^{ms}_{\lambda_R}}{{}^{//}P^{s}_{\lambda_R} + {}^{//}P^{ms}_{\lambda_R}} . \tag{2.12}$$

It was known that the depolarization ratio coming from single Raman backscattering by the vibration-rotation branch of nitrogen, $\delta_{\lambda_R} = \frac{{}^{\perp}P^{s}_{\lambda_R}}{{}^{//}P^{s}_{\lambda_R}} = 0.094$, is known to be constant. It is the depolarization ratio for linear-polarized incident light at scattering angle of 180° for

the complete Stokes vibration-rotation band of nitrogen (N_2). It is calculated from the equation:

$$\delta_\lambda = \frac{3\gamma'^2}{45a'^2 + 4\gamma'^2} \tag{2.13}$$

with $a'^2 = 2.62\times10^{-14} m^4/kg/(4\pi\varepsilon_0)^2$, $\gamma'^2 = 4.23\times10^{-14} m^4/kg/(4\pi\varepsilon_0)^2$ (Wandinger, 2005). Therefore, any deviation from the above value results from multiple scattering. The experimental result of the polarization Raman lidar for a cirrostratus cloud is shown in Figure 2.16. The backscatter profile indicates the cirrus cloud layer between 5 and 8.5 km. Below the cloud the molecular values of the depolarization ratios, 0.02 for Rayleigh and 0.1 for Raman scattering, which is very close to the theoretical value, 0.094, are obtained. The increasing Raman depolarization ratio indicates an increasing influence of multiple scattering with height.

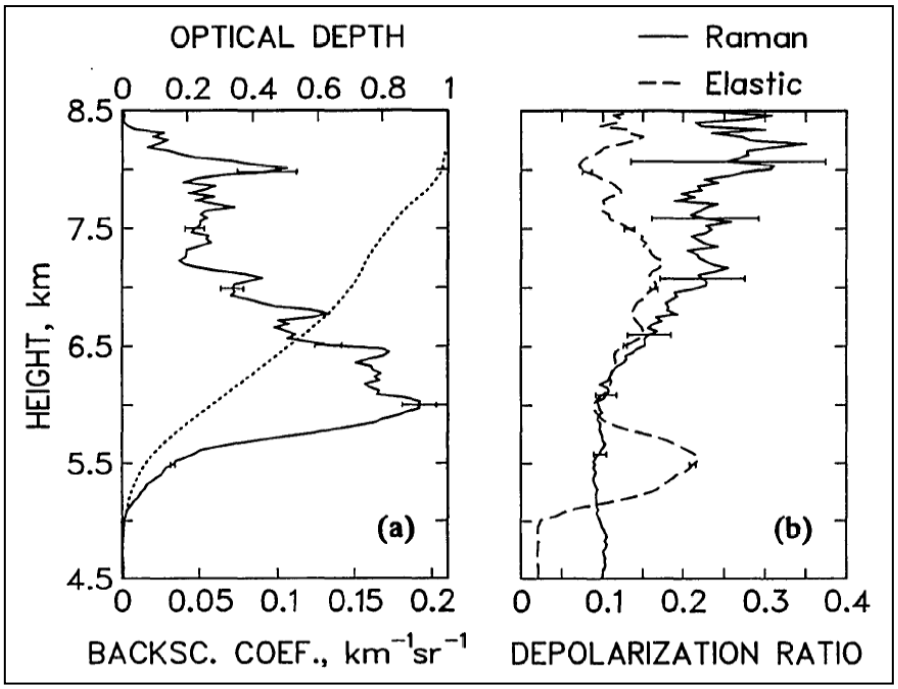

Figure 2.16 (a) Particle backscatter coefficient (solid curve) and optical depth (dotted curve) and (b) elastic (dashed curve) and Raman depolarization ratio (solid curve) (Wandigner *et al*., 1994).

However, Raman scattering is very weak. The magnitude of the scattered intensity of Raman scattering is much less than that of elastic scattering (Rayleigh scattering) by 3 ~ 4 orders of magnitude (Measures, 1984). Therefore, Raman lidars require powerful lasers and large telescopes in order to provide sufficient signal strength. Daytime operation is difficult because the small Raman signal must compete with scattered sunlight (Eloranta, 2005).

2.3.3 Differential Absorption Lidar (DIAL)

Differential absorption lidar (DIAL) was first developed by Schotland (1964), which was applied to measurements of the spatial distribution of humidity in the atmosphere. The idea of the method lied in spatial differentiation of the ratio of lidar signal at two close wavelengths in the vicinity of one of the lines of H_2O. This method is suitable for sensing of any components of the molecular atmosphere, which have the resolved spectral absorption, including ozone, which has the well-pronounced spectral behavior in Hartley-Higgins UV bands (Zuev, 1981). In differential absorption lidar operation two closely spaced wavelengths, λ_{on} and λ_{off}, where a trace gas of interest has correspondingly larger and smaller absorption cross section, are utilized to give high differential absorption and negligible differential scattering at the two wavelengths. The profile of a trace gas is derived from the slope of the ratio of backscatter signals, $P_{on}(z)$ and $P_{off}(z)$. However, it was known that DIAL measurements are almost impossible at altitudes with enhanced particle content because of elastic scattering by particles (Steinbrecht and Carswell, 1995). The influence of particle scattering on ozone concentrations retrieved from measured lidar profiles can be reduced if inelastic molecular return signals of molecular nitrogen or oxygen are used instead of the elastic lidar returns (Reichardt, 2000). This is called Raman DIAL technique. The standard lidar equations for on and off wavelengths follow the single-elastic backscatter lidar equation given as (Gimmestad, 2005),

$$P_{on}(z) = P_{ton} K_{on} \frac{1}{z^2} \frac{ct}{2} \beta_{on}(z) \exp[-2\int_0^z \alpha_{on}(z')dz'] \tag{2.14}$$

$$P_{off}(z) = P_{toff} K_{off} \frac{1}{z^2} \frac{ct}{2} \beta_{off}(z) \exp[-2\int_0^z \alpha_{off}(z')dz'], \tag{2.15}$$

which are similar to equation (2.8) with different on and off resonance wavelengths. However, one needs to have two more wavelengths in addition to the primary (transmitted) wavelengths, on and off resonance wavelengths at the vibrational-rotational Raman scattering in case of the Raman DIAL technique. The primary object of this approach is to find the molecular number density of the trace gas.

Multiple scattering effects should be considered in space DIAL application because of long laser beam path length and resulting large scattering volume. It was found by Pal and Bissonnette (1998) that the effect of multiple scattering on space DIAL ozone retrieval is negligible in the main stratospheric ozone layer and in most of the troposphere but it starts to become significant in the boundary-layer aerosol. They simulated the lidar backscattered signals $P_{on}(z)$ and $P_{off}(z)$ for single and multiple scattering with different atmospheric conditions of high visibility and low visibility. Their one of the main results is shown in Figure 2.17.

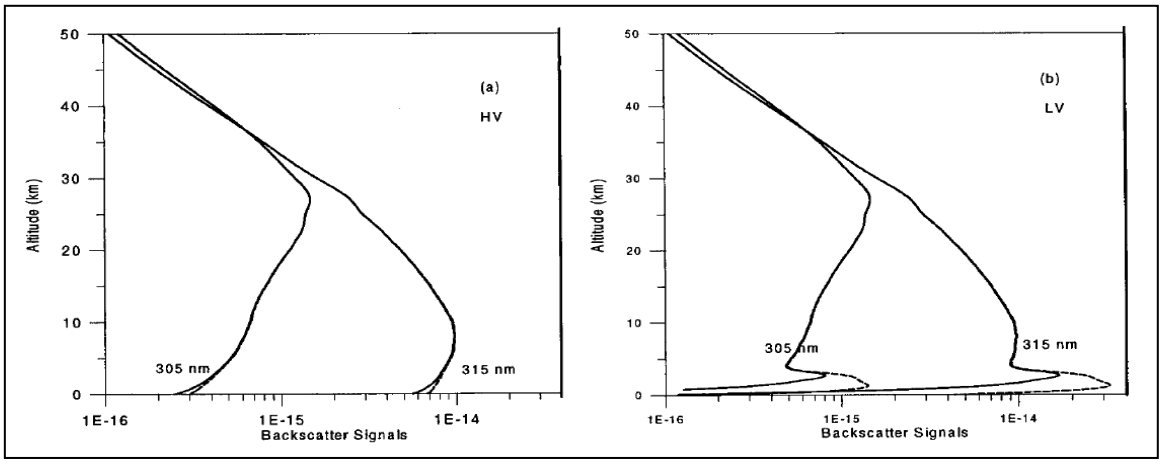

Figure 2.17 $P_{on}(z)$ and $P_{off}(z)$ for single scattering (solid curves) and multiple scattering (dashed curves) in (a) high visibility and (b) low visibility (Pal and Bissonnette, 1998).

The received signals at on-resonance wavelength ($P_{on}(z)$) of both high and low visibility cases decrease from the stratosphere to as low as the ground level. $P_{on}(z)$ and $P_{off}(z)$ for multiple scattering (dotted curves) show an increase in the planetary boundary layer. In the case of low visibility the increase in the returned signals due to multiple scattering is much larger than in the case of high visibility because of the influence of the boundary-layer aerosol.

2.3.4 Wide-Angle Imaging Lidar (WAIL)

At visible wavelengths, laser light in a cloud lidar experiment is not observed but merely scattered out of the beam, eventually escaping the cloud via multiple scattering. Mentioned in Chapter 2.1, there is much information available in this multiply scattered far from the input beam, which was ignored by conventional single scattering lidar.

The basic idea of wide-angle imaging lidar (WAIL) is to send a short-pulse, narrow laser beam into a scattering medium, and record, as a function of both space and time, the intensity of the returning light over a wide field-of-view (Love *et al*., 2001). The characteristics of the received signals in space and time will depend on its optical and geometrical properties. In order to measure the entire spatial broadening, a receiver FOV should be wide, in the case of WAIL, 60°. The extent of the temporal pulse stretching is dominated by the physical thickness of the cloud, while the lateral extent of spatial broadening is influenced strongly by cloud optical depth. Thus both thickness of the cloud and its optical density can be inferred from WAIL.

Figure 2.18 shows the spatially integrated total return as a function f time (graphs) and a sequence of selected images from the corresponding WAIL data set which shows the spatial distribution. The measurements were performed with two different filters on the receiver, one band center at 540 nm (top) and the other band center at 536 nm (bottom). The rightmost images of each case show spatial pulse broadening due to multiple scattering.

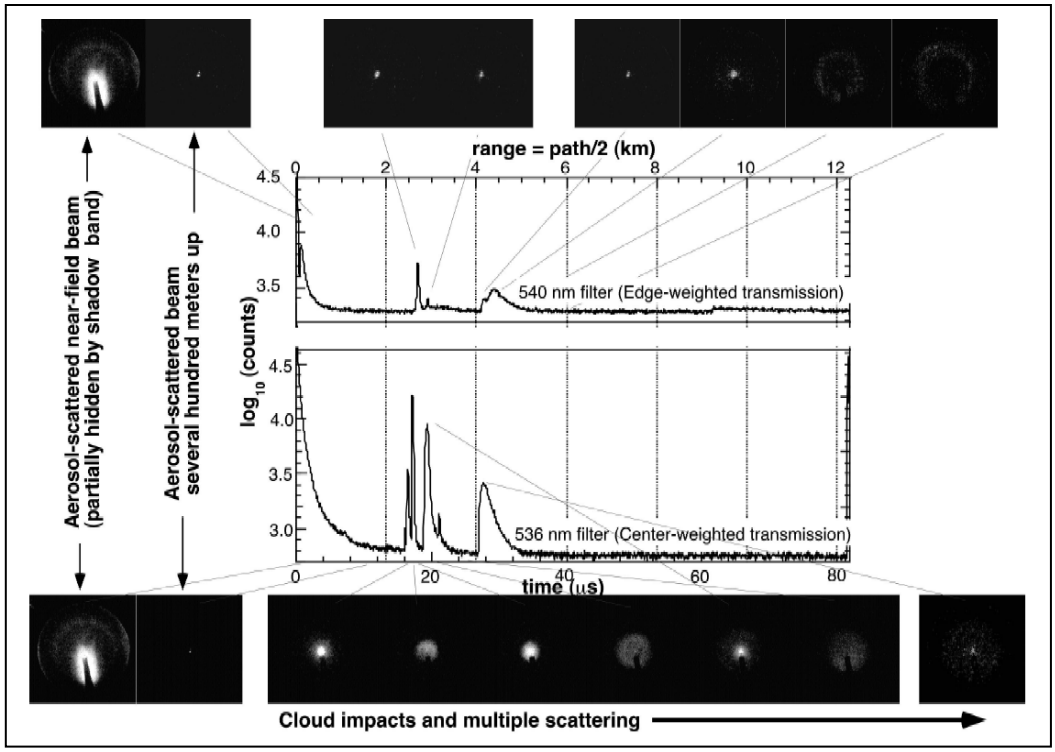

Figure 2.18 Nighttime WAIL measurements for a multi-layer cloud (Love *et al*., 2001).

Chapter 3

BISTATIC MONTE CARLO SIMULATION W/O POLARIZATION

Monte Carlo methods are widely used stochastic techniques which are based on the use of random numbers and probability statistics to investigate problems which include many variables. The starting point for any calculation concerning the propagation of a light beam in a cloud or a fog layer is the equation of radiative transfer, which describes a multiple scattering process by which energy spreads through the medium (Mannoni *et al*., 1995). Monte Carlo methods were commonly used to solve multiple scattering in atmosphere because of the lack of analytic solutions of the radiative transfer equation. These procedures calculate the length of trajectories of scattered photons, and the directions of each scattered photon in a scattering medium after each scattering event. A main advantage of the Monte Carlo method is that the calculation allows solutions with a desired accuracy. It can be employed to solve radiative problems within the intermediate scattering regimes where no approximation applies (Berrocal *et al*., 2007), but a primary drawback is the calculation time to achieve the desired accuracy (Bissonnette *et al*., 1995).

There are many Monte Carlo methods which have been developed to simulate interactions between light and atmospheric particles for a conventional monostatic lidar geometry. However, there are few computer simulation programs for a bistatic lidar geometry. The Bistatic Monte Carlo (BMC) program developed by Sergei M. Prigarin is one (according to my research, it is the only program) for successful simulation programs of a bistatic lidar. However, this Monte Carlo program was not fully verified with experimental results because of the lack of the bistatic or multistatic lidar systems. With the permission of the developer, the details of this program are introduced. In this chapter, the simulation geometry, medium characteristics, and results from our simulation are described.

3.1 Simulation Geometry

A simulation geometry of the Bistatic Monte Carlo method is shown in Figure 3.1. A Cartesian coordinate is used in this particular Monte Carlo simulation. A transmitter and a receiver can be located anywhere in the coordinates. However, for the simplicity of data analysis, the position of the transmitter is fixed at the origin, (0, 0, 0) and transmits along the $-z$ axis. The receiver is located on the $x-y$ plane depending on the actual bistatic lidar geometry. The pointing direction of the transmitter or the receiver is represented by the $xyz-$ coordinates with an end-point on each device respectively.

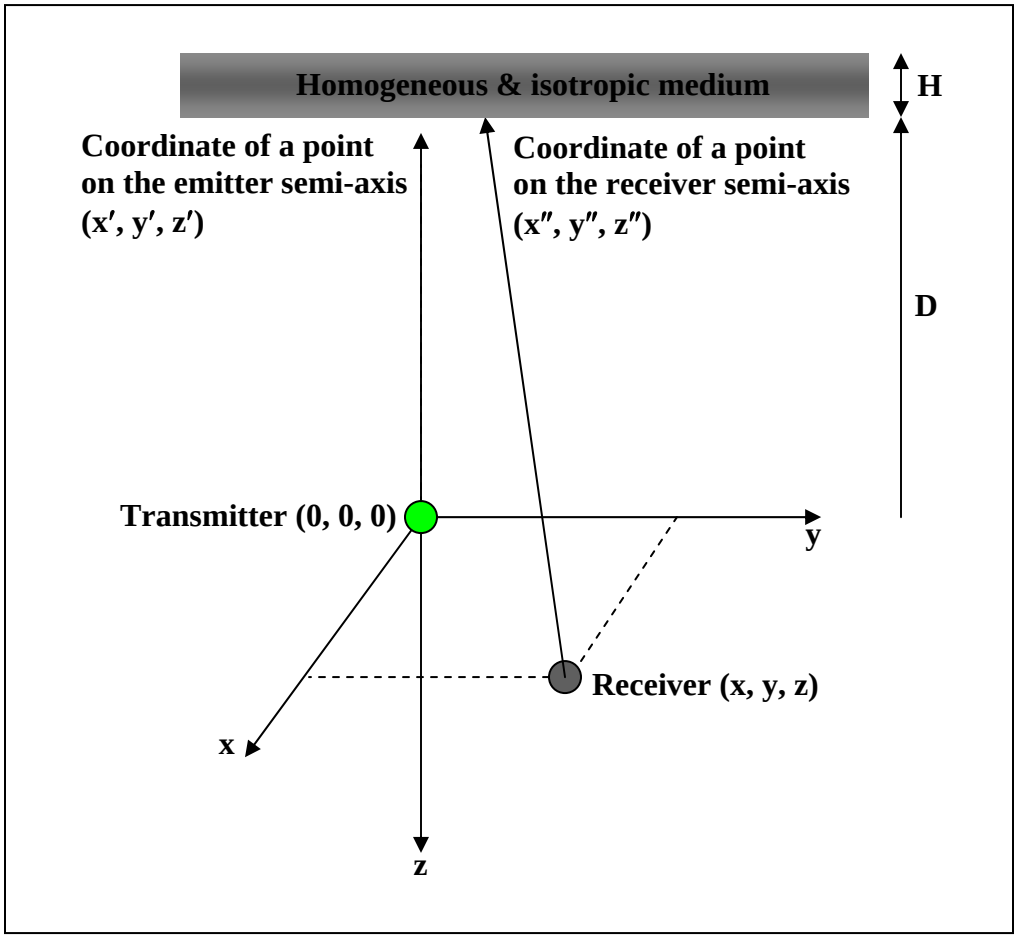

Figure 3.1 Simulation geometry of the Bistatic Monte Carlo program.

The position of a scattering medium is represented by a distance D above the $x-y$ plane. The scattering medium is a horizontal layer with a thickness of H. The characteristics of the scattering medium are represented by extinction coefficient, scattering albedo, and single scattering phase function. The input parameters for a transmitter and a receiver include half-angle fields of view of each device, and the active area of the receiver. The scattering media used will be explained in the next section.

3.2 Medium Characteristics

The scattering media used in Bistatic Monte Carlo simulation are assumed to be optically homogeneous and isotropic in a horizontal layer. The widely-used ten-aerosol models (Fenn *et al*., 1985; Werner, 2005) are used to simulate scattering effects under various atmospheric conditions. Particle size distributions (PSD) used are described by a modified gamma distribution (Deirmendjian, 1969) which can be used to describe various types of realistic aerosol distributions in rain and water clouds (Bissonnette *et al*., 2004; Hu *et al*., 2006),

$$\frac{dn(r)}{dr} = ar^{\alpha}\exp(-br^{\gamma}), \tag{3.1}$$

where $n(r)dr$ is the number volume density of particles with radii between r and $r+dr$. By assigning different values to the parameter α and γ one can obtain models in Table 3.1. The constants a, b, α, and γ are all real and positive. The values of α and γ describe the steepness of the rise and fall of the distribution and are taken as integer and half-integer values, respectively. The larger the values of α and γ, the steeper and narrower the size function. The effective radius is given by

$$r_e = \left(\frac{\alpha}{b\gamma}\right)^{\frac{1}{\gamma}}. \tag{3.2}$$

The total number density can be obtained by integration over all particle radii (Werner *et al*., 2005),

$$N_0 = a\int_0^\infty r^\alpha \exp(-br^\gamma)dr = a\gamma^{-1}b^{-(a+1)/\gamma}\Gamma((a+1)/\gamma)\,. \tag{3.3}$$

The constants a, b, α, γ, and N_0 are represented by A, B, ALP, GAM, and NPART respectively in the Monte Carlo program functions. The important parameters of ten aerosol models are tabulated in Table 3.1. The size distribution of each aerosol model is shown in Fig. 3.2 and 3.3.

Table 3.1 Parameters for the particle size distribution in Monte Carlo program (Werner *et al*., 2005).

Model #	Atmospheric type	a	α	b	γ	r_e (μm)	N_0 (cm^{-3})
1	Heavy advective fog	0.027	3	0.3	1.0	10.0	20
2	Moderate advective fog	0.066	3	0.375	1.0	8.0	20
3	Corona cloud C2	$1.085\cdot10^{-2}$	8	1/24	3.0	4.0	100
4, 9	Cumulus cloud C1, Heavy radiation fog	2.373	6	1.5	1.0	4.0	100
5	Haze H	$4.0\cdot10^{5}$	2	20.0	1.0	0.1	100
6	Haze L	$4.976\cdot10^{6}$	2	15.119	0.5	0.07	100
7	Haze M	$16/3\cdot10^{5}$	1	8.943	0.5	0.05	100
8	Cloud C3	5.556	8	1/3	3.0	2.0	100
10	Moderate radiation fog	607.5	6	3	1.0	2.0	200

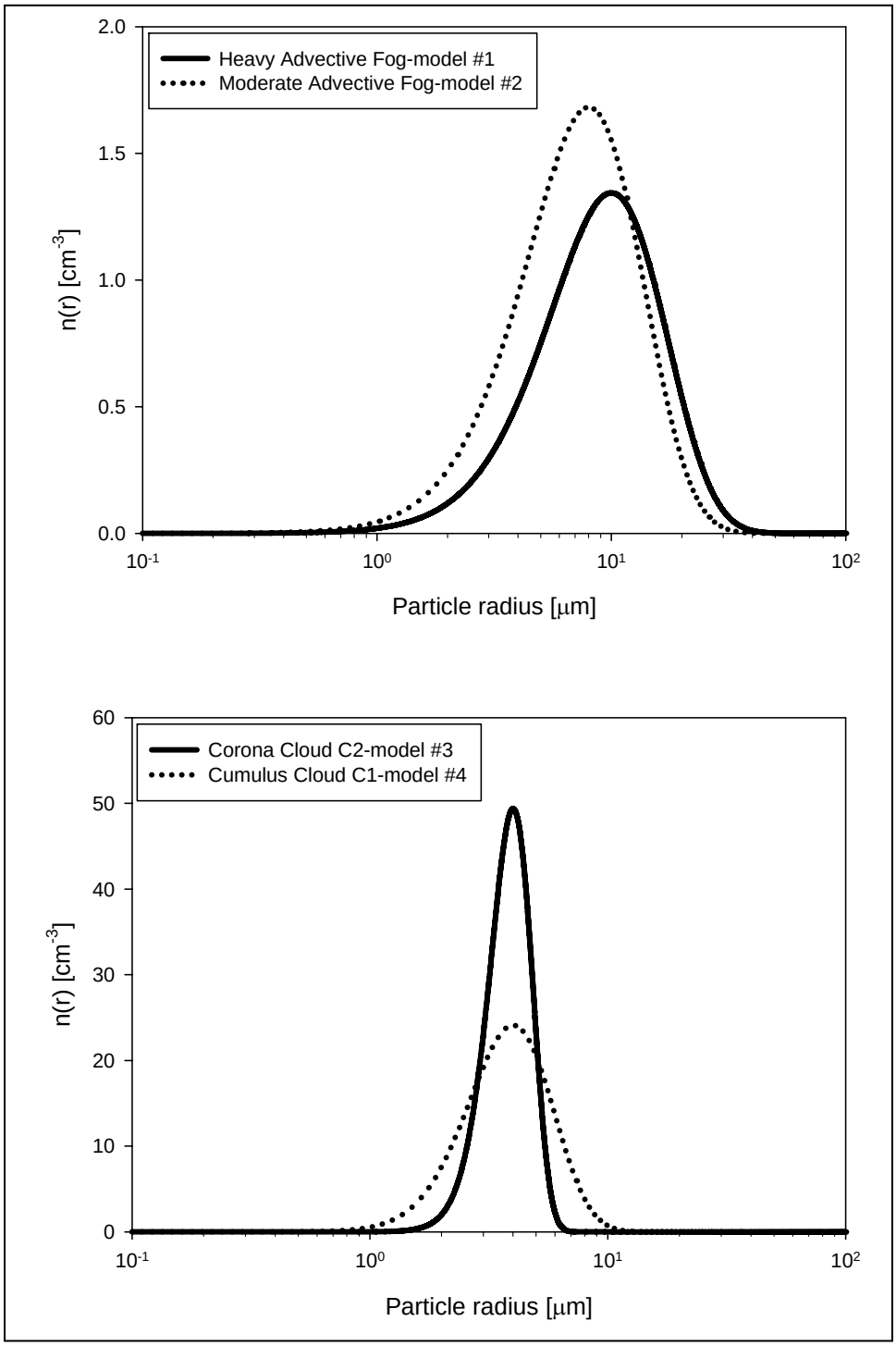

Figure 3.2 Size distributions of aerosol models (Advective fog, C2, and C1).

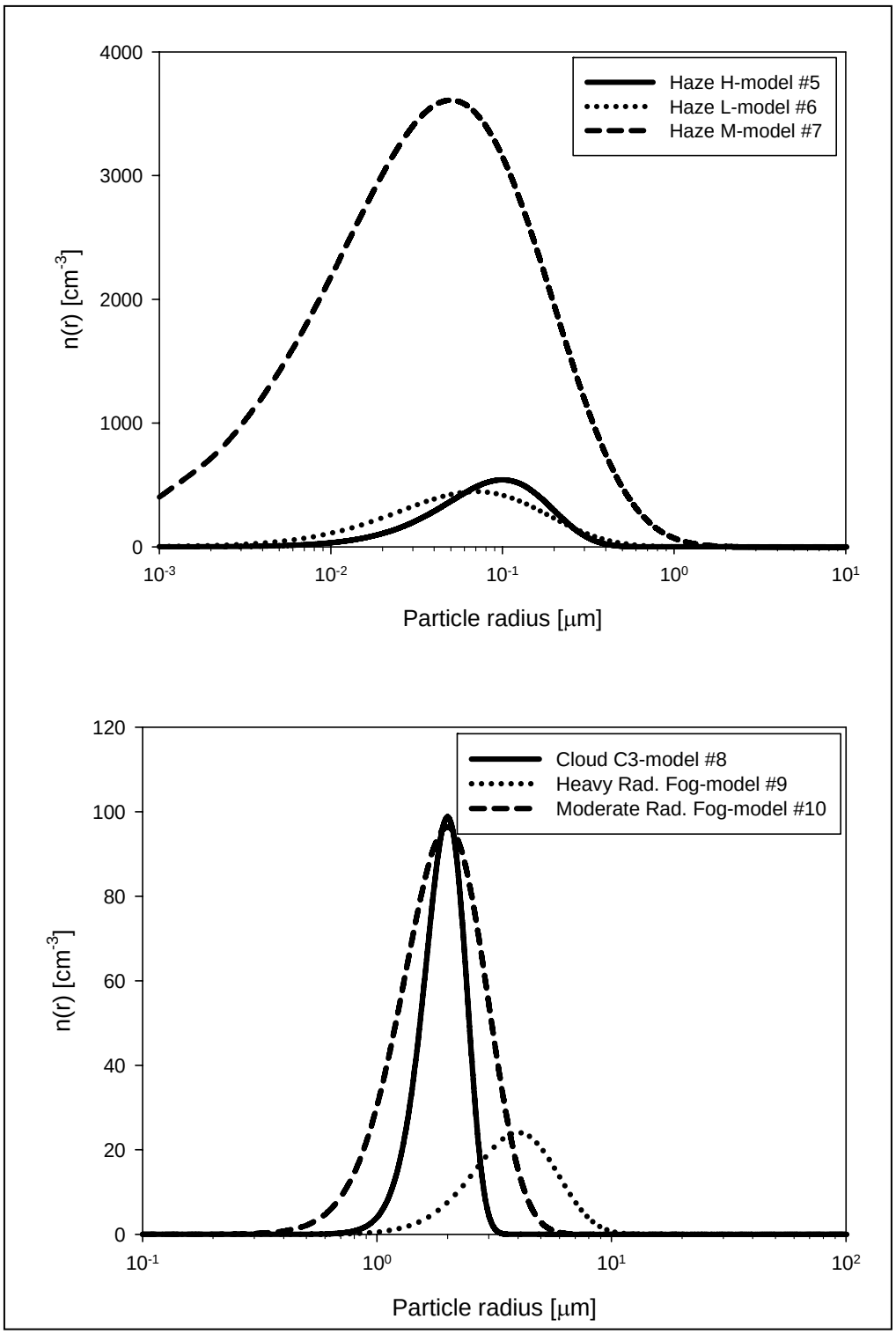

Figure 3.3 Size distributions of aerosol models (Haze, C3, and Radiation fog).

The ground-based multistaic lidar with a horizontal measuring path provides suitable opportunities for studying multiple scattering simulations in fog and haze models. In this thesis, multiple scattering from optically thick media is the primary focus. The aerosol models satisfying the conditions are the models representing heavy advective fog, moderate advective fog, heavy radiation fog, and moderate radiation fog. Therefore, these four fog models are simulated and studied. However, for comparison with single scattering from small particles, the analysis of Haze M model is also included in this chapter. Scattering phase functions, which are an input parameter in this simulation of fog models and Haze M model, are shown in Figure 3.4 and 3.5. These are calculated using Mie theory contained in the Bistatic Monte Carlo method.

Fog and haze are defined by visibility. According to international definition, fog reduces visibility below one kilometer. Haze is defined as dry or damp particles which are so small they cannot be seen by the naked human eye. Fog is a cloud in contact with ground.

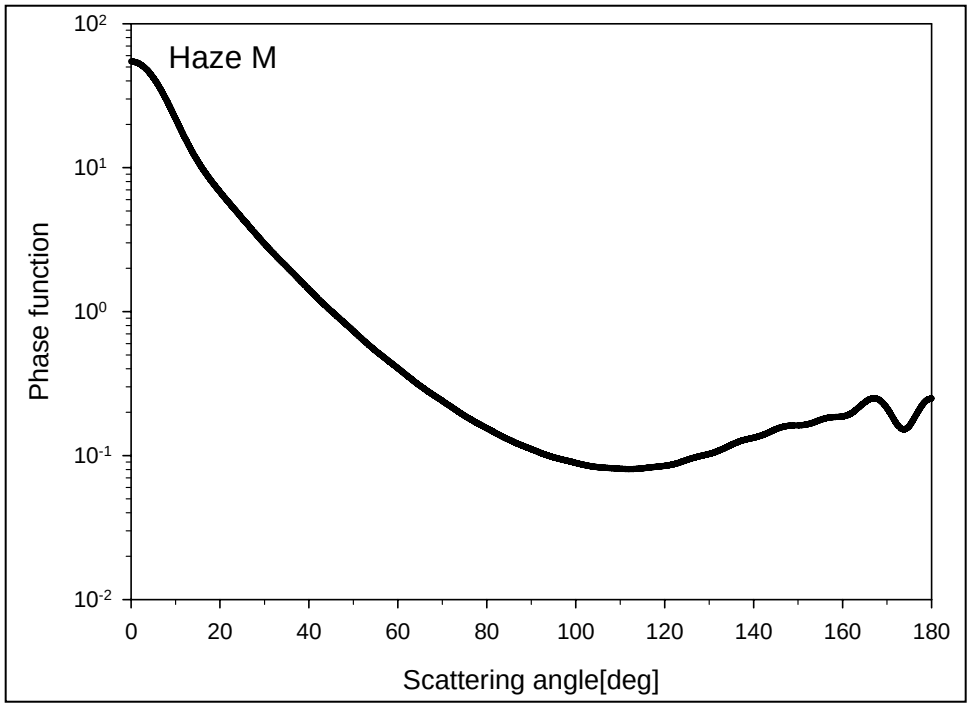

Figure 3.4 Scattering phase function of Haze M for a wavelength of 532 nm and refractive index of $1.33 + 0i$.

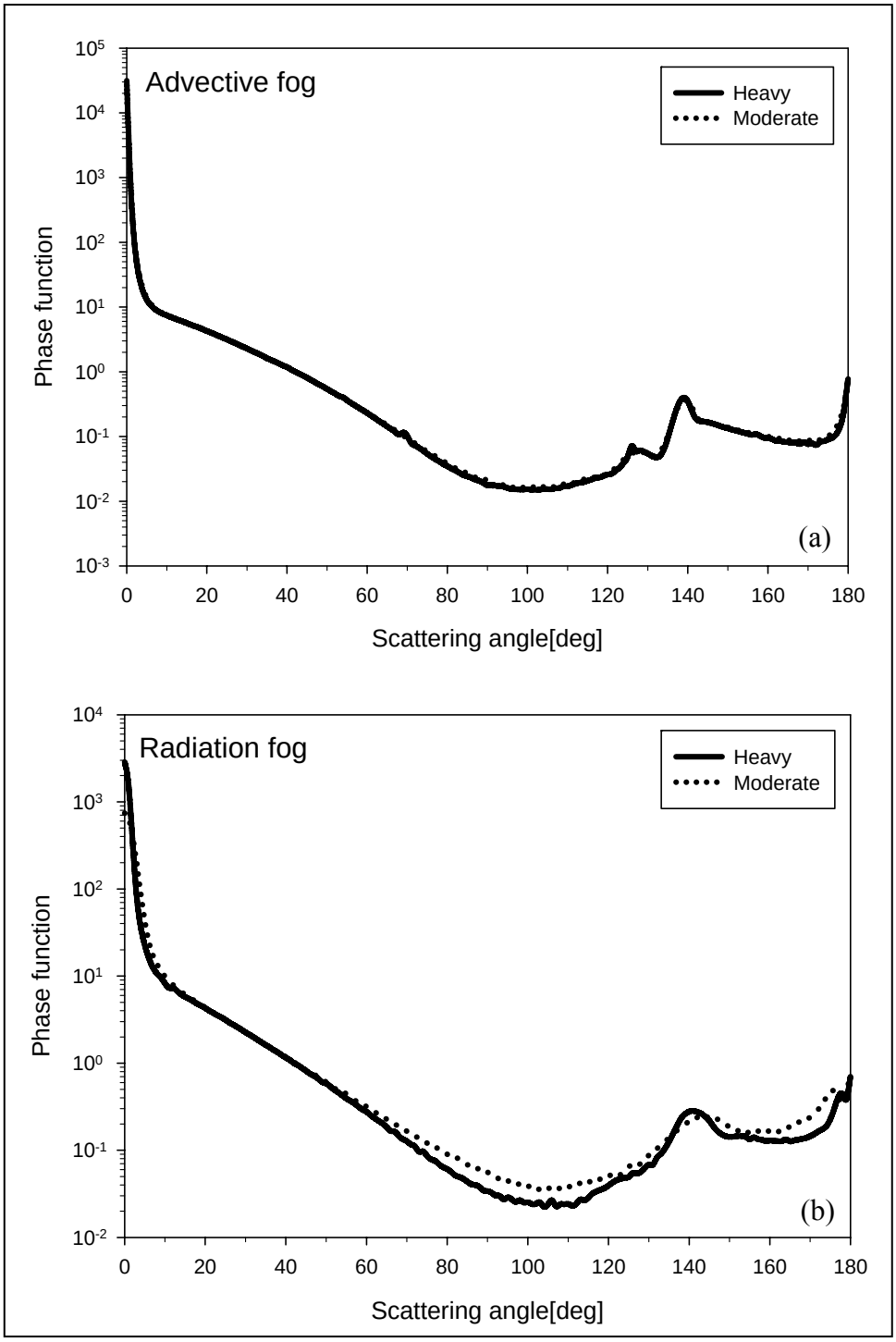

Figure 3.5 Scattering phase functions of fog models for a wavelength of 532 nm and refractive index of $1.33 + 0i$.

When moist air from the surface of the Earth evaporates and moves upward, it may cools and condenses into fog. Most types of fog form when the relative humidity rises from the surface and the air temperature drops below the dewpoint. As the temperature drops lower, it forces the water vapor to condense. Advective and radiation fogs are produced by different atmospheric processes. When the ground loses heat at night by radiational cooling, radiation fog forms if the air cools enough to become supersaturated. Both the size range of particles and the liquid water content are small in radiation fog compared to advective fog, see Table 3.1. Radiation fog is common in autumn, whereas advective fog forms when warm-moist air moves across water or land with a lower temperature; most sea fogs are advective (Fenn *et al*., 1985). Table 3.2 shows information about the vertical thickness, typical radii, and liquid water content (LWC) of fogs measured at different locations (Stewart and Essenwagner, 1982). The more detailed physical parameters of fogs can be found in the same reference. The measured parameters are varied depending on the measurement locations.

Table 3.2 Measured physical properties of advective and radiation fog (Stewart and Essenwagner, 1982).

Physical property	Advective fog		Radiation fog	
	Heavy	Moderate	Heavy	Moderate
Vertical thickness(m)	600	200	300	100
Typical radii(μm)	4 ~ 10		0.1 ~ 5	
LWC(g/m^3)	0.2 ~ 0.4		0.02 ~ 0.2	

Figure 3.6 shows scattered intensities of fog models as a function of visibility. Visibility or visual range, R, can be easily converted to extinction coefficient, σ_{ext}, by the approximation accorded to Koschmieder's theory. In case of horizontal visibility distances with homogeneous atmospheric conditions, visibility is given by,

$$R = \frac{3.912}{\sigma_{ext(\lambda=550nm)}}, \tag{3.4}$$

where R is expressed in meters. Visibility is therefore inversely proportional to the extinction coefficient derived from the visible range. Backscattered intensities vary by more than a factor of 1.5 for the four different fog conditions shown in the Figure 3.6 (a). However, at a forward scattering angle of $30° \pm 10°$ these differences nearly vanish, see the Figure 3.6 (b). This face can be verified by examining the phase functions shown in Figure 3.7 which shows the scattering phase functions of fog models overlaid Figure 3.5 (a) and (b).

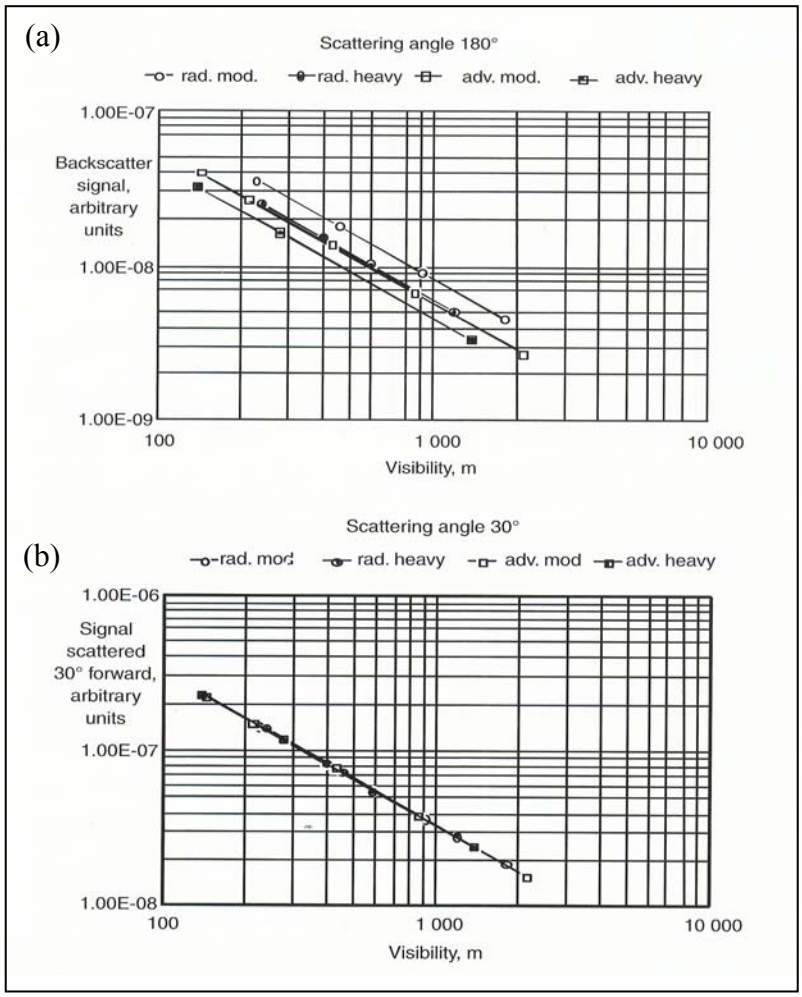

Figure 3.6 Relative magnitude of scattered signal for fog models (Werner *et al*., 2005).

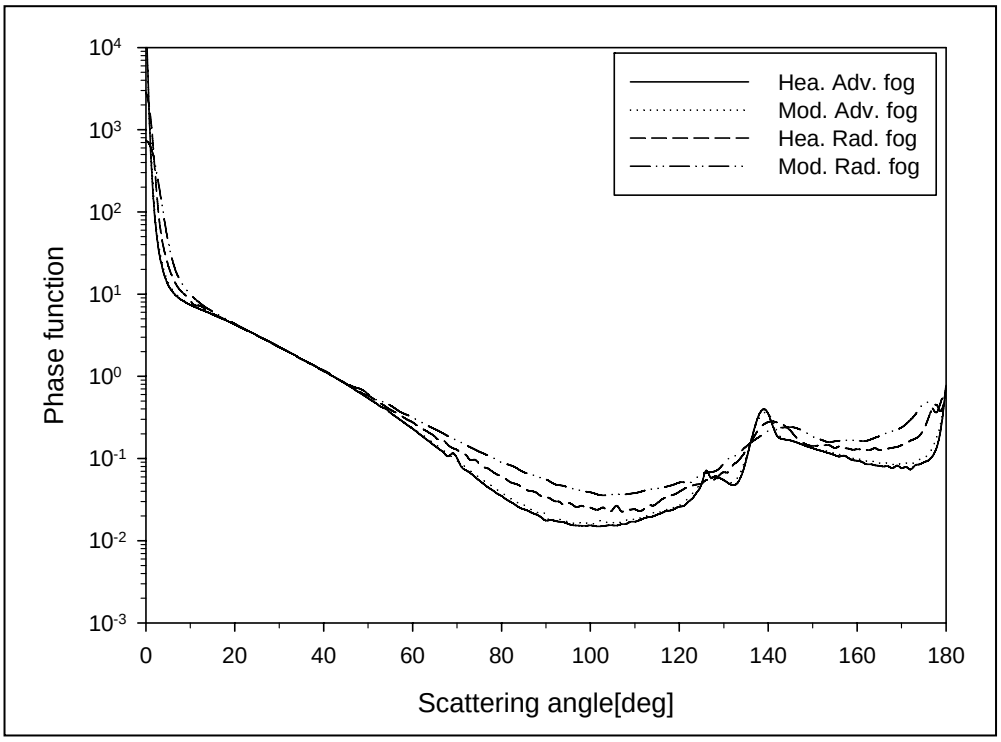

Figure 3.7 Scattering phase functions of fog models overlaid Figure 3.5 (a) and (b).

From these facts, one realizes that the scattered intensity is more sensitive to the particle size distribution in the backward direction than in the forward direction.

3.3 Simulation Results

It was known that the influence of multiply scattered light on lidar data depends on range, optical depth, transmitter divergence, and receiver field of view in a very complex manner (Seldomridge *et al*., 2006). In this section, we discuss how multiple scattering is affected by these factors. The numerical experiment consists of two parts. The first part includes simulations for a conventional monostatic lidar geometry and comparisons with the results from the previous Monte Carlo methods to demonstrate the acceptability of the Bistatic Monte Carlo method for the directly backscattered component that has been previously studied by others. The second part includes simulations for a multistaic lidar geometry to describe the angular distribution of multiply scattered radiation.

The objective of the first part is to verify the applicability of a Bistatic Monte Carlo method. Therefore, the lidar geometry and medium characteristics are adopted from the previous paper of Bissonnette *et al*.(1995). This also includes calculation of the lidar returns from a 300 m thick, uniform density of C1 cloud model, see Table 3.1. The cloud is at a distance, D, of 1000 m from the lidar and the atmosphere below is assumed to neither absorb nor scatter. The wavelength of a pulsed laser is 1.064 μm, the beam divergence is equal to 0.1 mrad full angle, and the pulse length is 40 ns. The cloud's scattering properties are calculated using Mie theory. The refractive index of cloud particles is taken as $m = 1.325 + 0i$ and an extinction coefficient is 0.01725 m^{-1}. In the first case, two laser divergences are used, 0.2 and 2 mrad with a receiver FOV of 10 mrad. In the second case, two fields of view for the detector are used, 1 and 10 mrad full angle, and with a laser beam divergence of 0.1 mrad. Figure 3.8 shows the result for the first case. For typical values of the laser beam divergence in lidar systems, multiple scattering contribution is almost same over the entire range in this calculation. It turns out that the laser divergence does not affect our multiple scattering measurements significantly. The simulation results for the second case are also shown in Figure 3.9 to Figure 3.12. Each figure was plotted for a multiple-to-single or double-to-single

scattering lidar return ratio as a function of range into the cloud. There are also previous results from different Monte Carlo methods shown in the same plots for comparison.

The different Monte Carlo methods shown in the plots fall into four main categories: numerical Monte Carlo methods, stochastic descriptions of photon scattering, analytical extension of the Mie theory, and approximations to the radiative transfer equation (Bissonnette *et al*., 1995). The models used by the Florance group, NASA group, and Israel group are the numerical Monte Carlo calculations. The model used by the Florance is a semi-analytic Monte Carlo method where the contributions of the different orders of scattering to the lidar returns are calculated separately, and the results are very similar to the model used by the Israel group. Unlike the Florance group, no variance-reduction techniques are used by the NASA group. Therefore the procedure of the NASA group is straightforward and can be used as a check of difference among the more sophisticated approaches. The model of the Munich group is the stochastic description of photon scattering. The main advantage of this model is a decrease of calculation time for a desired accuracy.

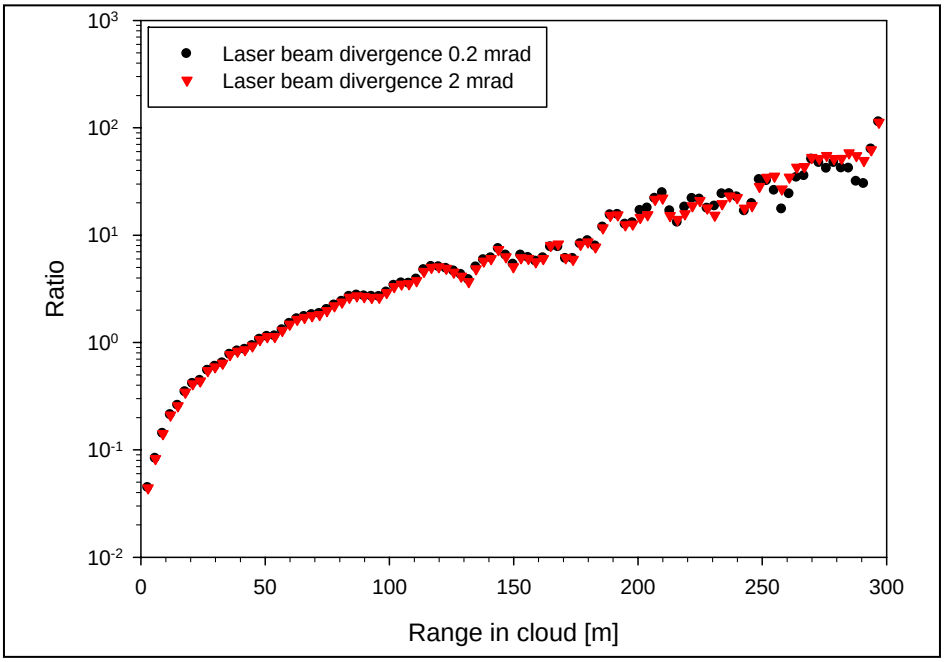

Figure 3.8 Calculated ratios of the multiple to single scattering contributions from a uniform C1 cloud for two laser beam divergences.

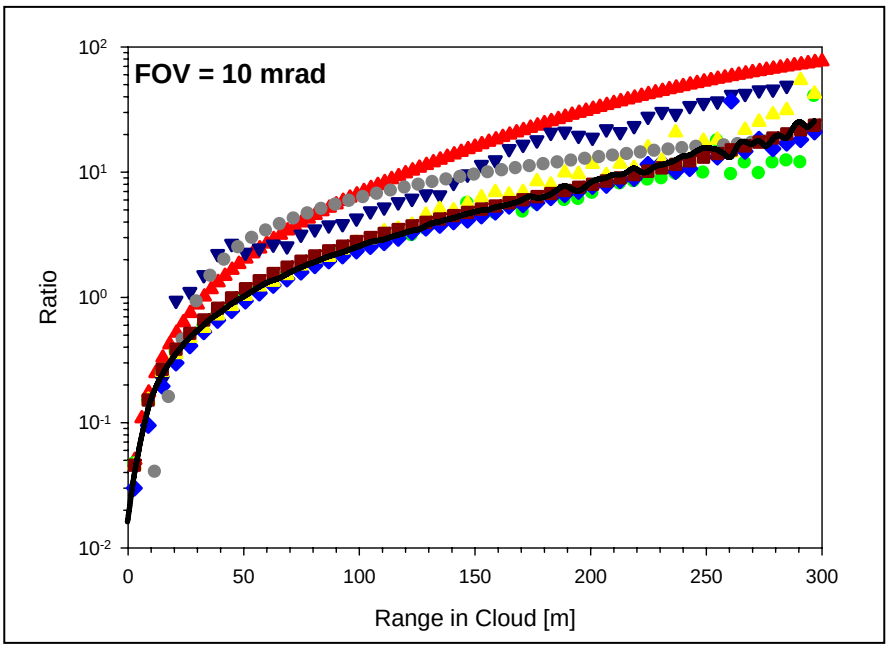

Figure 3.9 Calculated ratios of the multiple-to-single scattering contributions to the lidar return from a uniform C1 cloud for a receiver field of view of 10 mrad: ▲ DRDC's model; ● Florence group's model; ▼ Israel group's model; ♦ Munich group's model; ▬ NASA group's model; ● Swiss group's model; ■ Minsk group's model (replotted from Bissonnette *et al*., 1995), and Bistatic Monte Carlo model (black line).

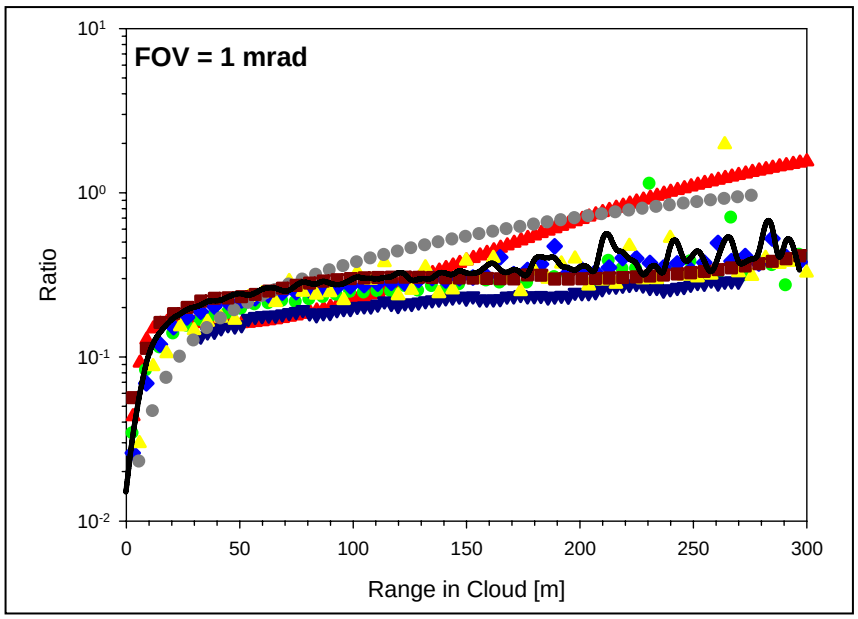

Figure 3.10 Same as Figure 3.9 but for a receiver field of view of 1 mrad (replotted from Bissonnette *et al*., 1995).

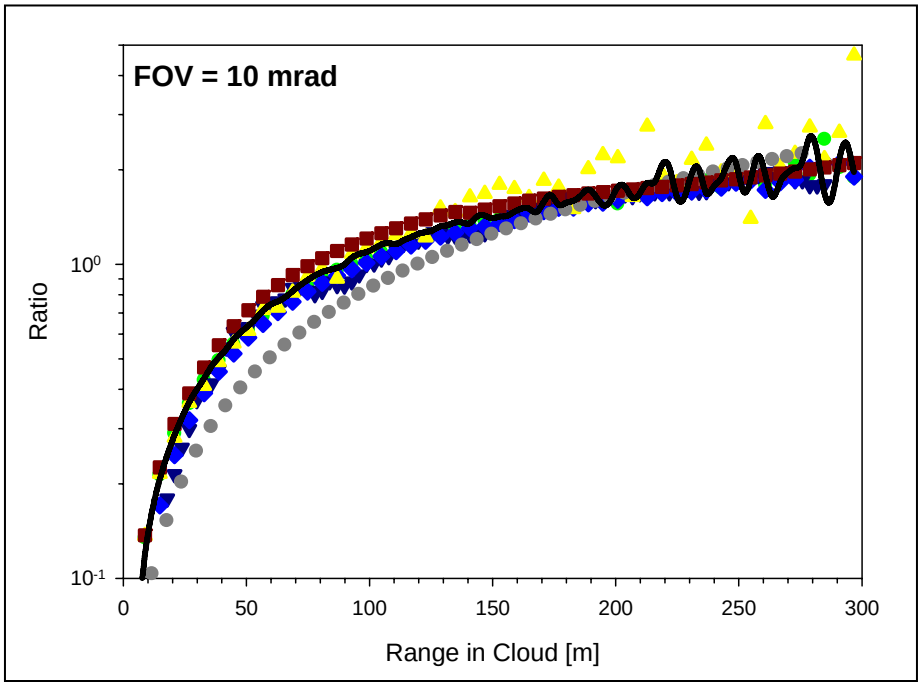

Figure 3.11 Calculated ratios of the double-to-single scattering contributions to the lidar return from a uniform C1 cloud for a receiver field of view of 10 mrad for the same models in Fig. 3.9 (replotted from Bissonnette *et al*., 1995), and Bistatic Monte Carlo model (black line).

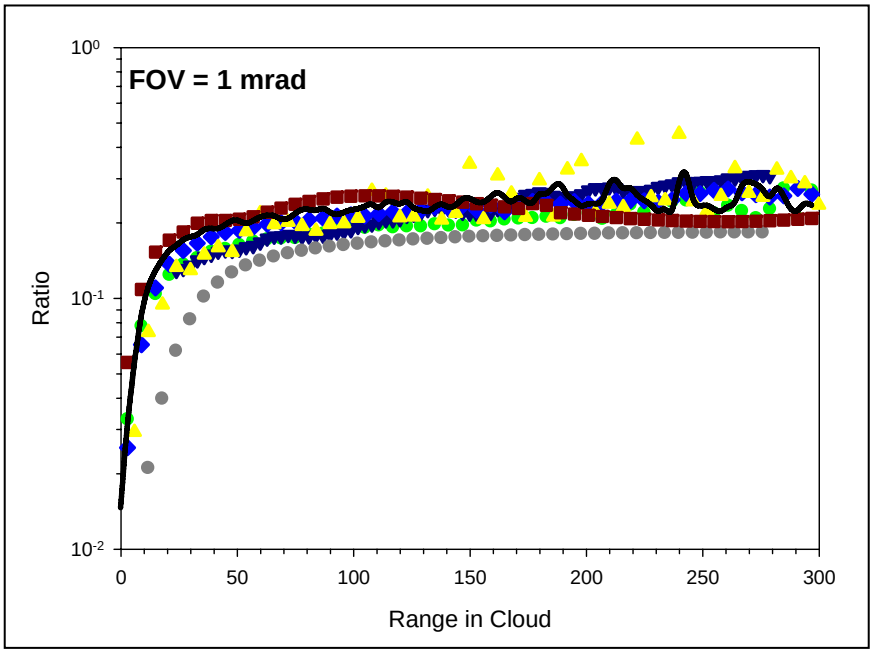

Figure 3.12 Same as Figure 3.11 but for a receiver field of view of 1 mrad (replotted from Bissonnette *et al*., 1995).

The approach adopted by the Swiss group is based on the analytical extension of Mie theory to include the effects of multiple scattering. The spherical wave scattered by the first particle is considered as the field impinging on the second one. This procedure can be repeated at all scattering orders. In case of higher scattering orders, the incident field is a superposition of spherical waves. Following analytically through this process, step by step, they construct the n-fold electromagnetic field scattered by an ensemble of particles. The models used by the DRDC group and the Minsk group are based upon approximations to the radiative transfer equation. The DRDC model is applicable to narrow incident light beams. This method relies on the paraxial approximation, and the representation of the flux normal to the incident beam axis as a diffusion process, which we are using in our multistatic lidar analysis. However, in the case of the Minsk group's model, the radiance in the forward direction is due to small-angle multiple scattering, whereas only single scattering is taken into account in the backward direction. As can be seen in Figures 3.8-3.12, the ratio is almost zero in the first 10 m of range. It can be explained in two cases. First, in case of a biaxial-monostatic lidar, the transmitted beam does not overlap the detector's field of view in the near range. Second, in case of a biaxial-monostatic lidar, it is caused by a telescope focal length limitation or an obstruction to the return radiation by a reflecting mirror. The detailed explanation about the geometrical form factor also can be found in Chapter 7.4 in Measures' book (1984). Results of the Bistatic Monte Carlo method show good agreement with other methods, especially Minsk group's model. One can draw a conclusion that multiple scattering increases with increasing penetration distance, and receiver field of view due to the acceptance of an increase of scattering volume.

The second part of the simulation is to calculate the lidar returns from a multistatic lidar geometry. Scattering from fog due to wavelengths in the visible is strongly anisotropic with a sharp forward peak of the phase function at least three or four orders of magnitude larger than the value of the phase function at any other angle and the phase function between 60° and 175° is very sensitive to polarization ratio. Therefore, detailed information in the forward and backward directions is required to extract multiple scattering effects (Liou and Schotland, 1971). The benefit of the Bistatic Monte

Carlo method is that the receiver can be located at both forward and backward directions so that one can describe the lidar returns at different scattering angles by adjusting the distance between the transmitter and the receiver or changing the location of the receiver. Figure 3.13 shows the simulation geometry for the second part of our calculation. The angular resolution is approximately 0.5° in the first 10 m and after 10 m, it's 1° at each direction. The simulation geometry for laser angular scattering measurement is similar to the approach performed by Raj *et al*. (2003).

As mentioned in the previous chapter, calculations were performed for the four fog models and the Haze M model. This part consists in calculating the lidar returns from a 36 m thick layer of a scattering medium. The scattering medium is at a distance D of 100 m from the lidar, which is similar in geometry to the chamber experiment at DRDC. The distance D will be increased as a receiver moves along the positive y axis, see Figure 3.13. However, the contributions to the lidar returns from the different ranges between the scattering medium and the receiver can be neglected because atmosphere below the scattering medium does neither absorb nor scatter. The wavelength of the laser is 532 nm and the beam divergence is 0.2 mrad full angle. The field of view of a detector is 840 mrad (48°). The refractive index of each scattering medium is taken as $m = 1.325 + 0i$. In each case, a single scattering albedo is assumed to be one, which means absorption by atmospheric particles is not considered in our simulation. Extinction coefficients are 0.02835 m^{-1} for the heavy advective fog, 0.01823 m^{-1} for the moderate advective fog, 0.01651 m^{-1} for the heavy radiation fog, 0.008554 m^{-1} for the moderate radiation fog, and 0.0009061 m^{-1} for the haze M, respectively. Lidar returns are plotted for both forward and backward directions. For comparison with single Mie calculation, scattering phase function (Figures 3.4 or 3.5) is also included in each plot. One can see the difference in angular distribution of multiply scattered light mainly due to different size distributions. This can be seen from results shown in Figures 14-18. In all cases, 1st order scattering (single scattering) follows scattering phase function very well between 0° and 20° in the forward direction and 160° and 180° in the backward direction. This phenomenon also can be seen in polarization ratio data measured at DRDC experiments,

which will be discussed in Chapter 6. The intensity of multiple scattering increases as the extinction coefficient increases over the whole angular region ($I^{ms}_{Adv.fog} > I^{ms}_{Rad.fog} > I^{ms}_{HazeM}$).

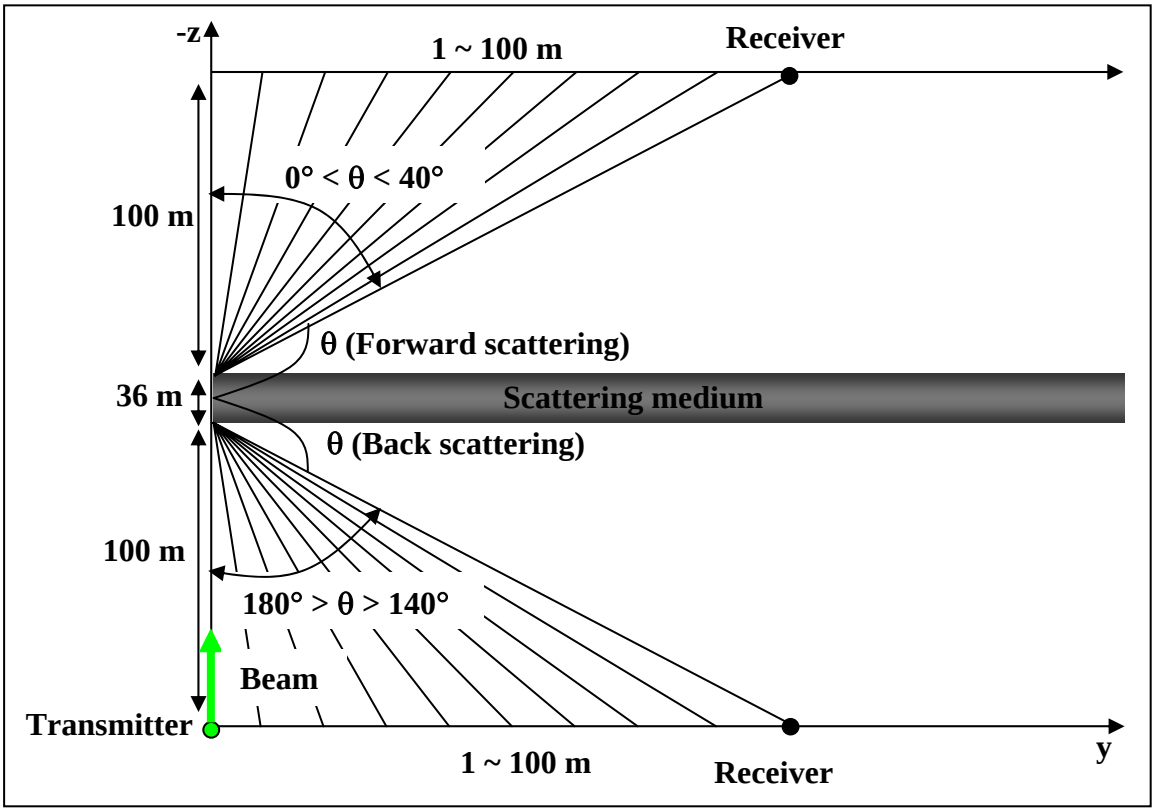

Figure 3.13 Geometry selected to study the bistatic Monte Carlo method for a multistatic lidar.

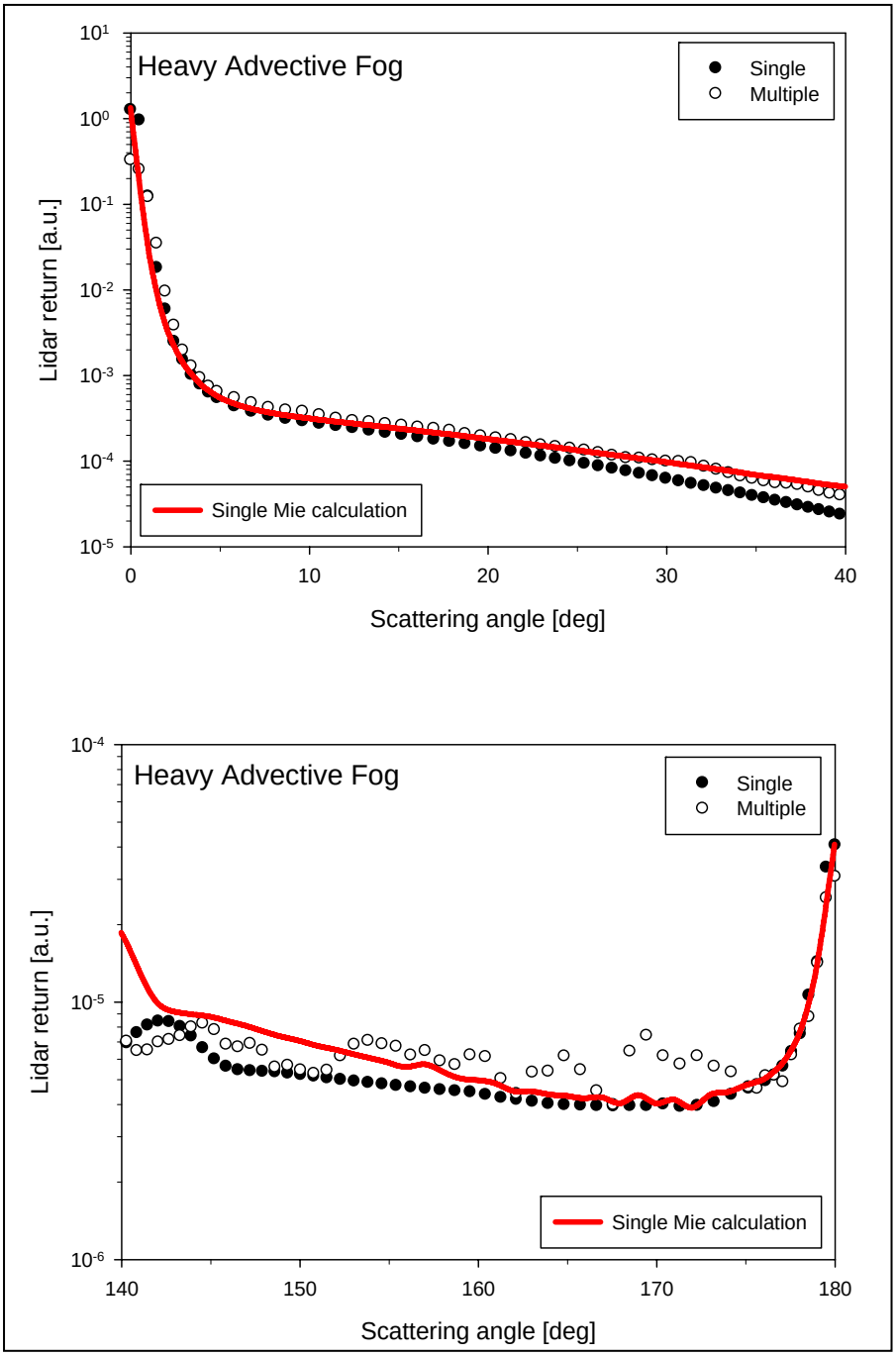

Figure 3.14 Angular distribution of multiply scattered light for a heavy advective fog.

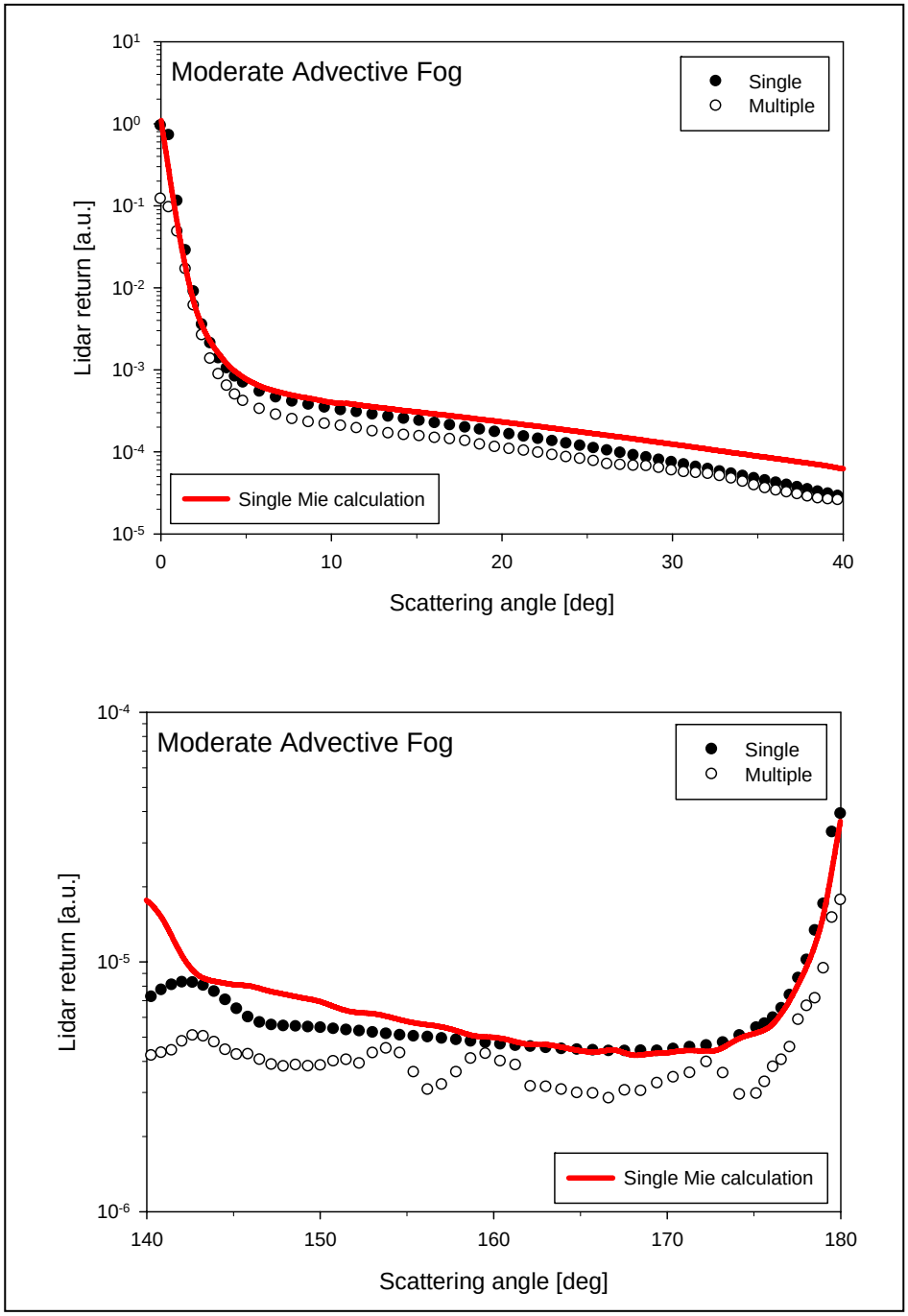

Figure 3.15 Angular distribution of multiply scattered light for a moderate advective fog.

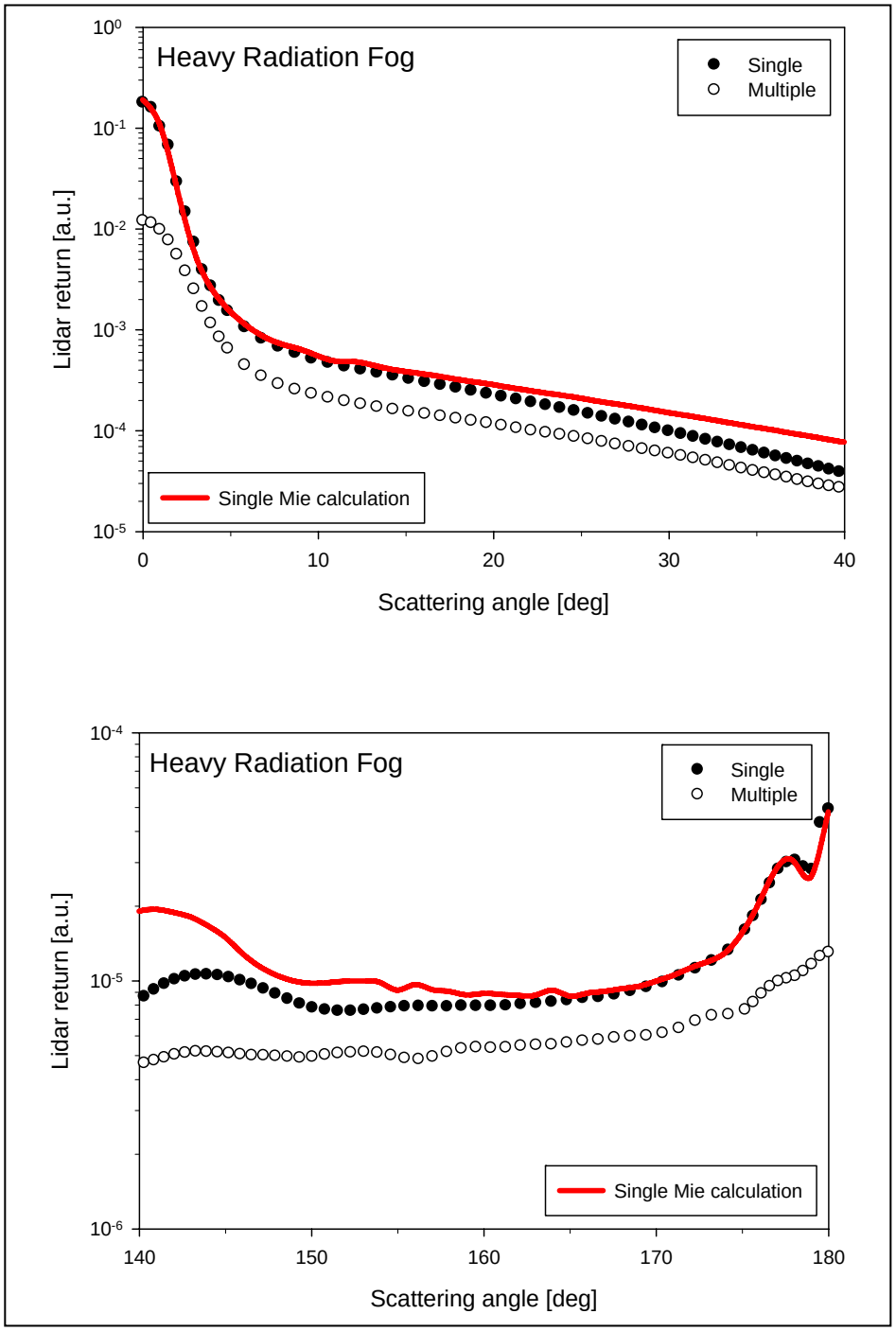

Figure 3.16 Angular distribution of multiply scattered light for a heavy radiation fog.

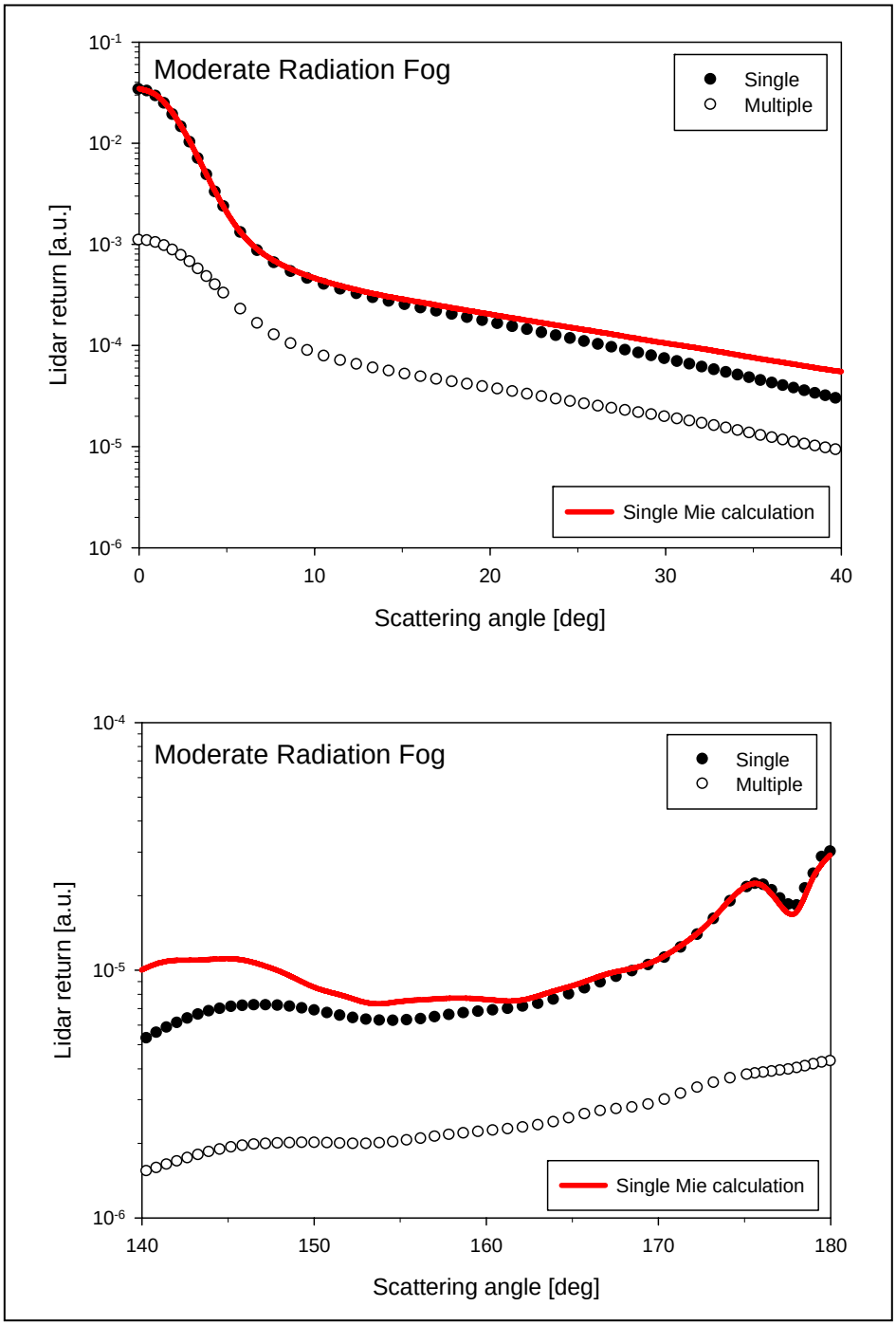

Figure 3.17 Angular distribution of multiply scattered light for a moderate radiation fog.

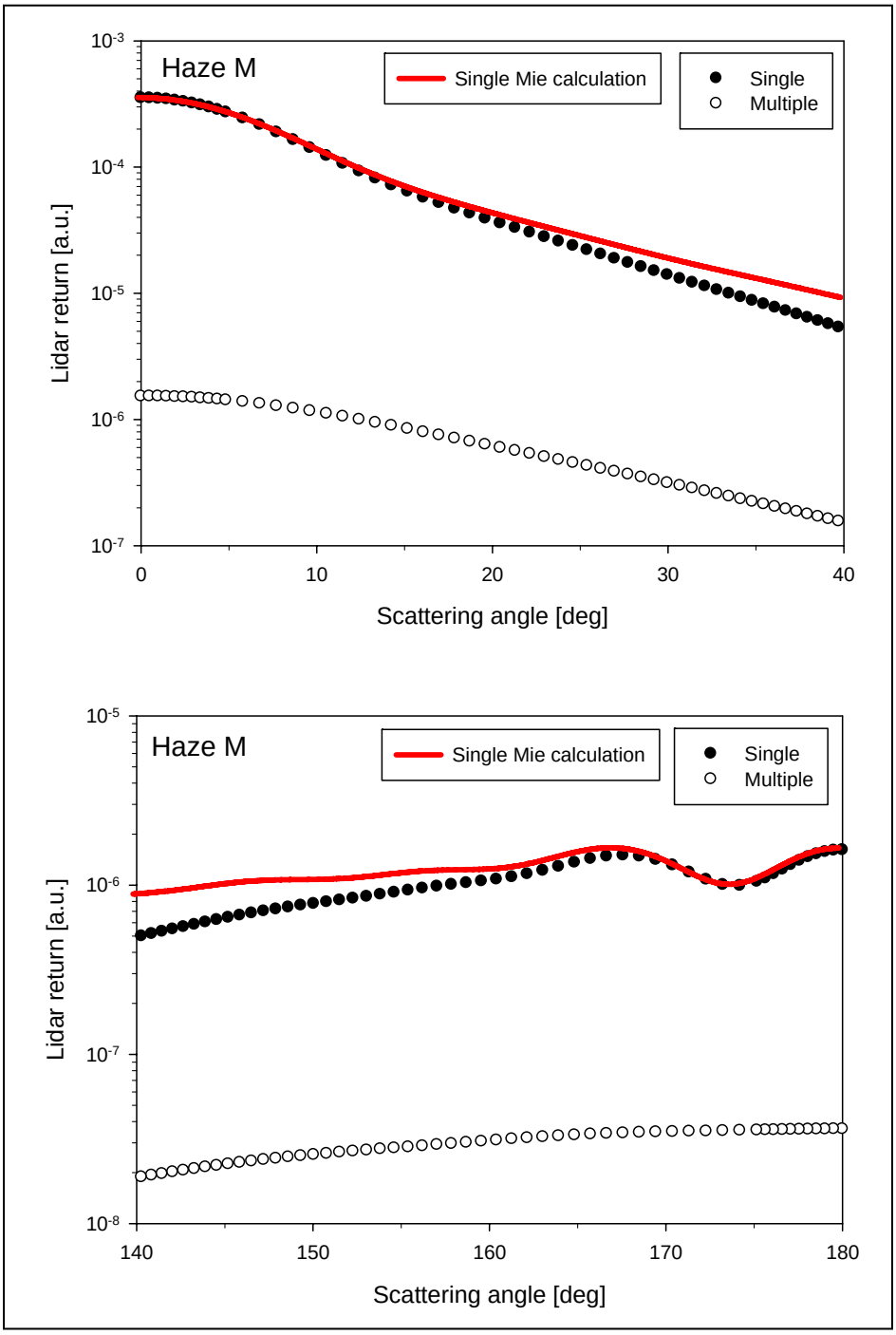

Figure 3.18 Angular distribution of multiply scattered light for a Haze M model.

In case of a heavy advective fog, the intensity of multiple scattering is comparable to or bigger than that of single scattering.

The angular behavior of lidar returns for multiple scattering follows a similar distribution as the single scattering events because multiple scattering is a sequential summation of many single scattering events (Pal and Carswell, 1985). In case of the particle size distribution of large particles, such as the advective fog models, multiple scattering contributions are comparable to single scattering in both the forward and backward directions. It is due to the fact that light scattered by particles larger than the wavelength of the incident light result in increased intensity of forward-scattered light confined in a very narrow angular region as the particle size increases. This makes it more likely that a photon is scattered forward in a first scattering event and will interact with another particle to be backscattered while in a second scattering event within the field of view of the lidar receiver. Therefore, multiple scattering is dominated by highly probable forward scattering. However, in the case of size distribution having small particles of the Haze M model, single scattering dominates in all angular regions.

Finally, numerical calculations are performed to define the atmospheric conditions where aerosol multiple scattering calculations are valid. The lidar geometry is very similar to that of Bissonnette *et al*. (1995). The detector's field of view is fixed as 10 mrad. Four atmospheric models having different particle size distributions are considered to study when optical depth increases multiple scattering significantly, and how rapidly multiple scattering increases as optical depth increases. The results are shown in Figures 3.19-20. The lidar returns of single and multiple scattering are plotted on a log-scale of optical depth. As shown in each lidar-return plot, the optical scattering in each case is important up to an optical depth of 10, which means that the transmitted laser beam is totally attenuated by scattering media after this point. Multiple scattering from atmospheric models having large particles (fog models) starts increasing from the optical depth of 0.1 and shows a maximum contribution between 0.3 and 0.7. However, in the case of haze M model which has an effective radius, r_e, of 0.05 μm, multiple scattering

effects are significantly smaller and can be considered to be negligible for optical depths in the range 0.1-10.

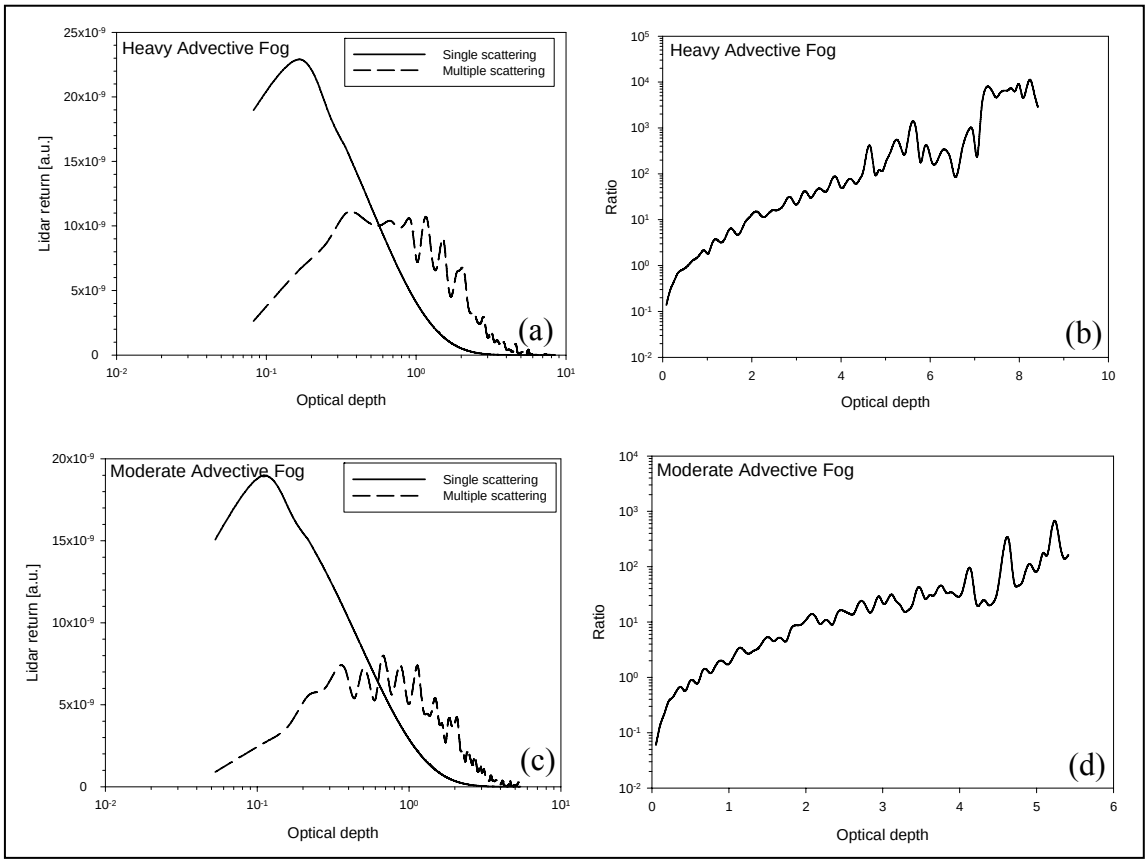

Figure 3.19 Lidar returns and calculated ratios of the multiple-to-single scattering contribution from different models; (a), (b) for heavy advective fog and (c), (d) for moderate advective fog.

The other important aspect obtained from these results is that multiple scattering contributions also increase with particle size. In the case of the haze M model, multiple scattering is always smaller than single scattering for optical depths up to 4.

In closing this chapter, the Bistatic Monte Carlo method was introduced. Good agreement is found in comparisons with other Month Carlo methods in the applicable region of small angles. It has ability to simulate the full angular distribution of multiply scattered radiation by adjusting the distance between the transmitter and the receiver or

changing the location of the receiver. In this chapter, multiple scattering effects are examined with different detector's FOVs, particle sizes, and optical depths. It turns out that it is very difficult to define the exact atmospheric conditions that multiple scattering should be considered because it depends upon all three factors in a coupled way.

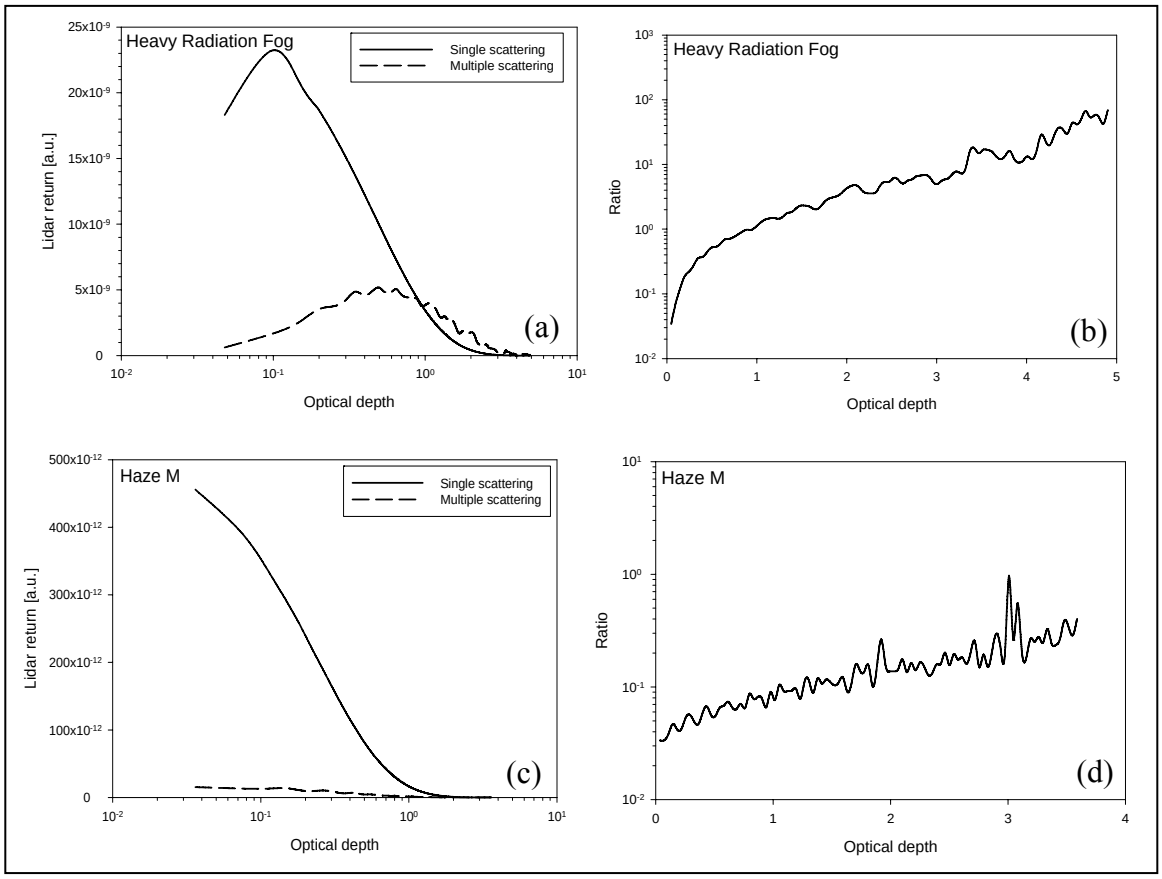

Figure 3.20 Lidar returns and calculated ratios of the multiple-to-single scattering contribution from different models; (a), (b) for heavy radiation fog and (c), (d) for haze M.

Chapter 4

MULTISTATIC LIDAR CONFIGURATION

A bistatic lidar technique was first used in late 1930s and early 1950s to understand molecular scattering in atmosphere using searchlights. Hulbert (1937) and Elterman (1951) used bistatic technique with high intensity searchlights to measure the scattered intensity from atmospheric molecules up to the range 20 km and 70 km. After the advent of laser in 1960s, several scientists (Reagan *et al*., 1982; Devara and Raj, 1989; Welsh and Gardner, 1989; Meki *et al*., 1996; Sugimoto, 1999; Barnes *et al*., 2003) have developed and applied the bistatic lidar systems to study atmospheric aerosols. However, this technique has been suffered from the inherent uncertainty of lidar returns from different scattering volume due to the lidar geometry and many vertical or horizontal scans needed for a height or range profile to be obtained. To overcome these drawbacks, polarization measurements and the choice of wide angle optics were attempted by Stevens (1996) using a bistatic lidar. A multistatic lidar configuration was first used by Novitsky (2002) to measure polarization properties of atmospheric aerosols to provide finer resolution measurements. It was found that one scattering angle is not enough to determine particle size of aerosols when sharp gradients such as layers of aerosols are present. Therefore, Novitsky measured scattered intensities at three different off-axis scattering angles using a vertical mode of a multistatic lidar, especially in the range of scattering angles between 145° and 175° where the polarization ratio is more sensitive to the size distribution.

The benefits of using the multistatic lidar configuration are the small dynamic range required for signal detection, the capability of measuring scattered intensity in the forward, sidelook, and backscattering directions simultaneously, and the simple and inexpensive detection optics (Barnes *et al*., 2003). In this chapter, the multistaic lidar theory will be described briefly and the instruments used in our chamber/field experiments will be introduced.

4.1 Multistatic Lidar Theory

There are two choices in order to observe the angular dependence of multiple scattering. One requires either multiple transmitters or multiple receivers. The disadvantage of using multiple transmitters is that the interfered lidar signals from each transmitter can overlap in a detector if a common volume is studied. Therefore, the technique proposed here is to use multiple receivers having similar optical characteristics. The geometry of the multistatic lidar with one CCD camera in the backscattering direction is shown in Figure 4.1. The benefits of the CCD-based imaging lidar method are low cost and simplicity of the lidar setup. The choice of wide angle optics eliminates the need for spatial scanning to cover the desired range of scattering angles.

The laser emits in the horizontal direction and the three cameras, which are separated from the laser by a distance, D, can be located at forward, side, and backward directions, see Figure 4.3. Measurements are made with linearly polarized incident laser beam, but a detection system is not polarization sensitive. The received power from a scattered volume with unit angle $d\theta$, which is the field of view of one pixel, can be described as (Meki *et al*., 1996),

$$P_r = P_t \frac{KAT_t T_r \beta(z,\theta)}{R^2} dz\,, \tag{4.1}$$

where P_r is the received power, P_t is the transmitted power, K is the optical efficiency of the receiver, A is the collecting area of the receiver, and T_t and T_r are the atmospheric transmittance from the laser to scatterers and from scatterers to the receiver at range R. However, in small scale experiments such as chamber experiments and/or small scale field experiments, the transmittances, T_t and T_r are almost same. The term $\beta(z,\theta)$ is the scattering coefficient, which is a function of range z and scattering angle θ. The scattering angle, θ, is measured from the beam propagation directions and can be denoted either as the forward ($0 < \theta < 90°$) or backward ($90 < \theta < 180°$) direction

depending on the location of a detector. The scattering angle θ at each location is determined from the distance between a laser beam and a receiver, D, FOV of the receiver, and the pointing direction.

As mentioned in Chapter 1, a bistatic or a multistatic lidar signal does not have $1/R^2$ dependence because the length of a volume element for a pixel, dz, is proportional to R^2 as shown below. From the geometry of Figure 4.1, the height z is given simply by,

$$\tan\theta = -\tan\alpha = -\frac{D}{z},\ z = -\frac{D}{\tan\theta}. \tag{4.2}$$

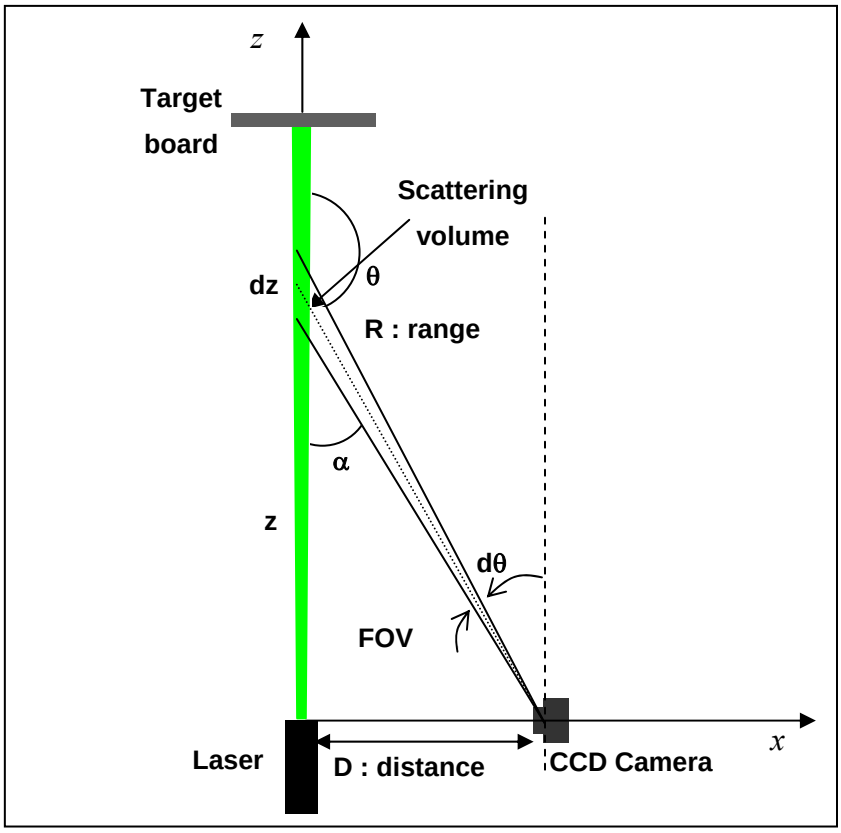

Figure 4.1 Geometry of a bistatic (multistatic) lidar.

Differentiating both sides of equation (4.2), the height resolution dz is given by,

$$dz = D\frac{\sec^2\theta d\theta}{\tan^2\theta} = \frac{Dd\theta}{\sin^2\theta} = \frac{Dd\theta}{D^2/R^2}, \tag{4.3}$$

$$dz = R^2\frac{d\theta}{D}. \tag{4.4}$$

Equation (4.1) thus becomes,

$$P_r = P_t\frac{KAT_tT_r\beta(z,\theta)}{D}d\theta, \tag{4.5}$$

which is independent of R^2. The cancellation of the R^2 dependence has important consequences for the dynamic range of the system (Meki *et al*., 1996 and Stevens, 1996).

Combining terms, we can rewrite the lidar equation in a simplified form as,

$$P_r = P_t\frac{C}{D}\beta(z,\theta)T^2d\theta, \tag{4.6}$$

where $C = KA$ which describes design characteristics of the lidar. Thus the equations representing the signals received in the multistatic receivers, which depend on the polarization state of the incident beam, can be written as,

$$P_{r,//} = P_t\frac{C}{D}\beta_{//}(z,\theta)T^2d\theta, \tag{4.7}$$

and,

$$P_{r,\perp} = P_t \frac{C}{D} \beta_{\perp}(z,\theta) T^2 d\theta \,. \tag{4.8}$$

Here, $P_{r,//}$ and $P_{r,\perp}$ represent the range and angle-resolved signals. The volume backscattering coefficients for the parallel and perpendicular polarizations are given by $\beta_{//}(z,\theta)$ and $\beta_{\perp}(z,\theta)$, respectively. For the multistatic lidar, both the D term and the two-way transmittance of the scattering medium, T^2, make identical contributions to both signals and the system constant term, C, because the same receiver detects the scattered intensities of the different polarization states at each location. If it is assumed that the transmitter and receivers are in the scattering plane exactly, the polarization ratio can be calculated by

$$\delta_p = \frac{P_{r,//}}{P_{r,\perp}} = \frac{P_t (C/D) \beta_{//}(z,\theta) T^2 d\theta}{P_t (C/D) \beta_{\perp}(z,\theta) T^2 d\theta} = \frac{\beta_{//}(z,\theta)}{\beta_{\perp}(z,\theta)}. \tag{4.9}$$

The effects of a multiple scattering during propagation of narrow light beams in aerosols can be investigated using two features; the radial distribution of scattered light and the changes of polarization ratio compared to single particle scattering. The radial distribution of multiply scattered light as a function of optical depth was examined by Bissonnette (1995). It was found that the central part of the transmitted beam, which has its Gaussian shape, is not affected by multiple scattering. The on-axis beam extinction along the direction of beam propagation is primarily governed by Beer-Lambert's law. The narrow central part of the beam is surrounded by an aureole, which is due to multiple scattering, that increases in width with increasing optical depth.

Polarization ratio is also a useful parameter because spatial and temporal aerosol number density variations in measurements made at different scattering angles are canceled (Reagan *et al*., 1982). Polarization ratio used in this thesis is given by the equation (2.4) and (4.9). We note that the definition for polarization ratio adopted here is not universally employed. Care must be taken when one sees the definition of

"polarization ratio", or "depolarization ratio". A comprehensive overview of the several different depolarization definitions used within the lidar community was mentioned in the Chapter 2.2.1 and also found in Cairo *et al*. (1999) with more detail. As pointed out in Chapter 2.2.1, depolarization can be caused by anisotropy of the atmospheric molecules, nonsphericity, or multiple scattering. However, depolarization components from the first two factors are ignored in our experiments because the polarization ratio from the molecular anisotropy is very small and fog particles studied here are almost spherical. Therefore, it is reasonable to assume that the primary source of depolarization in our experiments is multiple scattering.

The most probable multiple scattering patterns, which can be seen by multistatic lidar receivers at forward and backward directions, are shown in Figure 4.2.

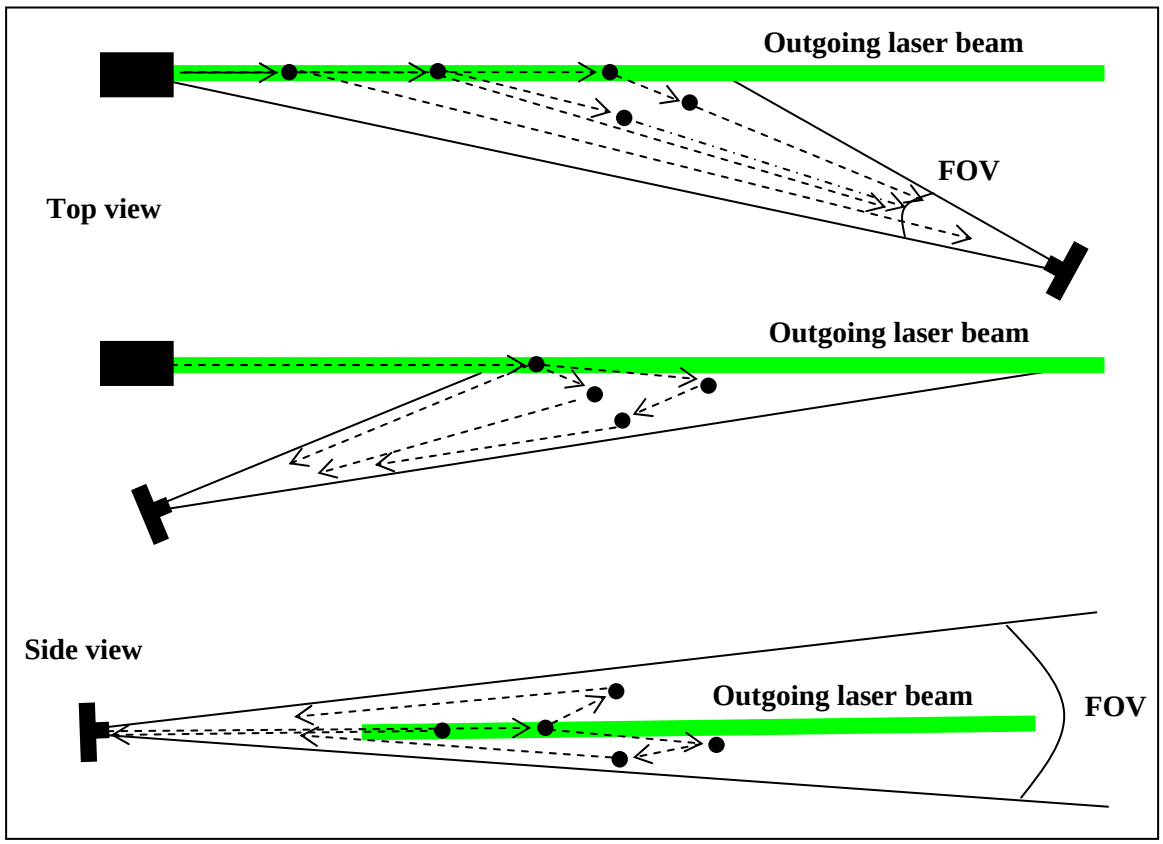

Figure 4.2 Multiple scattering patterns at forward and backward directions.

Within the optically dense medium of large particles (fog or clouds), which are comparable or larger than the incident wavelength, the forward scattering has much higher probability than backscatter. Therefore, lidar signals measured by a detector in the forward direction consist mainly of forward scattering. However, in the backward direction, lidar returns may consist of many forward scatterings and one backscattering.

4.2 Multistatic Lidar Hardware Implementation

As mentioned in Chapter 1.4, our major goal of this research investigation is to extend our understanding of optical scattering using a multistatic lidar system with particular emphasis on multiple scattering. In order to achieve this goal, the lidar system should have the capability of measureing multiple scattering effects in a wide angular region along the horizontal path. Our lidar configuratin is shown in Figure 4.3. This multistatic lidar transmitter employs a continuous wave (CW) Nd:VYO4 laser. The receivers, which are CCD cameras, measure the scattered intensities of different polarization states generated by switching the polarization plane of the laser beam from vertical to horizontal with a polarization rotator.

4.2.1 Laser Transmitter

The transmitter of the lidar system used in our experiments is a Nd-VYO4 (Yttrium Vanadate) continuous wave (CW) laser, which is growing in popularity because of its compact size, high gain, low threshold, and high efficiency due to the absorption coefficients at pumping wavelengths. The laser wavelength is 532 nm and output power 100 mW, with a beam divergence < 0.2 mrad and beam diameter 1 mm at aperture. The laser is composed of a laser head and exposed-circuit driver board, which are very compact and easy to handle. For aerosol remote sensing, the 532 nm wavelength is most promising. It is not only a common wavelength in lidar application but also is the wavelength where aerosol extinction is large compared to molecular extinction (Wiegner, 2004).

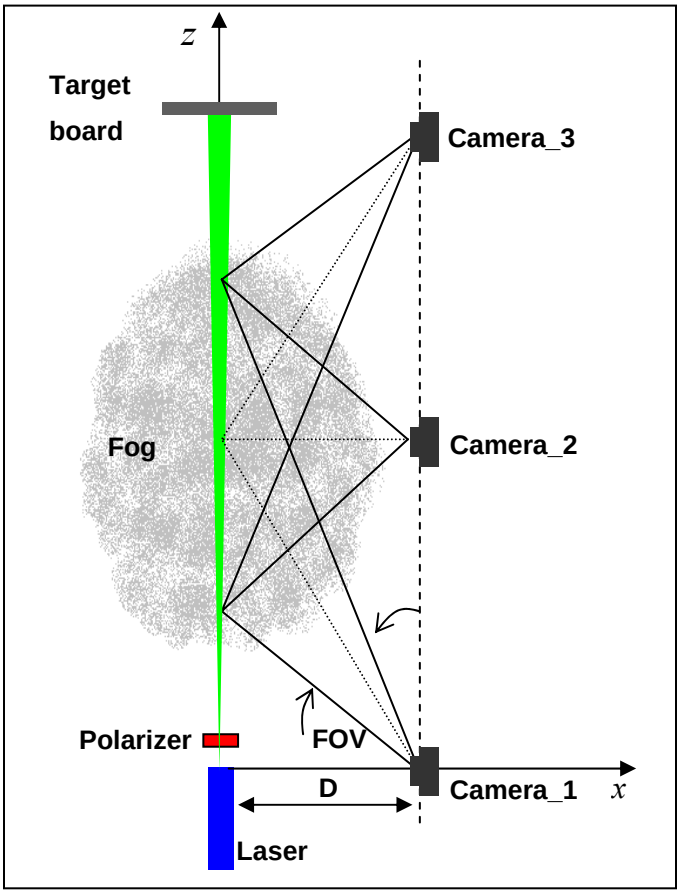

Figure 4.3 Multistatic imaging lidar setup.

A polarization cube, Glan Taylor prism, is inserted in front of the laser to obtain parallel polarization in the scattering plane. An 90° polarization rotator is remotely moved into the beam to change the polarization state of the transmitted beam. The transmitter parts are shown in Figure 4.4.

4.2.2 Multistatic Receivers

The detection was accomplished with two types of imaging devices. Pictor 416 XTE CCD cameras, whose detector array chip is the KAF-0401E manufactured by Kodak, were used in Defense Research Development Canada (DRDC) Aerosol Research chamber experiments conducted during 20 ~ 24 November, 2006 in Quebec, Canada.

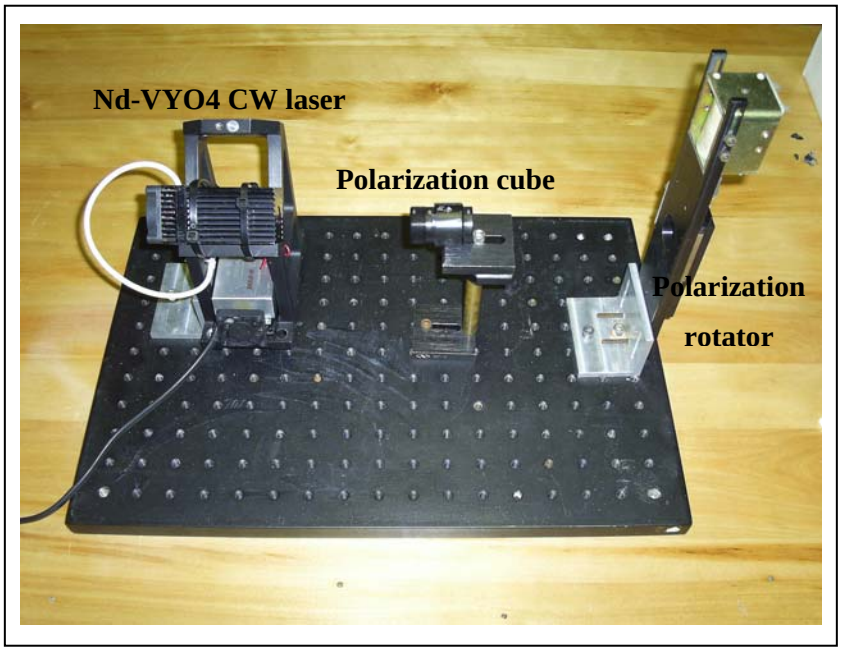

Figure 4.4 Transmitter parts used in a multistatic lidar.

The detail explanation about the experiments will be shown in later chapter. However, Pictor 416 XTE CCD cameras, which were used in Novitsky's experiments, are a little old, and sometimes, did not work in winter weather conditions. Each camera was connected to a laptop computer via a serial cable because we thought that portability of each device was important. Unlike Steven's and Novitsky's experiments, during conditions of a clearer atmosphere where measurements were based on the single scattering assumption, we were seeking multiple scattering conditions in optically dense media, like fog. Therefore, our experiments needed to be easy to move, and should not take too much time to set up.

The trade-off paid for using a long-length serial cable was a slow download of the image data into a laptop computer. Typically it took almost one minute to download one image. It is important to maintain uniform distribution of aerosols in a scattering volume between two different polarization images. For instance, in a windy night, two pictures with different polarization state taken each camera may come from different scattering volumes if the time interval between two images is too long. However, this effect was not important in DRDC experiments because the experiment was conducted inside a chamber

and there was no wind during the measurements. Dark count and noise of each 416 XTE CCD camera were analyzed by Novitsky and the results were summarized in his thesis (Novitsky, 2002, p. 147).

The second imaging camera used is the Deep Sky Imager PRO™ II connected to a computer via a USB cable that made the downloading of the image data much faster. The CCD chip in this camera was the high sensitivity Sony® EXview HAD™ CCD sensor, ICX429. This chip is a 16-bit, 752 × 582 pixels made up of 8.3 μm × 8.6 μm pixel size. The controlling software allowed exposure time from 0.1 ms and up to 1 hour. This new camera also does not need a control box to connect a CCD camera to a computer. A similar procedure to that used by Novitsky (2002) was applied to find the dark count and noise level at three different exposure times typical of those used in our experiments. Figure 4.5 shows the results. The dark counts and noise were subtracted from each polarization image by the controlling software. During the field tests and aerosol chamber measurements, the Deep Sky Imager PRO™ II camera was used only at backscattering direction and the exposure time did not exceed 2 seconds because the CCD chip of the Deep Sky Imager PRO™ II is more sensitive than the Pictor. The picture of each camera is also shown in Figure 4.6. The laser and detectors are separated by a distance along a horizontal, z, direction, and the detectors are pointed at a laser beam path, see Figure 4.3. In order to measure the angular distribution of multiply scattered radiation, a wide FOV was used in each camera. The early version of bistatic lidar configuration has not been popular because many vertical or horizontal scans were needed for a height or range profile to be obtained (Meki *et al*, 1996). However, our wide optics CCD cameras (FOV approximately 48°) make it possible to measure the profile from one laser beam trajectory image without scanning.

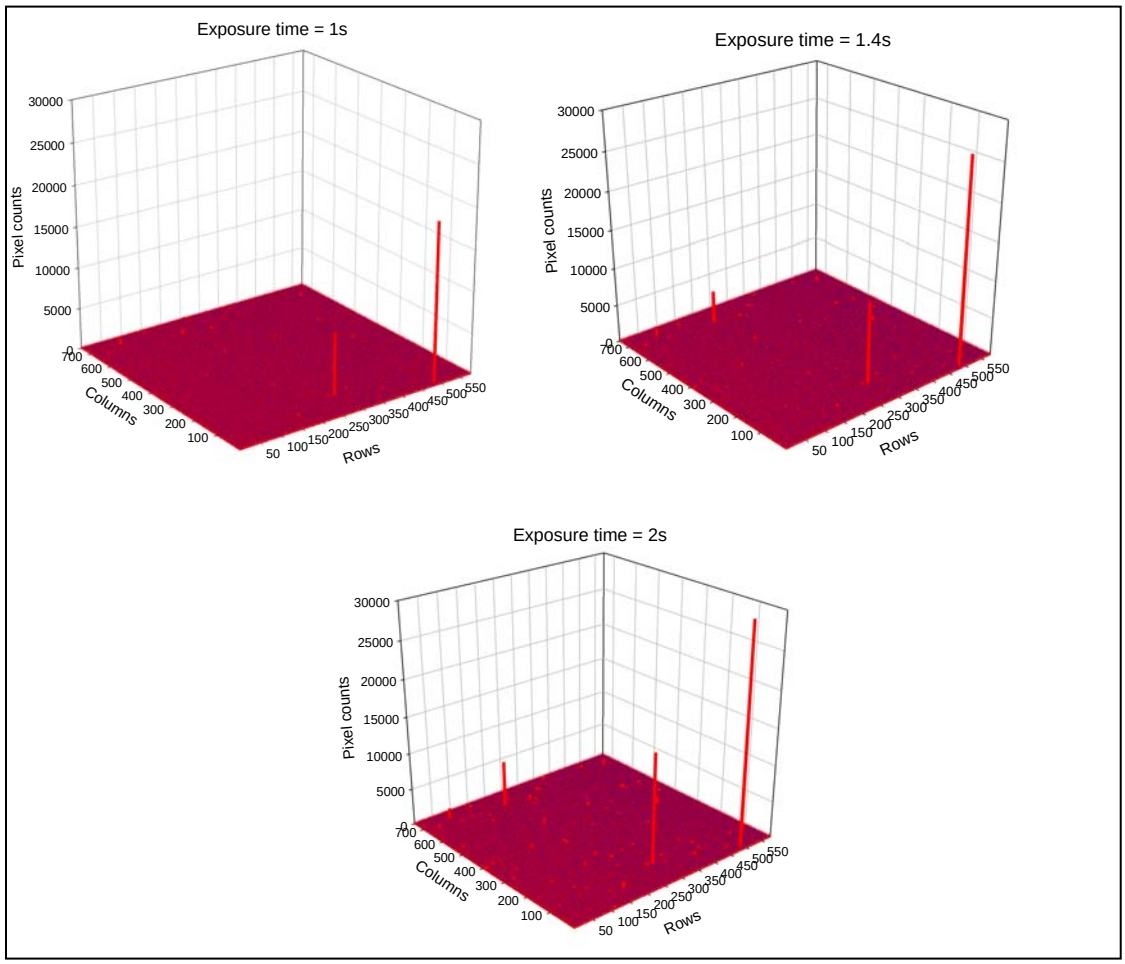

Figure 4.5 Pixel counts of the Deep Sky Imager PRO™ II under dark conditions.

Figure 4.6 CCD cameras used in multistatic lidar (a) Pictor 416 XTE (b) Deep Sky Imager PRO™ II .

4.2.3 Particle Size Spectrometer / Particle Counter

Two instruments are used in our experiments to obtain particle size information for artificial fog in the chamber tests, TSI Model 3934 scanning mobility particle sizer (SMPS) and TSI Model 3007 condensation particle counter (CPC). The SMPS is used mainly to measure size distribution and the CPC is used to monitor the total number density.

The SMPS consists of a differential mobility analyzer (DMA, TSI Model 3071A) and a condensation particle counter (CPC, TSI Model 3010). The following description is found in the Novitsky's thesis (2002). The DMA has a central rod to which a voltage is applied. The incoming particles are charge-neutralized in a Krypton-85 particle neutralizer to attain a nearly Boltzmann distribution of charges centered around 0 potential with most particles having a 0, ± 1 or ±2 charges attached. The central rod has a negative voltage that attracts particles of positive voltage. There is a laminar flow of clear air around the rod. Particles of the correct mobility will travel through the air flow, and out a narrow sampling gap to the CPC where they are counted. Particles that are too big or too small will exit in excess air or get stuck on the rod so that by choosing a particular voltage, only particles of a given size and +1 charge will be sampled at any given time. The instrument samples by ramping through voltages which separate particles equivalent to about 10 nm to 300 nm diameter. All particles sampled are counted in the CPC which contains a 400 % supersaturated butanol vapor, and a laser is used to count particles. Under supersaturation in the CPC, every particle grows large enough to be observed by the laser (Novitsky, 2002).

The SMPS can measure particle size range between 5 and 1000 nm depending on a polydispersed aerosol flowrate in the DMA unit. The main challenge of using the SMPS is to adjust a flowrate of the aerosol inlet for the right size range. In order to cover the whole size range that can be measured, the flowrate of the polydispersed aerosol inlet should be 0.2 liter per minute (lpm) to measure particle size between 16 and 1000 nm. A mass flow controller was connected to the aerosol inlet to maintain uniform flowrate. The

time needed to acquire a complete particle size distribution depends on the number of size intervals to be measured (Wang and Flagen, 1990). In our experiments, it took almost 120 s to obtain one data set of the complete size distribution. The SMPS used is shown in Figure 4.7. The computer is connected to the DMA analyzes and displays data. A sample of the data obtained by the SMPS at DRDC facility is shown in Fig. 4.8. The sample data shows approximately two modes, nucleation mode and accumulation mode. Unfortunately due to the limited particle size range, the coarse particle mode can not be seen in the plot.

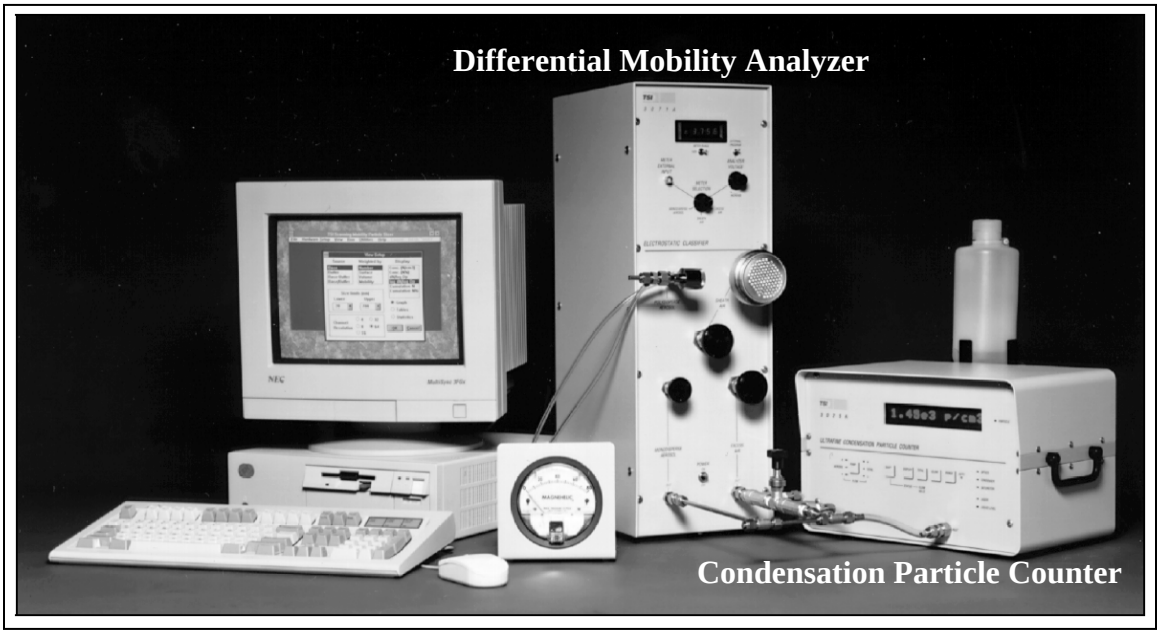

Figure 4.7 TSI Model 3934 Scanning mobility particle sizer (SMPS) (Model 3934 SMPS Instruction manual, 2002).

The CPC, TSI Model 3007, is a hand-held instrument for measuring particle total number density. Particle size range of 0.01 to > 1 μm and concentration range of 0 to 100,000 /cm^3 can be measured using this unit. The CPC 3007 is shown in Figure 4.9. The operating mechanism is found in TSI Model 3007 manual. This instrument's small size and ergonomic design make it the best choice for short-term outdoor research. Laminar-

flow CPCs operate by drawing an aerosol sample continuously through a heated saturator, in which alcohol is vaporized and diffuses into the sample stream.

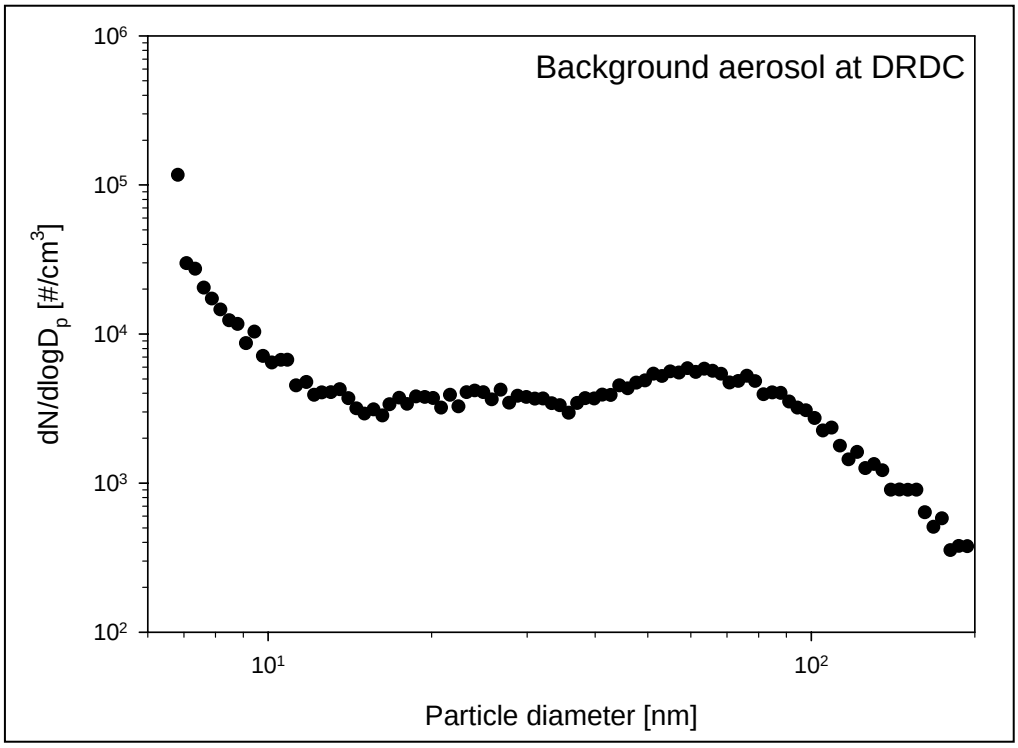

Figure 4.8 Background aerosols at DRDC measured by a SMPS.

Figure 4.9 TSI Model 3007 Condensation particle counter (CPC).

Together, the aerosol sample and alcohol vapor pass into a cooled condenser where the alcohol vapor becomes supersaturated and ready to condense. Particles present in the sample stream serve as condensation sites for the alcohol vapor. Once condensation begins, particles grow quickly into larger alcohol droplets and pass through an optical detector where they are counted easily (TSI Model 3007 manual). The main purpose of using this unit is to compare the total number density with transmittance of the laser beam measured by a power-meter at the path end point. This information can be used to define the limitations under which calculations of aerosol multiple scattering are valid. A sample of the data obtained by the CPC 3007 at DRDC facility is also shown in Figure 4.10. The sampling time is 240 s. The mean concentration is 6.92×10^3 /cm^3 and the standard deviation is 142/cm^3.

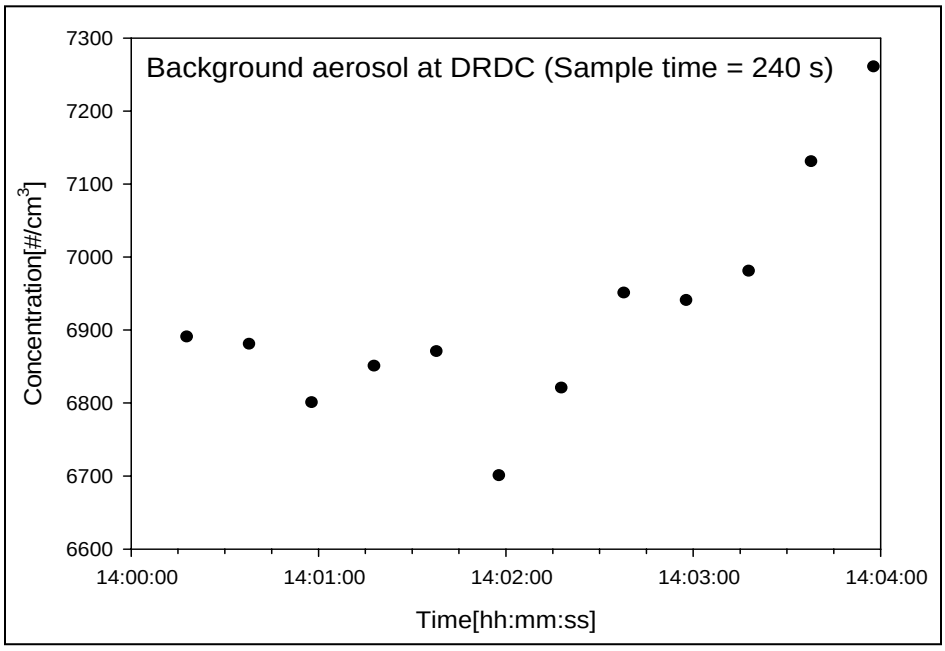

Figure 4.10 Background aerosols at DRDC measured by a CPC 3007.

The two instruments (SMPS and CPC) were used simultaneously to measure total number density in order to compare the difference between two instruments. The

result is shown in Figure 4.11. The plot shows the number concentration as a function of time measured with both SMPS and CPC. After disseminating fog into a small PSU chamber, measurements were continued for 80 minutes. In general, when a fog develops, its droplets tend to grow in size. Therefore, in the beginning of the measurements, there are many bigger particles than 1 μm in the chamber. Due to the limited size range which can be measured by the SMPS, particles bigger than 1 μm could not be detected. Therefore, the difference between two instruments is large. However, at the end of the measurements, large particles deposit faster than small particles. There are only small particles in the chamber, which are in the particle size range of both instruments. Therefore, the difference is getting close.

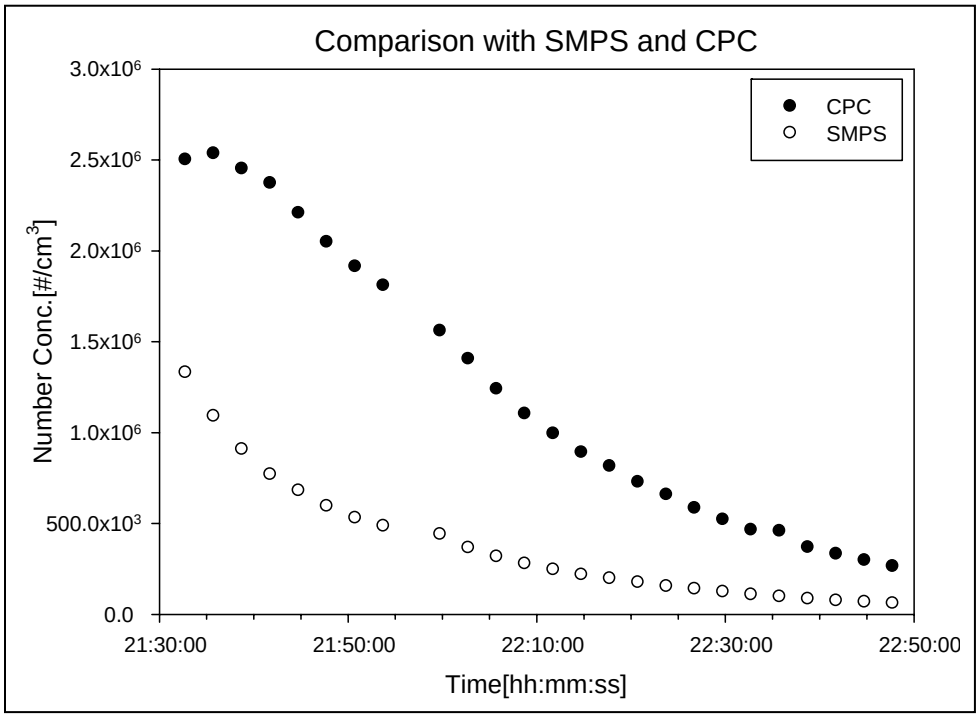

Figure 4.11 Number concentration as a function of time measured with SMPS and CPC.

Chapter 5

DRDC AEROSOL RESEARCH CHAMBER EXPERIMENTS

Although the Novitsky's multistatic lidar configuration in vertical mode can be used to obtain polarization properties of atmospheric aerosols, the horizontal operation mode permits easier measurements of the microphysical properties of a scattering medium. Beside that, the horizontal measurements of scattered radiation allow us to obtain additional information from a forward scattering direction. As mentioned in the previous chapter, the main focus in this thesis is in understanding multiple scattering effects from optically dense media. Interesting scattering media, such as fog, can not be easily observed in normal atmospheric conditions. Well-controlled laboratory experiments should precede field tests to collect data for different atmospheric conditions. One such approach is to conduct experiments in an aerosol chamber. One aerosol chamber available during November, 2006 was the Aerosol Research Chamber at the Defence Research and Development Canada (DRDC) facility. The DRDC chamber is located at north-west side of Quebec in Canada. This chamber was chosen for testing because of its well-developed design, and because of the possibility of collaboration with other researchers using a transmissometer and other experimental techniques. During the experiments, we collaborated Roy Gilles and two researchers from DRDC who contributed to our experiments by helping setting up the arrangements and giving technical advice. They have had the experience of many chamber tests while developing their multiple field-of-view (MFOV) lidar, which focuses on multiple scattering.

5.1 Objectives and Test Plan

The major goal of this experiment is to collect data with our multistatic lidar using two different aerosol substitutes such as fog oil and glass beads to investigate the effects

of multiple scattering on the polarization ratio technique. In order to do that, the following measurements and analysis are carried out:

1. Measurements of scattered intensities of two polarization states over a range of angles in both forward and backward directions.
2. Measurements of path extinction along the horizontal path.
3. Measurements of aerosol size distribution/number density in the chamber.
4. Analysis of polarization ratio to study the multiple scattering effect.

The multistatic lidar measured scattered intensities of two polarization states in both forward and backward directions and the DRDC transmissometer measured optical depth inside the chamber. The size distribution and number density were also measured by a particle size spectrometer, TSI 3934 SMPS, and a particle counter, TSI 3007 CPC.

The multistatic lidar was deployed at the DRDC on November 20, 2006, and located right next to the aerosol chamber. The multistatic lidar was set up at the first day, November 20. The equipment items, such as a laser, CCD cameras, a power-meter, a size spectrometer, a particle counter, and aerosol chamber, were tested to make sure working properly. Data was collected every night from November 21 to November 23. A weather station was located near the control booth to measure meteorological conditions. Figure 5.1 shows the locations of lidar (MFOV and multistatic lidar), transmissometer, and target board. The following section describes the experimental test procedures.

5.2 Experimental Setup and Operation

Experiments were performed in a cooperative research project between researchers from the Pennsylvania State University and from DRDC. The DRDC Aerosol Research Chamber provided an opportunity to investigate multiple scattering characteristics. The multistatic lidar measurements were made in a 22-m long aerosol chamber located at the DRDC facility. The chamber has a 2.4 m × 2.4 m cross-section. It has doors at each end of the chamber that can be opened quickly, see Figure 5.2. The

inside of the chamber is coated with optical-black paint to avoid reflecting light from the walls. In order to collect the data at both forward and backward directions, the multistaitc lidar was operated in the horizontal mode.

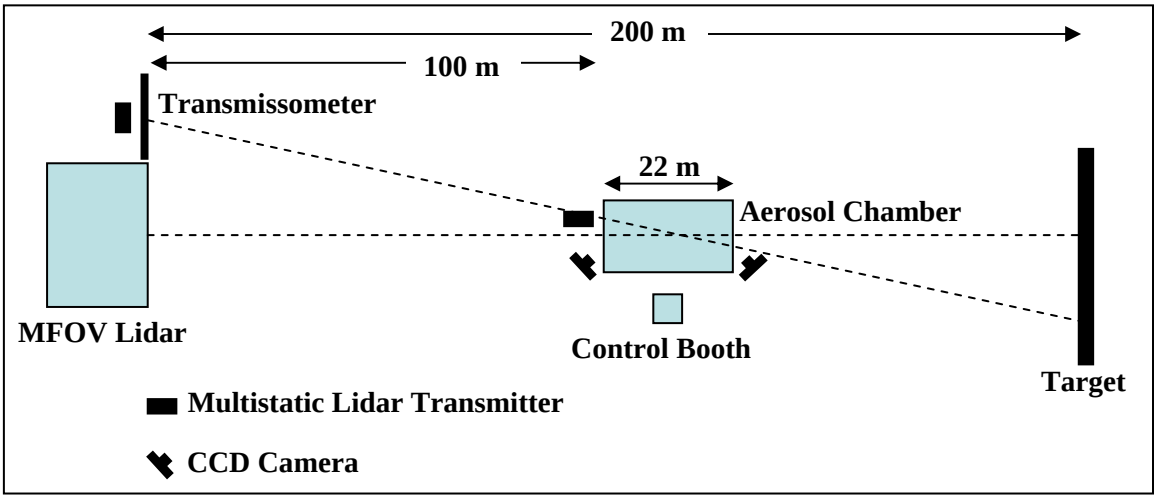

Figure 5.1 Locations of experimental devices at the DRDC facility.

5.2.1 Experimental Geometry and Conditions

The detailed optical setup of the multistatic receivers used for this experiment is shown in Figure 5.3. Due to the cold weather or some other reasons, one camera did not work properly on the first day of the data collection. It was revealed later that the camera had a crack in the CCD chip. Therefore, only two cameras were used at forward and backward directions. The detailed explanation of each device is introduced in Chapter 4. The laser and two cameras were separated by 1.95 m at backward direction and 2.04 m at forward direction respectively. Each camera was in line with the direction of the beam propagation in the chamber pointing the laser beam. Two aerosol substitutes such as fog oil and glass beads were used.

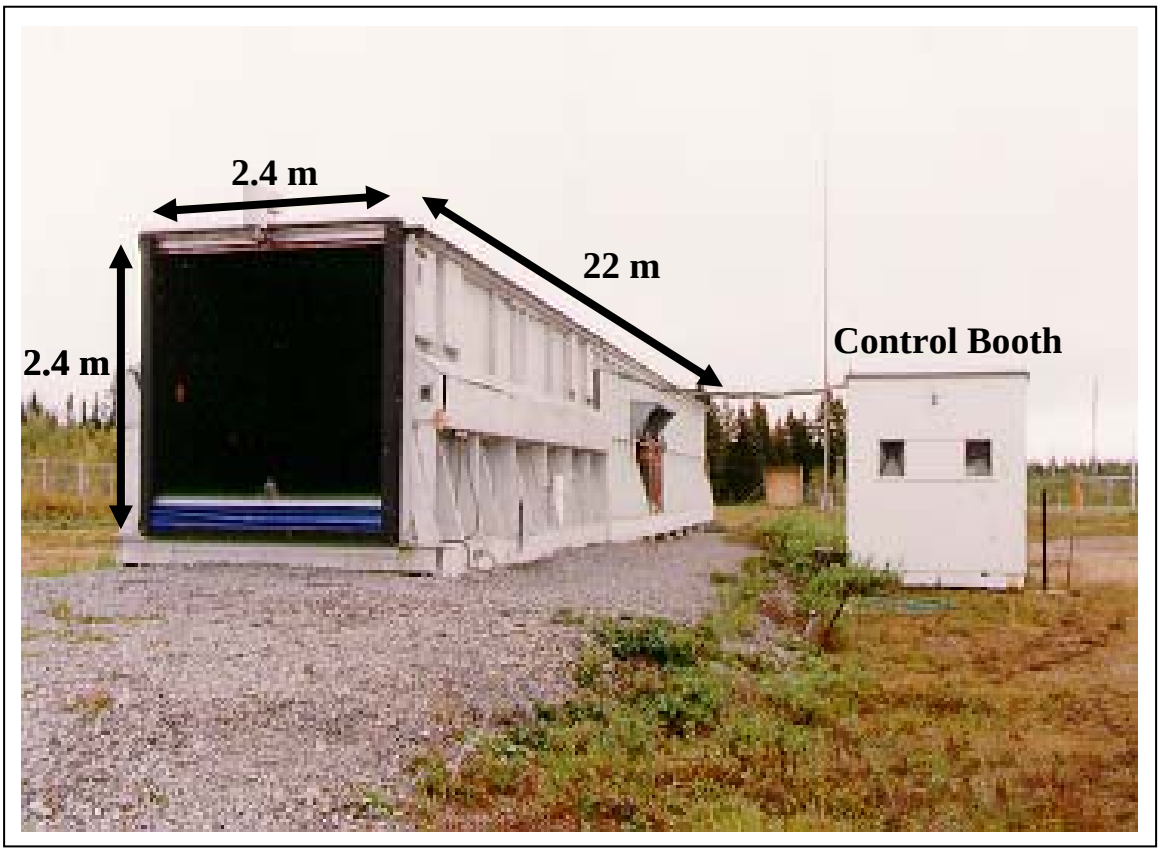

Figure 5.2 Aerosol chamber at the DRDC facility.

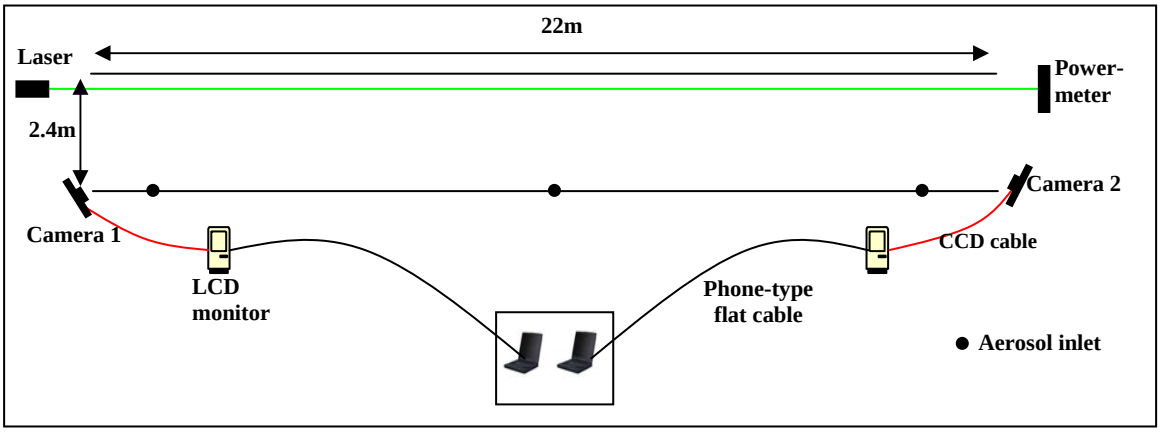

Figure 5.3 Detailed experimental setup for the DRDC aerosol chamber experiment.

Fog oil was generated by a MDG Super Max 5000 fog-oil generator located inside the chamber and two types (Type 1000 and Type 6000) of spherical glass beads, which were made by Potters Industries Inc., were disseminated from a high pressure gas nozzle into three aerosol inlets to ensure a good homogeneity in the chamber.

The cameras used are commercial CCD cameras from Meade Instrument Corporation and are fitted with wide field lenses (fov approximately 34° and 48°), see Figure 5.4. The CCD array chip is a 16-bit blue-enhanced, 768 × 512 array made up of 9 μm square pixels giving it dimensions of 6.9 mm × 4.6 mm. Each camera can cover the scattering angles between 125 ~ 173° at backward direction and between 6 ~ 40° at forward direction respectively. The choice of wide angle optics eliminates the need for spatial scanning to cover the desired range of scattering angles. The cameras interface with laptop PCs to record the images. The two PCs were in the control booth, see Figure 5.3. The particle size spectrometer and the particle counter are located at the middle aerosol inlet outside near the center of the chamber to measure size distribution and number density of aerosol substitutes. In order to ensure that only one polarization (parallel or perpendicular polarization) is received, the location of the camera should be in the same plane as the aerosols (Stevens, 1996).

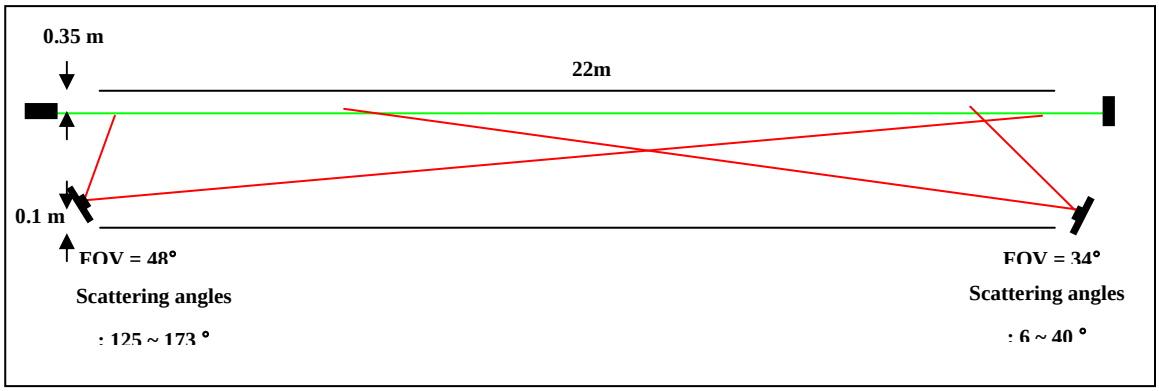

Figure 5.4 Detection ranges of each camera.

5.2.2 Data Collection Procedures

In order to measure path length corresponding to each pixel imaged by a CCD camera at each location, 10 highly reflective jiggling wires were used. Each wire was separated each 2 meter in the chamber and could be raised from or lowered into the laser beam path, see Figure 5.5. Figure 5.6 is a photograph showing the laser propagating horizontally in the chamber. It is seen in the photograph that there are several bright spots which were reflected by jiggling wires. The images like Figure 5.6 were also taken using the two CCD cameras with a 2 second exposure to image the laser beam from both back and forward direction.

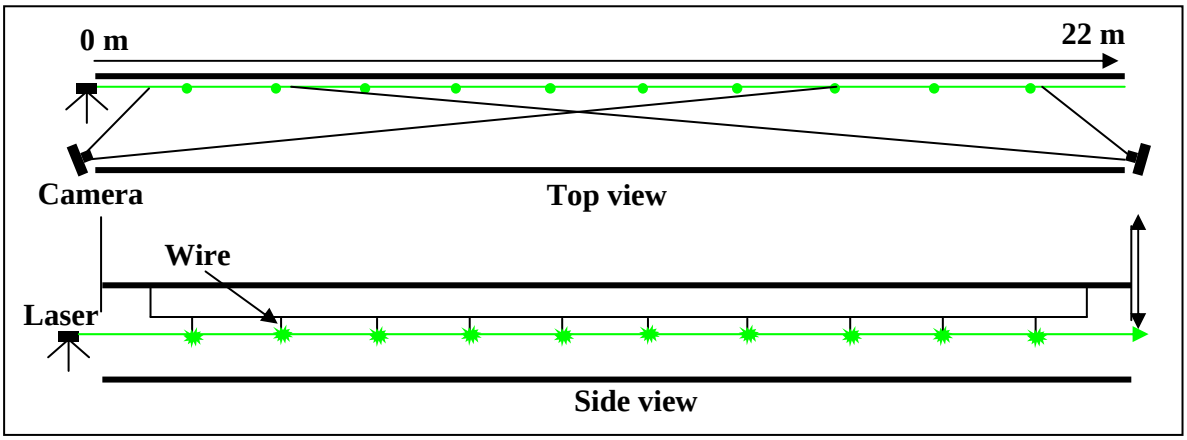

Figure 5.5 Detection setup for a laser beam path measurement using jiggling wires.

These CCD images were analyzed to find out the beam path positions to locate angles for each camera. The results are shown in Figure 5.7. The peak intensities are separated by a 2 meter spatially. However, due to the lidar geometry, the distance between two peaks in the CCD image is getting shorter away from the camera. Performing simple calculations shows that the camera at backward direction can cover the laser beam from 1 to 16 m, which corresponds to the backscattering angles 125° to 173°, and the camera at forward direction can cover the range between 2 to 20 m, which corresponds to the forward scattering angles 6° to 40°.

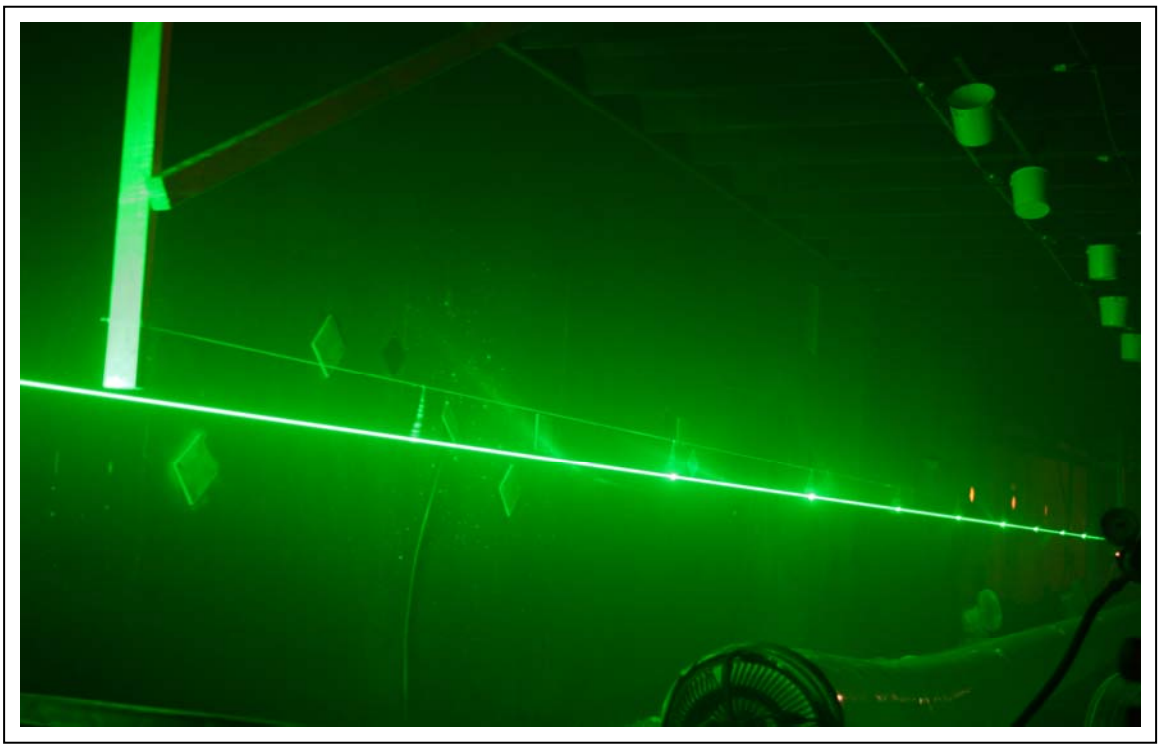

Figure 5.6 A photograph of the laser propagating in the chamber and jiggling wires.

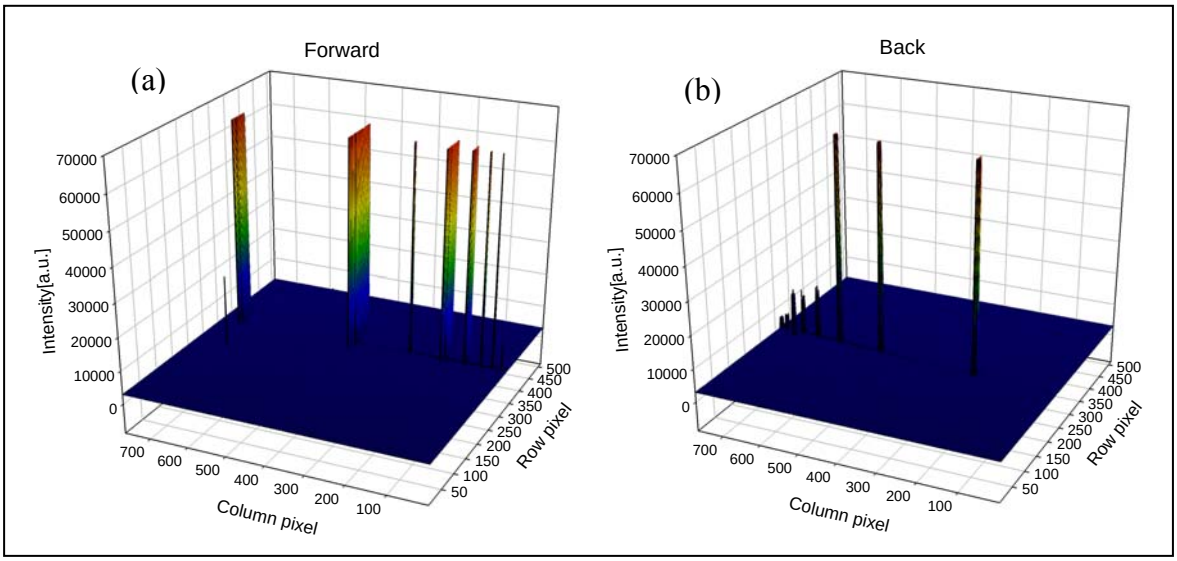

Figure 5.7 Intensities reflected from jiggling wires at both forward and backward directions.

Two types of spherical glass beads and fog oil were used in this experiment. The optical depth inside the chamber was controlled by the amount of glass beads and the dissemination and mixing time in case of fog oil. The experimental conditions are tabulated in Table 5.1. The median particle diameters of Type 1000 and 6000 are 2.3 and 6 μm respectively, from data record of the manufactures, and fog oil particles exhibit a submicron diameter range. The refractive index of glass beads is 1.51-1.52 and that of fog oil is $1.5077 - i(2.94 \times 10^{-5})$ at the wavelength of 0.44 μm and $1.5077 - i(9.53 \times 10^{-6})$ at the wavelength of 0.632 μm. In the case of fog oil, the effect of the imaginary part of refractive index on the scattering phase function is small and ignored in this thesis.

Table 5.1 Experimental conditions.

Aerosol substitute	Experimental condition	
Fog oil	Dissemination time : 10 s, 20 s Mixing time : 45 s	
Glass beads	Type 1000	15 g, 30 g, 60 g
	Type 6000	30 g, 60 g

To get polarization properties of aerosols, the scattered intensities of two polarization states were measured with different conditions, see Table 5.1. The measurements were conducted late in the evening in order to reduce background light. The actual procedure followed is: (1) the rear chamber door was closed, (2) aerosol substitutes are disseminated, (3) a mixing fan was operated for 45 seconds to produce homogeneity inside the chamber, (4) the rear door was then dropped, and (5) the CCD cameras started taking images of scattered intensities while the transmissometer measured optical depth inside the chamber.

Chapter 6

DATA ANALYSIS AND RESULTS

In this chapter, we present the experimental results for chamber tests and field tests and describe the analysis approach. The data analysis focuses on data from both forward and backward directions. Data from the forward direction is analyzed to study the radial distribution and polarization ratio of multiply scattered radiation. Measurement from the backward direction is analyzed to study the polarization ratio. In Chapter 5, the experimental method and conditions used in DRDC Aerosol Research chamber test are explained in detail. A similar experimental geometry was used in the other two experiments, the PSU small chamber experiments and the field experiments. The small PSU chamber has been assembled to conduct scattering experiments under better controlled laboratory environment conditions. The PSU chamber is much smaller in size than the chamber at the DRDC facility. However, it is much easier to control particle characteristics in the chamber. The field experiments were conducted outside of College of Engineering Research building in Cato Park on the west side of State College. It is easy to deploy experimental instruments there, and it is often that fog is encountered there. Data are shown from several nights of field experiments to provide examples for both clear and heavy fog conditions.

Data on the size distribution, number density, and transmittance are calculated to assist in analyzing the data collected from the multistatic lidar. The number density of the scattering medium was converted to an optical depth to define the limitations under which conditions of aerosol multiple scattering are valid. This chapter consists of three sub-sections; DRDC data analysis, PSU small aerosol chamber data analysis, and field data analysis. Each section includes the analysis of multiple scattering and the results of single particle scattering calculated by Mie theory in order to compare with multiple scattering. The multiple scattering effects are deduced from the data analysis of polarization ratio and radial distribution of the scattered radiation.

6.1 Data Analysis Procedure

The processing of the multistatic lidar data is very similar to that used in the analysis of Stevens (1996) and Novitsky (2002). In order to decrease the error signals in the CCD images from the camera itself, the background image and a dark image are taken before each polarization image. Then, the dark image is subtracted from the background images and subtracted from the images of the parallel and perpendicular components. The corrected background image signals are then subtracted from the parallel and perpendicular images, which are then divided to obtain the polarization ratio. The next step is to assign the scattering angle associated with each pixel. The angle assignment can be different depending upon the detector's field of view and the distance between the transmitter and the detector.

Up to this point, the processing of the data is similar to what Stevens (1996) and Novitsky (2002) did. However, the intensity of each pixel in the CCD image has to be converted to the actual intensity of a beam itself. This can be explained using Figure 6.1. In a conventional way of measuring a scattering phase function, see Figure 6.1 (a), the beam produced by a light source passes through a scattering chamber. Light scattered by a scattering medium at a scattering angle θ is measured by a detector. In this case, the return path from the scattering medium to the detector is always same wherever the detector is located and the incident intensity is same at different scattering angles. However, in our case, the return paths from $\overline{CP_1}$ to $\overline{CP}_{768}$ are different and the intensity at each pixel from P_1 to P_{768} assigned to a specific scattering angle is attenuated because the beam is in a scattering medium, see Figure 6.1 (b). Therefore, these two factors are compensated in our CCD data analysis in order to measure accurately an angular distribution of the scattered intensity.

In our experiments, the radial distribution of the multiply scattered radiation is included. The most tedious and difficult part during the experiments is to align the laser beam parallel in the CCD image, however, this makes it much easier to analyze the data.

In the case of single scattering measurements, the beam width is found to be less than 10 pixels over the entire path length of the beam (Novitsky, 2002).

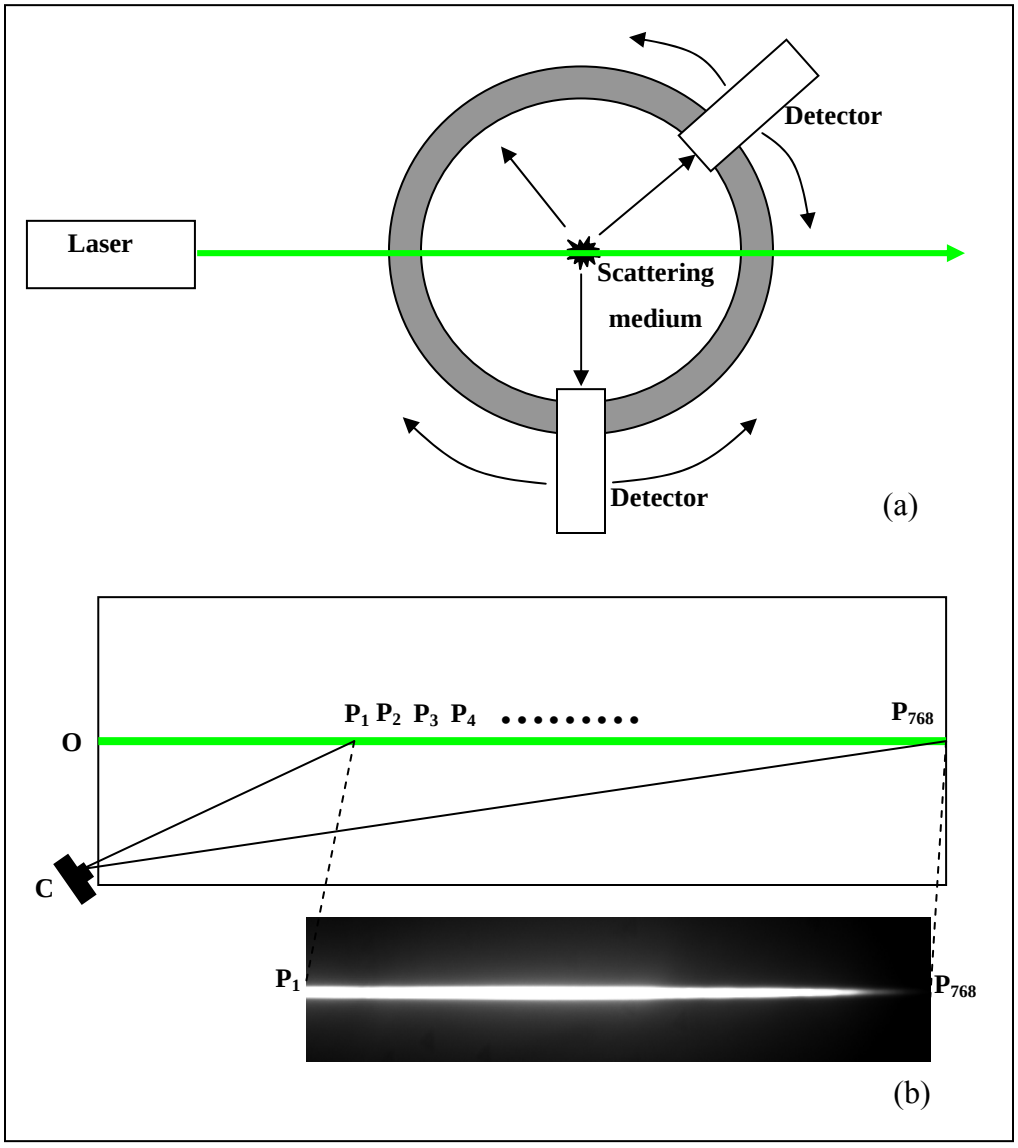

Figure 6.1 Schematic view of an experimental setup for the measurement of a scattering phase function (a) conventional method (b) multistatic lidar method.

Novitsky also did not want his data to be contaminated by multiple scattering, which could have made it difficult to invert his lidar data. Therefore, he only used the data extracted from 8 pixels in width in the CCD image where the single-scattering-dominated

laser beam is located. However, in our case of multiple scattering measurements, the beam width slowly increases along the direction of beam propagation, see Figure 6.14. It is important to determine the optimal number of pixels in the CCD image that include the multiple scattering components, and minimize the error signals. After many trial and errors, it was determined that 20 ~ 25 pixels provide a reasonable choice to satisfy our requirement.

The FTS-type file of the polarization image is converted to a data file using a Matlab. The data corresponding to the width of 20 ~ 25 pixels are extracted for use in the multiple scattering analysis along the horizontal direction, and these are summed to get the polarization ratio. The information about the radial distribution is determined using five pixels selected vertically for analysis, see Figure 6.2.

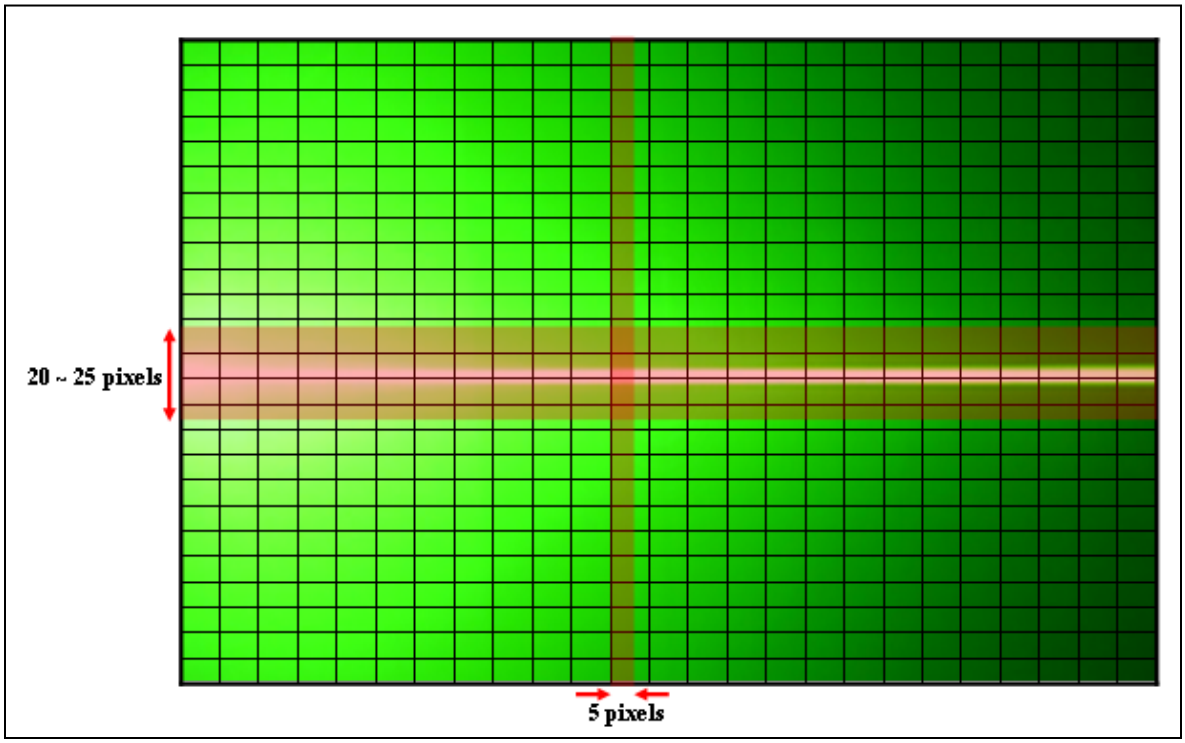

Figure 6.2 Data extraction method from a CCD image.

6.2 DRDC Data Analysis

In Chapter 5, the experimental method and conditions used in DRDC chamber test were explained in detail. The multistatic lidar measurements were started on several days in late November 2006. Most valuable data set was obtained on November 22, 2006. After sunset, the temperature was between -5°C and 0°C and the wind speed was almost zero, and did not affect the distribution of aerosol simulant inside the chamber.

In this section, the measured data will be reported. In order to analyze the measurements, the medium characteristics should be defined in advance. The microphysical properties of the medium can be described by the aerosol size distribution and optical depth inside the chamber. The aerosol substitutes at the DRDC experiments were glass beads and fog oil disseminated by a MDG Super Max 5000 fog-oil generator. The refractive index of fog oil is $1.51+0i$ and it is assumed spherical. Two types (Type 1000 and Type 6000) of spherical glass beads were disseminated from a high pressure gas nozzle at three aerosol inlets to provide a good homogeneity inside the chamber and mixed with fans located through the chamber for one-minute prior to taking the data. It is known that the median particle diameters of Type 1000 and Type 6000 are 2.3 and 6 μm respectively. The size distribution of fog oil was measured using a TSI Model 3934 SMPS, particle size spectrometer, and the number density was measured using a TSI Model 3007 CPC, particle counter. The size distribution of fog oil is shown in Figure 6.3. Table 6.1 summarizes the important parameters of the best-fit log-normal size distribution of the aerosol substitutes. This information is used as an input parameter for Mie calculation. However, due to the limited particle size range of the SMPS, up to 1 μm, the size distribution of glass beads could not be measured and is not available.

The scattering phase function is calculated with the best-fit size distribution using a MIETAB computer program. The result is shown in Figure 6.4. As can be seen in Figure 6.4, the phase functions of the DRDC fog with the measured size distribution and a single scatter with the same median diameter of the measured distribution are plotted for comparison.

Table 6.1 Parameters of the best fit log-normal distribution of fog oil and glass beads.

	Median diameter[μm]	Geo. St. Dev	Total Conc.[#/cm^3]
Fog oil	0.1176	1.71	6.03×10^4
Glass beads Type 1000	2.3	.	.
Glass beads Type 6000	6.0	.	.

In Rayleigh scattering, the shape of scattered light intensity is symmetrical in the forward and backward direction and has minimum value at 90° due to $(1+\cos^2\theta)$ term in the scattering phase function. However, larger aerosols ($a >> \lambda$) Mie scattering exhibit very strong forward scattering peak and more complicated structure of the angular distribution in the backward direction depending on the particle size. This phenomenon becomes prominent as a particle size increases. In contrast to the phase function of clouds, which have a strong peak in the forward direction, we observe not only noticeable forward scattering but also the minimum parallel-polarized intensity between 100 and 110° in Figure 6.4. If a photon encounters a particle in the case of fog oil, the chance of the photon getting scattered away at a large scattering angle (side scattering region) is high.

During the experiments, transmittance was measured to provide a distinction between single and multiple scattering conditions. Transmissometer was a laser used in the MFOV experiments and was located in the trailer which contains the MFOV lidar (see Figure 5.1). The measured transmittance was converted to optical depth, τ, within the chamber to describe the scattering characteristics which are related to the number and size of scatterers. In this case, it was assumed that the aerosol substitutes were uniformly distributed inside the chamber. As pointed out at the end of Chapter 5, measurements were made for several experimental conditions with each aerosol substitutes. However, the data of optical depth for glass beads of 2.3 μm (30g) and 6 μm (30g) were not

measured properly at that time. The measurements of optical depth for each condition are shown in Fig. 6.5 to 6.7. In each plot, the red arrows represent the measurement time of the scattered intensity of each polarization. Figure 6.5 shows the data of optical depth for fog oil with dissemination time (DT) of 10 s and 20 s and Figure 6.6 shows the data for 2.3 μm glass beads (15g, 60g). Finally, Figure 6.7 shows the data for 6 μm glass beads (60g). It turned out that the difference of the optical depth for fog oil between the cases of 10 sec and 20 sec DT right after dissemination is similar. However, in the case of 20 sec DT, the optical depth stays high values for the same time interval compared to the case of 10 sec DT. The difference for large particles like glass beads, is notable. The optical depth for 2.3 μm glass beads (60g) is 1.7 times that for 15g.

A particle size also affects optical depth. With the same amount of 2.3 μm and 6 μm-diameter glass beads, it shows that the optical depth of 6 μm is 1.5 times larger than 2.3 μm, and the faster settling time for the 6 μm beads. In each plot, one observes a couple of big "spikes" in optical depth due to blocking the beam path. At the time, the polarization rotator was not operated remotely from the control booth. Instead, the polarization state of the incident beam was changed manually switching a polarizer by one of our research team. The multistatic lidar receivers took measurements right before and after each spike. The optical depths during the multistatic lidar measurements were larger than 1 most of the time. That means there are multiple scattering effects in the scattered radiation, which can be seen from polarization ratio data.

A single scattering analysis is described first in the backscattering direction to study the performance of our multistatic lidar. As mentioned in the previous section, only 8 pixels of data in the beam-contained region are used for the single scattering analysis. The results are shown in Figures 6.8–6.9. The symbols represent the measurements and the blue curves represent the single scattering calculation using Mie theory and the best-fit size distribution. Figure 6.8 shows the measured scattering phase function of two polarization states of fog oil with dissemination time with 10 and 20 s, respectively. The measured scattered intensity values in a CCD image are adjusted to the values of the phase function of the best-fit size distribution.

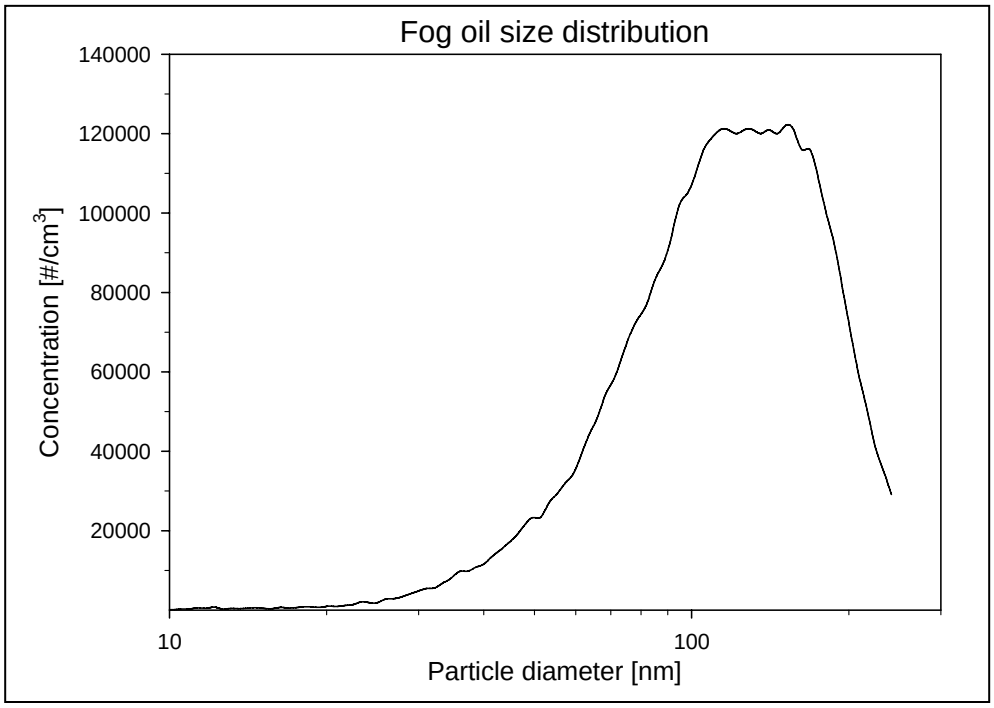

Figure 6.3 Size distribution of fog oil measured by a TSI Model 3934 SMPS.

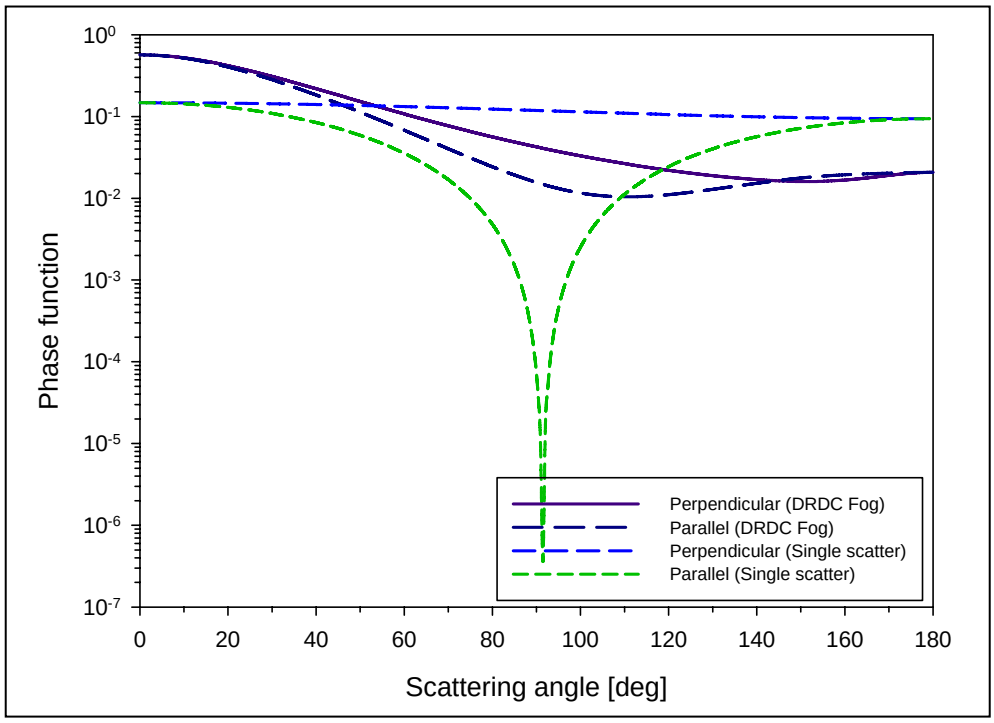

Figure 6.4 Scattering phase functions of DRDC fog oil with the measured size distribution and a single scatter with the same median diameter.

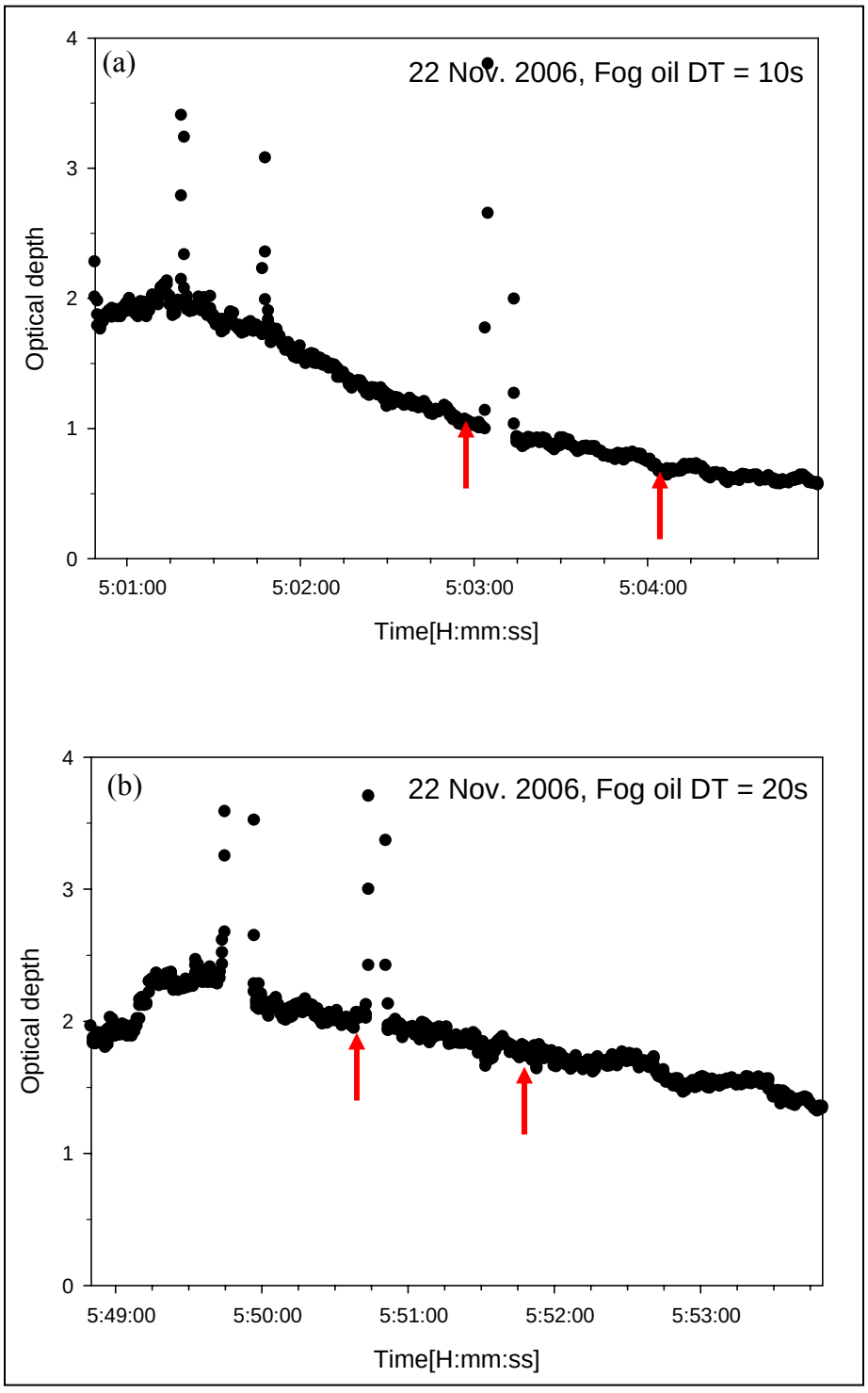

Figure 6.5 Optical depths during experimental conditions (a) fog oil, dissemination time (DT) = 10 s, (b) fog oil, DT = 20 s.

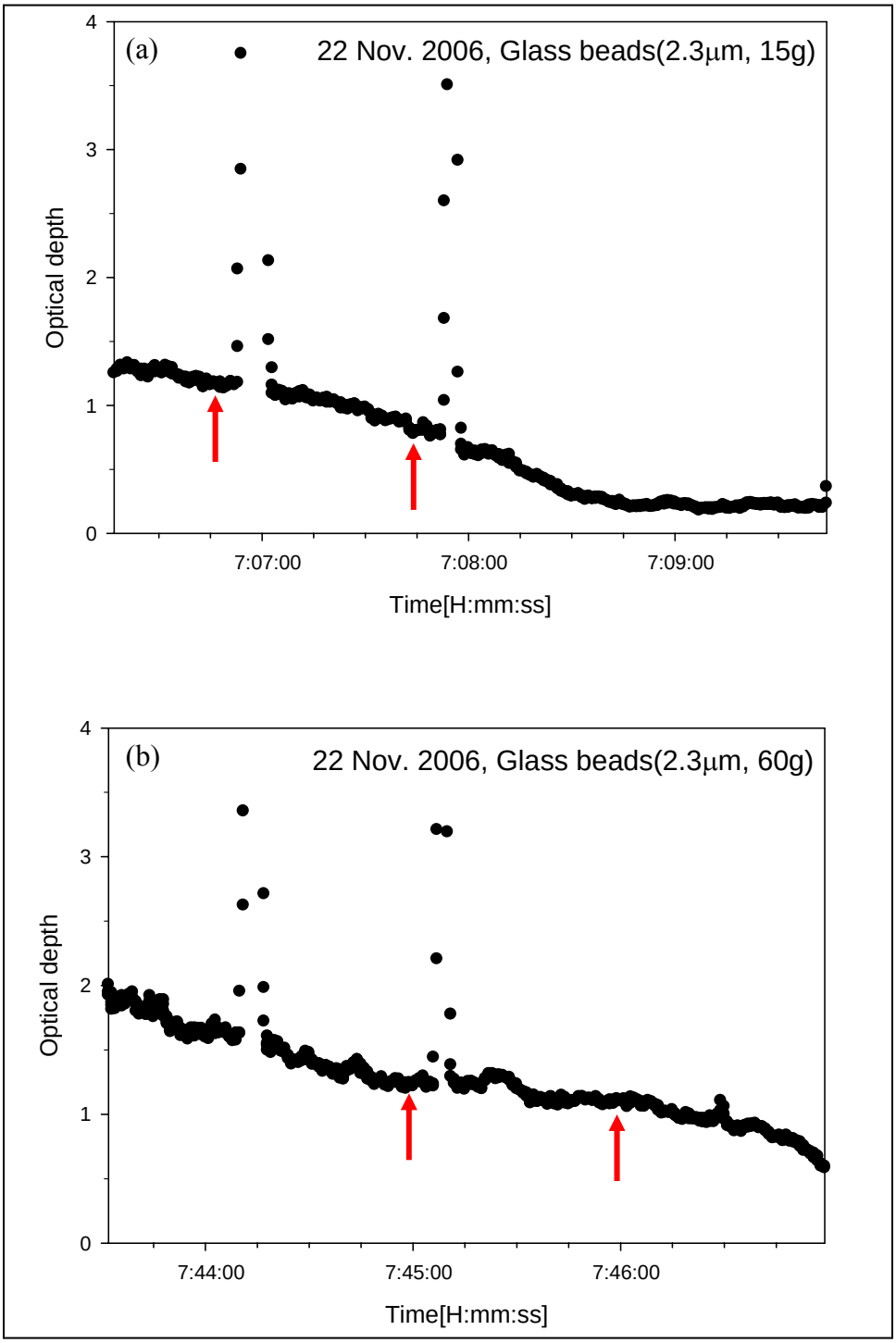

Figure 6.6 Optical depths during experimental conditions (a) glass beads, 2.3 μm, 15 g (b) glass beads, 2.3 μm, 60 g.

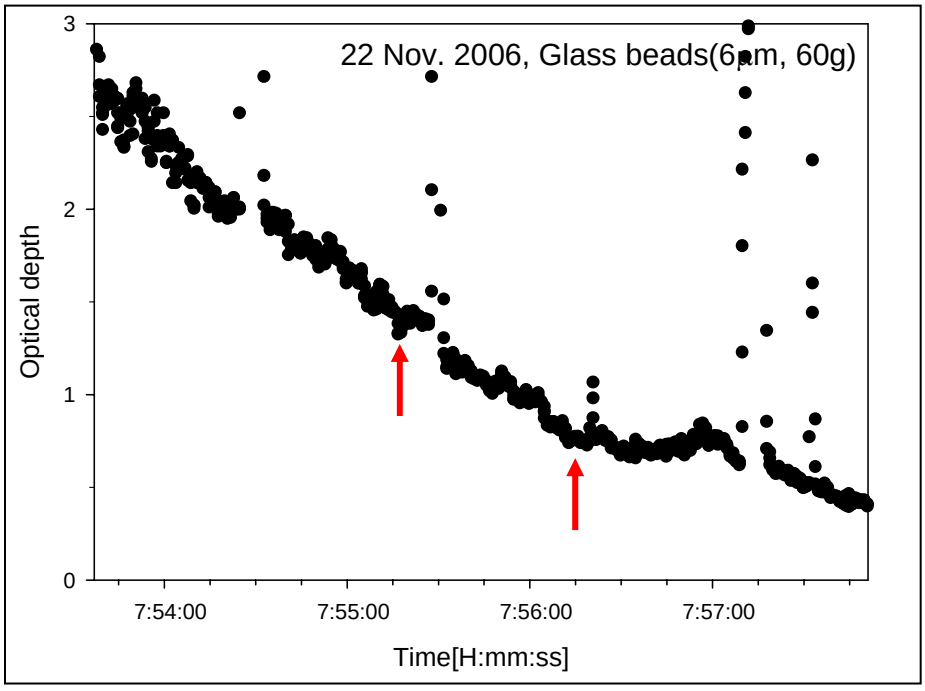

Figure 6.7 Optical depths for glass beads, 6 μm, 60 g.

The data in Figure 6.8 (a) are measured right before the third spike and 1 minute later in Figure 6.5 (a) due to the downloading time into a computer. The extinction coefficients of before and after the spike , which are calculated from the optical depth are 0.09 m^{-1} and 0.07 m^{-1}, respectively. The data in Figure 6.8 (b) are measured in the same way using the second spike in Figure 6.5 (b). The extinction coefficients of before and after the spike are 0.05 m^{-1} and 0.03 m^{-1}, respectively. An excellent match was found with the scattering phase function of fog oil calculated with the measured size distribution. However, in the case of fog oil with dissemination time of 20 s, there is a little dip between scattering angles 155° and 160°. This may be because of an unwanted-blocking of a returning path into the detector. Figure 6.9 also shows the measured scattering phase function of glass beads with diameter 2.3 μm and 6 μm. Figure 6.9 (a) is measured where the chamber conditions correspond to the data in Figure 6.6 (a), and Figure 6.9 (b) correspond to the data in Figure 6.7.

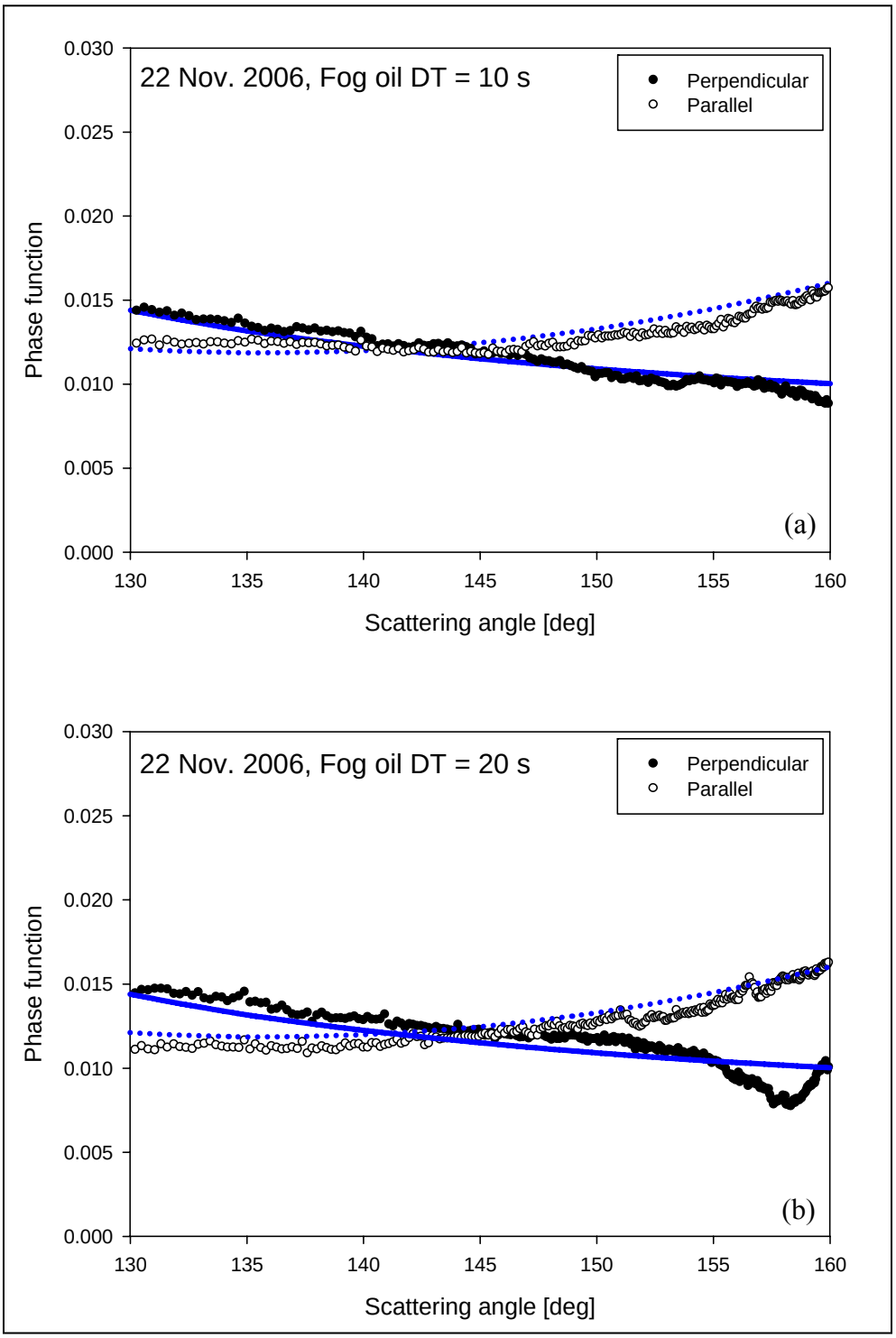

Figure 6.8 Measured scattering phase function (a) fog oil with dissemination time of 10 s (b) fog oil with dissemination time of 20 s.

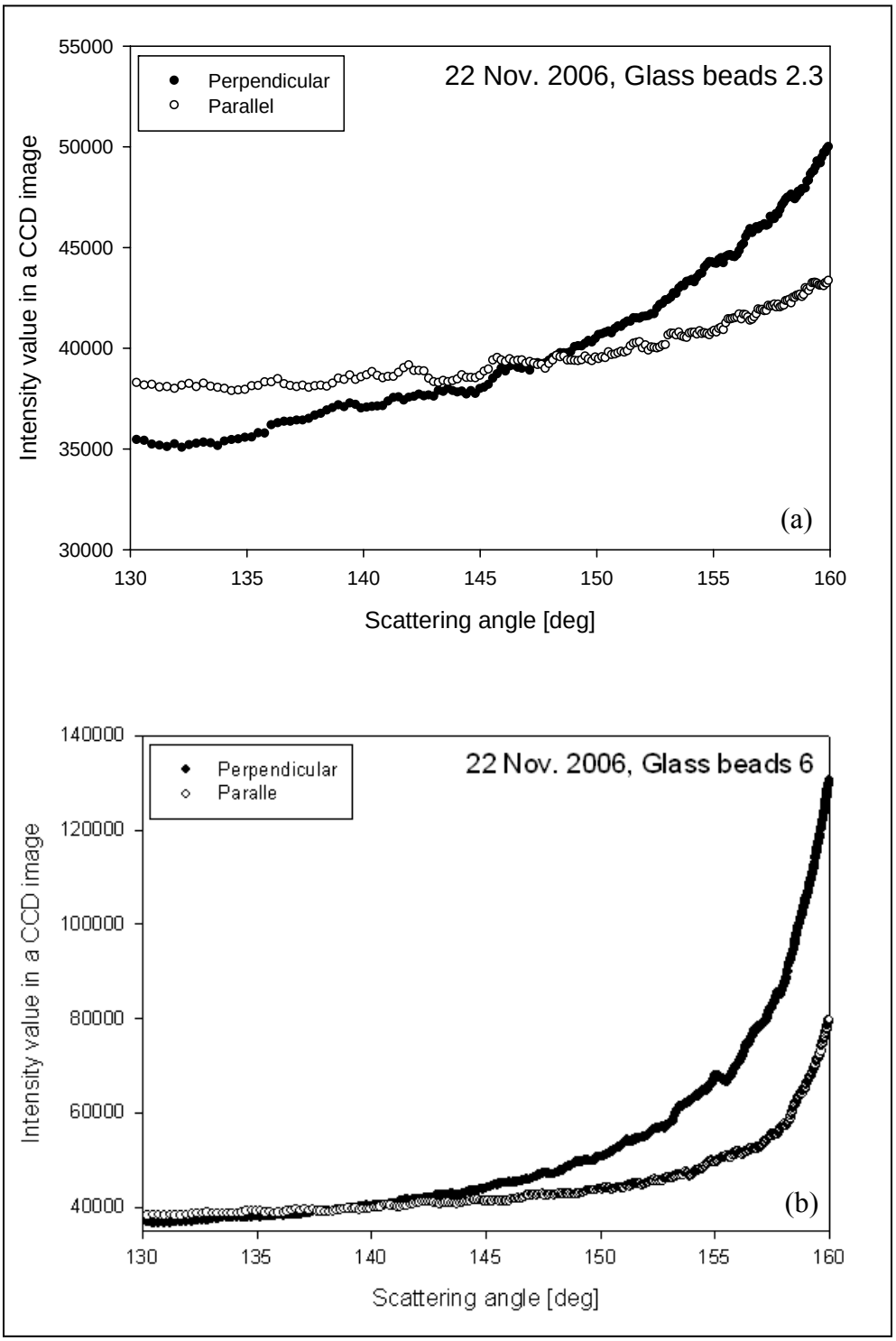

Figure 6.9 Measured scattering phase function (a) glass beads 2.3 μm (b) glass beads 6 μm.

In these cases, the actual size distribution of glass beads could not be measured using the SMPS due to the limited range of size measurements allowed by the device. However, we can explain qualitatively the pattern of the measured scattering phase function. As the particle size increases from 2.3 μm to 6 μm in diameter, the scattered intensities of two polarization states become comparable to each other between 130° and 145° and increase abruptly at scattering angles larger than 155° in our case. These phenomena are observed in single Mie calculations using the same diameter of spherical particles. However, it is not perfectly matched with the measured data because of uncertainty of the size distribution of glass beads. Therefore, the data of glass beads are not used in the analysis of multiple scattering.

Polarization ratios from fog oil in both forward and backward directions are shown in Figures 6.10 and 6.11. In order to compare single scattering with multiple scattering, the polarization ratio of single scattering is also included in the same plots, and include the results calculated from the best fit log-normal size distribution of fog oil (see Figure 6.3 and Table 6.1) using the Mie theory for particle scattering. Polarization ratio is calculated as the ratio of the scattered intensity of a parallel component to a perpendicular component. As pointed out in the previous chapter, the fog particles are spherical and the polarization ratio of molecular scattering is negligible. Therefore, the differences in observed polarization ratios should be a result of multiple scattering. In the data shown in Figure 6.10, some background and CCD readout noise were introduced in each pixel, which is summed in the beam-containing regions. In each scattering region, multiple scattering causes the scattered radiation to be more depolarized as the scattering angle increases from 0° and 180° respectively. This effect also can be seen in the results of the bistatic Monte Carlo simulation in Chapter 3. The multiple scattering effects on the total scattered intensity are becoming significant in side scattering regions (around 90°), see Figures 3.13-3.17.

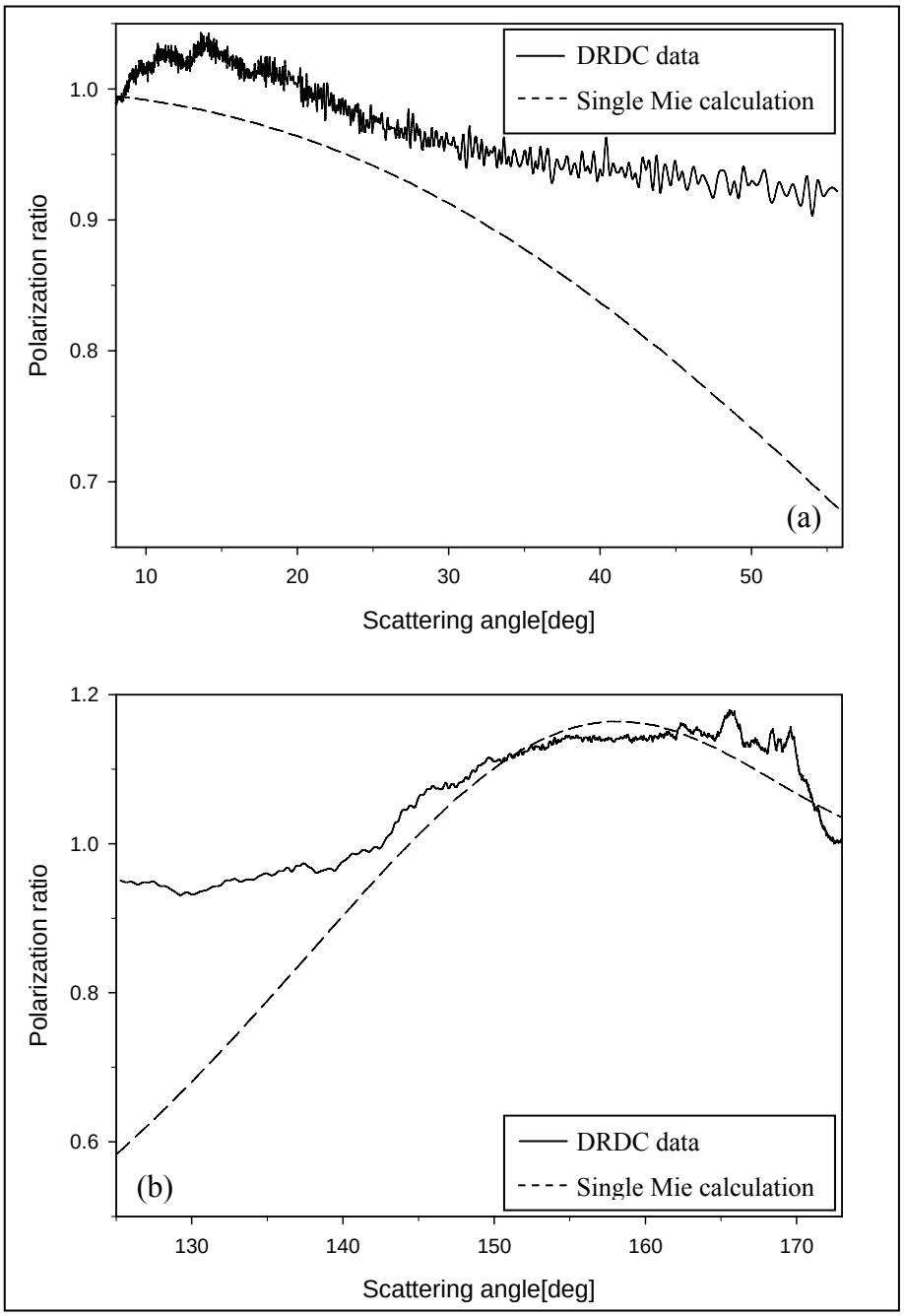

Figure 6.10 Polarization ratio of fog oil in (a) forward scattering region (b) backscattering region.

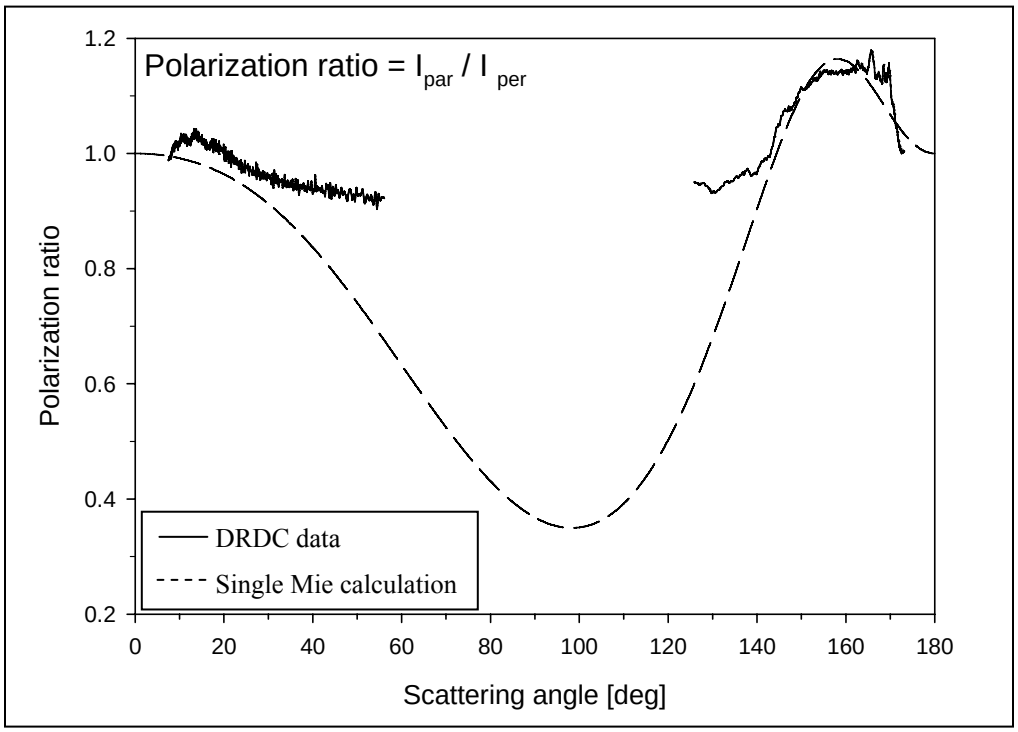

Figure 6.11 Polarization ratio of fog oil.

6.3 PSU Small Chamber Data Analysis

A small chamber has been assembled at PSU to conduct scattering experiments in a more controlled laboratory environment using aerosols from a generator that are characterized using a size spectrometer and a particle counter. The chamber is much smaller than that at the DRDC facility. However, it is much easier to control particle characteristics in the chamber. The PSU chamber is 360 cm long and has a 60 cm × 60 cm cross-section. The inside of the chamber is also coated with black paint for the same reason of the DRDC chamber. A small fan was operated to distribute fog particles uniformly inside the chamber. The chamber is shown in Figure 6.12. There are three camera windows at forward, side and backward directions. Before disseminating fog oil into the chamber, each camera window is closed to make sure uniform distribution of fog oil. An aerosol inlet is located at the side of the chamber.

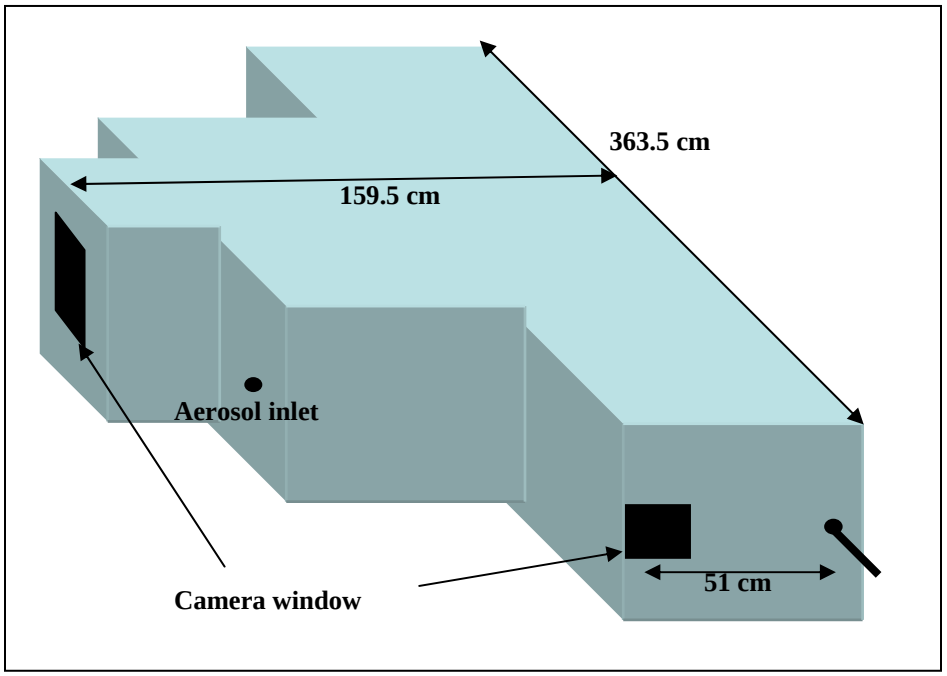

Figure 6.12 PSU small aerosol chamber.

6.3.1 Medium Characteristics

In this laboratory experiment, a TDA-5A Aerosol Generator produced fog oil, which was well characterized by a log-normal size distribution and the real part of refractive index of the fog oil is 1.47, given by the PAO (Poly Alpha Olefin) company, that provided the liquid used in the aerosol generator. The size distribution of fog oil was measured using the same size spectrometer used in the DRDC experiments. Due to the small size of the aerosol and the low specific gravity of PAO fog fluid (0.852 gm/cm^3 at 15.6 °C), the measurements could be continued for about 90 minutes. Table 6.2 summarizes the measured data on the fog oil aerosol. A total of 30 individual measurements were collected every three minutes. The total number concentration gradually decreases due to the deposition of particles, see Figure 4.10. However, the median diameter and geometric standard deviation (SD) of the size distribution of fog oil show similar values during the measurements. The average values and standard deviations of the median diameter and geometric SD are 317 nm ± 6.95 nm and 1.66 ± 0.04 respectively, which shows the size distribution of fog oil is fairly uniform during the measurements. One example measurement from the SMPS, and the best fit with a log-normal size distribution are shown in Figure 6.13.

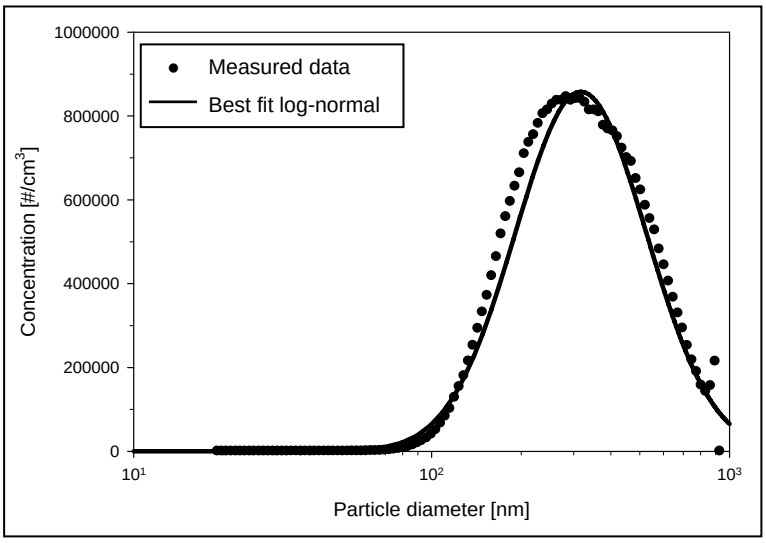

Figure 6.13 Size distribution of fog oil used in the PSU chamber experiments.

Table 6.2 Summary of the size distribution data for PAO fog oil measured by a SMPS.

Data #	Time	Median diameter[nm]	Geo. SD	Total Conc.[#/cm^3]
1	9:21 pm	289	1.68	9.80×10^5
2	9:24 pm	301	1.61	1.99×10^6
3	9:27 pm	307	1.61	1.68×10^6
4	9:30 pm	313	1.61	1.33×10^6
5	9: 33 pm	316	1.61	1.09×10^6
6	9:36 pm	319	1.62	9.07×10^5
7	9:39 pm	320	1.62	7.69×10^5
8	9:42 pm	322	1.62	6.80×10^5
9	9:45 pm	322	1.63	5.95×10^5
10	9:48 pm	322	1.63	5.30×10^5
11	9:51 pm	323	1.63	4.86×10^5
12	9:57 pm	319	1.64	4.40×10^5
13	10:00 pm	322	1.64	3.65×10^5
14	10:03 pm	322	1.65	3.17×10^5
15	10:06 pm	321	1.65	2.78×10^5
16	10:09 pm	321	1.65	2.45×10^5
17	10:12 pm	320	1.66	2.17×10^5
18	10:15 pm	319	1.66	1.97×10^5
19	10:18 pm	320	1.67	1.75×10^5
20	10: 21 pm	319	1.67	1.54×10^5
21	10:24 pm	317	1.68	1.39×10^5
22	10:27 pm	318	1.68	1.23×10^5
23	10:30 pm	318	1.69	1.08×10^5
24	10:33 pm	316	1.70	9.66×10^4
25	10:36 pm	318	1.70	8.43×10^4
26	10:39 pm	318	1.71	7.52×10^4
27	10:42 pm	316	1.72	6.72×10^4
28	10:45 pm	316	1.72	5.93×10^4
29	10:48 pm	317	1.71	5.24×10^4
30	10:51 pm	318	1.71	4.68×10^4
Average		317	1.66	
Standard deviation		6.95	0.04	

The scattering phase function is calculated with the best fit size distribution using a MIETAB computer program and a plot of the result is shown in Figure 6.14. Scattering phase function of particle size comparable to the incident wavelength does not show strong polarization dependence in the forward direction, and the change of polarization is negligible. Therefore, polarization ratio analysis of PSU chamber experiments is presented only for the backscattering region. The theoretical values of polarization ratio are calculated with the best fit log-normal size distribution using the Equation 2.4, which is shown in Figure 6.15. It should be noted that this variation of polarization ratio was calculated with the assumption of single particle scattering. As pointed out previously, the polarization ratio shows dramatic changes in the backscattering region between 130° and 180°, which can be covered by a multistatic lidar receiver.

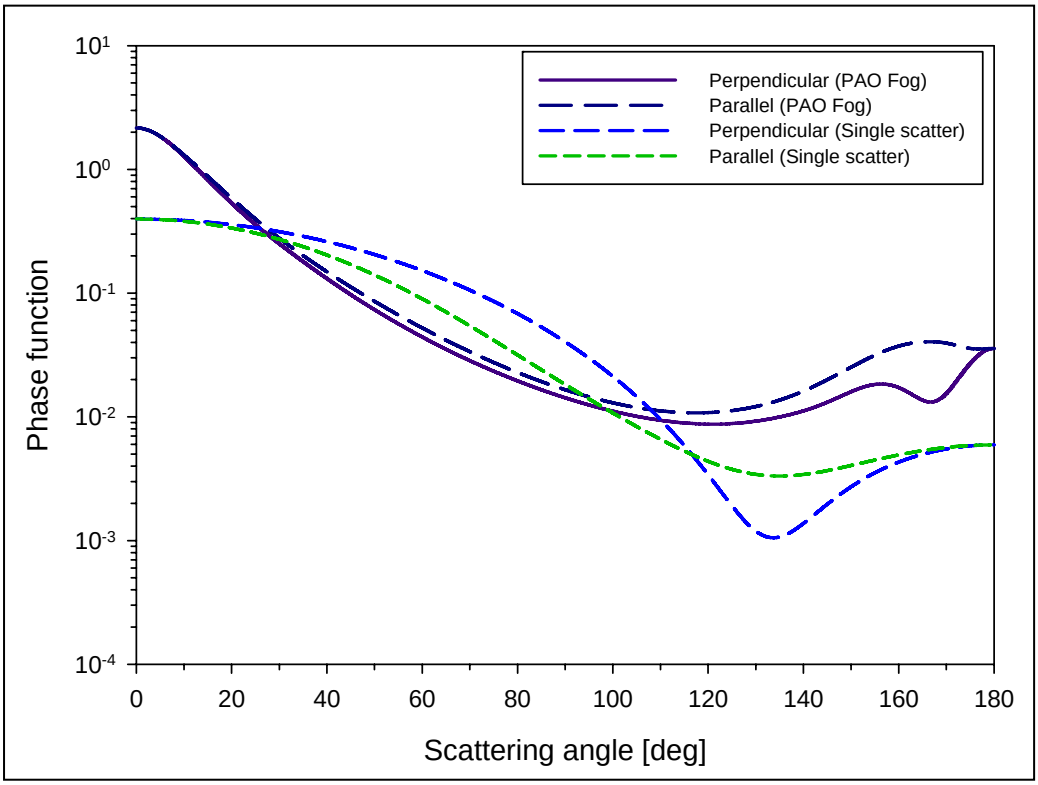

Figure 6.14 Scattering phase functions calculated using the best fit log-normal size distribution and a single scatter with the same median diameter.

The particle counter (TSI Model 3007) and a power-meter were used to measure the total number density and extinction inside the chamber. The extinction was converted to optical depth. The optical depth provides an estimation of the average number of times that photons have interacted with the scattering particles (Berrocal *et al*., 2007). The effective area of the detector of the power-meter is small enough that only the transmitted beam is measured. It is important to remove the multiple scattering in the measurement of extinction. Because by calculating the total extinction the assumption is that all the energy scattered out of the beam is lost forever. Multiple scattering allows this lost light back into the receiver. The total number density and optical depth were measured simultaneously as a function of time. Then, these data were compared with each other. The measurements were continued around 4 hours. The result is shown in Figure 6.16. For the first three and half hours, the total number density and optical depth decreases very slowly and then drops suddenly to the level of background number density when a small fan was operated to observe how the optical depth changes with low aerosol concentrations, see Figure 6.16 (a). From the Figure 6.16 (b), one can definitely see the linear relationship between two parameters.

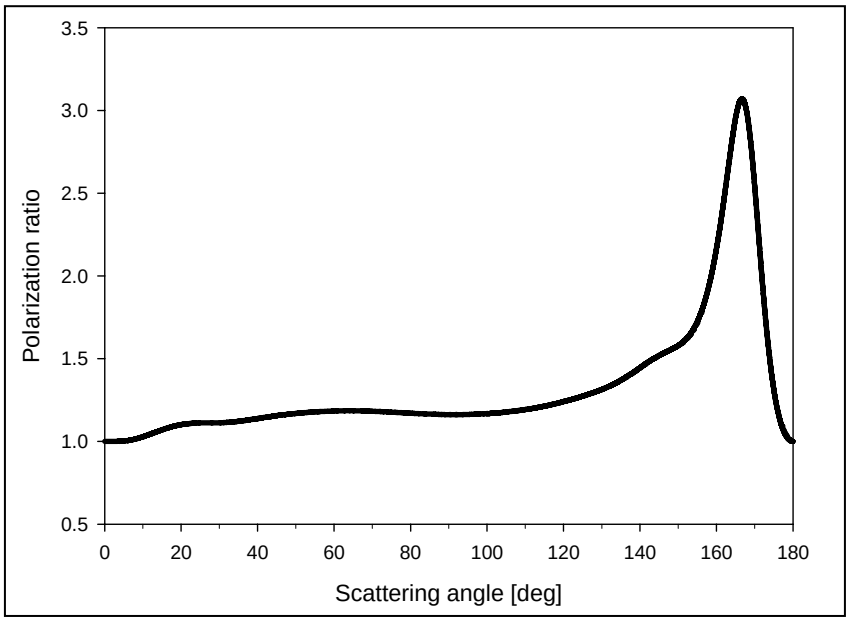

Figure 6.15 Polarization ratio calculated using the best fit log-normal size distribution.

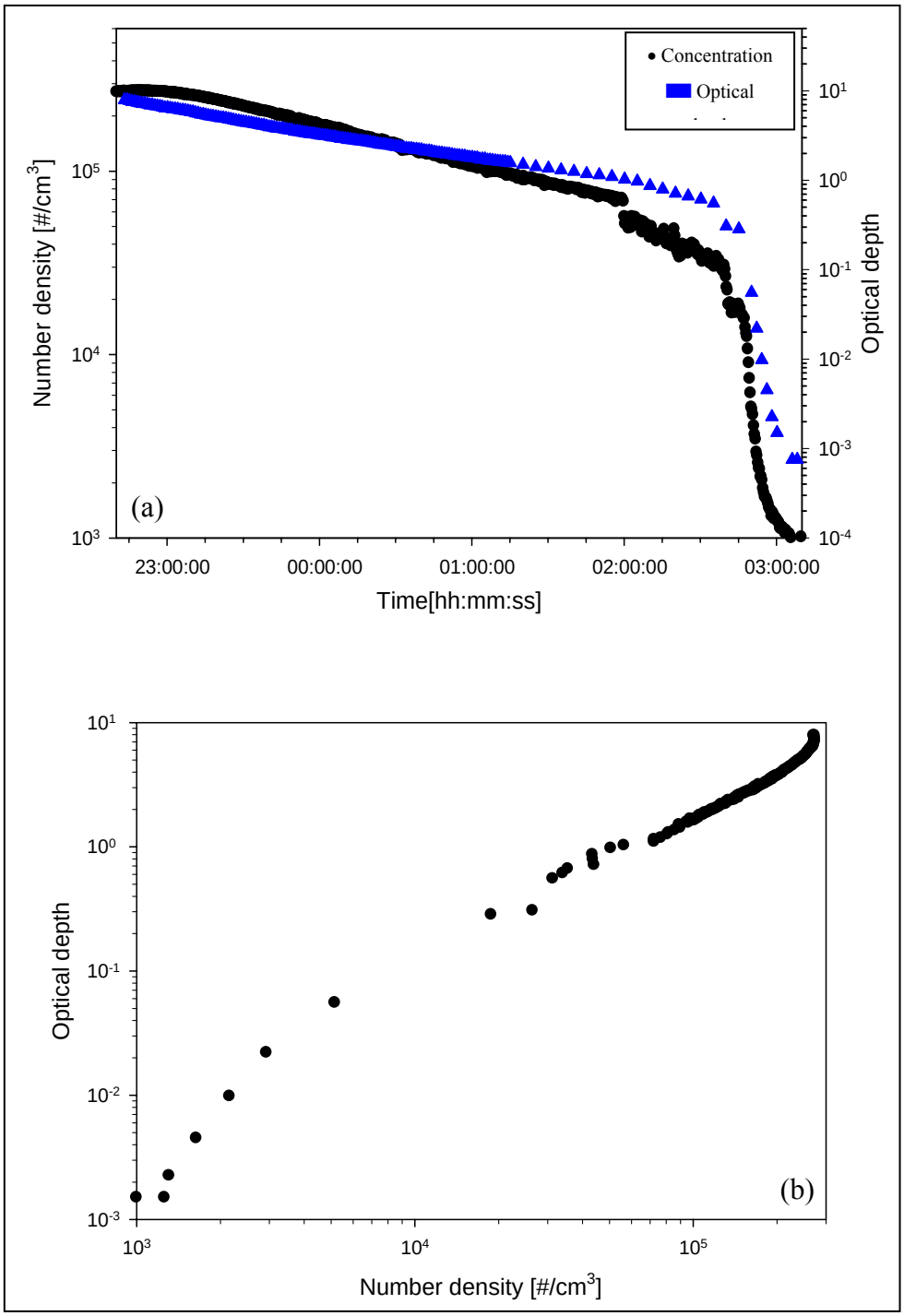

Figure 6.16 The measured total number density and optical depth of PAO fog inside the PSU small chamber.

6.3.2 Data Analysis

This section consists of the analysis of polarization ratio and radial distribution of scattered radiation. As mentioned before, polarization ratio is sensitive in the backward direction and the radial distribution of multiply scattered radiation is useful for the data from the forward scattering direction because of the increase in a signal-to-noise ratio (SNR).

Figure 6.17 shows the relationship between polarization ratio and optical depths, τ. The number density inside the chamber is converted to optical depth. Polarization ratios with optical depths of 6.83, 2.72, 0.82, and 0.35 are plotted in the backscattering direction, 127° ~ 175°. For comparison, polarization ratio of the single Mie scattering is also included in the same plot, which is adopted from Figure 6.14. Two aspects should be pointed out for this result. First, the location of the maximum polarization ratio of a large optical depth is at large scattering angle, around 168°. As the optical depth decreases, the maximum moves toward the smaller scattering angle. In case of the single Mie scattering, the peak occurs at 165°. The second point is that the shape of the angular distribution of the polarization ratio approaches single Mie scattering case as the optical depth decreases. It is quite reasonable that as the particle concentration decreases to some level, the single scattering assumption is valid when the multiple scattering is quite small, and there it can be taken to be negligible.

Light scattering close to the forward scattering direction is sensitive to size but rather insensitive to refractive index and particle shape. The width of the intensity peak centered at $\theta = 0°$ is inversely proportional to the particle size (Veihelmann et al., 2006). Therefore, the knowledge of the radial distribution of multiply scattered intensity at small scattering angles is also important to explain the propagation of light beams in optically dense media. Figure 6.18 shows the expected results of the scattered intensity in forward scattering directions using Mie theory. It was calculated with the same wavelength and refractive index used in our experiments.

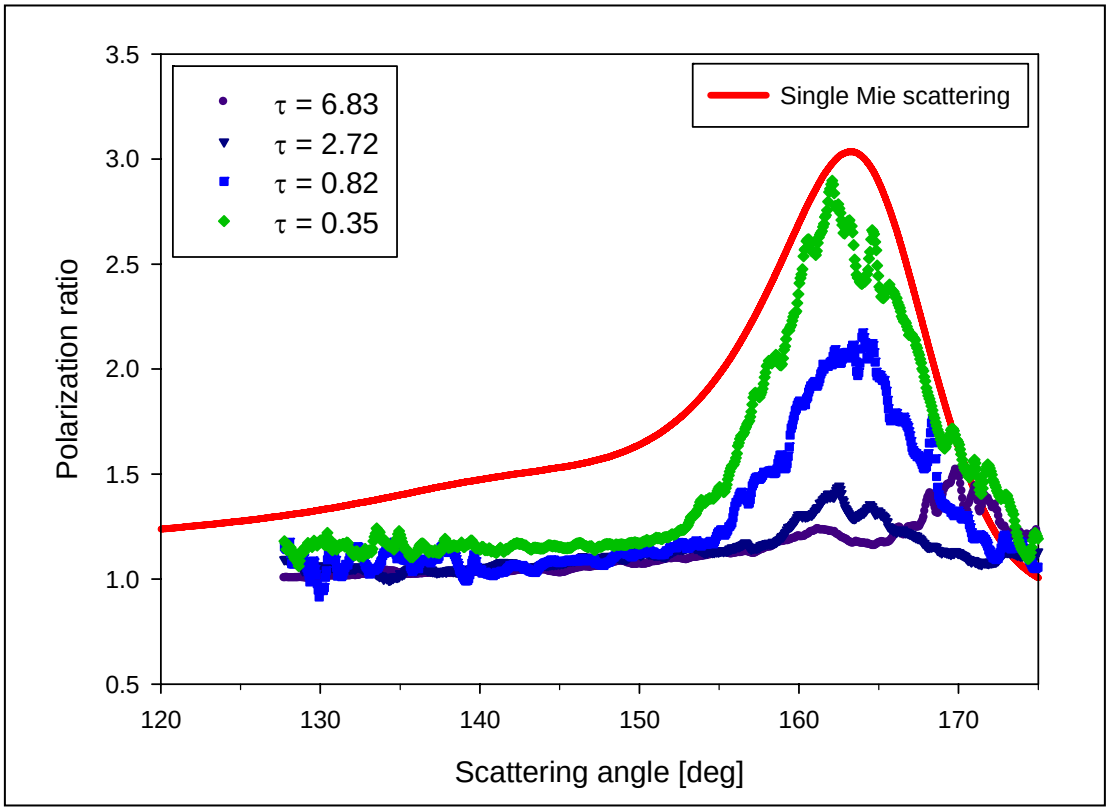

Figure 6.17 Polarization ratios of PSU small chamber data with optical depths of 6.83, 2.72, 0.82, and 0.35 at the backscattering direction. For comparison, polarization ratio of the single Mie scattering is adopted from Fig. 6.15.

The scattered intensity is normalized at scattering angle θ = 0°. Figure 6.18 (a) shows the normalized scattered intensity in forward scattering directions with mono-disperse size distributions, which are particle radii of 0.1, 1, and 10 μm. Figure 6.18 (b) shows the same calculations with log-normal size distributions of a geometric mean radius, r_g, with geometric standard deviations (SD) of 1.21, 1.31, and 1.41. Each size distribution used in Figure 6.18 (b) is shown in Figure 6.19. Due to the inverse proportion of the scattered intensity to the particle size and the width of the size distribution, it is possible to extract size information from the measurements of the radial distribution of the scattered intensity. In our case, the scattering angle was converted to a beam radius seen by a multistatic receiver.

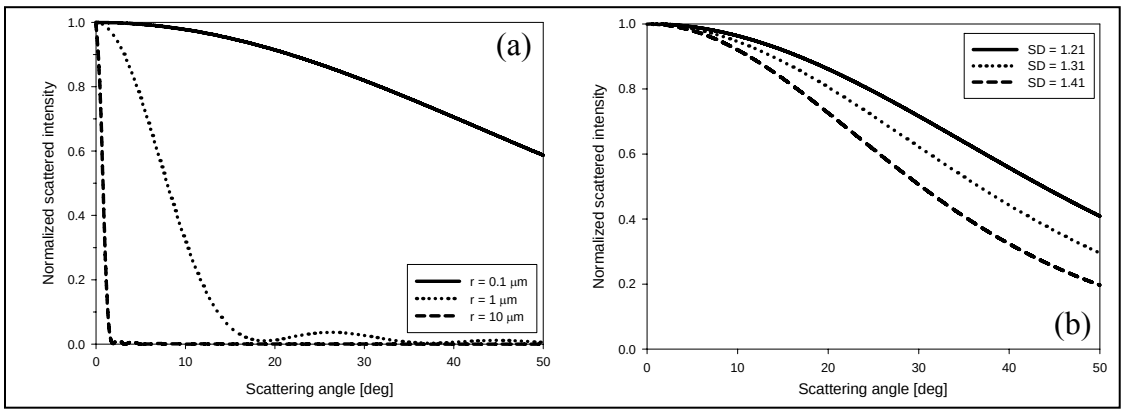

Figure 6.18 Normalized scattered intensity in forward scattering directions using Mie theory (λ = 532 nm, refractive index $n = 1.47 + 0i$) (a) Mono-disperse size distribution, particle radius r = 0.1, 1, and 10 μm (b) Log-normal size distribution, r_g = 0.13 μm with geometric standard deviations (SD) of 1.21, 1.31, and 1.41.

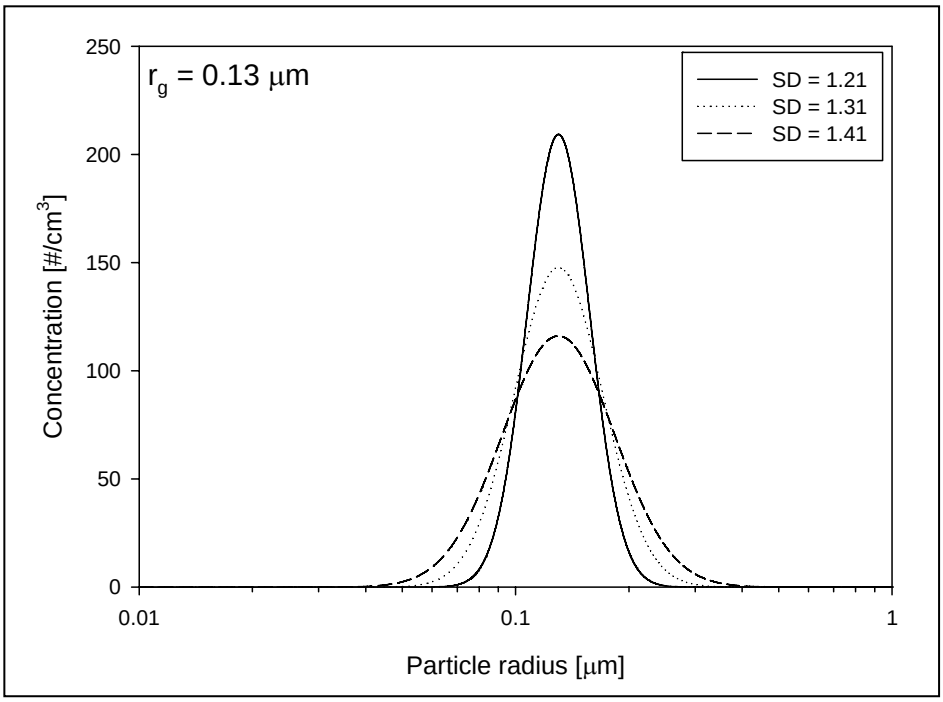

Figure 6.19 Log-normal size distributions used in the calculations of Figure 6. 18 (b).

The measurements were performed by changing the number density inside the chamber. Figure 6.20 shows the CCD image of a laser beam propagation in fog, which was taken in PSU small chamber. Each vertical white line represents the position where the data were analyzed. It is clearly shown that the unscattered narrow beam continues far into the scattering medium but it is surrounded by a halo which has the geometry of a forward beam although much wider due to multiple scattering.

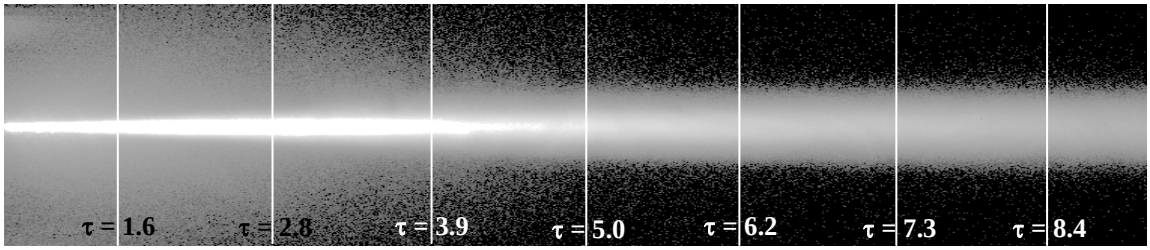

Figure 6.20 CCD image of a laser beam propagating through artificial fog in the small PSU chamber.

The central part of the transmitted beam, which has its Gaussian shape, is not affected by multiple scattering. The on-axis beam extinction along the direction of beam propagation is governed closely by Beer-Lambert's law. The radial distribution of multiply scattered light as a function of optical depth was examined in detail by Bissonnette (1995). Bissonnette's earlier results are shown in Figure 6.21 for comparison with our results, which will be presented next. Bissonnette's results were obtained from a laboratory chamber, which was small compared to our chamber. The radial distributions of a laser beam with a wavelength of 1.06 μm were measured at the exit plane of a 3.2 m long chamber filled with a homogeneous water droplet aerosol of different concentrations. The concentrations are given in terms of optical depths, τ. The symbols represent the measurements (points) and the calculations (curves) are shown for calculations using his diffusion model. Good agreement is shown with the measurements and model calculations.

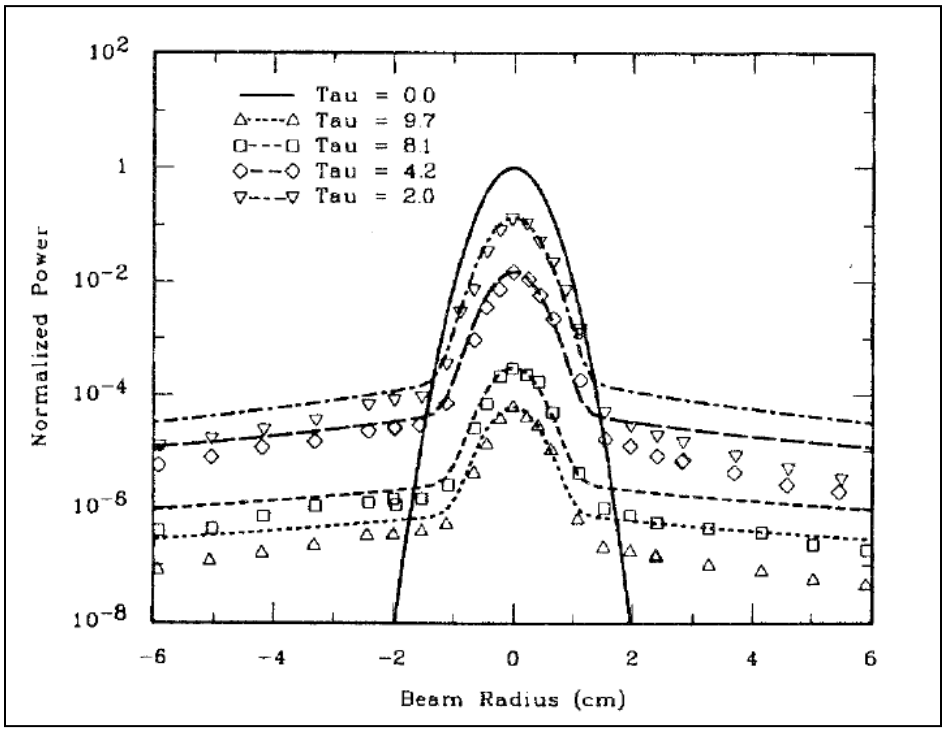

Figure 6.21 Profiles of a 1.06 μm beam measured at the exit plane of a 3.2 m long chamber filled with a homogeneous water droplet aerosol of different concentrations. The concentrations are given in terms of optical depths (τ). The symbols represent the measurements and the curves represent the solutions calculated with the diffusion model (Bissonnette, 1995).

The measurements were conducted by changing optical depth inside the chamber. Two methods were used to visualize the radial distribution of scattered radiation. The first method is to visualize the data at some locations along the beam path, see Figure 6.20. In this case, the total number density inside the chamber was fixed. Each vertical white line represents different optical depth because of the assumption of uniform particle distribution. It shows how multiple scattering affects the beam propagation along the beam path. The second method is to analyze the data at a fixed location from different CCD images with different number densities in the path. Multiple scattering effects are revealed with different number densities at a specific location of the beam path. Figure 6.22 and 6.23 show the results.

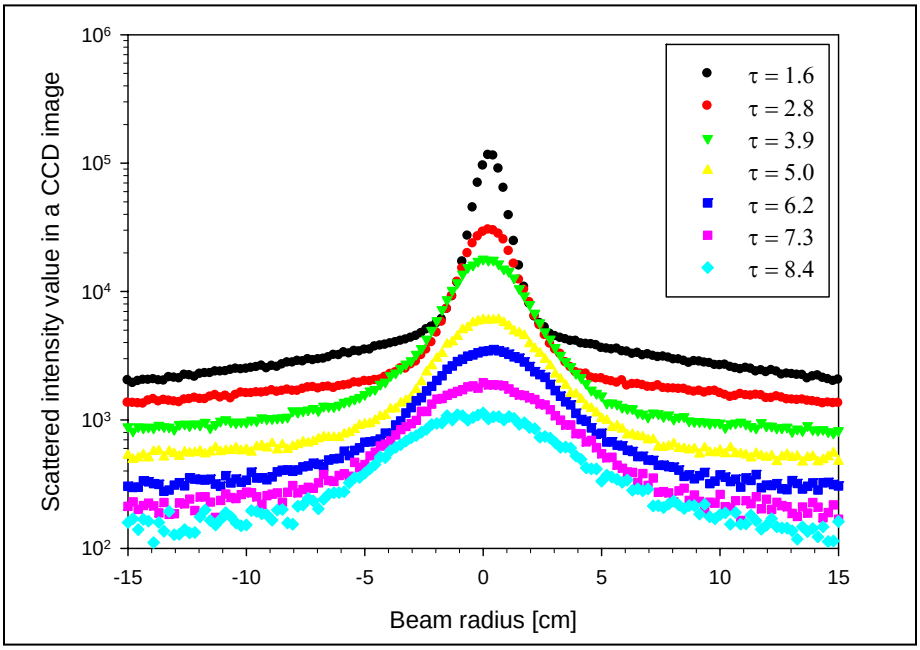

Figure 6.22 Radial distribution of multiply scattered beam with different optical depths in one CCD image at the forward direction.

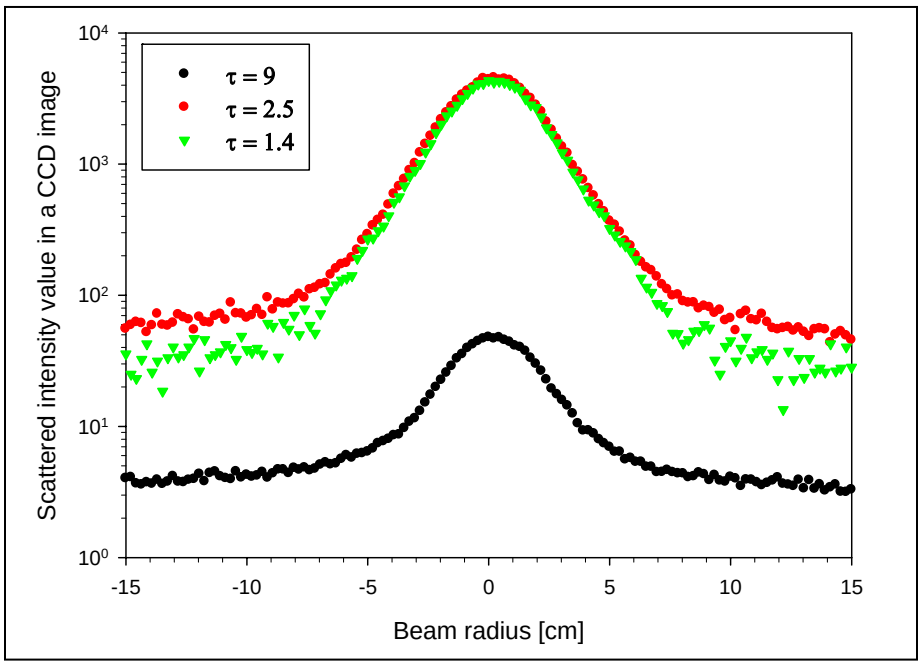

Figure 6.23 Radial distribution of multiply scattered beam with different number densities from three CCD images.

Figures 6.22 and 6.23 give a qualitative explanation about the effects of a multiple scattering along the laser beam propagation in atmospheric aerosols as mentioned previously. In the case of Figure 6.22, the number density inside the chamber is fixed and high enough to see multiple scattering effects. Each graph is extracted from each white line in Figure 6.18. However, in Figure 6.23, the number densities inside the chamber are 2.23×10^5 /cm^3 (τ = 9.0), 7.42×10^4 /cm^3 (τ = 2.5), and 5.50×10^4 /cm^3 (τ = 1.4) respectively. There is little difference between τ = 2.5 and τ = 1.4 because of small difference of the number density compared to the case of τ = 9.0. Multiple scattering components also increase with optical depth. Figure 6.24 shows a quantitative explanation. Bissonnette (1995) mentioned that the transmitted beam along the beam path followed closely Beer-Lambert's law.

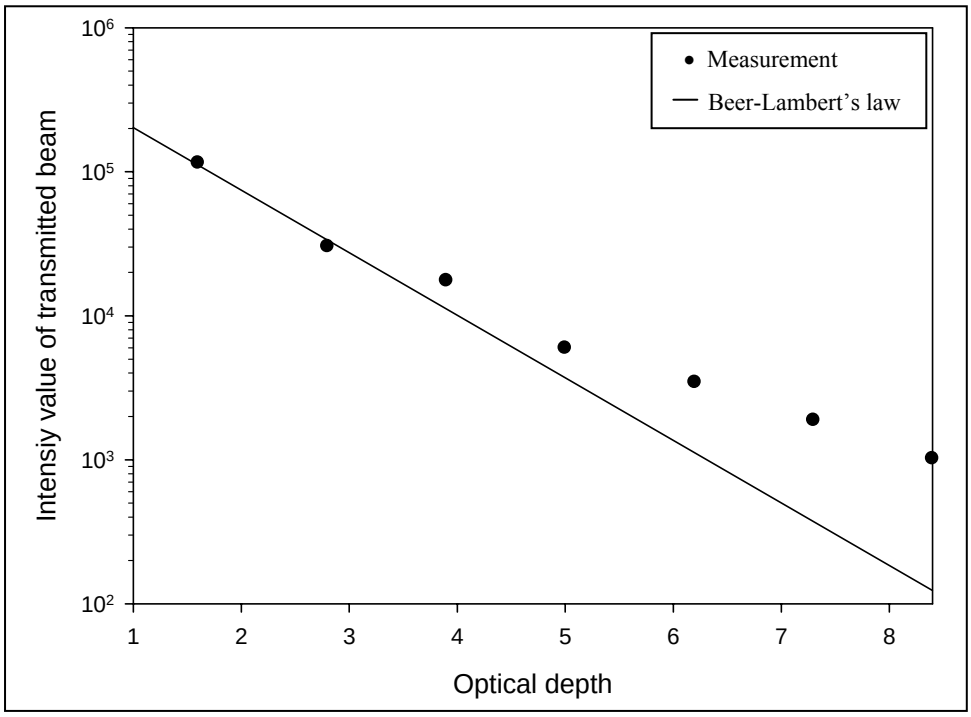

Figure 6.24 Transmitted beam intensity as a function of optical depth inside the chamber.

However, in our measurements, the intensity of the transmitted beam is getting larger than that expected by Beer-Lambert's law at the end of beam path, see Figure 6.24. This is because multiple scattering compensates for the loss of the transmitted beam in spite of the small active area of the detector. When one calculates the total extinction coefficient, the assumption is that all the energy scattered out of the optical beam is lost forever. However, multiple scattering allows this lost light back into the field of view of the detector (Pierce *et al*., 2001). Therefore, the presence of multiple scattering leads to an underestimation of the extinction measurements. This phenomenon has already mentioned by Pierce *et al*. (2001) and Wang *et al*. (2006). The intensity of an aureole, which is due to multiple scattering, increases with optical depth. Good agreement is shown with Bissonnette's result and the result obtained from the multistatic lidar. From the above results, one can define the limitations under which calculations of aerosol multiple scattering are valid.

6.4 Field Data Analysis

This section describes multistatic lidar field measurements under two different atmospheric conditions at State College. The field experiments were performed outside of College of Engineering Research Laboratory at Cato Park at the west side of State College because it is easy to set up instruments and observe fog. Figure 6.25 is a photograph showing the experimental setup for the field tests outside of the PSU Lidar Laboratory in the COE Research Laboratory. An experimental geometry was similar to that used in the chamber test. The size of the experimental setup is exactly 10 times larger than that of the PSU small chamber experiment. The weather station data were used to verify the classification of the meteorology on both clear and foggy nights. In this section, the multistatic lidar results will be described from each of these conditions.

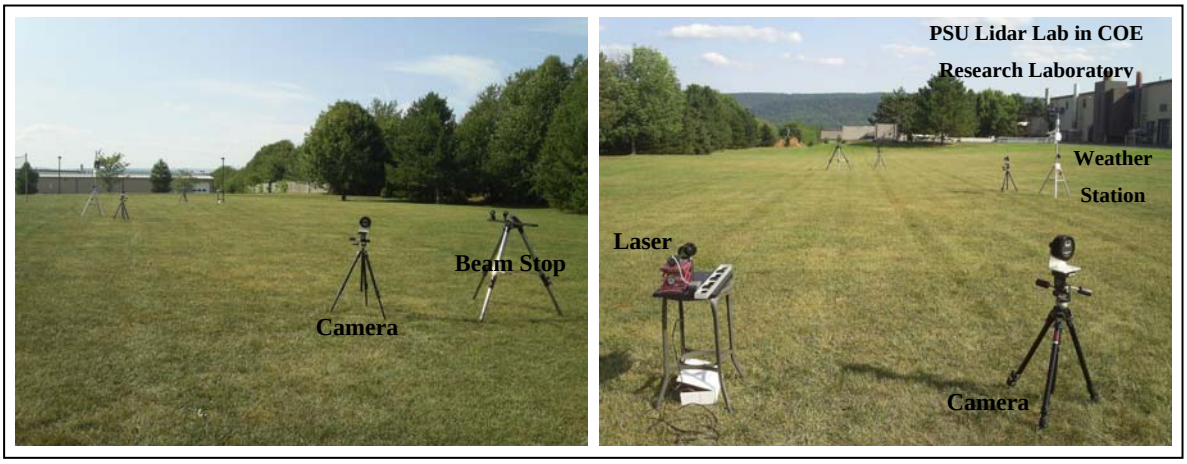

Figure 6.25 A photograph of the experimental setup for field test outside of PSU Lidar-Laboratory.

6.4.1 Clear Night Results

This section presents the results of the multistatic lidar for a clear night. Because of a low-power laser used in our experiments, see Chapter 4.2, it is very difficult to measure scattered intensities on a clear night. Therefore, the results obtained by

Novitsky, and not used in his thesis, are used in our analysis. A high-power lidar, the Lidar Atmospheric Profile Sensor (LAPS), was used to measure scattered intensities of the two polarization states. As shown in Figure 5-5 of his thesis, the measurements show a clear image even on a clear night without increasing an integration time of the detector, which is not the case in our experiments. Novitsky conducted an excellent study of single scattering properties using the polarization ratio to carry out the data inversion. In this section, we analyze a data set obtained on the night of July 23, 2001 to compare with our multiple scattering investigation. We are only using a set of his data, obtained from three cameras, and inverting them using his algorithm. Our analysis of this segment of his unused measurements provides a case to compare our multiple scattering with single scattering conditions. The basic meteorological parameters such as temperature and relative humidity were measured on that night. The relative humidity was found to be between 80 ~ 90 % and the temperature was between 20 ~ 25 °C, these conditions were shown to be typical conditions for particle condensation into spheres during earlier investigations (Stevens, 1996). Figure 6.26 shows the extinction on the night of July 23, 2001. The extinction up to 200 m, which was the main interest in his thesis, is almost 0.2 km^{-1}.

Three data measured at 01:00, 02:00, and 03:00 AM with the camera B are selected for the analysis of polarization ratio and radial distribution of multiple scattering. There were three cameras used in Novitsky's experiments, camera A, B, and C. Each camera was on line with a laser, see Figure 1.9. In order to observe an angular distribution of polarization ratio, the field of view (15.4°) of camera A is not enough compared to the other detectors and the polarization dependency of the camera C is not uniform at the end of row pixels, see Figure 6.27. This is why the data measured from the camera B are chosen. Figures 6.28 and 6.29 show the polarization ratio for cases of single scattering and multiple scattering. The black dot presents polarization ratio of single scattering in the laser beam while the red triangle represents polarization ratio using multiple scattering analysis, including the transmitted laser beam and aureole components.

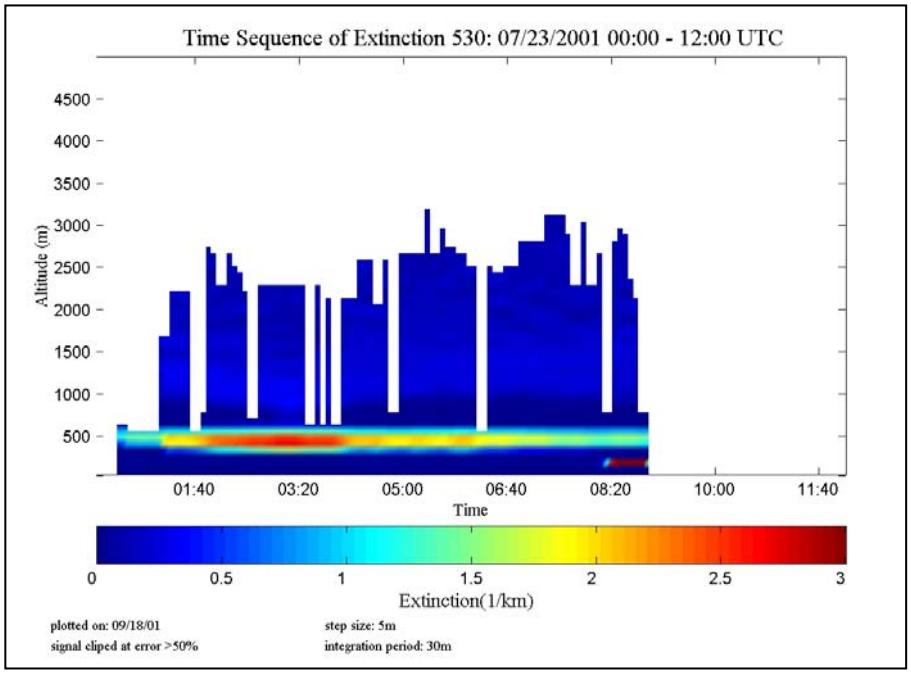

Figure 6.26 Extinction on the night of July 23, 2001 (Novitsky, 2002).

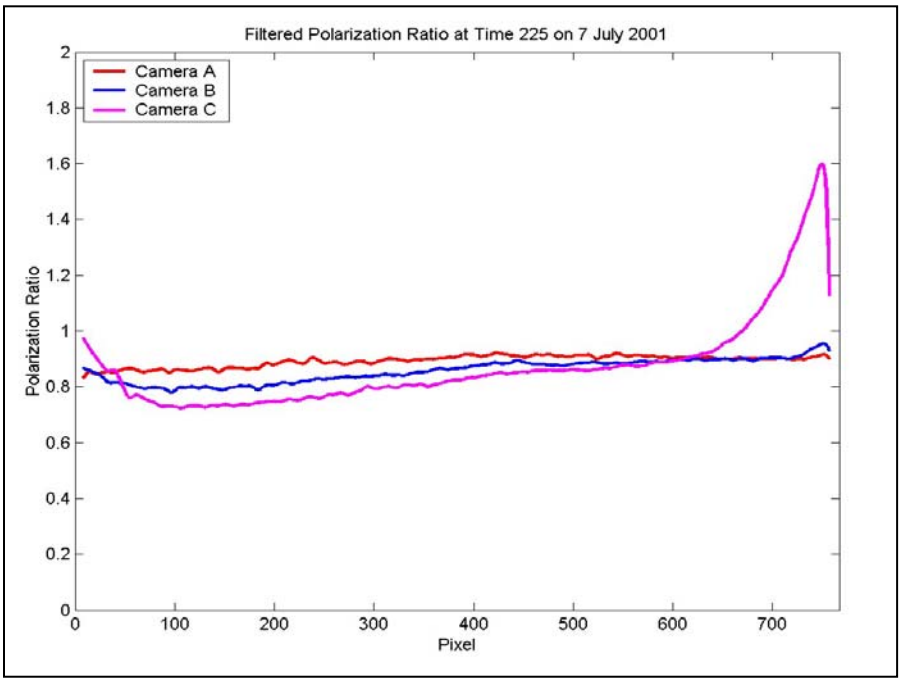

Figure 6.27 Polarization dependency of camera A, B, and C used in Novitsky's experiments (Novitsky, 2002).

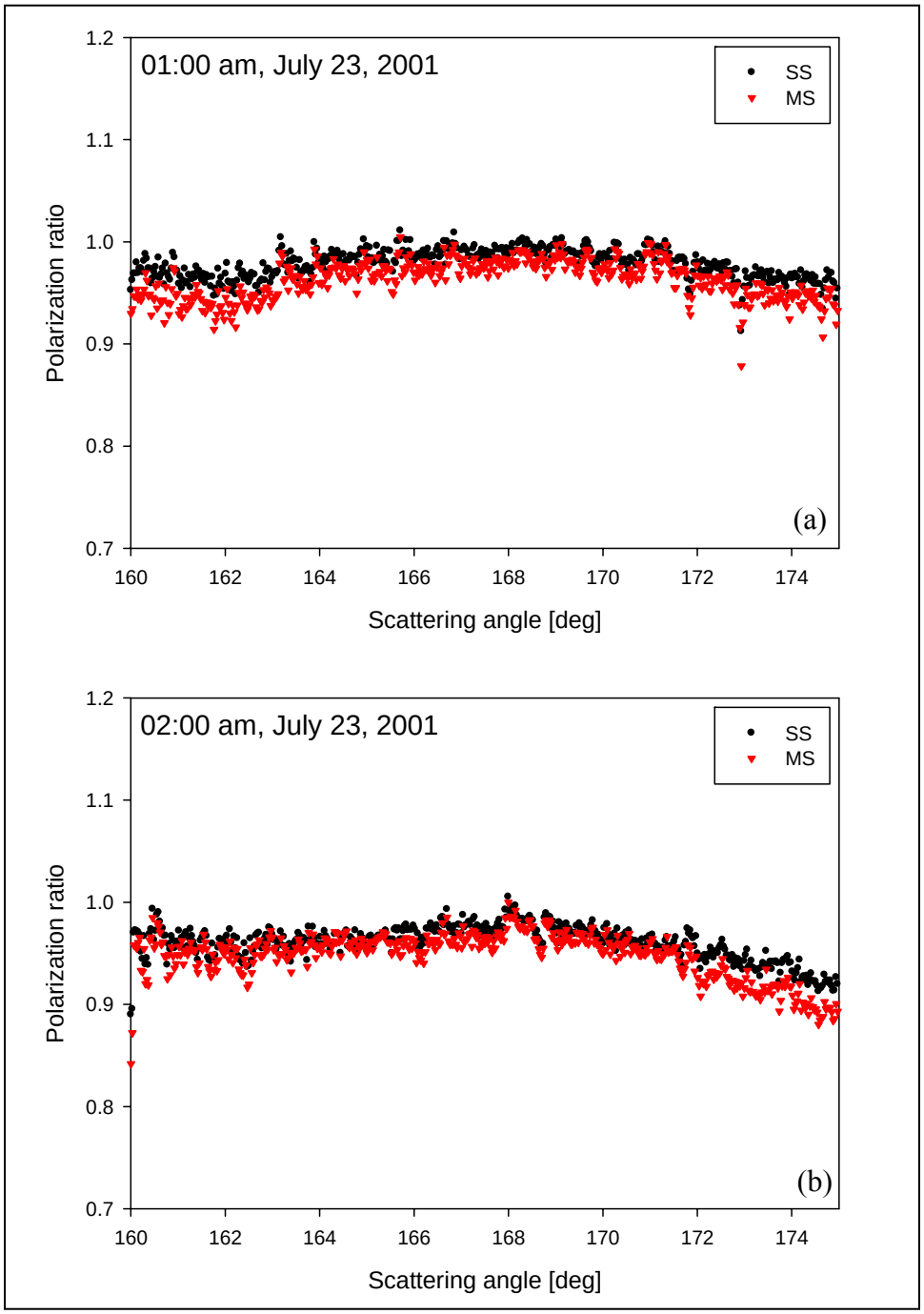

Figure 6.28 Examples of polarization ratio of single and multiple scattering measured at (a) 01:00 AM (b) 02:00 AM on the night of July 23, 2001.

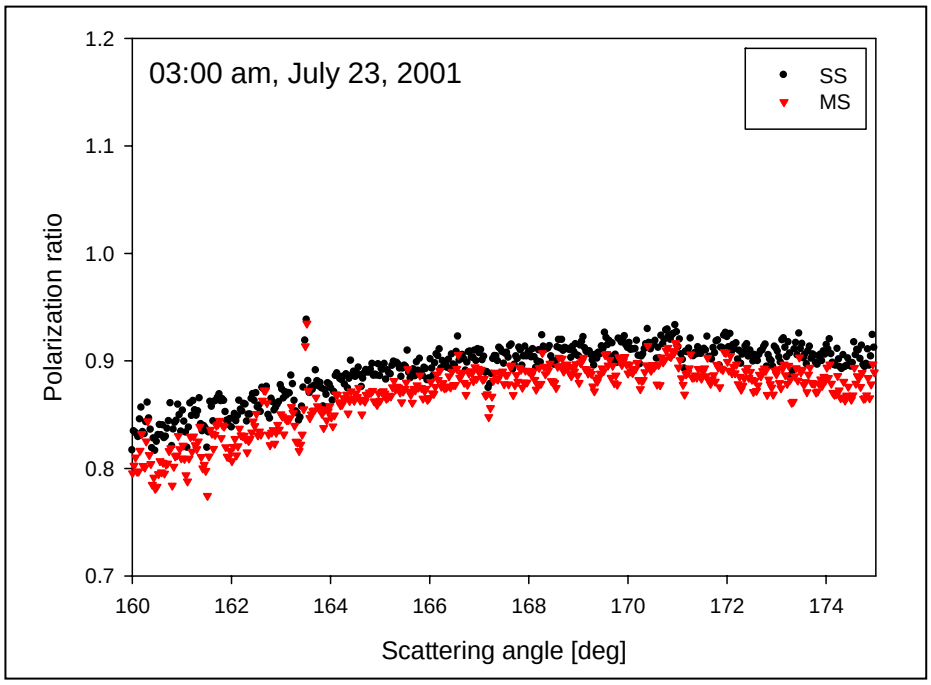

Figure 6.29 Example of polarization ratio of single and multiple scattering measured at 03:00 AM on the night of July 23, 2001.

As can be seen in each plot, the difference of polarization ratio between single and multiple scattering is very small compared to the case of chamber experiments and field experiments at foggy night, which are discussed in Sections 6.2 - 4 of this chapter. This means that multiple scattering analysis provides the same results when applied along the path of laser propagation into a relatively clear atmosphere.

The cross-section distributions of a transmitted laser beam are shown in Figures 6.30 and 6.31. In this case, we find little specific difference the laser beam profile, such as a beam radius in front of the laser and a beam divergence. Instead of using a beam radius in cm, the column with pixel numbers is used to display the spatial distribution of scattered intensities across the beam. This is because the object of these plots is not to see an exact beam profile along the beam propagation, but to investigate how the cross-sectional distribution changes with different optical depths. Each data set was measured along the beam at 22 m (●), 30 m (○), and 48 m (▼) in height, and the optical depth (τ) at each height is 0.004, 0.006, and 0.01, respectively.

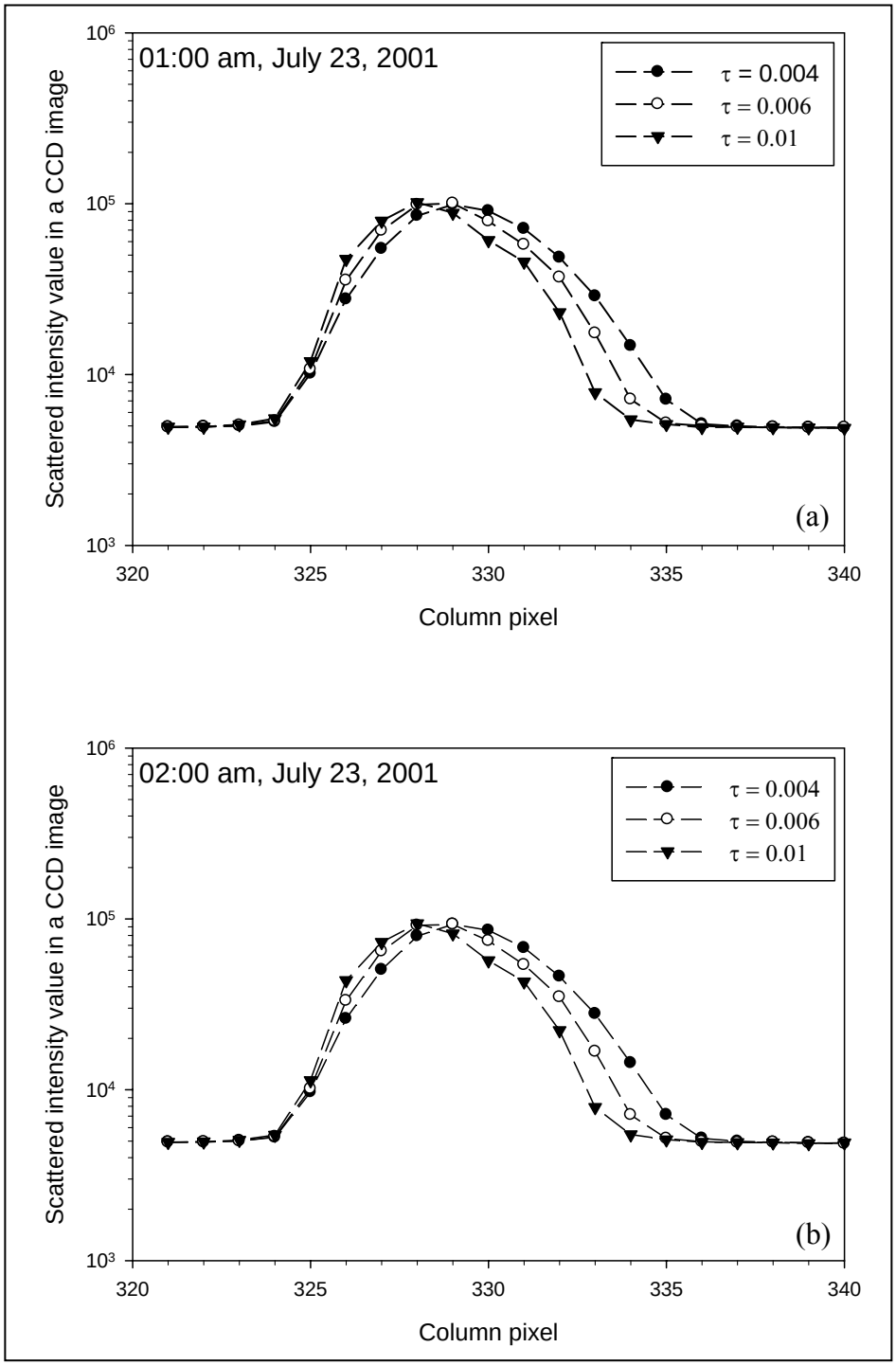

Figure 6.30 Examples of cross-sectional distribution of a transmitted laser beam measured at (a) 01:00 AM (b) 02:00 AM on the night of July 23, 2001.

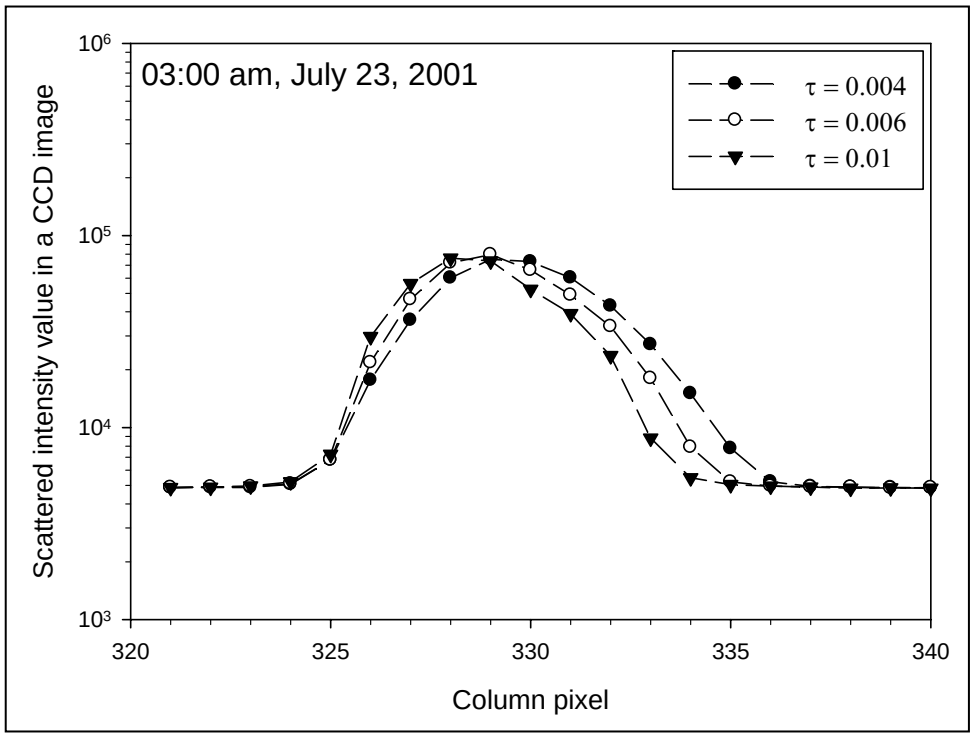

Figure 6.31 Example of cross-sectional distribution of a transmitted laser beam measured at 03:00 AM on the night of July 23, 2001.

The differences are small enough that multiple scattering can be ignored. As can be seen in each plot, the maximum intensity is almost same at different optical depths. The locations of the maximum intensity are not perfectly matched with each other simply due to the small angle of the laser beam across the image plane in a CCD image. The intensity of multiple scattering components (aureole parts) is very small and does not change with different optical depths, which means that single scattering is dominant along the beam propagation.

6.4.2 Foggy Night Results

This section presents the results of the multistatic lidar on a foggy night. The results are from the night of June 2, 2007. The temperature, relative humidity and wind speed were recorded each minute during the test periods. A field experiment was

conducted at June 2, 2007 when the conditions were very foggy and humid, a perfect night to measure multiple scattering. The experiment setup was started at 10:00 pm on June 1 and finished around 00:00 AM on June 2. The multistatic lidar measurements were started from 00:40 AM to 04:40 AM. Figure 6.32 shows a variation in the condition between 10:20 PM and 05:00 AM for the temperature and relative humidity. Here one can see that the relative humidity increases from 83 % to 91 % in the early measurements as the fog develops, and then remains almost constant at about 91 ~ 92 % until 05:00 AM. During the experiments, the temperature dropped from 19°C to 15.5°C. After 01:45 AM, when most data were obtained, the wind speed was almost zero and we can assume that a scattering medium is nearly homogeneous along the horizontal direction.

It is difficult to make an exact distinction between fog types, which were described in Chapter 3.2, from these atmospheric conditions. It was impossible to measure size distribution of these types of fog with the SMPS size spectrometer used in our chamber experiments because of the limited size range of this device. Instead, we suggest that the fog type encountered at that night is categorized as a moderate advective fog based on atmospheric conditions. The data shows how the size of fog particle changes during that night. The data were obtained every three minutes from 12:44 pm on June 1 to 04:00 am on June 2. After that, the measurements were made every two minutes by 04:40 am before the strong background of approaching morning made the measurements difficult.

First, we will perform the single scattering analysis following the approach described by Novistky in his thesis (2002). It will give us a comparison and confidence that the multistatic lidar with polarization measurements also provides useful results in optically dense media. From the atmospheric data we measured, see Figure 6.32, it is assumed that the fog on the night of 2 June 2007 can be described as a moderate advective fog. A reference for the expected result is first obtained by calculating using the size distribution from the fog model. We will start with calculations of the scattering phase function of two polarization states for conditions representative of the moderate advective fog model. The detailed explanation of each fog model is shown in Chapter 3.2.

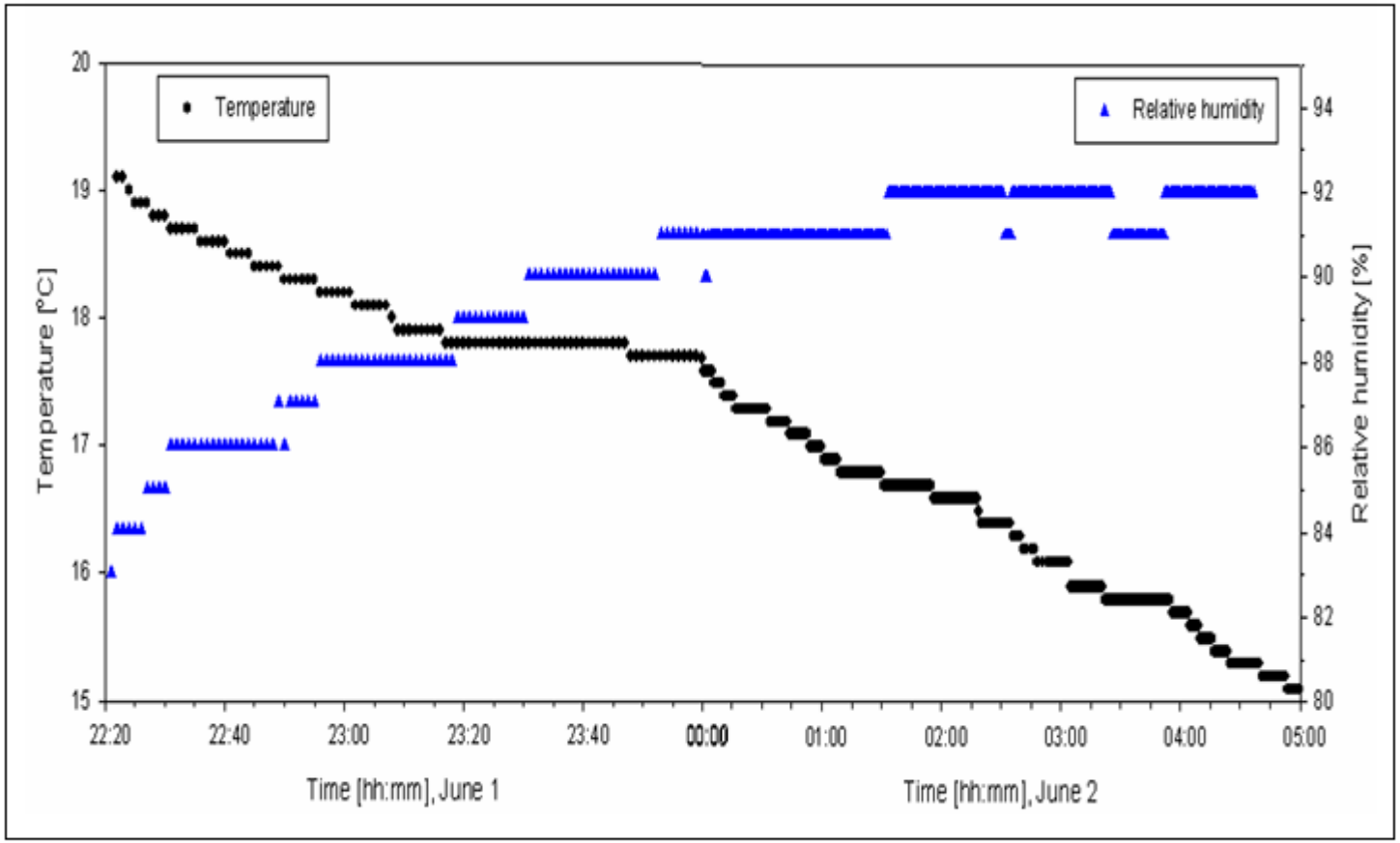

Figure 6.32 Plot of the temperature and relative humidity versus time measured on the night of June 1 to June 2, 2007

The phase function in that chapter only shows averaged intensities as a function of angle. However, in this section, the phase function of two polarization states in the backscattering region between 130° and 160° is needed to obtain the polarization ratio because this region is more sensitive to the size distribution compared to the forward scattering region. The theoretical result of the single scattering phase function is shown in Figure 6.33. This is calculated for an incident wavelength of 532 nm and refractive index of $n = 1.33 + 0i$. The effective radius, r_e, of moderate advective fog is 8 μm with α of 3 and γ of 1 in a modified gamma distribution. The scattered intensity difference of the parallel and perpendicular component is quite large between 130° and 160°, and clearly shows the advantage of using this specific angular region in our analysis. In order to see changes of size distribution of the scattering particles, it is sufficient to observe a scattering phase function. The data correspond to 7 pixels (Novitsky used 8 pixels in his single scattering analysis) in the CCD image were used to visualize an angular distribution of scattered intensity. As Novitsky mentioned in his thesis, it is known that these pixels only contain a single scattering component. At this time, it is not expected that our measured data perfectly match up with the theoretical values and it is hard to invert our lidar data using the Novitsky's algorithm because the atmospheric conditions in his measurements are totally different from ours.

Before we describe the details of our analysis, we want to know how a scattering phase function changes with the variation of a modified gamma size function different values of α and γ. As pointed out in Chapter 3.2, the shape of the particle size distribution described by the modified gamma function is mainly affected by two variables, α and γ.

These variables are also related to the effective radius given by Equation 3.2. The larger α and γ, the steeper and narrower the size function. In our case of moderate advective fog, it turns out that the γ value has more impact on the phase function than α. The larger γ, the smaller the effective radius of the size distribution. This explanation can be seen in Figure 6.34, which shows the scattering phase function of moderate advective fog with different γ values.

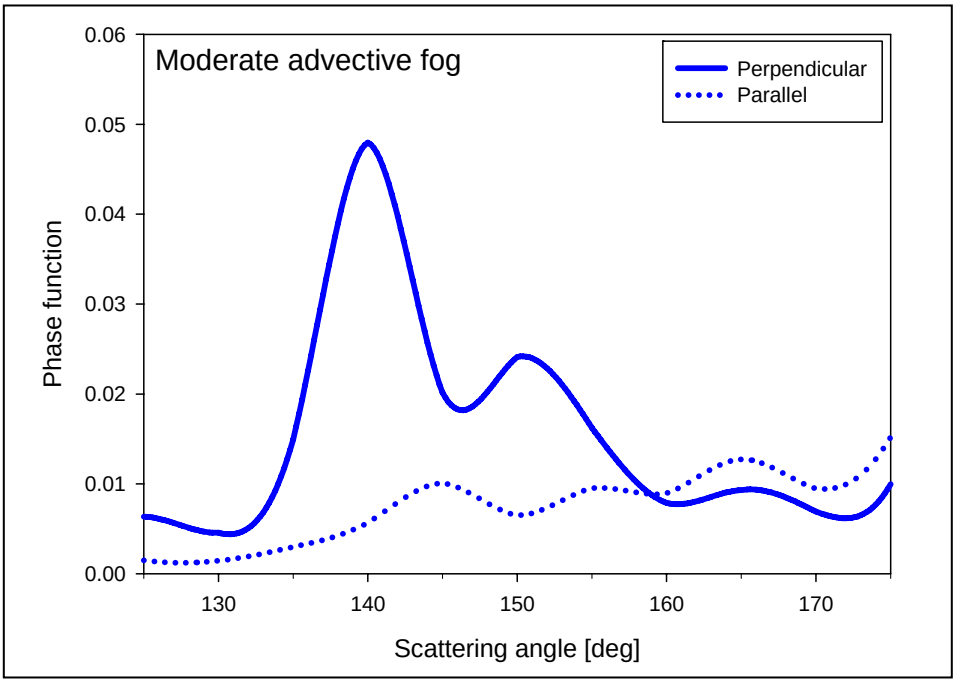

Figure 6.33 Phase function of moderate advective fog ($\lambda = 532$ nm, $n = 1.33 + 0i$).

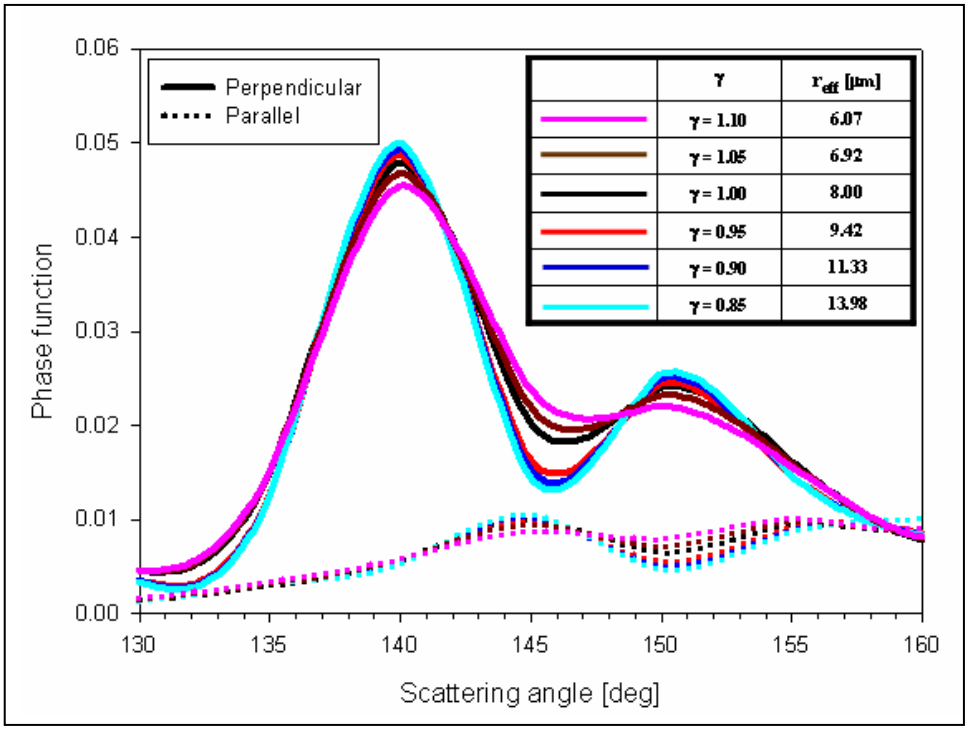

Figure 6.34 Phase functions of moderate advective fog with different γ values of the modified gamma distribution.

It is also revealed that changing the α value from 2.6 to 3.2 does not seriously affect the change of the phase function between 130° and 160° and the parallel component of the scattered intensity is less sensitive to changes in the γ value. The effective radii for γ = 1.10, 1.05, 1.00, 0.95, 0.90, 0.85 are 6.07, 6.92, 8, 9.42, 11.33, and 13.98 μm, respectively. There is little difference in the phase functions at scattering angles between 130° and 145°. However, the difference of the scattering phase functions between different γ values becomes significant after 145°.

Figures 6.35 - 6.38 display examples of the measured phase function and the best-fit gamma size distribution at different measurement times during the night of 2 June 2007. The symbols represent the measurements and the color curves represent scattering phase functions calculated using the best-fit gamma size distributions given in the lower part in the same figure. These plots show the raw data, for both the parallel and perpendicular components, with the background subtracted on the night of 2 June 2007. The measured data are scaled down to the values of the scattering phase function. Figure 6.35 (a) shows a plot of data for both scattered polarization components late night at 01:23. This figure shows the rough structure of the measured intensities is similar to the advective fog model. However, the measured intensities show a little difference between 145° and 155° from the theoretical values. This discrepancy between the measured data and the theoretical values in this region may be simply due to the difference of the effective radius and width of the size distribution with the model. Therefore, we attempt to fit our data to more accurate scattering phase function by changing the gamma (γ) values of the size distribution. One way to decrease the theoretical values of scattered intensity between 145° and 155° is to decrease the distribution width by changing the γ value from 1 to 1.05. Figure 6.35 (b) shows the best-fit gamma size distribution. A good match was found with a particle radius of 6.92 μm and the γ value of 1.05. The disagreement between the model and the data from 155° to 160° is probably due to a different particle size distribution at the end of the beam path.

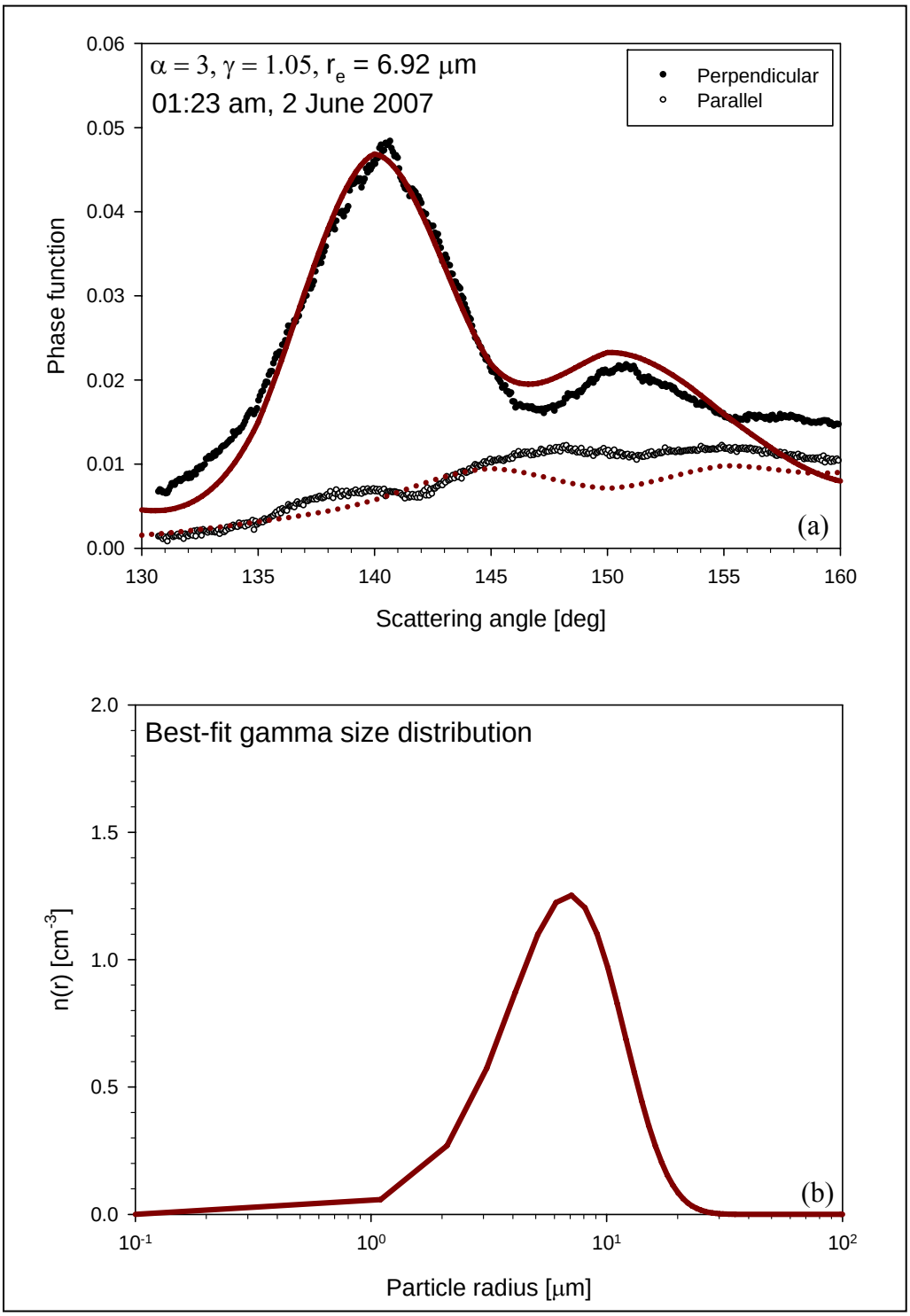

Figure 6.35 (a) An example of the measured phase function of two polarization states in the image measured at 01:23 am (b) Best-fit gamma size distribution.

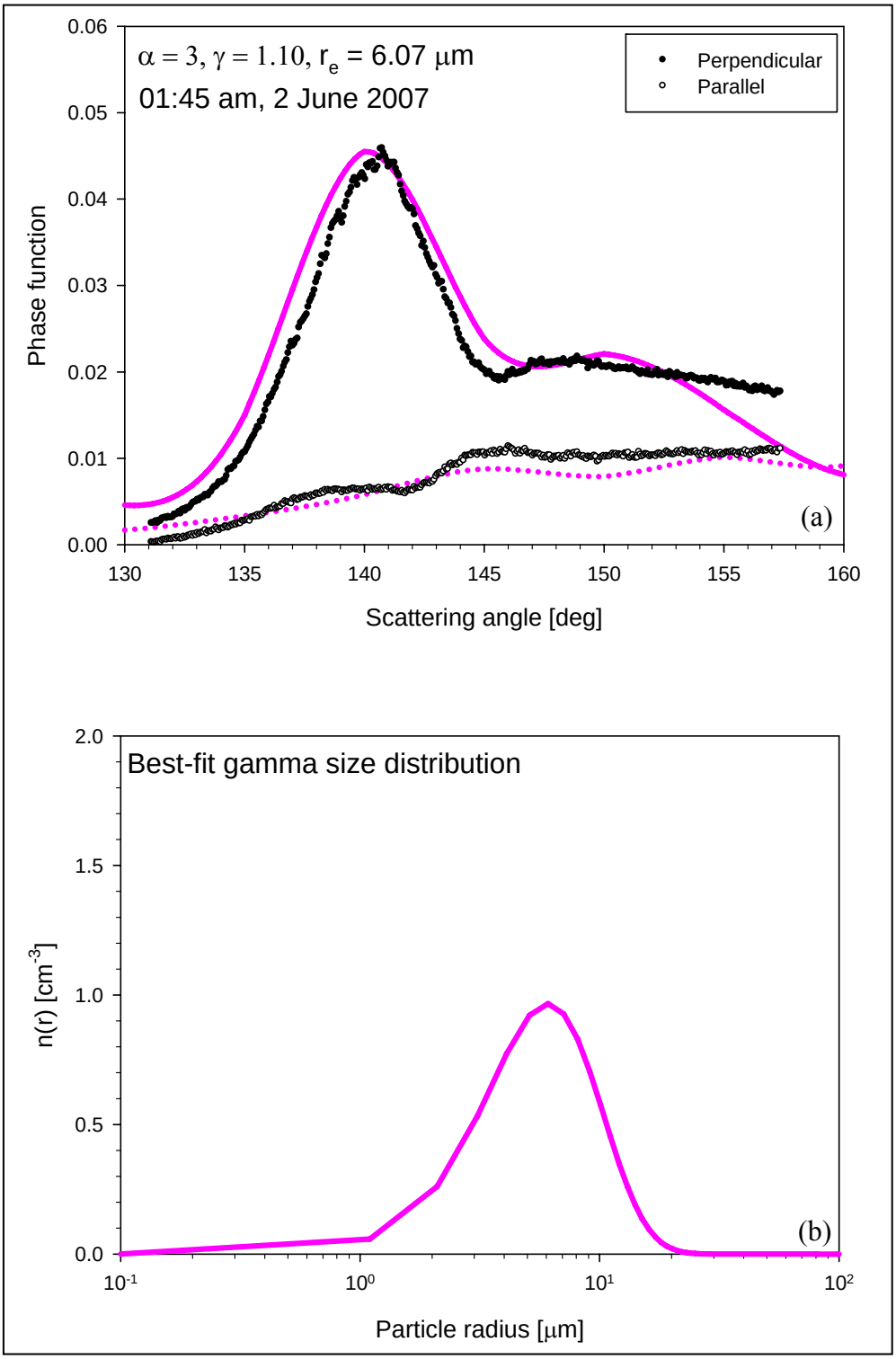

Figure 6.36 (a) An example of the measured phase function of two polarization states in the image measured at 01:45 am (b) Best-fit gamma size distribution.

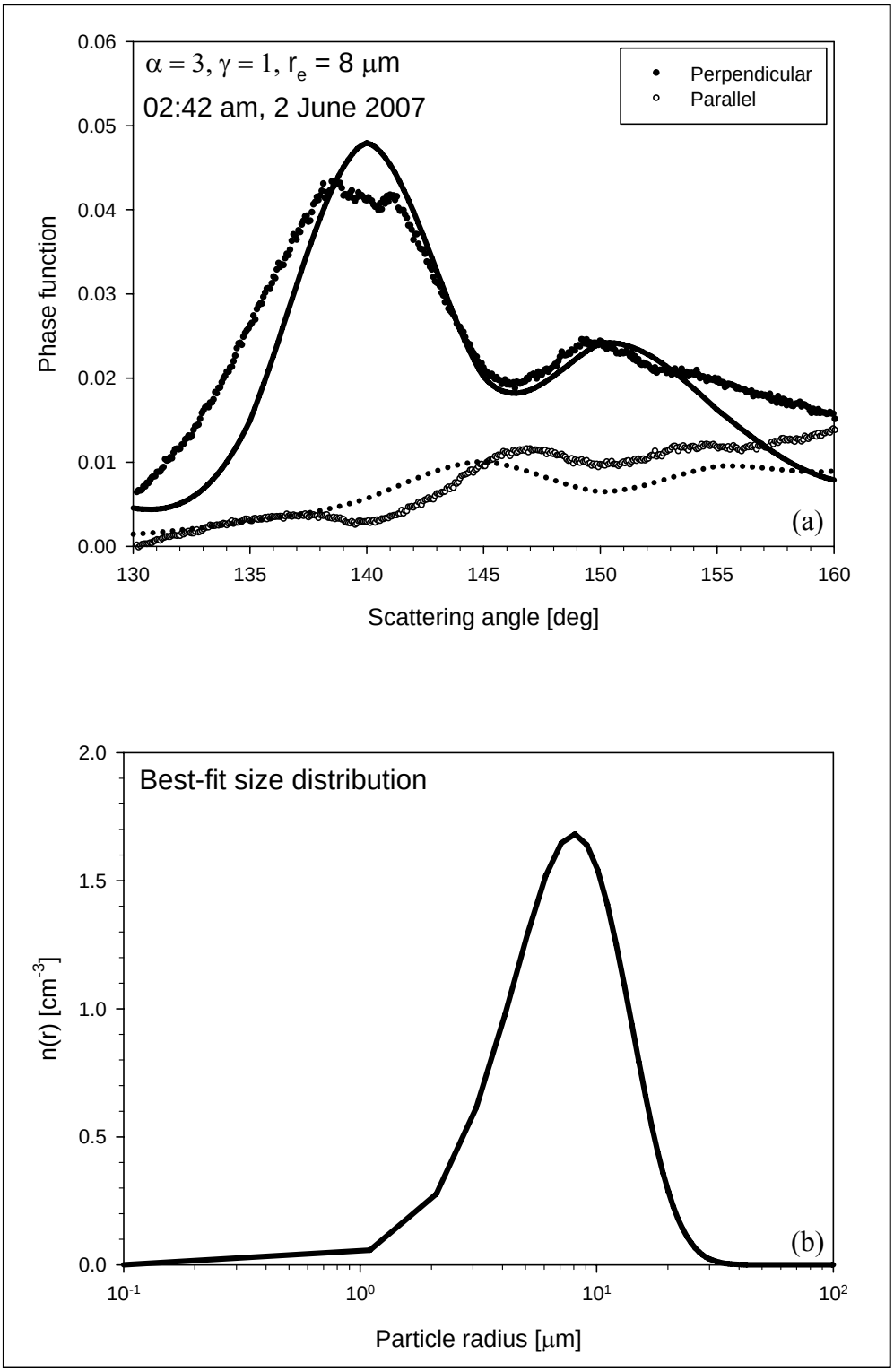

Figure 6.37 (a) An example of the measured phase function of two polarization states in the image measured at 02:42 am (b) Best-fit gamma size distribution.

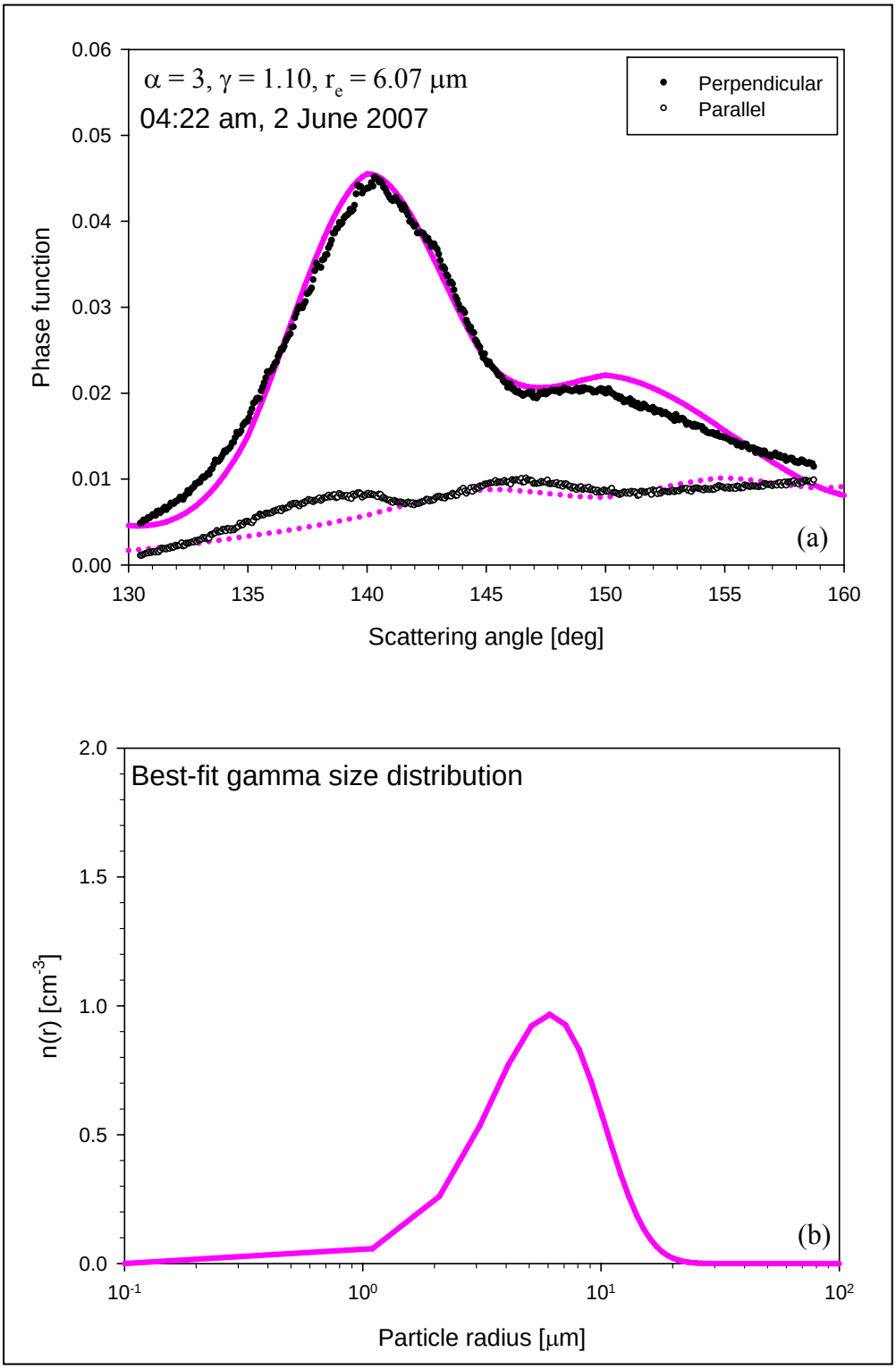

Figure 6.38 (a) An example of the measured phase function of two polarization states in the image measured at 04:22 am (b) Best-fit gamma size distribution.

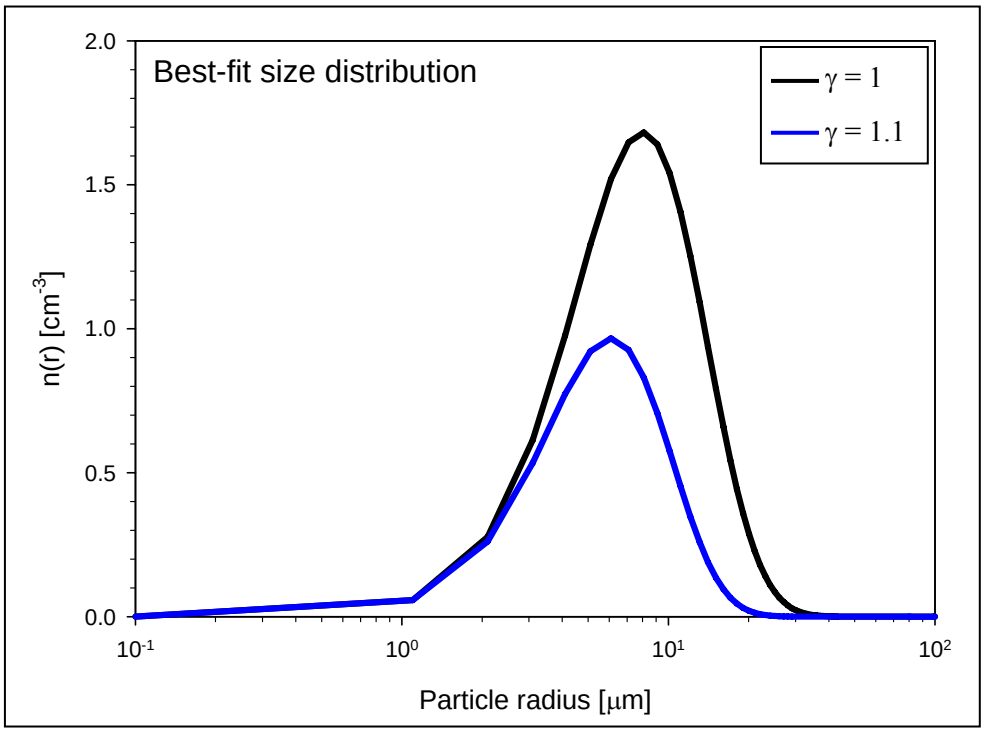

Figure 6.39 Range of best-fit gamma size distributions of fog on the night of June 2, 2007.

Figure 6.36 (a) shows the data collected almost 20 minutes later than the data in Figure 6.35. The parallel component remained almost same. However, the perpendicular component changed due to the different particle size distribution present at that time. The best-fit size distribution for this case uses $\alpha = 3$, $\gamma = 1.10$, and $r_e = 6.07$ μm, and is shown in Figure 6.36 (b). Figure 6.37 also shows the measured scattering phase function and the best-fit size distribution at 02:42 AM. The data approaches more closely to the moderate advective fog model. In the late (04:22 AM) measurements, see Figure 6.38, one can see that the scattering phase function approaches the case of $\gamma = 1.10$. In Figure 6.38 (a), the measured scattering phase function is shown. An excellent match is found with the calculated phase function. Figure 6.38 (b) shows the best-fit size distribution with $\alpha = 3$, $\gamma = 1.10$, $r_e = 6.07$ μm.

From the above analysis, the effective radius of fog measured on the night of June 2 is between 6 μm and 8 μm. The time sequence shows that the size of fog decreases at the end of the measurements because of dissipation of fog particles. This result is in good agreement with Stevens work (1996). His results from the night of September 14, 1995 showed that fog had nearly monodisperse size distribution having particle size range between 6.46 μm and 8.91 μm over a period of 2.5 hours. The size distributions are shown in Figure 6.39. The multistatic lidar showed its applicability in Novitsky's work. In our case, this analysis also demonstrates the use of the multistatic lidar method to extract aerosol properties in atmosphere in even optically dense conditions.

Now, we report our results on multiple scattering effects upon the polarization ratio and the radial distributions of scattered intensities. As mentioned earlier, the scattered intensity can be used to extract optical characteristics of atmospheric aerosols. However, it still has device non-linearities and setup uncertainties due to the lidar geometry. These problems are minimized by using a polarization ratio. The two data (01:45 AM and 04:22 AM data) are used to visualize the changes of polarization ratio due to multiple scattering, see Figure 6.40. The 20 pixels containing a single scattering component of a transmitted laser beam and multiple scattering components are summed and analyzed. In order to minimize the error from the mismatch of the scattering phase function of the measured and theoretical data, the data measured at 01:45 AM and 04:22 AM are used to calculate a polarization ratio. The polarization ratio is defined by the ratio of parallel component to perpendicular component of scattered intensity. The mathematical form is shown in Equation 2.4 to be,

$$\delta_p = \frac{I_{//}(\theta)}{I_{\perp}(\theta)}. \tag{6.1}$$

Therefore multiple scattering can increase or decrease polarization ratio depending on the value of polarization ratio of a single scattering component. This can be explained qualitatively.

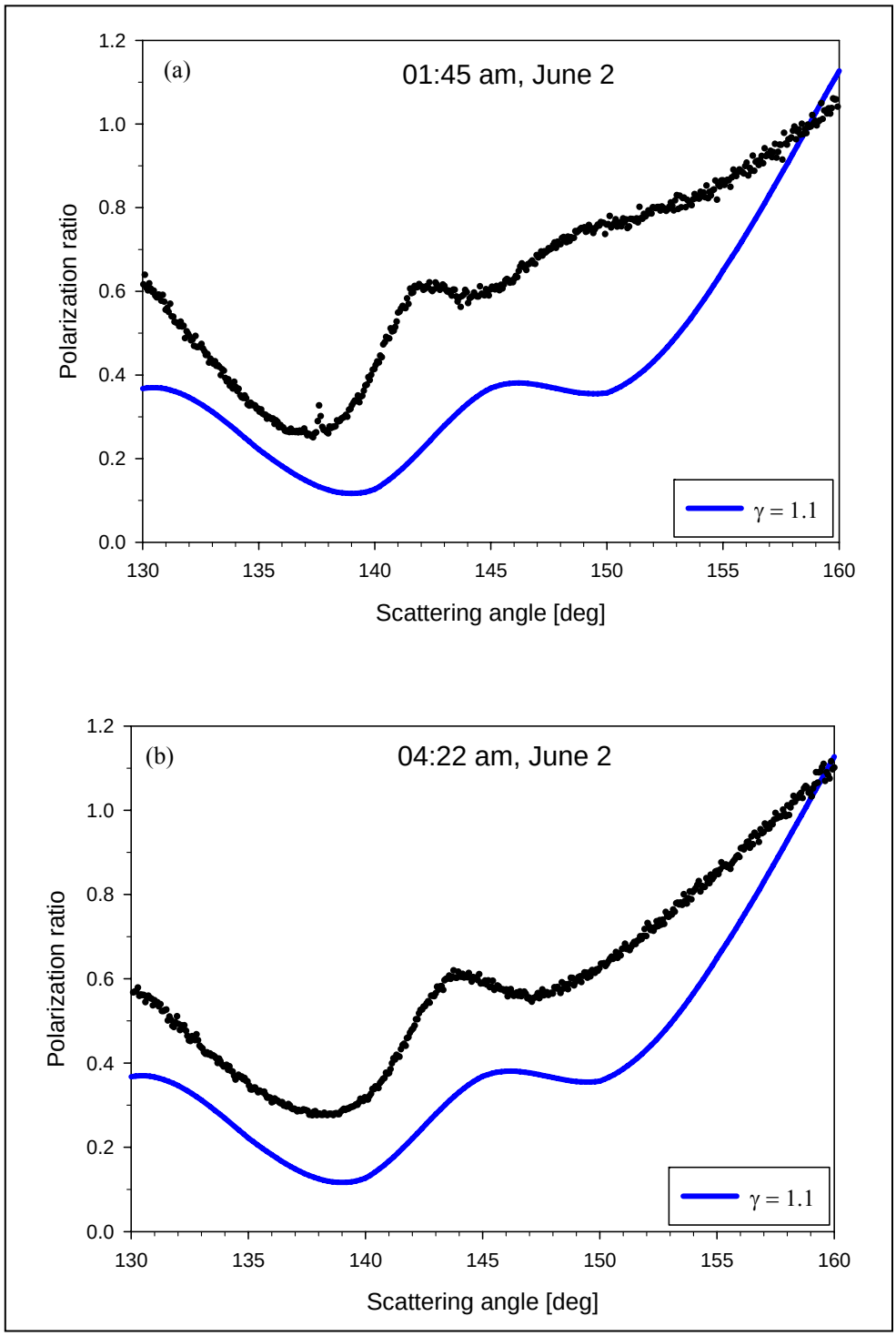

Figure 6.40 Plots of polarization ratio at the night of June 2, 2007 (a) 01:45 AM (b) 04:22 AM.

The scattering phase function in side-scattering regions becomes progressively smooth and featureless. This is caused by light undergoing many scattering events forgets its initial incidence direction and polarization state, and is more likely to contribute equally to all scattering directions (Mishchenko *et al*., 2007). Therefore, the difference of the scattered intensities of two polarization states becomes smaller. Because of this, a polarization ratio for single scattering larger than 1 results in a multiple scattering polarization ratio decrease, see Figure 6.17. However, when it is smaller than 1, multiple scattering increases the polarization ratio. This phenomenon is also shown in Figure 6.40. The black dots show the polarization ratio of multiple scattering components and the blue graph represents the polarization ratio of single scattering from the best-fit gamma size distribution shown in each Figure 6.36 (b) and 6.38 (b). The polarization ratio of multiple scattering increases by almost 100 % between 140° and 150° and approaches that of single scattering at larger scattering angles. This is because the phase functions at scattering angles $\theta > 160°$ begin to develop a single backscattering enhancement.

Figure 6.41 shows the CCD image of a laser beam propagation measured on the night of June 2, 2007. Each white line shows the position of the data extraction and optical depth, τ. In the case of the chamber experiments, see Figure 6.20, because of the short path length, a beam expander in front of the laser was used to increase the scattering volume along the path and thus obtain a better image.

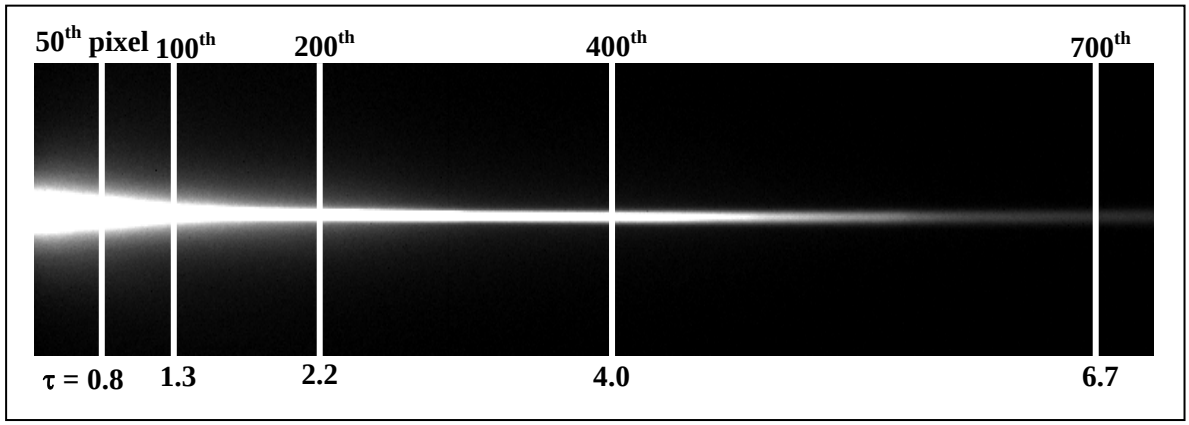

Figure 6.41 CCD image of a laser beam propagation in advective-type fog measured at the night of June 2, 2007.

However, the beam expander was not used in this field experiments. The optical depths are calculated from the on-axis power which is not significantly affected to any measurable amount by multiple scattering.

The results of radial distribution of a laser beam for the advective-type fog of different values of optical depth are shown in Figures 6.42-6.43. The plots show a central peak surrounded by a wide aureole formed by aerosol scattered light like the previous chamber experiments. The data are extracted from the images measured in the forward direction for the reason described in the case of the chamber experiments. There is some asymmetry in the measured beam profiles, especially in the center part. This effect is attributed to the fact that the transmitted laser beam is not aligned perfectly in the horizontal direction in the CCD image. Away from the beam axis, the profiles suddenly level off to show beam broadening effect. The two sets of data in Figure 6.42 were measured with 3-minute interval. The shapes at different distances along the optical path are very similar to each other. However, the data in Figure 6.43 shows a little difference. The intensity of the beam center at optical depth $\tau = 0.8$ is same as the previous results in Figure 6.42. However, the intensities of the beam center at different optical depths increase by almost 30-40 %. The data in Figure 6.43 exhibits a widening of the beam with a slope a little less than for the previous results in Figure 6.42, which is interpreted as an increase in multiple scattering effects. The possible reasons are increases of particle size and/or number density of fog particles.

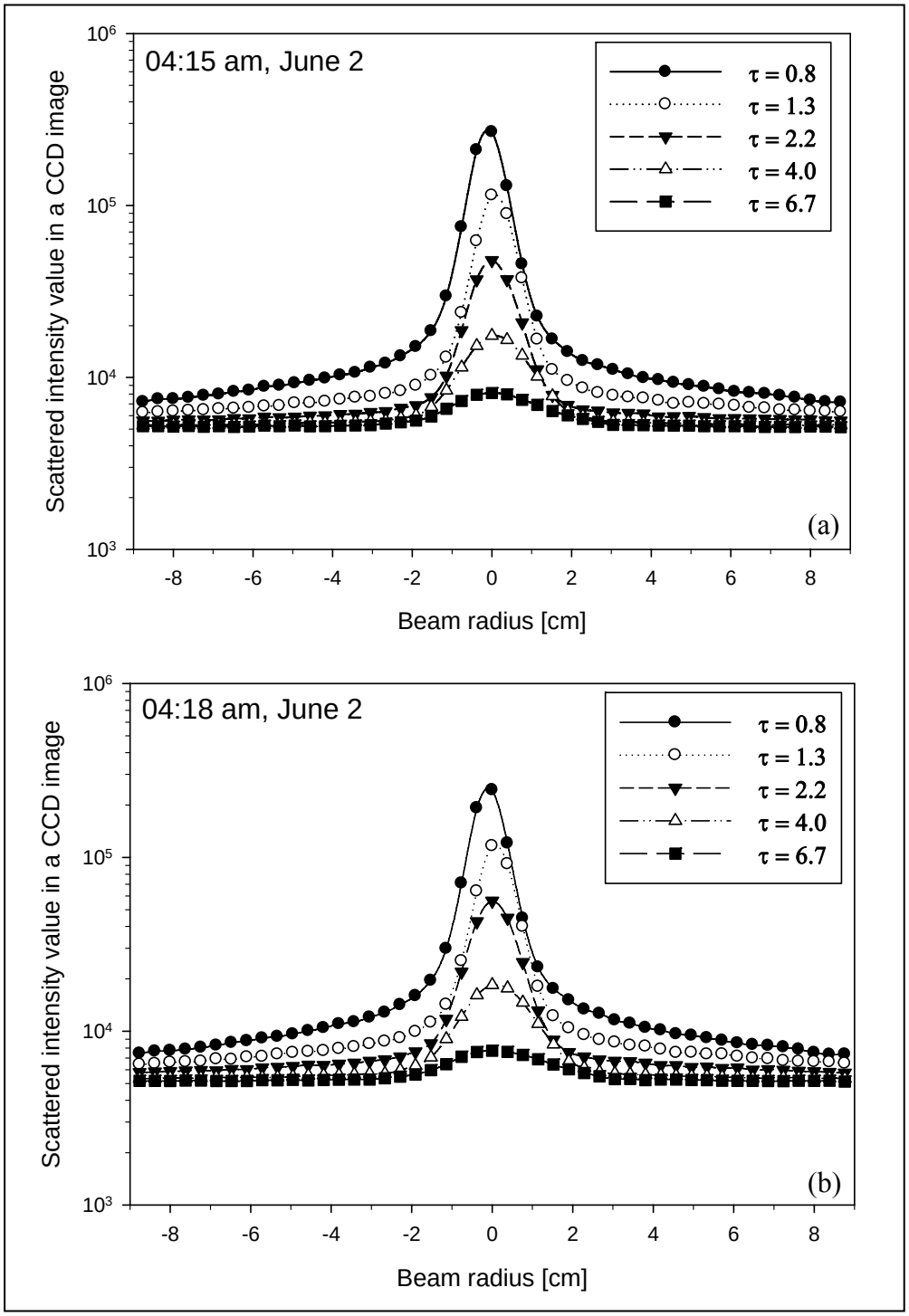

Figure 6.42 Profiles of the 532 nm transmitted beam for the advective-type fog for different values of the optical depth (τ) measured at (a) 04:15 AM (b) 04:18 AM.

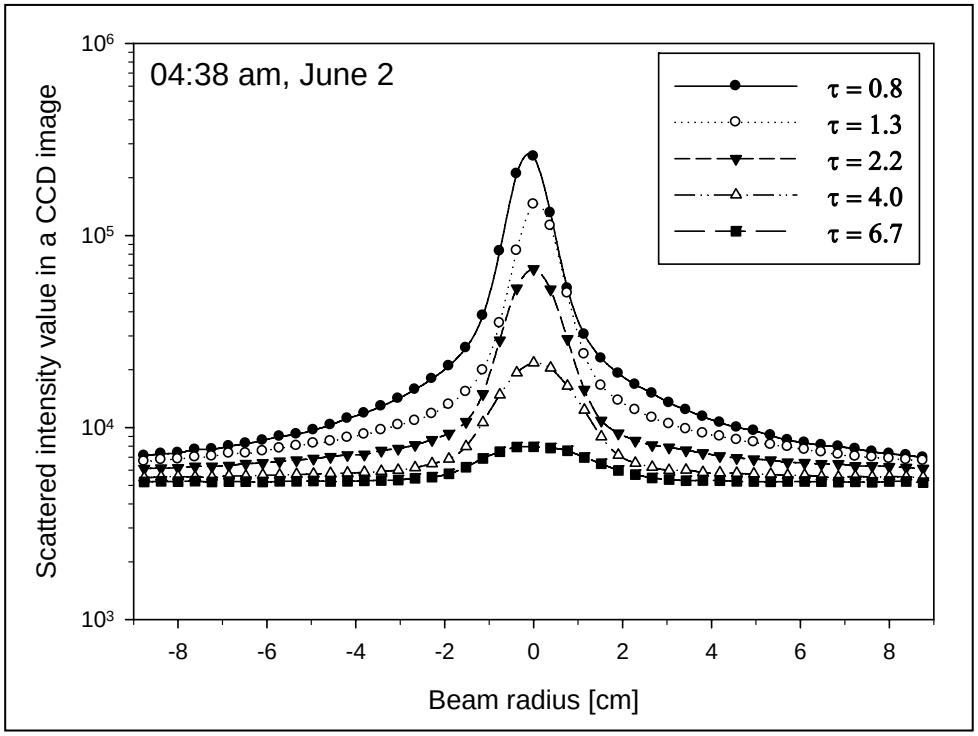

Figure 6.43 Profiles of the 532 nm transmitted beam for the advective-type fog for different values of the optical depth (τ) measured at 04:38 AM.

Chapter 7

CONCLUSIONS

7.1 Summary

The purpose of this thesis was to develop a multistatic imaging lidar system and extend the interpretation to measurements under conditions of multiple scattering. Prior studies by other groups to use remote detection measurements of multiple scattering in lidar experiments have all relied on signals backscattered by atmospheric aerosols. These measurements have used the intensity difference between single and multiple scattering components, molecular Raman depolarization ratio, or pulse stretching (Hutt *et al*., 1994; Wandinger *et al*., 1994; Pal and Bissonnette, 1998; Love *et al*., 2001). A thorough explanation of each measurement technique was presented in Chapter 2. However, those methods suffered from difficulty about the manipulation of lidar systems, weak signal intensity, and sophisticated detection system. They did not investigate scattering-angle dependent information to study multiple scattering, and each method investigated only one physical quantity to visualize multiple scattering effects. We demonstrated it was possible to investigate both the angular-dependent polarization ratio from multiple scattering and radial distributions along the beam path simultaneously by using the multistatic lidar approach.

The bistatic (Stevens, 1996) and multistatic lidar approach (Novitsky, 2002) have been applied under the single-scattering-dominant atmospheric conditions. Therefore, their previous investigations using bistatic and multistatic lidar systems mainly focused on the analysis of polarization ratio of single scattering signals, and the development of inversion algorithm to investigate optical properties of atmospheric aerosols, such as nine parameters of the trimodal log-normal size distribution and refractive index. However, their data analysis methods and inversion algorithms could not be applied to the measurements of optically dense media. To overcome this problem, multistatic lidar

arrangement in horizontal configuration was used for the present work. The measures in the backward direction were used to calculate polarization ratio of multiple scattering and those measured at forward direction were used to visualize radial distribution along the beam propagation path in an optically dense medium. The details of the multistaic lidar configuration and supporting instrument used in this research were explained in Chapter 4. Our multistatic lidar was then tested during November 2006 at DRDC, Canada in collaboration with the group of Dr. Gilles Roy, and July 2007 at the PSU Lidar Laboratory. Several laboratory experiments were performed under different atmospheric conditions at the PSU Lidar Laboratory. To verify the applicability of the multistaic lidar arrangement in the measurements of angular-dependent multiple scattering effects, numerical simulations using the Bistatic Monte Carlo method were performed. The simulation results were presented in Chapter 3. The results showed that, when compared to the results of Haze M model, the multiple scattering contributions of fog models were comparable to single scattering components at both forward and backward scattering directions because of higher extinction coefficient.

Our approach allowed us to investigate multiple scattering by measurements of polarization ratio and radial distribution along the beam propagation path. The polarization ratio approach demonstrated that it is useful not only for single-scattering dominated atmospheric conditions but also in the atmospheric conditions when multiple scattering is significant. Experimental results were presented in Chapter 6. Our results showed that multiple scattering strongly depends on microphysical properties of atmospheric particles such as particle size and number density, and the geometry of lidar systems. It turned out that multiple scattering effects increase as particle size increases as expected based on the cross-section dependence and number density described in terms of optical depth, τ. Based on Bistatic Monte Carlo calculations, multiple scattering does not depend on the laser beam divergences of typical lidar systems. However, multiple scattering strongly depends on the detector's FOV and penetration distance. The angular distribution of multiple scattering in optically dense media significantly deviated from that of Mie calculation of a single scatter in the side-scattering region. Our results, obtained from chamber experiments, showed that even in the small particle size

distribution, multiple scattering increases with number density within the scattering volume. Specifically, multiple scattering increases the depolarization of the scattered radiation in the side scattering region. That means multiple scattering does not contribute equally over the range of different scattering angles.

Our results on radial distribution of a laser beam as it propagates into dense media showed that the central part of the transmitted beam, which has Gaussian shape, was not affected as much by multiple scattering. This narrow central part was surrounded by a wide aureole due to multiple scattering and increases with optical depth relative to the transmitted beam intensity. The transmitted beam intensity along the direction of propagation became larger than that expected by Beer-Lambert's law at the end of beam path. This is because multiple scattering compensates for part of the loss of the single scattering components probably when due to larger aerosols with this large forward scatter component of the transmitted beam. Multiple scattering also led to beam broadening along the laser beam path. Compared to single scattering atmospheric conditions, multiple scattering in optically dense media was quite large and showed a slope of radial distribution much less than for the clear atmospheric condition. Our results showed good agreement with the previous Bissonnette's calculations, which were obtained by a diffusion theory applied to the lateral transport of the scattered intensity.

Based on our Bistatic Monte Carlo calculations and experimental results, it was found that the single scattering assumption is valid under conditions of optical depth of less than around 0.3. However, it was difficult to define the exact atmospheric conditions corresponding aerosol multiple scattering conditions which are valid for our calculation approach because it turned out that multiple scattering is significantly affected by many different factors, such as detector's field of view, particle size and penetration distance, in a complicated way.

7.2 Future Work

The results from this work have demonstrated that multistatic lidar can be used to study multiple scattering. Several problems have been addressed in the process of initial

trials to determine the measurement scales of our lidar system, effects of multiple scattering from nonspherical particles, and solutions of inversion problems. It will take a significant effort and time by many researchers in order to resolve all of these problems. However, we believe it is worth it to mention these in this chapter. The following sections explain briefly the above three problems and how our recent work can be improved.

First, improvements could be made to the experiment that would permit operation in vertical lidar configuration. Our measurements were only made in small-scale field experiments in horizontal mode because of interest in measurements of forward scattering. However, it is insufficient to investigate optical properties of atmospheric aerosols in regional or global scale. We suggest that an advanced multistatic lidar configuration should be used. This was first proposed to NASA by PSU lidar group in 2004, which was called "Species Spectra & Aerosol Scatter Instrument (SSASI)" proposal (Philbrick et al., 2004). More imaging detectors could be used in our multistatic configuration to obtain enhanced spatial resolution of the vertical path to provide sufficient independent information at various azimuth/elevation locations to enable the inversion process to retrieve the aerosol properties (Philbrick *et al*., 2004). In order to make this work, there should be ground-based and space-based elements working together as a system as shown in the schematic diagram in Figure 7.1. The high power laser transmitter beam (such as LAPS) is imaged from both space and ground during the ground-based experiment. The beam is pointed at preplanned locations and satellite detectors used to obtain multi-angle information in the forward direction, while the ground-based detectors observe it from backward direction. Even though there may be some problems to solve with regarding detector's sensitivity, data transmission from such a long distance, tracking the satellite during the measurement, and eye-safety issues, it is still a very doable concept. The measurements would be used to characterize properties of the different aerosol layers in the lower atmosphere.

Second, our work was based on multiple scattering of spherical particles. However, in real world, there are so many different shapes of particles in atmosphere.

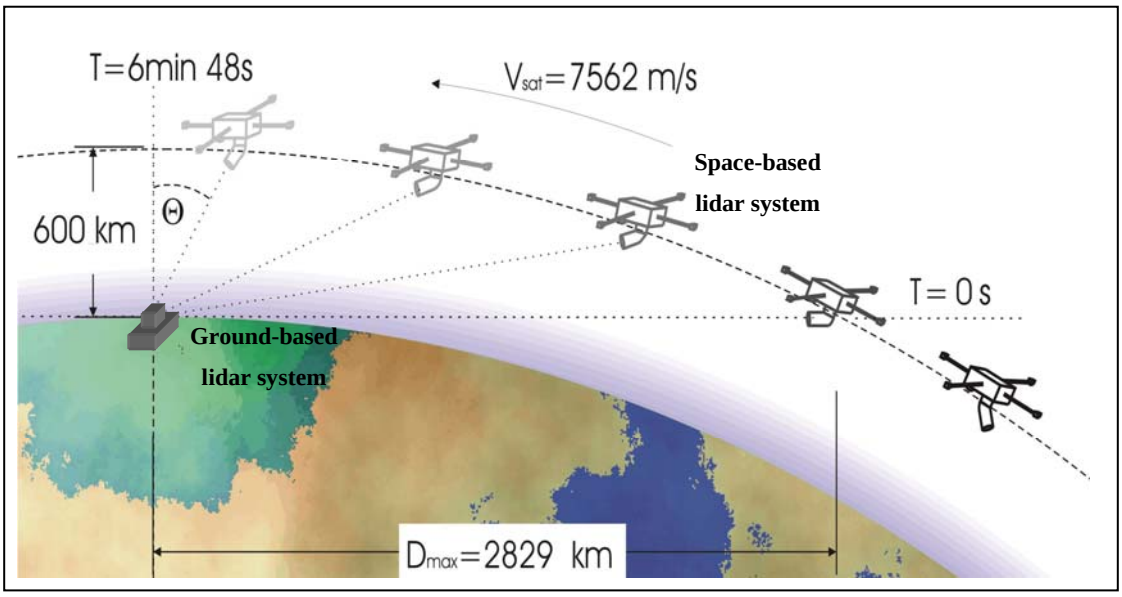

Figure 7.1 A ground- and space-based instrument for remote sensing of gas species and aerosols (Philbrick *et al*., 2004).

At this moment, we suggest that the polarization ratio method can be applied to multiple scattering of spherical particles. It is known that scattering properties of nonspherical particles are significantly different from those of volume- or surface-equivalent spheres (Mishchenko *et al*., 2002).

Examples in Figures 7.2 and 7.3 show the results of T-matrix computations of the intensity scattered by spheres and different spheroids. The spheroids in these plots have same surface area of sphere shown in Figure 7.2 (a). The scattering phase functions of oblate and prolate are shown in Figure 7.2 (b) and 7.3, respectively. These are calculated with an incident wavelength of $\lambda = 532nm$, refractive index of $n = 1.325 + 0i$, and a size parameter $kr = 13.2$ which would correspond to an aerosol of 1.1 μm radius at the 532 nm wavelength. Particles are illuminated by an unpolarized beam of light incident along the z-axis, which is the red axis in each subplot. These examples point out the huge differences of single scattering phase function between different particle shapes. Therefore, this difference would be a significant factor when dealing with the case of multiple scattering.

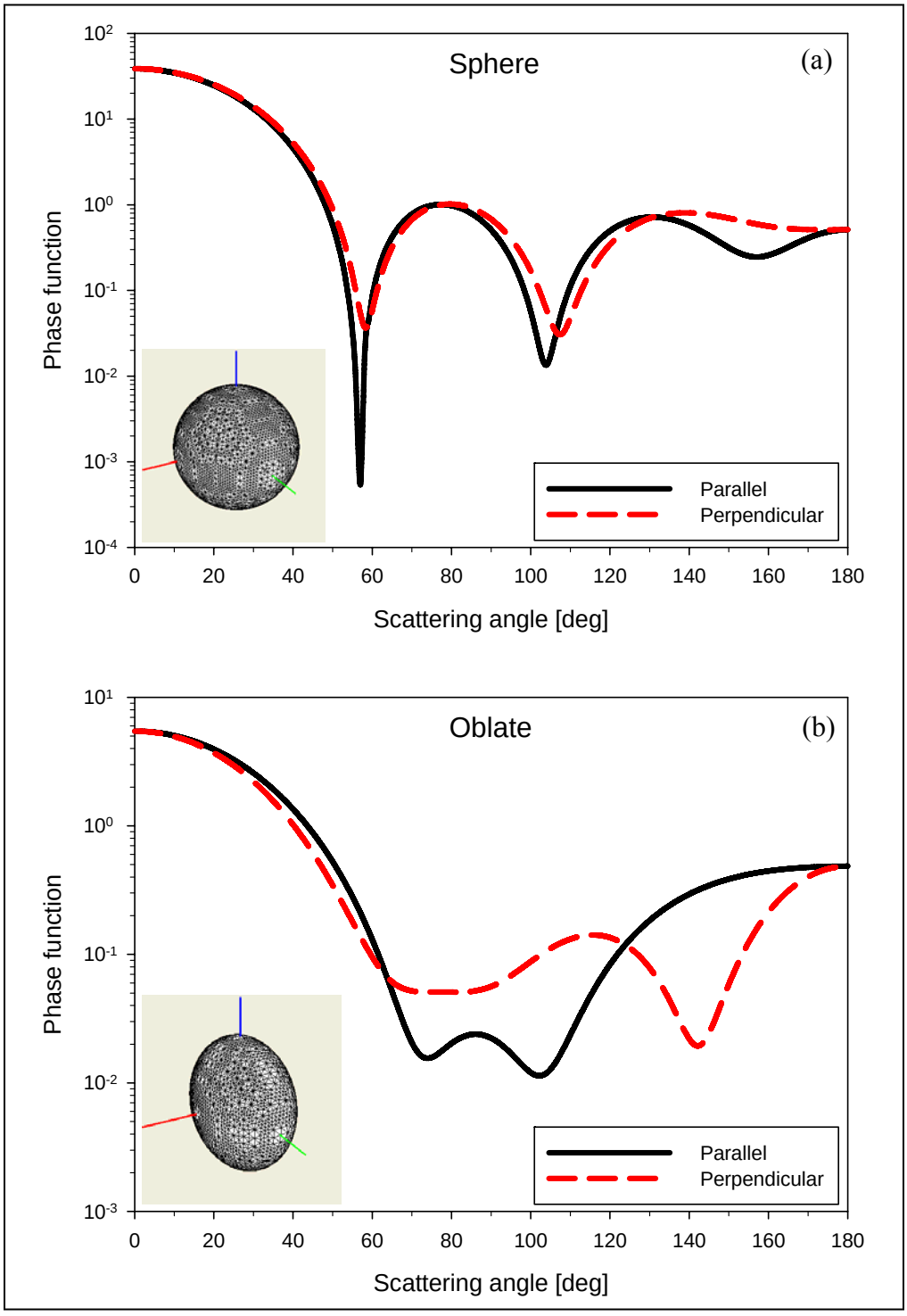

Figure 7.2 Scattering phase function of (a) sphere and (b) oblate having same surface area of sphere shown in (a) calculated with an incident wavelength of 532 nm, refractive index $n = 1.325 + 0i$, and a size parameter $kr = 13.2$ illuminated by an polarized laser beam.

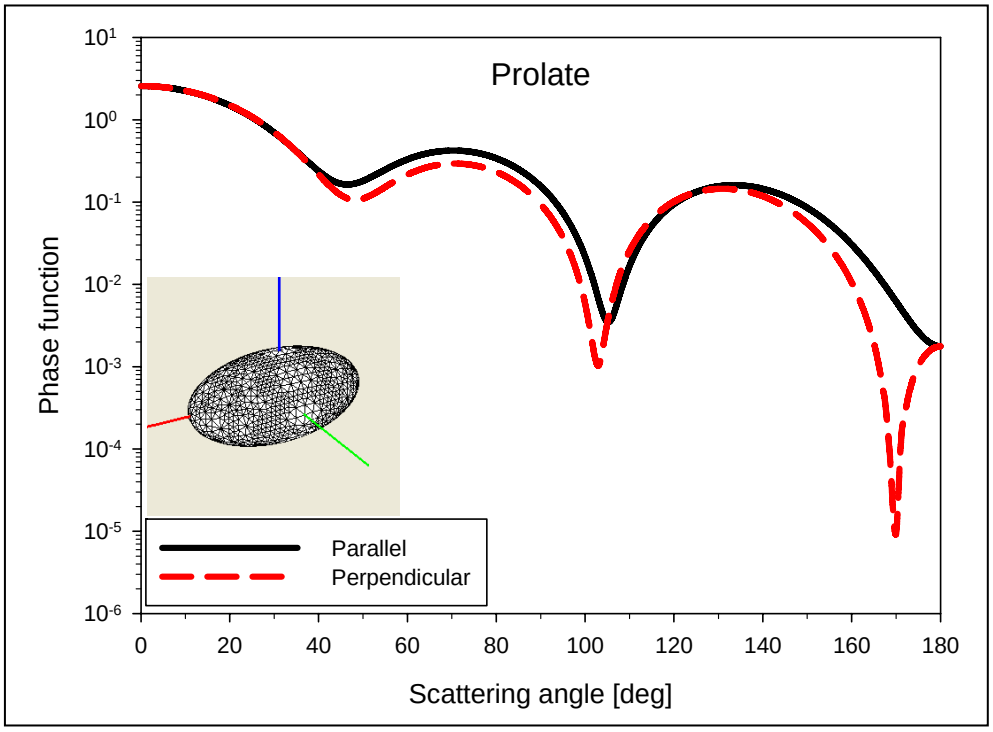

Figure 7.3 Scattering phase function of prolate having same surface area of sphere shown in Fig. 7.1 (a) calculated with an incident wavelength of 532 nm, refractive index $n = 1.325 + 0i$, and a size parameter $kr = 13.2$ illuminated by an polarized laser beam.

Third, future work could be focused on data inversion including multiple scattering. Data inversion algorithms for bistatic and multistatic lidar have been developed by Stevens (1996) and Novitsky (2002). They used a couple of assumptions to simplify their analysis, such as fixed refractive index of atmosphere, log-normal size distribution, spherical particle shape, and single-scattering dominant atmospheric condition. They both suggested that one should include more general distributions of the index of refraction, particle shape, and size distribution as parameters to be inverted. However, they didn't pay much attention to multiple scattering problems in their data inversion process. There could be two ways of doing this. First, if one can introduce a parameter that represents multiple scattering effects, for example, multiple scattering coefficient, $F(\lambda_0, z)$, like that used by Wang *et al*. (2003), and apply it to our multistatic lidar equation, then we could still use single-scattering-based data inversion methods developed by Stevens or Novitsky. The second way would be more complicated than the first one. It would

involve developing a data inversion algorithm based on the measurement of polarization ratio from multiple scattering.

As pointed out in this work, depolarization rises not only from multiple scattering, but also from molecular anisotropy and nonspherical particles. In our work, depolarization from the latter two factors was normally ignored due to our measurement environment of water aerosols. However, in case of long-scale measurements such as space-based lidar, those effects could be significant. The problem is that one should find a way to separate depolarization from multiple scattering, from those contributions from the other factors in advance.

REFERENCES

Allen, R. J. and C. M. R. Platt, "Lidar for multiple backscattering and depolarization observations", Appl. Opt., Vol. 16, 3193-3199, 1977.

Ashikhmin, Michael, Simon Premoze, Ravi Ramamoorthi, and Shree Nayar, "Blurring of Light due to Multiple Scattering by Participating Medium: A Path Integral Approach", Technical report, CUCS-017-04, 2004.

Atkins, Peter and Julio de Paula, *ATKINS' Physical Chemistry*, 7th Edition, Ch. 16 (Oxford University Press, New York, 2002)

Barnes, John E, Sebastian Bronner, Robert Beck, and N. C. Parikh, "Boundary layer scattering measurements with a charge-coupled device camera lidar", Appl. Opt., Vol. 42, No. 15, 2647-2652, 2003.

Berrocal, Edouard, David L. Sedarsky, Megan E. Paciaroni, Igor V. Meglinski, and Mark A. Linne, "Laser light scattering in turbid media Part I: Experimental and simulated results for the spatial intensity distribution", Opt. Exp., Vol. 15, 10649-10665, 2007.

Bissonnette, Luc R., "Multiscattering model for propagation of narrow light beams in aerosol media", Appl. Opt., Vol. 27, No. 12, 2478-2484, 1988.

Bissonnette, L. R. and D. L. Hutt, "Multiple scattering lidar", Appl. Opt., Vol. 29, 5045-5046, 1990.

Bissonnette, L. R., "Multiple scattering of narrow light beams in aerosols", Appl. Phys., Vol. 60, 315-323, 1995.

Bissonnette, L. R. and D. L. Hutt, "Lidar remote sensing of cloud and fog properties", SPIE, Vol. 2506, 512-523, 1995.

Bissonnette, L. R., P. Bruscaglioni, A. Ismaelli, G. Zaccanti, A. Cohen, Y. Benayahu, M. Kleiman, S. Egert, C. Flesia, P. Schwendimann, A. V. Starkov, M. Noormohammadian, U. G. Oppel, D. M. Winker, E. P. Zege, I. L. Katsev, and I. N. Polonsky, "LIDAR multiple scattering from clouds", Appl. Phys., Vol. 60, 355-362, 1995.

Bissonnette, Luc R., Gilles Roy, and Nathalie Roy, "Ground-based lidar measurement of liquid water content and effective droplet diameter in water clouds: instrumentation, retrieval method and results", Proc. of SPIE, Vol. 5235, 537-548, 2004.

Bissonnette, Luc R., "Lidar and Multiple Scattering", in Lidar Range-Resolved Optical Remote Sensing of the Atmosphere, Ch. 3 (Springer, New York, 2005)

Born, Max and Emil Wolf, *Principle of Optics*, 6th Edition, Ch. 13 (Pergamon Press, New York, 1980)

Cairo, Francesco, Guido Di Donfrancesco, Alberto Adriani, Lucio Pulvirenti, and Federico Fierli, "Comparion of various linear depolarization parameters measured by lidar", Appl. Opt., Vol. 38, 4425-4432, 1999.

Cohen, A., M. Kleiman, and J. Cooney, "Lidar measurements of rotational Raman and double scattering", Appl. Opt., Vol. 17, No. 12, 1905-1910, 1978.

Conant, William C., Athanasios Nenes, and John H. Seinfeld, " Black carbon radiative heating effects on cloud microphysics and implications for aerosol indirect forcing: 1. Extended Kohler theory, Journal of Geophysical Research, Vol. 107, AAC 23-1, 2002.

Deepak, Adarsh and Gail P. Box, "REPRESENTATION OF AEROSOL SIZE DISTRIBUTION DATAT BY ANALYTIC MODELS", in *ATMOSPHERIC AEROSOLS THEIR FORMATION, OPTICAL PROPERTIES, AND EFFECTS*, pp 79-109 (Spectrum Press, Hampton, 1982)

Deirmendjian, D., *Electromagnetic Scattering on Spherical Polydispersions* (Elsevier, New York, 1969)

Devara, P. C. S. and P. Ernest Raj, "REMOTE SOUNDING OF AEROSOLS IN THE LOWER ATMOSPHERIC USING A BISTATIC CW HELIUM-NEON LIDAR", J. Aerosol Sci., Vol. 20, 37-44, 1989.

Eloranta, E. W., CALCULATION OF DOUBLY SCATTERED LIDAR RETURNS, Ph. D Thesis, University of Wisconsin, 1972.

Elterman, L., "A series of stratospheric temperature profiles obtained with the searchlight technique", J. Geophys. Res., Vol. 58, 519-530, 1953.

Fenn, R. W., S. A. Clough, W. O. Gallery, R. E. Good, F. X. Kneizys, J. D. Mill, L. S. Rothman, E. P. Shettle, and F. E. Volz, "Optical and Infrared Properties of the Atmosphere" in *Handbook of Geophysics and the Space Environment*, Ch. 18 (Air Force Geophysics Laboratory, Springfield, 1985).

Gimmestad, Gary G., "Differential-Absorption Lidar for Ozone and Industrial Emissions", in *Lidar Range-Resolved Optical Remote Sensing of the Atmosphere*, Ch. 7 (Springer, New York, 2005)

Haywood, James and Olivier Boucher, "ESTIMATES OF THE DIRECT AND INDIRECT RADIATIVE FORCING DUE TO TROPOSPHERIC AEROSOL: A REVIEW", Review of Geophysics, Vol. 38, 513-543, 2000.

Hecht, Eugene, *OPTICS*, 2nd Edition (Wiley, Reading, 1987)

http://www.phys.unsw.edu.au/RESEARCH/ATMOSPHERIC/atmospheric_research.htm

Hu, Yongxiang, Zhaoyan Liu, David Winker, Mark Vaughan, and Vincent Noel, "Simple relation between lidar multiple scattering and depolarization for water clouds", Opt. Lett., Vol. 31, 1809-1811, 2006.

Hulbert, E. O., "Observations of a searchlight beam to an altitude of 28 kilometers", J. Opt. Soc. Am., Vol. 27, 377-382, 1937.

Hutt, D. L., L. R. Bissonnette, and L. Durand, "Multiple field of view lidar returns from atmospheric aerosols", Appl. Opt., Vol. 33, 2338-2348, 1994.

Kerker, M., *The scattering of Light and other Electromagnetic Radiation* (Academic Press, New York, 1969)

Kunkel, K. E. and J. A. Weinman, "Monte Carlo Analysis of Multiply Scattered Lidar Returns", J. Atmos. Sci., Vol. 33, 1772-1781, 1976.

Kunzli, N., R. Kaiser, S. Medina, and M. Studnicka, "Public-health impact of outdoor and traffic-related air pollution: a European assessment", THE LANCET, Vol. 356, 795-801, 2000.

Liou, K. N., An *Introduction to Atmospheric Radiation*, (Elsevier Science, San diego, 2002)

Liou, K. N. and R. M. Schotland, "Multiple Backscattering and Depolarization from Water Clouds for a Pulsed Lidar System", J. Atmos. Sci., Vol. 28, 772-784, 1971.

Losacco, Aurora Maria, Marco Giannini, Vincenzo Lombardo, Giovanni Pappalettera, and Francesco Tedeschi, "STUDYING FEASIBILITY OF USING LIDAR TO CONTROL THE EFFECT OF ARTIFICIAL COLD FOG DISSIPATION", ILRC 2004, 259-262, 2004.

Love, Steven P., Anthony B. Davis, Cheng Ho, and Charles A. Rohde, "Remote sensing of cloud thickness and liquid water content with Wide-Angle Imaging Lidar", Atmos. Res., 295-312, 2001.

Mannoni, A., C. Flesia, P. Bruscaglioni, and A. Ismaelli, "Simulated Multiply-Scattered Lidar Returns From Nonspherical Particls", SPIE, Vol. 2506, 666-676, 1995.

Measures, R. M., *Laser Remote Sensing* (Wiley, New York, 1984)

Meki, K, K. Yamaguchi, X. Li, Y. Saito, T. D. Kawahara, and A. Nomura, "Range-resolved bistatic imaging lidar for the measurement of the lower atmosphere", Opt. Lett., Vol. 21, No. 17, 1318-1320, 1996.

Mie, G., "Contributions to the optics of turbid media, particularly of colloidal metal solutions", Ann. Physik, Vol. 25, 377-445, 1908.

Miller, S. D. and G. L. Stephens, "Multiple scattering effects in the lidar pulse stretching", J. Geophys. Res., Vol. 104, 205-219, 1999.

Mishchenko, M. I., L. D. Travis, and A. A. Lacis, *Scattering, Absorption, and Emission of Light by Small Particles*, Ch. 10 (Cambridge, New York, 2002)

Mishchenko, Michael I., Li Liu, Daniel W. Mackowski, Brian Cairns, and Gorden Videen, "Multiple scattering by random particulate media: exact 3D results", Opt. Exp., Vol. 15, 2822-2836, 2007.

Mooradian, G. C. and M. Geller, "Temporal and angular spreading of blue-green pulses in clouds", Appl. Opt., Vol. 21, 1572-1577, 1982.

Novitsky, E. J., Multistatic Lidar Profile Measurement of Lower Troposphere Aerosol and Particulate, Ph. D Thesis, Ch. 4, The Pennsylvania State University, 2002.

Pal, Shiv R. and Luc R. Bissonnette, "Multiple-scattering effect on ozone retrieval from space-based differential absorption lidar measurements", Appl. Opt., Vol. 37, No. 27, 6500-6510, 1998.

Pal, S. R. and A. I. Carswell, "Polarization Properties of Lidar Backscattering from Clouds", Appl. Opt., Vol. 12, 1530-1535, 1973.

Pal, S. R. and A. I. Carswell, "Multiple scattering in atmospheric clouds: lidar observations", Appl. Opt., Vol. 15, 1990-1995, 1976.

Pal, S. R. and A. I. Carswell, "Polarization anisotropy in lidar multiple scattering from atmospheric clouds", Appl. Opt., Vol. 24, 3464-3471, 1985.

Philbrick, C. R., "Application of Raman lidar advancements in meteorology and air quality monitoring", SPIE, Vol. 4893, 61-69, 2002.

Philbrick, C. R. , Zhwen Liu, Sven Bilen, William Brune, Hans Hallen, Yang Zhang and Philip Hopke, “Speices Spectra & Aerosol Scatter Intrument (SSASI)”, A proposal to the NASA Intrument Incubator Program (IIP)-2004 NN-H-04-Z-YF-009-N, 2004.

Pierce, R. M., Java Ramaprasad, and Eric Eisenberg, “Optical attenuation in fog and clouds”, SPIE, Vol. 4530, 58-71, 2001.

Piironen, P., A High Spectral Resolution Lidar Based on an Iodine Absorption Filter, Ph. D Thesis, University of Joensuu, 1994.

Platt, C. M. R. and David M. Winker, “Multiple scattering effects in clouds observed from LITE”, SPIE, Vol. 2580, 60-71, 1995.

Raj, P. Ernest, P. C. S. Devera, G. Panduthurai, R. S. Maheskumar, and K. K. Dani, “Some atmospheric aerosol characteristics as determined from laser angular scattering measurements at a continental urban station”, Atmosfera, 39-52, 2003.

Reagan, J. A., D. M. Byrne, and B. M. Herman, “Bistatic lidar: a tool for characterizing particulates. Part 1. The remote sensing problem”, IEEE Trans. Geosci. Remote Sens., 229-235, 1982.

Reichardt, Jens, “Error analysis of Raman differential absorption lidar ozone measurements in ice clouds”, Appl. Opt., Vol. 39, No. 33, 6058-6071, 2000.

Rowell, R. L., G. M. Aval, and J. J. Barrett, “Rayleigh-Raman Depolarization of Laser Scattered by Gases”, J. Chem. Phys., Vol. 54, 1960-1964, 1971.

Roy, G., L. R. Bissonnette, C. Bastille, and G. Vallee, “Estimation of cloud droplet size density distribution form multiple-field-of-view lidar returns”, Opt. Eng., Vol. 36, 3404-3415, 1997.

Roy, G., L. R. Bissonnette, C. Bastille, and G. Vallee, “Retrieval of droplet-size density distribution from multiple-field-of-view cross-polarized lidar signals: theory and experimental validation”, Appl. Opt., Vol. 38, No. 24, 5202-5211, 1999.

Roy, Nathalie, Gilles Roy, Luc R. Bissonnette, and Jean-Robert Simard, “Lidar depolarization asymmetry measurements and its relation with the optical depth”, Proc. of SPIE, Vol. 5829, 209-218, 2005.

Sassen, K., An evaluation of polarization diversity lidar for cloud physics research, Ph. D Thesis, University of Wyoming, 1976.

Sassen Kenneth and Kou-Nan Liou, " Scattering of Polarized Laser Light by Water Droplet, Mixed-Phase and Ice Crystal Clouds. Part II: Angular Depolarizing and Multiple-Scattering Behavior", J. Atmos. Sci., Vol. 36, 852-861, 1979.

Sassen, K. and R. L. Petrilla, "Lidar depolarization from multiple scattering in marine stratus clouds", Appl. Opt., Vol. 25, 1450-1459, 1986.

Schotland, R. M., "The detection of the vertical profile of atmospheric gases by means of a ground-based optical radar", Proc. Third Symp. *On Remote Sensing of the Environment*, 215-225, 1964.

Segelstein, D., The Complex Refractive Index of Water, MS Thesis, University of Missouri, 1981.

Seinfeld, John H. and Spyros N. Pandis, *ATMOSPHERIC CHEMISTRY AND PHYSICS*, Ch. 7 (John Wiley & Sons, Inc., New York, 1998)

Seldomridge, Nathan L., Joseph A. Shaw, and Kevin S. Repasky, "Dual-polarization lidar using a liquid crystal variable retarder", Opt. Eng., Vol. 45, 106202-1~106202-10, 2006.

Steinbrecht, W. and A. I. Carswell, "Evaluation of the effects of Mount Pinatubo aerosol on differential absorption lidar measurements of stratospheric ozone", J. Geophys. Res., Vol. 100, 955-958, 1995.

Stevens, T. D., Bistatic Lidar Measurements of Lower Tropospheric Aerosols, Ph. D Thesis, The Pennsylvania State University, 1996.

Stewart, Dorathy A. and Oskar M. Essenwagner, "A Survey of Fog and Related Optical Propagation Characteristics", Review of Geophysics and Space Physics, Vol. 20, 481-495, 1982.

Sugimoto, Nobuo, "Feasibility of a Lidar Utilizing the Glory for Measuring Particle Size of Water Clouds", Opt. Rev., Vol. 6, 539-544, 1999.

Sugimoto, Nobuo, "Two-Color Dual-Polarization Pulsed Bistatic Lidar for Measuring Water Cloud Droplet Size", Opt. Rev., Vol. 7, No. 3, 235-240, 2000.

Tatarov, B., B. Kaprielov, and I. Kolev, "Multiple scattering effect on the lidar signal depolarization in the study of atmospheric objects in the planetary boundary layer", SPIE, Vol. 3433, 365-373, 1998.

Tatarov, B., T. Trifonov, B. Kaprielov, and I. Kolev, "Dependence of the lidar signal depolarization on the receiver's field of view in the sounding of fog and clouds", Appl. Phys., B 71, 593-600, 2000.

Thomas, By L., "Laser radar observations of middle-atmosphere structure and composition", Phil. Trans. R. Soc. Land., Vol. 323, 77-89, 1987.

Van Deelen, Rutger, Jochen Landgraf, and Ilse Aben, "Multiple elastic and inelastic light scattering in the Earth's atmosphere: a doubling-adding method to include rotational Raman scattering by air", JQSRT, Vol. 95, 309-330, 2005.

Van de Hulst, H. C., *Light Scattering by Small Particles*, Ch. 1 (Wiley, New York, 1957)

Veihelmann, Ben, Martin Konert, and Wim J. van der Zande, "Size distribution of mineral aerosol: using light-scattering models in laser particle sizing", Appl. Opt., Vol. 45, 6022-6029, 2006.

Walker, Ronald E. and John W. McLean, "Lidar equations for turbid media with pulse stretching", Appl. Opt., Vol. 38, 2384-2397, 1999.

Wandinger, Ulla, Albert Ansmann, and Claus Weitkamp, "Atmospheric Raman depolarization-ratio measurements", Appl. Opt., Vol. 33, No. 24, 5671-5673, 1994.

Wandinger, Ulla, "Multiple-scattering influence on extinction and baskscatter-coefficient measurements with Raman and high-spectral-resolution lidars", Appl. Opt., Vol. 37, No. 3, 417-427, 1998.

Wandinger, Ulla, "Raman Lidar", in *Lidar Range-Resolved Optical Remote Sensing of the Atmosphere*, Ch. 9 (Springer, New York, 2005).

Wang, Shih Chen and Richard C. Flagen, "Scanning Electrical Mobility Spectrometer", Aerosol Science and Technology, Vol. 13, 230-240, 1990.

Wang, X., A. Boselli, L. D' avino, R. Velotta, N. Spinelli, P. Bruscaglioni, A. Ismaelli, and G. Zaccanti, "An algorithm to determine cirrus properties from analysis of multiple-scattering influence on lidar signals", Appl. Phys., B 80, 609-615, 2005.

Watson, J. G. and J. C. Chow, *Reconciling Urban Fugitive Dust Emissions Inventory and Ambient Source Contribution Estimates: Summary of Current Knowledge and Needed Research* (Desert Research Institute, Energy and Environment Engineering Center, DRI Document No. 6110.4D2, 1999)

Welsh, Byron M. and Chester S. Gardner, “Bistatic imaging lidar technique for upper atmospheric studies”, Appl. Opt., Vol. 28, 82-88, 1989.

Werner, Christian, Jurgen Streicher, Hartmut Herrmann, and Hans-Gunter Dahn, “Multiple-scattering lidar experiment”, Opt. Eng., Vol. 31, 1731-1745, 1992.

Werner, Christian, Jurgen Streicher, Ines Leike, and Christoph Munkel, “Visibility and Cloud Lidar” in *Lidar Range-Resolved Optical Remote Sensing of the Atmosphere*, Ch. 6 (Springer, New York, 2005).

Whitby, K. T., R. B. Husar, and B. Y. H. Liu, “The Aerosol Distribution of Los Angeles Smog”, Journal of Colloid and Interface Science, Vol. 102, No. 1, 177-204, 1972.

Whiteman, David N. and S. Harvey Melfi, “Raman lidar measurements of cloud liquid water and droplet size”, SPIE, Vol. 3867, 82-90, 1999.

Whiteman, David N., “Examination of the traditional Raman lidar technique. I. Evaluating the temperature-dependent lidar equations”, Appl. Opt., Vol. 42, 2571-2592, 2003.

Widada, Wahyu, Hideki Kinjo, Hiroaki Kuze, Nobuo Takeuchi, and Makoto Sasaki, “Effect of Multiple Scattering in the Lidar Measurement of Tropospheric Aerosol Extinction Profiles”, Opt. Rev., Vol. 8, No. 5, 382-387, 2001.

Wiegner, Mattias, “Potential of Lidars for Aerosol Remote Sensing”, Proc. of SPIE, Vol. 5235, 1-14, 2004.

Young, Andrew T., “Rayleigh Scattering”, Phys. Today, Vol. 35, 42-48, 1982.

Zaccanti, Giovanni, Piero Bruscaglioni, and Michele Dami, “Simple inexpensive method of measuring the temporal spreading of a light pulse propagating in a turbid medium”, Appl. Opt., Vol. 29, 3938-3944, 1990.

Zuev, V. E., *Laser Beam in the Atmosphere* (Plenum Publ. Co., New York, 1981)

VITA

Jin Hyen Park

Jinhyen Park was born in Young-Ju, Korea on January 30, 1973. He attended Young-Ju High School and graduated in 1991. He obtained a Bachelor of Science degree in Physics from the Korea Military Academy in 1995 and earned a Master of Science degree in Electrical Engineering from the University of Pittsburgh in 2000. During the years between 1995 and 2003 he served in the 7^{th} Division as a platoon leader, the 11^{th} Airborne Brigade as an aide-de-camp, the 8^{th} Division as an intelligence officer, and at the Korea Military Academy as an instructor in the Physics Department. He was promoted to Major in 2006. He received a Doctor of Philosophy in Electrical Engineering from The Pennsylvania State University in May 2008. His primary research interests are in optical scattering in atmosphere and remote sensing.